STABILITY AND TRANSITION OF THREE-DIMENSIONAL ROTATING BOUNDARY LAYERS

by

ZAHIR HUSSAIN

A thesis submitted to
The University of Birmingham
for the degree of
DOCTOR OF PHILOSOPHY

School of Mathematics
The University of Birmingham
March 2010

Abstract

The flow over a rotating cone in still fluid is susceptible to crossflow and centrifugal instability modes of spiral nature, depending on the cone half-angle. For parameters ranging from propeller nose cones to rotating disks, the instability triggers co-rotating vortices, whereas for slender spinning missiles, counter-rotating vortices are observed. Upon introduction of an oncoming flow, the problem essentially becomes a battle between the streamwise and azimuthal shear flow, due to the rotating surface. The boundary layer instability is again visualized by the formation of spiral vortices, which wrap around the cone surface in a helical nature.

For both crossflow and centrifugal instabilities, we derive the mean flow boundary layer equations and investigate the high Reynolds number asymptotic linear stability of the flow to inviscid crossflow modes (type I), type II modes, which arise from a viscous-Coriolis force balance, and neutral modes for a slender cone. The influence of the cone half-angle (ψ) and axial flow strength (s or T_s) on the number and orientation of the spiral vortices is examined, with comparisons made with previous experimental and numerical results.

Keywords: crossflow/centrifugal instability, co-rotating/counter-rotating vortices, inviscid type I/viscous type II modes, rotating cone/disk, three-dimensional boundary layers.

This thesis is devoted to the memory of my parents,
Mukhtar Begum & Ashiq Hussain.

ACKNOWLEDGEMENTS

I would like to thank my supervisor, Dr. Sharon Stephen, for her outstanding guidance and insight into my research work during writing this thesis. I am grateful to Dr. Stephen Garrett for providing me with his PhD thesis as well as helpful discussions on his research papers. I would also like to acknowledge financial support from the School of Mathematics and the Engineering and Physical Sciences Research Council. Finally, I am greatly indebted to my family and friends for their sustained encouragement and support since I started at Birmingham.

CONTENTS

CHAPTER 1

Introduction

There has been considerable recent interest in the exact mechanisms governing the instability and transition to turbulence of flow in three-dimensional boundary layers. Comprehensive reviews covering geometries ranging from swept-wings to rotating disks and rotating spheres are given by Reed & Saric [36], Saric *et al.* [40] and Reshotko [37]. A great deal of emphasis of this work has been placed on understanding the instability mechanisms that lead to breakdown of the boundary layer, with much of the application directed towards developing the modern day design of laminar aerofoils. The nature of a three-dimensional boundary layer lends itself to stream-wise as well as cross-stream flow components. Therefore, within the linear framework, the types of mechanisms at work, which have been discovered to date include the instability of flow due to stream-wise Tollmien-Schlichting waves, co-rotating crossflow vortices and counter-rotating Görtler vortices, for example on the concave underside of an aerofoil wing (see Hall [15]). Since the first study by Gray [12] for a swept-wing, the effects of crossflow instability have been the subject of both theoretical and experimental studies by Gregory *et al.* [13] and Hall [16] for a rotating disk and Hall & Malik [19] for a three-dimensional attachment-line boundary layer.

In this study, we examine the effects of these instabilities on three-dimensional axisymmetric rotating bodies, such as the rotating cone. Physically, the rotating cone models the nose of a missile head travelling through the atmosphere, with ogive-nose cone shapes (such as those studied by Kohama [29] and Mueller *et al.* [35]) representing more realistic aerodynamic models for designs of modern missile heads. The first experimental work for this problem was carried out by Kreith, Ellis & Giesing [31], Tein & Campbell [43] and Kappesser, Greif & Cornet [21] for a rotating cone in still fluid, and by Salzberg & Kezios [39] for a rotating cone in axial flow, which is found to exhibit a stabilising effect on the flow to disturbances. These experiments were restricted to measuring Reynolds numbers for transition to turbulence, but were unable to sufficiently resolve the nature of the mechanisms at work within the region governing laminar to turbulent flow.

In the 1980s, experimental studies mainly at the Institute of High Speed Mechanics, Sendai, Japan, once again excited interest in the theoretical structure of the transition region on rotating axisymmetric bodies, as well as the underlying instabilities causing the boundary layer to breakdown. Studies by Kobayashi *et al.* [25] and Kobayashi & Izumi [26] (for rotating cones) as well as by Kohama [29] and Mueller *et al.* [35] (for ogive-nose rotating cones) observed the existence of spiral vortices, which are generated in the region of steep shear velocity gradients near the cone wall. Using a high-speed strobe light flow visualisation technique, these studies were able to show in detail the spiral vortices being shed from the cone boundary layer under the action of strong distorting forces from the mean velocity field. A hot-wire anemometer technique was used to produce measurements of the flow field. Interestingly, the spiral vortices were observed to be stationary relative to the cone, wrapping round its surface and remaining fixed for all rotation and axial flow rates on the cone.

It was noticed that a key influence on the nature of rotation of these vortices is the cone half-angle. For example, the experimental study by Kobayashi & Izumi [26] for

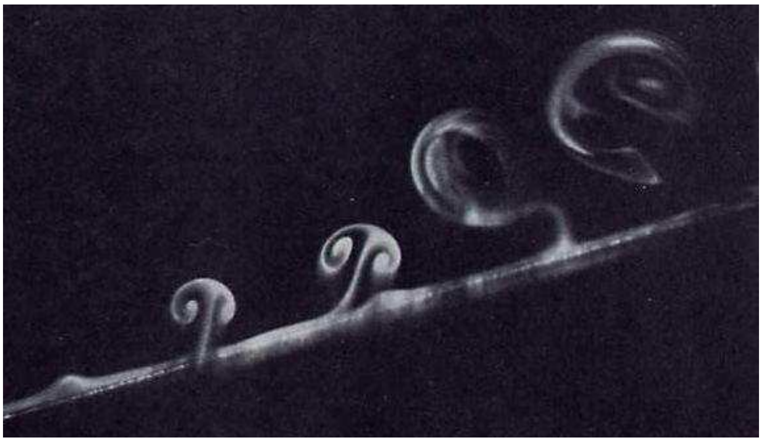

Figure 1.1: Cross-sectional flow visualisation showing pairs of counter-rotating Görtler vortices at $\psi = 15°$ (Kobayashi & Izumi [26]).

cones with slender half-angles, ψ, as low as 15° in still fluid, show the existence of pairs of counter-rotating Görtler vortices, which arise from a dynamic instability, induced by the centrifugal force of the flow field (as shown in figure 1.1).

However, as the half-angle is increased beyond 30°, their results clearly show the spiral vortices change from pairs of counter-rotating Görtler vortices to co-rotating crossflow vortices (see figure 1.2). Indeed, their measurements of the spiral angle (the angle between the normal to the vortices and the cone meridian) are shown to approach those observed for a rotating disk as the half-angle tends to 90°. It is well known from the studies of Gregory *et al.* [13] and Hall [16] that the stationary spiral vortices observed on the rotating disk are in fact co-rotating vortices attributed to an underlying crossflow instability, based on an unstable inflexion point in the crossflow component of the flow field. The observed centrifugal instability for cones with smaller half-angles stems from an inherently different process to that governing the crossflow instability for cones of larger half-angles. Therefore, there seems to be a distinct variation in the underlying physical mechanism governing instability for more slender cones.

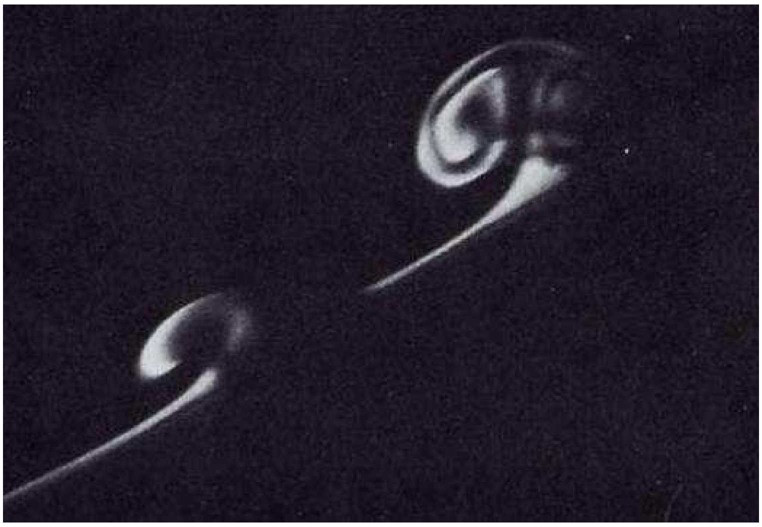

Figure 1.2: Cross-sectional flow visualisation showing co-rotating crossflow vortices at $\psi = 30^\circ$ (Kobayashi & Izumi [26]).

Furthermore, Garrett [7], in his PhD thesis, uses a parallel flow approximation to setup the problem of a rotating cone in still fluid and axial flow. Including viscous and streamline-curvature effects, the resulting eigenvalue problem involving the Orr-Sommerfeld equation is solved computationally using a finite difference approach. Both convective and absolute instabilities of axisymmetric rotating bodies are investigated, and it is found that the respective Reynolds numbers at the onset of each type of instability for the rotating cone compare well with experimentally observed critical Reynolds numbers for the appearance of spiral vortices and transition to turbulent flow on cones rotating in still fluid with half-angles between $50^\circ - 90^\circ$. However, for half-angles less than 50°, he found an increasing discrepancy between these Reynolds numbers, again suggesting an apparent change in the physical nature of the instability, which provides the route to transition. For the absolute instability case of the rotating cone, Garrett's work is developed in a recent study (see Garrett & Peake [10]), where this discrepancy for more slender cones is discussed more in the context of existing experimental results.

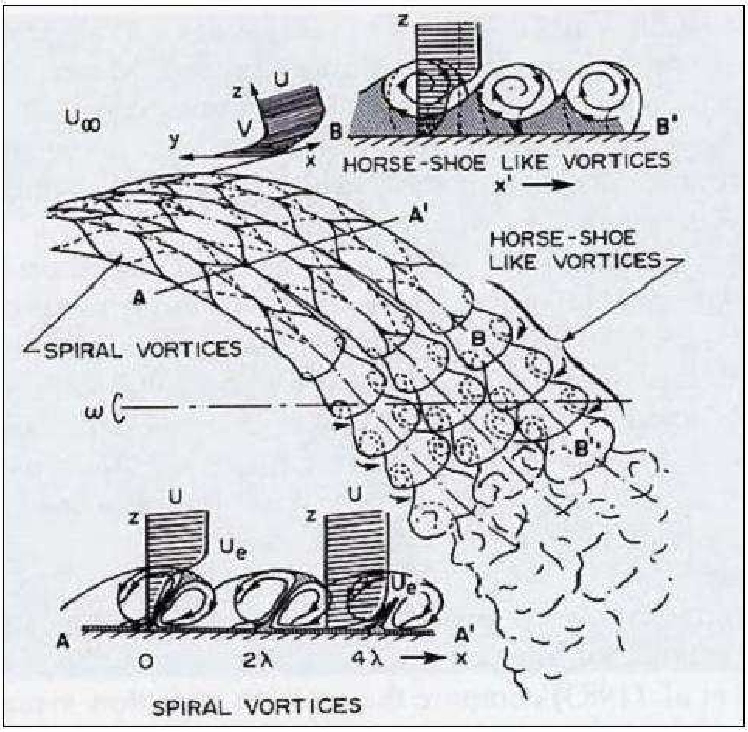

Figure 1.3: Schematic representation of the secondary instability (Kohama [30]).

In the present study, we examine this transformation of the underlying instability mechanism. As the cone half-angle is reduced, we investigate the existence of a possible critical half-angle, predicted by theory, for the variation from a predominantly crossflow instability to a distinct centrifugal instability, manifested in the appearance of Görtler vortices.

The Görtler instability is a type of centrifugal mechanism, which occurs in the presence of wall curvature. When the boundary layer thickness is small compared with radius of curvature, the flow instability is visualised through the formation of Görtler vortices, which break down to form successive pairs of counter-rotating vortices. Early work on the Görtler instability mechanism concerned the linear stability of two-dimensional flows over concave walls, for example by Görtler [11] and Smith [41]. The parallel-flow approximation was used, and higher-order curvature effects were neglected. Later, Hall [14] considered non-parallel effects in the basic flow. In particular, the stability of short-wavelength disturbances in fully developed flows between concentric cylinders was considered (with the inner cylinder rotating). Hall found that the disturbances are concentrated in internal viscous or critical layers well away from the wall and the free stream. Further numerical investigation by Hall [17] observed the development of nonlinear non-parallel vortices in growing boundary layers. It was found that as the nonlinear disturbance evolves, the perturbation energy becomes concentrated in the mean flow direction. The first attempt to characterise the three-dimensional effects of the centrifugal Görtler instability mechanism was made by Hall [15], who investigated flow over an infinitely long swept cylinder. Importantly, it was observed that it is the relative size of crossflow and chordwise flow over the cylinder which determines the vortex structure. These wide ranging applicability and generality of these studies led to the establishment of the governing scales, which have become useful in analysing the Görtler instability mechanism. By scaling the coordinate spanwise to the vortex structures on the boundary layer thickness, along with the normal coordinate, it was possible to develop a linear analysis of neutral modes characterised by a large vortex wavenumber.

A comprehensive review of these studies may be found in Hall [18], where the receptivity problem for Görtler vortices impinging on the leading edge of the wall was also considered. The neutral curve of the most dangerous mode was obtained, and shown to agree well with available experiments. Furthermore, Denier *et al.* [3] investigated the receptivity of Görtler vortices in terms of how they may be triggered by wall roughness elements. They identified the most unstable Görtler mode governed by linear stability theory within a two-dimensional boundary layer. Bassom & Hall [2] subsequently extended some of this work analyse the effect of altering the amount of crossflow present in a boundary-layer flow as a mechanism for representing the degree of three-dimensionality within the flow in both small- and large-wavenumber limits. It was found that sufficiently strong levels of crossflow eventually eradicate the presence of the Görtler instability mechanism within the boundary. This is of particular interest in the boundary-layer flow over a rotating cone, as we see from the experiments of Kobayashi & Izumi [26] that the centrifugally dominated Görtler-type instability for small cone half-angles eventually is visualised as a crossflow dominated instability for larger half-angles.

We now focus on experimental and numerical studies, which have investigated the existence of counter-rotating vortices for slender rotating cones. The cone half-angles considered are sufficiently small, such that the centrifugal instability mechanism dominates.

Firstly, in the case of still fluid, the study of Kobayashi & Izumi [26] used five smoothly finished Aluminium alloy test cones of cone half-angles ranging from 15° to 75°. A hot-wire anemometer was used to enable accurate measurements of the velocity field and the cones were spread with Titanium tetra-Chloride to enable visualisation of the boundary-layer flow. As mentioned earlier, their results clearly show the presence of counter-rotating vortex pairs at a cone half-angle of 15°, which undergo a transition to co-rotating crossflow vortices for a cone half-angle of 30°. We identify the counter-rotating vortices at small half-angle as pairs of Görtler vortices and suggest that as in the study of Bassom & Hall [2], increasing the level of crossflow eventually leads to the eradication of the counter-rotating Görtler vortex pairs. In addition to experiments, Kobayashi & Izumi [26] also developed numerical calculations of the vortex pairs for a slender cone. Streamlines at an unstable state for a cone of half-angle 15° are obtained from the velocity perturbations as eigenfunctions; their results clearly show the counter-rotating orientation of successive vortex structures. Furthermore, the study presents a numerical stability diagram showing vortex wavenumber against Reynolds number for a slender 15° cone. It is our aim to develop an asymptotic comparison with the large-wavenumber branch of Kobayashi & Izumi [26] to further identify the observed counter-rotating vortices as pairs of Görtler vortices.

Secondly, we consider the slender rotating cone placed in an oncoming axial flow. Koh & Price [27] have analysed heat transfer characteristics for a slender cone of half-angle 15° and developed a novel method for obtaining the velocity profiles with in the laminar boundary layer. In addition, Salzberg & Kezios [39] report the stabilising effect of increasing the axial flow strength on the flow stability. However, using a parallel probe of two hot wires to measure the velocity field over a 15° rotating cone spread with Titanium tetra-Chloride, the experiments of Kobayashi *et al.* [25] clearly show the laminar-turbulent transition region. Furthermore, close-up images show the presence of counter-rotating vortex pairs, which appear forced along the cone surface, due to the streamwise forcing of the oncoming axial flow. Earlier, Kobayashi [23] developed a numerical procedure for solving the eigenvalue problem for the 15° rotating cone in an axial flow of varying strength. As with the still fluid case, a stability diagram is presented showing the vortex wavenumber against Reynolds number. Once again, it is our aim to develop a large vortex wavenumber asymptotic comparison with the neutral stability curve presented by Kobayashi [23]. We use appropriate scalings outlined in Hall [18] to capture the effect of the centrifugal Görtler instability mechanism in order to model the small perturbations in the slender rotating cone boundary layer, which are visualised as spiral vortices.

Interestingly, the studies by Kohama [28], for a rotating cone, as well as Kohama [29] and Mueller *et al.* [35], for an ogive-nose rotating cone, led to the detection of a further secondary instability as the Reynolds number was increased towards the transitional value. The primary mode counter-rotating vortices were observed to transform into horseshoe-like vortices, exhibiting rapid growth over small convective time and length-scales. This led to a swift breakdown to turbulent flow. Figure 1.3 shows the observed counter-rotating primary mode vortices (along the cross-section $A - A'$) as they breakdown into horseshoe vortex disturbances, which 'roll-up' along the cone surface in the effective velocity direction $B - B'$. Notice that each horseshoe-like disturbance still consists of a pair of counter-rotating vortices. The structures display a phase velocity relative to the wall, after originating on the surface of the primary-mode spiral vortices with very steep or near-discontinuous velocities. The fact that these horseshoe-like vortices travel along the cone surface suggests physically they arise from a viscous instability, such as the streamwise Tollmien-Schlichting kind. In fact, the steep turbulent breakdown nature of this secondary instability indicates a nonlinear viscous structure is present for the transition to take place.

An alternative area of investigation involves the introduction of an imposed external flow applied to the rotating cone in the axial direction. Importantly, computation of the basic flow in this case proves challenging, as we shall show in §2. However, some progress has been made by Koh & Price [27] by expressing the basic flow as a function of both streamwise and surface-normal variables as opposed to solely the normal. Experimental studies have been conducted by Kreith *et al.* [31], Mueller et al. [35], Tein & Campbell [43]. However, these investigations were unable to fully resolve or visualise the nature of the instability governing the spiral vortices and were restricted to analysing heat and mass transfer. Eventually, studies by Salzberg & Kezios [39] and Kobayashi [23] showed that the introduction of such a flow has been found to stabilise the fluid to centrifugal instabilities for slender cones. Furthermore, Kobayashi *et al.* [25] have conducted experiments on a cone of half-angle 15° for a range of external axial flow ratios. Kobayashi & Izumi [26] observe that the counter-rotating vortices are initially aligned with each other in the azimuthal direction as circular 'Taylor' vortices. However, as the axial flow is applied and increased, the vortices are forced in the streamwise direction by the centrifugal forcing of the mean flow. Eventually, for sufficiently large axial flow, the circular waves develop into spiral vortices which grow further downstream. In terms of axial flow studies for larger half-angle cones, there exist only the numerical studies conducted by Garrett [7] and later Garrett & Peake [10]. They find that for each half-angle, increasing the axial flow has a stabilising effect on the crossflow vortices, forcing the fluid further in the downstream direction.

The aim of this study is to follow and extend the analysis of Hall [16] for a rotating disk, to a rotating cone, formulating the linear disturbance equations in §2, before identifying the upper branch inviscid modes in §3, which are referred to as type I modes where the boundary layer becomes unstable away from the wall. We investigate the change in behaviour for variations in the cone half-angle, as well as for rotating cones in still fluid and in axial flows of increasing strength. In §4, we subsequently consider the structure of the stationary short-wavelength viscous wall modes at high Reynolds number, corresponding to the lower branch of the neutral stability curve. In the literature, these are termed type II modes, with the instability stemming from effects near to the wall. Furthermore, it is worth noting that the type I/type II modes are sometimes distinguished as crossflow and streamline curvature modes, respectively (see Garrett [7]). Next, in §5, we formulate the problem for flow over a slender rotating cone, which governed by the centrifugal instability. We utilise a large Reynolds number analysis and also assume a large vortex wavenumber, attempting to extend the work of Hall [14] for a fully developed flow. Subsequently, in §§§6, 7 and 8 we derive estimates for the right-hand branch of the neutral stability curve in terms of the Taylor number against the vortex wavenumber. There are three distinct cases: a slender cone (of half-angle 15° or less) rotating in still fluid exhibiting circular waves; growing spiral waves (or half-angles in the range $15^\circ - 45^\circ$) and in varying axial flow. Finally, in §9, we draw our results together and present our conclusions, with a view to explaining some of the underlying physical mechanisms at work governing the instability of the rotating cone boundary layer as it undergoes transition to turbulence.

Chapter 2

Problem formulation for the crossflow instability

Consider a cone rotating about its axis of symmetry, with dimensional angular velocity Ω^*. The cone is placed in a fluid with an oncoming axial flow parallel to its axis of rotation, with the angle between the cone's slanting surface and its symmetry axis being defined as the cone half-angle, denoted by ψ. The arrangement is shown in figure 2.1, where we have set up Cartesian coordinates (X^*, Y^*, Z^*) with origin at the apex of the cone, and subsequently transformed to the orthogonal curvilinear coordinates (x^*, θ, z^*), representing a streamwise coordinate along the cone surface, an azimuthal coordinate and a surface-normal coordinate, respectively. The local surface radius of the cone is given by $r_0^* = x^*\mathrm{sin}\psi$ and the coordinate transformation takes the form

$$
\begin{aligned}
X^* &= x^*\mathrm{cos}\psi - z^*\mathrm{sin}\psi, && (2.1)\\
Y^* &= (x^*\mathrm{sin}\psi + z^*\mathrm{cos}\psi)\mathrm{sin}\theta, && (2.2)\\
Z^* &= (x^*\mathrm{sin}\psi + z^*\mathrm{cos}\psi)\mathrm{cos}\theta, && (2.3)
\end{aligned}
$$

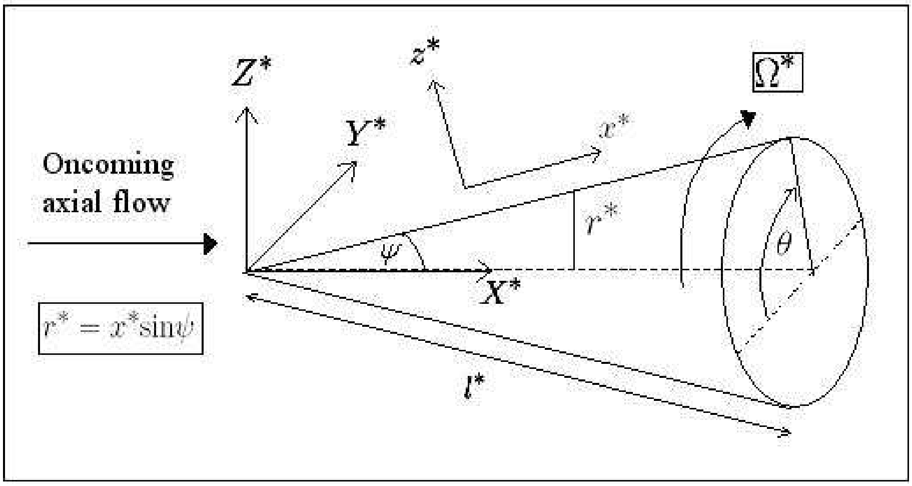

Figure 2.1: Diagram showing model setup for a rotating cone.

where $h_1 = 1$, $h_2 = h^* = x^*\sin\psi + z^*\cos\psi$ and $h_3 = 1$ are the scale factors of the curvilinear coordinate system (x^*, θ, z^*).

The Navier-Stokes equations and continuity equation to be applied in a reference frame rotating with the cone about the X^*-axis at an angular velocity $\mathbf{\Omega}$ are given by

$$\begin{aligned} \frac{\partial \boldsymbol{u}}{\partial t} + (\boldsymbol{u}.\nabla)\boldsymbol{u} + 2\mathbf{\Omega} \times \boldsymbol{u} + \mathbf{\Omega} \times (\mathbf{\Omega} \times \boldsymbol{r}) &= -\frac{1}{\rho^*}\nabla p^* + \nu^*\nabla^2\boldsymbol{u}, && (2.4) \\ \nabla.\boldsymbol{u} &= 0, && (2.5) \end{aligned}$$

where $\boldsymbol{u} = (u^*, v^*, w^*)$ represents the dimensional velocity flow field, $\mathbf{r} = (x^*, 0, z^*)$ the position vector and p^* the dimensional fluid pressure. The quantities ρ^* and ν^* define the density and kinematic viscosity of the fluid, respectively. We note the appearance of the Coriolis forcing term, $2\mathbf{\Omega} \times \boldsymbol{u}$, due to the rotating coordinate frame.

The coordinate transformations (2.1)−(2.3) lead to the full Navier-Stokes equations in orthogonal curvilinear coordinates (see also Garrett [7] for the case of a rotating cone considered with a fixed frame of reference)

$$\frac{\partial u^*}{\partial x^*}+\frac{u^*\sin\psi}{h^*}+\frac{1}{h^*}\frac{\partial v^*}{\partial \theta}+\frac{\partial w^*}{\partial z^*}+\frac{w^*\cos\psi}{h^*}=0, \tag{2.6}$$

$$\begin{aligned}\frac{\partial u^*}{\partial t^*}+u^*\frac{\partial u^*}{\partial x^*}+\frac{v^*}{h^*}\frac{\partial u^*}{\partial \theta}+w^*\frac{\partial u^*}{\partial z^*}-\frac{v^{*2}\sin\psi}{h^*}-2\Omega^*v^*\sin\psi-\Omega^{*2}h^*\sin\psi\\ =-\frac{1}{\rho^*}\frac{\partial p^*}{\partial x^*}+\nu^*\Big(\nabla^{*2}u^*-\frac{(u^*\sin\psi+w^*\cos\psi)\sin\psi}{h^{*2}}-\frac{2\sin\psi}{h^{*2}}\frac{\partial v^*}{\partial \theta}\Big),\end{aligned} \tag{2.7}$$

$$\begin{aligned}\frac{\partial v^*}{\partial t^*}+u^*\frac{\partial v^*}{\partial x^*}+\frac{v^*}{h^*}\frac{\partial v^*}{\partial \theta}+w^*\frac{\partial v^*}{\partial z^*}+\frac{(u^*\sin\psi+w^*\cos\psi)v^*}{h^*}+2\Omega^*(u^*\sin\psi+w^*\cos\psi)\\ =-\frac{1}{\rho^*h^*}\frac{\partial p^*}{\partial \theta}+\nu^*\Big(\nabla^{*2}v^*+\frac{2\sin\psi}{h^{*2}}\frac{\partial u^*}{\partial \theta}+\frac{2\cos\psi}{h^{*2}}\frac{\partial w^*}{\partial \theta}-\frac{v^*}{h^{*2}}\Big),\end{aligned} \tag{2.8}$$

$$\begin{aligned}\frac{\partial w^*}{\partial t^*}+u^*\frac{\partial w^*}{\partial x^*}+\frac{v^*}{h^*}\frac{\partial w^*}{\partial \theta}+w^*\frac{\partial w^*}{\partial z^*}-\frac{v^{*2}\cos\psi}{h^*}-2\Omega^*v^*\cos\psi-\Omega^{*2}h^*\cos\psi\\ =-\frac{1}{\rho^*}\frac{\partial p^*}{\partial z^*}+\nu^*\Big(\nabla^{*2}w^*-\frac{(u^*\sin\psi+w^*\cos\psi)\cos\psi}{h^{*2}}-\frac{2\cos\psi}{h^{*2}}\frac{\partial v^*}{\partial \theta}\Big),\end{aligned} \tag{2.9}$$

where

$$\nabla^{*2}=\frac{\partial^2}{\partial x^{*2}}+\frac{1}{h^{*2}}\frac{\partial^2}{\partial \theta^2}+\frac{\partial^2}{\partial z^{*2}}+\frac{\sin\psi}{h^*}\frac{\partial}{\partial x^*}+\frac{\cos\psi}{h^*}\frac{\partial}{\partial z^*} \tag{2.10}$$

is the dimensional Laplacian operator for the coordinate set (x^*,θ,z^*). The appropriate boundary conditions, taking into account the rotating frame of reference, are

$$\begin{gathered}u^*=0,\quad v^*=0,\quad w^*=0,\quad \text{on } z^*=0,\\ u^*\to {U_0}^*(x^*)=C^*x^{*m},\quad v^*\to -x^*\Omega^*\sin\psi,\quad \text{as } z^*\to\infty,\end{gathered} \tag{2.11}$$

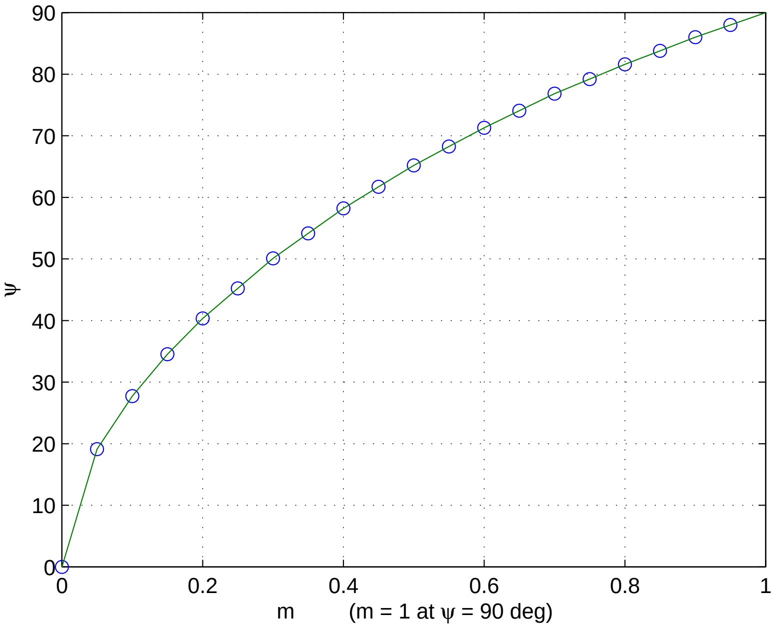

Figure 2.2: Plot of the cone half-angle variation, ψ, with velocity parameter, m.

representing the no-slip condition on the cone surface, the quiescent fluid potential-flow solution and the Coriolis force balance condition at the outer edge of the cone boundary layer, respectively. The local slip-velocity at the edge of the cone boundary layer, ${U_0}^*(x^*)$ takes the power-law form (as outlined in Rosenhead [38] and Evans [4]). This is derived under the assumption of an inviscid potential-flow solution, with the velocity parameter, m, being linked to the cone half-angle, as shown in figure 2.2, where the data points are adapted from Rosenhead [38]. We see for $\psi = 90°, m = 1$. For varying cone half-angles, m is determined as the index of the potential-flow solution for the velocity. Physically, it represents the strength of the axisymmetric potential-flow. Furthermore, as the separated boundary layer from the cone runs parallel to the cone surface, the inviscid potential-flow solution is a good representation of the actual slip velocity at the outer edge of the boundary layer. The scale factor, C^*, is determined by the free-stream axial flow incident upon the cone.

We non-dimensionalise and scale the equations (2.6)−(2.9) according to the distance measured along the cone surface, l^*, whereas the surface-normal coordinate is scaled on the boundary layer thickness, so we have

$$x^* = l^* x, \quad z^* = l^* z, \quad z = \mathrm{R}^{-1/2}\eta. \tag{2.12}$$

Here η is the re-scaled wall-normal coordinate within the boundary layer and R denotes the Reynolds number

$$\mathrm{R} = \frac{\Omega^* l^{*2} \mathrm{sin}\psi}{\nu^*}. \tag{2.13}$$

Velocity scales for the basic flow are given by

$$\mathbf{u} = \mathbf{u}_b = \Omega^* l^* \mathrm{sin}\psi (xU(\eta), xV(\eta), \mathrm{R}^{-1/2} W(\eta)), \tag{2.14}$$

whereas the basic flow pressure is expressed in the form

$$p^* = {p_b}^* = \rho^* \Omega^{*2} l^{*2} \sin^2\psi (P_0(x) + \mathrm{R}^{-\frac{1}{2}} x P(\eta)), \tag{2.15}$$

with

$$P_0(x) = -\frac{C^{*2} x^2}{2\Omega^{*2} \sin^2\psi} \tag{2.16}$$

representing the inviscid Bernoulli pressure condition, which is found by matching pressure just inside the boundary layer to the pressure forcing from the oncoming free stream flow just outside. The non-dimensional ratio of the oncoming free stream slip velocity to the cone rotational velocity is defined as the axial flow parameter

$$T_s = \frac{C^* x^{*m}}{x^* \Omega^* \sin\psi}. \tag{2.17}$$

It is important to note the case $T_s = 0$ represents a cone rotating in still fluid, whereas non-zero, positive values of T_s correspond to a cone placed in an oncoming axial flow. In experiments Kobayashi *et al.* [25] obtain estimates for the Reynolds number at transition to turbulent flow for $T_s \sim 0.15 - 0.5$, whereas Garrett & Peake [10] consider values of T_s ranging from $0.00 - 0.25$.

We wish to obtain the equations governing steady mean flow within the boundary layer, at large Reynolds number. We use (2.12)−(2.17) and expand (2.6)−(2.9) in terms of the Reynolds number, R, ignoring terms of $O(\mathrm{R}^{-1/2})$. This leads to the mean flow boundary layer equations

$$\begin{aligned} W' + 2U &= 0, && (2.18)\\ WU' + U^2 - (V+1)^2 &= m{T_s}^2 + U'', && (2.19)\\ WV' + 2U(V+1) &= V'', && (2.20)\\ (V+1)^2 \cot\psi &= \frac{\mathrm{d}P}{\mathrm{d}\eta}, && (2.21) \end{aligned}$$

with (2.11) yielding the modified non-dimensional boundary conditions

$$\begin{aligned} U = 0,\ \ V = 0,\ \ W = 0, &\quad \text{on } \eta = 0,\\ U \to T_s,\ \ V \to -1, &\quad \text{as } \eta \to \infty. \end{aligned} \tag{2.22}$$

Ignoring (2.21), we observe that our choice of non-dimensionalisation, scaling lengths on the distance along the cone surface, l^*, results in the cone-half angle, ψ, being scaled out of the problem, except for the dependence of the velocity parameter, m, on the cone half-angle, as depicted in figure 2.2. Importantly, we note here that this basic flow is only valid for $T_s = 0$ or if $T_s \neq 0$ only for $m = 1$ (i.e. $\psi = 90°$, corresponding to a rotating disk). The case of a rotating cone in an oncoming axial flow is considered in §2.3.

2.1 Case A: Rotating cone in still fluid

We first consider the solution of the mean flow boundary layer equations for varying cone-half angles, ψ, but fixed axial flow parameter $T_s = 0$, representing the absence of an oncoming axial stream flow. In this case, with our choice of length non-dimensionalisation, and the case of a still fluid, the equations reduce to the von Kármán [22] equations for boundary layer flow over a rotating disk. However, the solution now covers cone-half angles ranging, for example, from $\psi = 20° - 90°$, the $90°$ case corresponding to a rotating disk.

The system of equations (2.18)−(2.20) together with the boundary conditions (2.22) are solved using a fourth-order Runge-Kutta integration method, in conjunction with a two-dimensional Newton-Raphson searching routine to iterate on the boundary conditions at infinity. Figure 2.3 shows the streamwise, azimuthal and surface-normal components of the steady mean flow velocity in the boundary layer on the surface of a rotating cone placed in still fluid.

2.2 Case B: Rotating disk in axial flow

For the case where the cone becomes a rotating disk ($\psi = 90°$) placed in an oncoming axial flow, the equations (2.18)−(2.20) with the boundary conditions (2.22) are again solved using a fourth-order Runge-Kutta integration method, applying a two-dimensional Newton-Raphson search routine to iterate on the boundary conditions at infinity. This is carried out for varying values of T_s. Figures 2.4−2.6 show the streamwise, azimuthal and surface-normal components of the steady mean flow velocity in the boundary layer

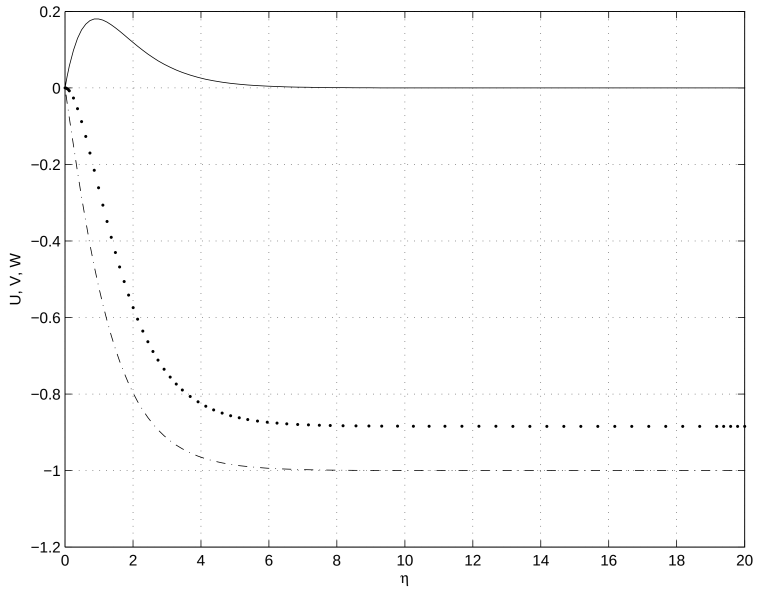

Figure 2.3: Plot of mean flow profiles U(—), V(-.-), W(...) against η for $T_s = 0$.

of a disk for $T_s = 0.00 - 0.25$. The case $T_s = 0.00$ is shown here for convenience, whereas the increasing non-zero values of T_s represent a disk placed in an oncoming axial flow of increasing strength.

2.3 Case C: Rotating cone in axial flow

In order to formulate the problem correctly for a rotating cone of half-angle $\psi < 90°$, we first identify a number of important problems with the equations in the current formulation.

Firstly, the case of $m \neq 1$, with $\psi \neq 90°$ results in our axial flow parameter being

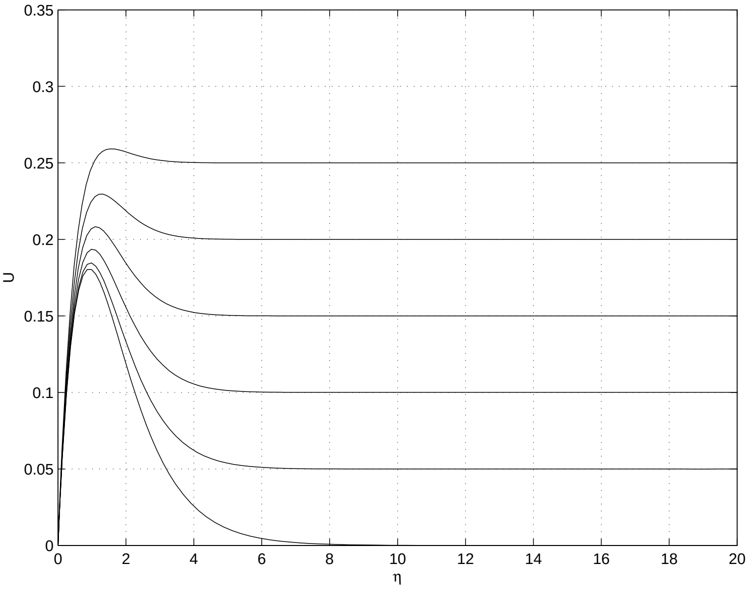

Figure 2.4: Plot of steady mean flow streamwise velocity profile, U, against η for $\psi = 90^\circ$, $T_s = 0.00$ (lowermost) to $T_s = 0.25$ (uppermost) in increments of 0.05.

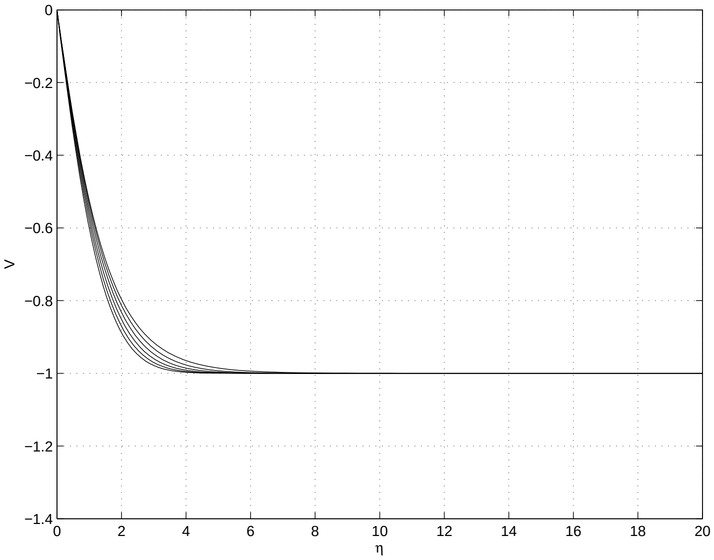

Figure 2.5: Plot of steady mean flow azimuthal velocity profile, V, against η for $\psi = 90^\circ$, $T_s = 0.00$ (uppermost) to $T_s = 0.25$ (lowermost) in increments of 0.05.

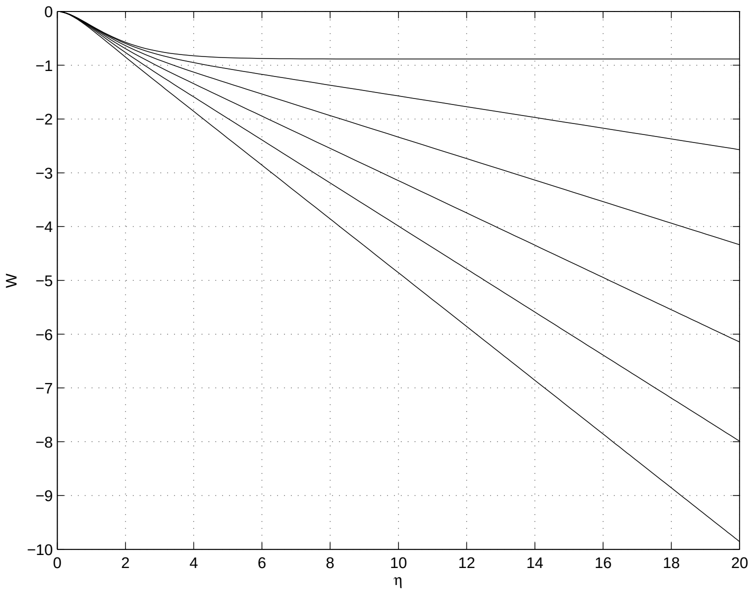

Figure 2.6: Plot of steady mean flow surface-normal velocity profile, W, against η for $\psi = 90°$, $T_s = 0.00$ (uppermost) to $T_s = 0.25$ (lowermost) in increments of 0.05.

dependent on the streamwise coordinate, x from (2.17). In effect, this causes the solution to breakdown, as the problem (2.18)−(2.20) now becomes a system of PDEs, with dependence on the two independent variables η and x. It is not feasible to set x to some constant, as we require the streamwise location to vary during our stability analysis.

However, it turns out that with this method of non-dimensionalisation, it is not possible to fully eliminate the x-dependence from the equations. We therefore appeal to a slightly different method, which formulates the problem as a system of PDEs. We revert to a system of rotating axes to set up the basic flow equations using a new non-dimensionalisation. This formulation is similar to that of Koh & Price [27] who used a set of fixed axes. However, we will show that it is possible to transform our resulting solutions between the two co-ordinate systems. We make a similarity-type transformation yielding the boundary layer equations in terms of a governing streamfunction. This is achieved by making a Mangler transformation on the governing equations, which yields the boundary layer equations as a system of PDEs, which are dependent upon only two distinct variables, as opposed to three. Suppose we define a new set of streamwise and surface-normal coordinates, $\overline{x}^*$ and $\overline{z}^*$ respectively, and corresponding velocities $\overline{u}$, $\overline{v}$ and $\overline{w}$, given by

$$\begin{aligned} \overline{x}^* &= \frac{1}{l^{*2}}\int_0^{x^*} r^{*2}\mathrm{d}x^*, \qquad \overline{z}^* = \frac{r^*}{l^*}z^*, && (2.23)\\ \overline{u} &= u^*, \qquad \overline{v} = v^*, \qquad \overline{w} = \frac{l^*}{r^*}\Big(w^* + \frac{1}{r^*}\frac{\mathrm{d}r^*}{\mathrm{d}x^*}z^*u^*\Big), && (2.24) \end{aligned}$$

where $r^* = x^*\sin\psi$. The resulting boundary layer equations may be derived in dimensional form using (2.6)−(2.9), which leads to

$$\begin{aligned} \frac{\partial\overline{u}}{\partial\overline{x}^*} + \frac{\partial\overline{w}}{\partial\overline{z}^*} &= 0, && (2.25)\\ \overline{u}\frac{\partial\overline{u}}{\partial\overline{x}^*} + \overline{w}\frac{\partial\overline{u}}{\partial\overline{z}^*} - \frac{\overline{v}^2}{3\overline{x}^*} - \frac{2\Omega^*x^*\overline{v}\sin\psi}{3\overline{x}^*} - \frac{\Omega^{*2}x^{*2}\sin^2\psi}{3\overline{x}^*} &= \overline{U}^*_e\frac{\partial\overline{U}^*_e}{\partial\overline{x}^*} + \nu^*\frac{\partial^2\overline{u}}{\partial\overline{z}^2}, && (2.26)\\ \overline{u}\frac{\partial\overline{v}}{\partial\overline{x}^*} + \overline{w}\frac{\partial\overline{v}}{\partial\overline{z}^*} + \frac{\overline{u}\,\overline{v}}{3\overline{x}^*} + \frac{2\Omega^*x^*\overline{u}\sin\psi}{3\overline{x}^*} &= \nu^*\frac{\partial^2\overline{v}}{\partial\overline{z}^{*2}}, && (2.27) \end{aligned}$$

where $\overline{U}^*_e(\overline{x}^*) = U^*_0(x^*) = C^*x^{*m}$. Here, m represents the velocity parameter identified previously in (2.11). The no-slip, quiescent fluid and Coriolis-balance boundary conditions subsequently become

$$\begin{aligned} \overline{u} = 0,\ \ \overline{v} = 0,\ \ \overline{w} = 0, \quad \text{on } \overline{z}^* &= 0,\\ \overline{u} \to \overline{U}^*_e = \overline{C}^*\overline{x}^{*m/3},\ \ \overline{v} \to -\overline{V}^*_w = -\omega^*\overline{x}^{*1/3}, \quad \text{as } \overline{z}^* &\to \infty, && (2.28) \end{aligned}$$

where

$$\overline{C}^* = C^*\Big(\frac{3l^{*2}}{\sin^2\psi}\Big)^{\frac{m}{3}} \quad \text{and} \quad \omega^* = \Omega^*(3l^{*2}\sin\psi)^{1/3}. \qquad (2.29)$$

The characteristics of this system of equations include the effects of an oncoming forced axial flow onto the cone, as well as the simultaneous rotation about the cone's axis. As a result, there exists no direct similarity transformation to convert the PDEs to ODEs. Therefore, we use the following similarity-type transformation which involves the stream-function in the form

$$\overline{\psi} = \Big(\frac{6\nu^*\overline{x}^*\overline{U}_e^*}{m+3}\Big)^{\frac{1}{2}} f(s,\eta_1), \quad \overline{u} = \frac{\partial\overline{\psi}}{\partial\overline{z}^*}, \quad \overline{w} = -\frac{\partial\overline{\psi}}{\partial\overline{x}^*}, \tag{2.30}$$

where the parameters

$$s = \Big(\frac{\overline{V}_w^*}{\overline{U}_e^*}\Big)^2 = \Big(\frac{\omega^*}{\overline{C}^*}\overline{x}^{*\frac{1-m}{3}}\Big)^2 \quad \text{and} \quad \eta_1 = \overline{z}^*\Big(\frac{m+3}{6}\frac{\overline{U}_e^*}{\nu^*\overline{x}^*}\Big)^{\frac{1}{2}} \tag{2.31}$$

define the transformed coordinates for the system. The η_1-coordinate represents the new surface-normal coordinate scaled on displacement thickness according to the new velocity scales, whereas the s-coordinate represents the ratio of rotational flow with respect to oncoming axial flow, and as such $s^{-1/2} = T_s$. The case $s = 0$ corresponds to either Ω^* or $\overline{x}^*$ being equal to zero. The latter is not physical, as it represents the cone tip, where the problem formulation breaks down. Therefore, we may identify small s values to correspond to flows with a larger oncoming flow in comparison with the rotational flow. Conversely, large values of s represent the physically interesting case of a relatively small axial flow in comparison with a larger rotational flow. The limiting case $s \to \infty$ describes a cone rotating in otherwise still fluid. Now, since $\overline{V}_w^*$ is proportional to x^* and $\overline{U}_e^*$ is proportional to x^{*m}, we see that s is expressible in terms of x^*. This dependence is only eliminated for the case $m = 1$, which as we have seen earlier corresponds to a rotating disk. It is for this reason we were able to obtain asymptotically converging solutions previously for the case of a rotating disk in oncoming axial flow. Using these modified coordinates and scales, the velocity components may then be non-dimensionalised according to

$$\begin{aligned}
\overline{u} &= \overline{U}^*_e \frac{\partial f}{\partial \eta_1}, \quad \overline{v} = \overline{V}^*_w g(s, \eta_1), \\
\overline{w} &= -\Big(\frac{6}{m+3}\nu^* \overline{x}^* \overline{U}^*_e\Big)^{\frac{1}{2}} \Big[\Big(\frac{1}{2\overline{x}^*} + \frac{1}{2\overline{U}^*_e}\frac{\partial \overline{U}^*_e}{\partial \overline{x}^*}\Big) f(s, \eta_1) + \frac{\mathrm{d}s}{\mathrm{d}\overline{x}^*}\frac{\partial f}{\partial s} + \frac{\partial \eta_1}{\partial \overline{x}^*}\frac{\partial f}{\partial \eta_1}\Big],
\end{aligned} \tag{2.32}$$

which when substituted into (2.26)−(2.27) yields the governing partial differential equations in non-dimensional form

$$f''' + ff'' + \frac{2m}{(m+3)}(1 - f'^2) + \frac{2s}{(m+3)}\Big[(g+1)^2 + 2(1-m)\Big(f''\frac{\partial f}{\partial s} - f'\frac{\partial f'}{\partial s}\Big)\Big] = 0, \tag{2.33}$$

$$g'' + fg' - \frac{4}{(m+3)}f'(g+1) + \frac{4(1-m)s}{(m+3)}\Big(g'\frac{\partial f}{\partial s} - f'\frac{\partial g}{\partial s}\Big) = 0, \tag{2.34}$$

where $'$ denotes differentiation with respect to η_1. The boundary conditions (2.28) become

$$\begin{aligned}
f = 0, \quad f' = 0, \quad g = 0, \quad \text{on } \eta_1 &= 0, \\
f' \to 1, \quad g \to -1, \quad \text{as } \eta_1 &\to \infty.
\end{aligned} \tag{2.35}$$

The next step is to transform these equations into a form which produces asymptotically converging solutions at the edge of the boundary layer. We make the substitution

$$f \to \tilde{f}, \quad g \to \tilde{g} - 1. \tag{2.36}$$

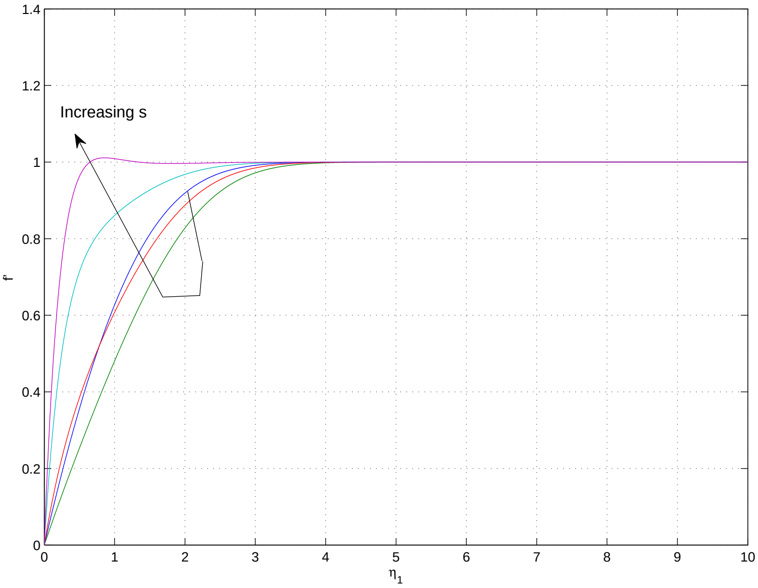

Figure 2.7: Plot of steady mean flow streamwise velocity profile, f', against η_1 for $\psi = 70°$, $s = 0$ to $s = 10$ (uppermost). Increasing s shifts the curves as shown.

The resulting equations and boundary conditions become

$$\tilde{f}''' + \tilde{f}\tilde{f}'' + \frac{2m}{(m+3)}(1-\tilde{f}'^2) + \frac{2s}{(m+3)}\left[\tilde{g}^2 + 2(1-m)\left(\tilde{f}''\frac{\partial \tilde{f}}{\partial s} - \tilde{f}'\frac{\partial \tilde{f}'}{\partial s}\right)\right] = 0, \tag{2.37}$$

$$\tilde{g}'' + \tilde{f}\tilde{g}' - \frac{4}{(m+3)}\tilde{f}'\tilde{g} + \frac{4(1-m)s}{(m+3)}\left(\tilde{g}'\frac{\partial \tilde{f}}{\partial s} - \tilde{f}'\frac{\partial \tilde{g}}{\partial s}\right) = 0, \tag{2.38}$$

$$\begin{aligned} \tilde{f} = 0, \quad \tilde{f}' = 0, \quad \tilde{g} = 1, \quad \text{on } \eta_1 &= 0, \\ \tilde{f}' \to 1, \quad \tilde{g} \to 0, \quad \text{as } \eta_1 &\to \infty. \end{aligned} \tag{2.39}$$

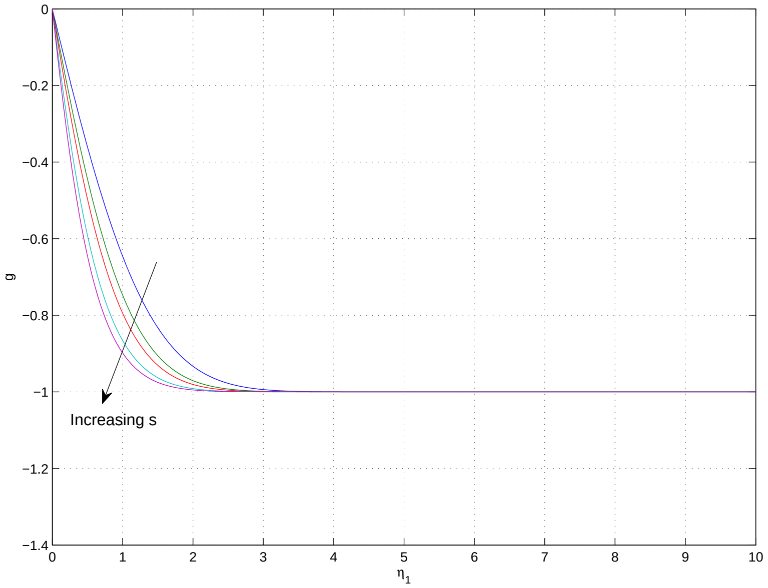

Figure 2.8: Plot of steady mean flow azimuthal velocity profile, g, against η_1 for $\psi = 70°$, $s = 0$ (uppermost) to $s = 10$ (lowermost). Increasing s shifts the curves as shown.

In order to solve this system numerically, we decompose the equations into a fifth-order system of first-order PDEs in η_1 and s. We obtain solutions for the case $s = 0$ using a similar fourth-order Runge-Kutta integration method as before, with a Newton-Raphson searching routine to iterate on the boundary conditions at infinity. These initial profiles are subsequently used to integrate the equations for non-zero s and obtain profiles for varying η_1 and s. The substitution (2.36) effectively transforms the equations into the form for which Koh & Price [27] obtained numerical solutions, using a finite difference scheme and employing the Crank-Nicholson method for a cone rotating within a fixed coordinate frame. However, we use the commercial NAG routine D03PEF, which is efficient and easy to use. More importantly, it has been used by Garrett [7] to obtain successful basic flow solutions in the closely related boundary layer problem of a rotating sphere. The approach involves employing a Keller box scheme and the method of lines to reduce the system of PDEs to a system of ODEs in η_1. The solution vector is arranged into the form $U = (\tilde{f}, \tilde{f}', \tilde{f}'', \tilde{g}, \tilde{g}') = (U_1, U_2, U_3, U_4, U_5)$, where the governing equations and boundary conditions (2.37)−(2.39) are written in the form

$$U_2 = \frac{\partial U_1}{\partial \eta_1}, \quad U_3 = \frac{\partial U_2}{\partial \eta_1}, \quad U_5 = \frac{\partial U_4}{\partial \eta_1}, \tag{2.40}$$

$$\frac{\partial U_3}{\partial \eta_1} + U_1U_3 + \frac{2m}{(m+3)}(1-U_2^2) + \frac{2s}{(m+3)}\Big[U_4^2 + 2(1-m)\Big(U_3\frac{\partial U_1}{\partial s} - U_2\frac{\partial U_2}{\partial s}\Big)\Big] = 0, \tag{2.41}$$

$$\frac{\partial U_5}{\partial \eta_1} + U_1U_5 - \frac{4}{(m+3)}U_2U_4 + \frac{4(1-m)s}{(m+3)}\Big(U_5\frac{\partial U_1}{\partial s} - U_2\frac{\partial U_4}{\partial s}\Big) = 0, \tag{2.42}$$

$$\begin{aligned} U_1 = 0, \ \ U_2 = 0, \ \ U_4 = 1, \quad \text{on } \eta_1 &= 0, \\ U_2 \to 1, \ \ U_4 \to 0, \quad \text{as } \eta_1 &\to \infty. \end{aligned} \tag{2.43}$$

Once we obtain the solutions for $\tilde{f}$ and $\tilde{g}$ we are able to transform back easily to yield solutions for f and g respectively. The resulting system of ODEs is solved at each value of s starting from the initial profile at $s = 0$ provided from the fourth-order Runge-Kutta scheme and integrating up to the value $s = 10$. Figures 2.7 and 2.8 show the streamwise and azimuthal velocity profiles for $s = 0$, 0.1, 1.0, 5 and 10. We note that as s increases towards 1, the streamwise profiles are shifted down and the velocities approach the inviscid potential flow solution slower. However, as s increases further the rotational effect of the flow begins to dominate over the oncoming axial stream flow. The streamwise profiles are then shifted back up above the $s = 0$ profile and begin to develop an inflexional nature, overshooting before converging to the inviscid flow solution at the edge of the boundary layer. In contrast, the azimuthal profiles exhibit a continuous shift downwards as s increases, due to the increasing Coriolis effect of the flow. This is because the flow has a stronger rotational component for larger s values and so converges faster to the azimuthal shear velocity at the edge of the boundary layer.

Importantly, we note at this stage that the basic flow solutions for cases A, B and C correspond to full non-parallel flow solutions. In all cases, we have accounted for dependence on the streamwise variation through the $x-$coordinate in cases A and B, and through the $s-$parameter in case C, which implicitly carries the spatial variation in the $\overline{x}^*-$coordinate. Furthermore, surface-normal dependence is include through the boundary layer coordinates η and η_1 in cases A,B and case C, respectively.

2.4 Linear disturbance equations (cases A and B)

For the cases of a cone rotating in still fluid ($T_s = 0, m \in (0, 1]$) or a rotating disk in axial flow ($T_s \neq 0, m = 1$), we linearise (2.6)$-$(2.9) about the steady mean flow profile (2.14) and the basic fluid pressure (2.15) by introducing (small) perturbation quantities $\tilde{\mathbf{u}}$ and $\tilde{p}^*$ according to:

$$\mathbf{u} = \mathbf{u}_b + \tilde{\mathbf{u}}, \quad p^* = {p_b}^* + \tilde{p}^*, \tag{2.44}$$

where

$$\tilde{\mathbf{u}} = \Omega^* l^* \sin\psi (\tilde{u}, \tilde{v}, \tilde{w}), \quad \tilde{p}^* = (\rho^* \Omega^{*2} l^{*2} \sin^2\psi) \tilde{p}. \tag{2.45}$$

Non-dimensionalising and ignoring nonlinear terms on the left-hand side (keeping only the convective cross-terms with the basic flow) and retaining the perturbation terms on the right-hand side, leads to the linearised perturbation equations

$$\frac{\partial \tilde{u}}{\partial x} + \frac{\tilde{u}\sin\psi + \tilde{w}\cos\psi}{h} + \frac{1}{h}\frac{\partial \tilde{v}}{\partial \theta} + \frac{\partial \tilde{w}}{\partial z} = 0, \tag{2.46}$$

$$\begin{aligned}&\Big(xU\frac{\partial}{\partial x}+\frac{xV}{h}\frac{\partial}{\partial\theta}+\mathrm{R}^{-1/2}W\frac{\partial}{\partial z}\Big)\tilde{u}+U\tilde{u}+x\tilde{w}\frac{\partial U}{\partial z}-2\Big(\frac{xV\sin\psi}{h}+1\Big)\tilde{v}\\&\qquad=-\frac{\partial\tilde{p}}{\partial x}+\frac{1}{\mathrm{R}}\Big(\nabla^2\tilde{u}-\frac{(\tilde{u}\sin\psi+\tilde{w}\cos\psi)\sin\psi}{h^2}-\frac{2\sin\psi}{h^2}\frac{\partial\tilde{v}}{\partial\theta}\Big),\end{aligned}\tag{2.47}$$

$$\begin{aligned}&\Big(xU\frac{\partial}{\partial x}+\frac{xV}{h}\frac{\partial}{\partial\theta}+\mathrm{R}^{-1/2}W\frac{\partial}{\partial z}\Big)\tilde{v}+V\tilde{u}\\&+x\tilde{w}\frac{\partial V}{\partial z}+\Big(\frac{xV\sin\psi}{h}+2\Big)(\tilde{u}+\tilde{w}\cot\psi)+\frac{(xU\sin\psi+\mathrm{R}^{-1/2}W\cos\psi)\tilde{v}}{h}\\&\qquad=-\frac{1}{h}\frac{\partial\tilde{p}}{\partial\theta}+\frac{1}{\mathrm{R}}\Big(\nabla^2\tilde{v}++\frac{2\sin\psi}{h^2}\frac{\partial\tilde{u}}{\partial\theta}+\frac{2\cos\psi}{h^2}\frac{\partial\tilde{w}}{\partial\theta}-\frac{\tilde{v}}{h^2}\Big),\end{aligned}\tag{2.48}$$

$$\begin{aligned}&\Big(xU\frac{\partial}{\partial x}+\frac{xV}{h}\frac{\partial}{\partial\theta}+\mathrm{R}^{-1/2}W\frac{\partial}{\partial z}\Big)\tilde{w}+\mathrm{R}^{-1/2}\tilde{w}\frac{\partial W}{\partial z}-2\Big(\frac{xV\sin\psi}{h}+1\Big)\tilde{v}\cot\psi\\&\qquad=-\frac{\partial\tilde{p}}{\partial z}+\frac{1}{\mathrm{R}}\Big(\nabla^2\tilde{w}-\frac{(\tilde{u}\sin\psi+\tilde{w}\cos\psi)\cos\psi}{h^2}-\frac{2\cos\psi}{h^2}\frac{\partial\tilde{v}}{\partial\theta}\Big),\end{aligned}\tag{2.49}$$

where $h=\frac{h^*}{l^*}$ and $\nabla^2=l^{*2}\nabla^{*2}$ is the non-dimensional Laplacian operator.

2.5 Linear disturbance equations (case C)

For the case of a cone rotating in axial flow ($s\in(0,100]$ say, $m\in(0,1]$), we linearise (2.6)−(2.9) about a more general steady mean flow profile

$$\mathbf{u}_b=\Omega^*l^*\sin\psi(U(x,\eta),V(x,\eta),\mathrm{R}^{-1/2}W(x,\eta))\tag{2.50}$$

with the basic fluid pressure remaining as in (2.15). The standard perturbation quantities $\tilde{\mathbf{u}}$ and $\tilde{p}^*$ are introduced in the form:

$$\mathbf{u}=\mathbf{u}_b+\tilde{\mathbf{u}},\quad p^*={p_b}^*+\tilde{p}^*,\tag{2.51}$$

where

$$\tilde{\mathbf{u}} = \Omega^* l^* \mathrm{sin}\psi(\tilde{u}, \tilde{v}, \tilde{w}), \quad \tilde{p}^* = (\rho^* \Omega^{*2} l^{*2} \mathrm{sin}^2\psi)\tilde{p}. \tag{2.52}$$

Non-dimensionalising and ignoring nonlinear terms on the left-hand side (keeping only the convective cross-terms with the basic flow) and retaining the perturbation terms on the right-hand side, leads to the linearised perturbation equations

$$\frac{\partial \tilde{u}}{\partial x} + \frac{\tilde{u}\mathrm{sin}\psi + \tilde{w}\mathrm{cos}\psi}{h} + \frac{1}{h}\frac{\partial \tilde{v}}{\partial \theta} + \frac{\partial \tilde{w}}{\partial z} = 0, \tag{2.53}$$

$$\begin{aligned}\Big(U\frac{\partial}{\partial x} + \frac{V}{h}\frac{\partial}{\partial \theta} + \mathrm{R}^{-1/2}W\frac{\partial}{\partial z}\Big)\tilde{u} + \frac{\partial U}{\partial x}\tilde{u} + \tilde{w}\frac{\partial U}{\partial z} - 2\Big(\frac{V\mathrm{sin}\psi}{h} + 1\Big)\tilde{v} \\ = -\frac{\partial \tilde{p}}{\partial x} + \frac{1}{\mathrm{R}}\Big(\nabla^2\tilde{u} - \frac{(\tilde{u}\mathrm{sin}\psi + \tilde{w}\mathrm{cos}\psi)\mathrm{sin}\psi}{h^2} - \frac{2\mathrm{sin}\psi}{h^2}\frac{\partial \tilde{v}}{\partial \theta}\Big),\end{aligned} \tag{2.54}$$

$$\begin{aligned}\Big(U\frac{\partial}{\partial x} + \frac{V}{h}\frac{\partial}{\partial \theta} + \mathrm{R}^{-1/2}W\frac{\partial}{\partial z}\Big)\tilde{v} + \frac{\partial V}{\partial x}\tilde{u} \\ +\tilde{w}\frac{\partial V}{\partial z} + \Big(\frac{V\mathrm{sin}\psi}{h} + 2\Big)(\tilde{u} + \tilde{w}\mathrm{cot}\psi) + \frac{(U\mathrm{sin}\psi + \mathrm{R}^{-1/2}W\mathrm{cos}\psi)\tilde{v}}{h} \\ = -\frac{1}{h}\frac{\partial \tilde{p}}{\partial \theta} + \frac{1}{\mathrm{R}}\Big(\nabla^2\tilde{v} + + \frac{2\mathrm{sin}\psi}{h^2}\frac{\partial \tilde{u}}{\partial \theta} + \frac{2\mathrm{cos}\psi}{h^2}\frac{\partial \tilde{w}}{\partial \theta} - \frac{\tilde{v}}{h^2}\Big),\end{aligned} \tag{2.55}$$

$$\begin{aligned}\Big(U\frac{\partial}{\partial x} + \frac{V}{h}\frac{\partial}{\partial \theta} + \mathrm{R}^{-1/2}W\frac{\partial}{\partial z}\Big)\tilde{w} + \mathrm{R}^{-1/2}\tilde{w}\frac{\partial W}{\partial z} - 2\Big(\frac{V\mathrm{sin}\psi}{h} + 1\Big)\tilde{v}\mathrm{cot}\psi \\ = -\frac{\partial \tilde{p}}{\partial z} + \frac{1}{\mathrm{R}}\Big(\nabla^2\tilde{w} - \frac{(\tilde{u}\mathrm{sin}\psi + \tilde{w}\mathrm{cos}\psi)\mathrm{cos}\psi}{h^2} - \frac{2\mathrm{cos}\psi}{h^2}\frac{\partial \tilde{v}}{\partial \theta}\Big),\end{aligned} \tag{2.56}$$

where, as in cases A and B, $h = \frac{h^*}{l^*}$ and $\nabla^2 = l^{*2}\nabla^{*2}$ is the non-dimensional Laplacian operator. These equations are effectively the linearised equations (2.46)−(2.49) with the streamwise and azimuthal velocities transformed as $U \to U/x$ and $V \to V/x$.

Chapter 3

The Inviscid Type I Modes

To analyse the type I modes on the rotating cone, we follow the analysis of Hall [16], who investigated the stationary spiral modes of oscillation on a rotating disk. In cases A and B, we extend the analysis for varying rotating cone angles and a rotating disk with an axial flow added, respectively. This is followed by case C, where we combine cases A and B to consider a cone rotating within a forced axial flow. It is important to note that the analysis for a cone in still fluid (case A) follows very closely to that of Hall [16], with the much of the equations and corresponding exactly, up to a scale factor $\sin\psi$. This is the case for both the leading order and first order terms in §§3.1 and 3.2.1 However, once we consider the problems of case B (§§3.1 and 3.2.2) and case C (§§3.3 and 3.4), while the method of the stability analyses follows that of Hall [16] closely, the actual equations and calculated results differ somewhat more so. We scale the inviscid mode wavelengths on the boundary layer thickness, of order $\mathrm{R}^{-\frac{1}{2}}$, in the x and θ directions. Our small parameter ϵ is given by

$$\epsilon = \mathrm{R}^{-\frac{1}{6}}$$

and we subsequently define the perturbation velocities as functions of the wall-normal coordinate z, in the form

$$\tilde{u} = u(z)\mathrm{exp}\Big(\frac{\mathrm{i}}{\epsilon^3}\Big\{\int^x \alpha(x,\epsilon)\mathrm{d}x + \beta(\epsilon)\theta\Big\}\Big), \tag{3.1}$$

with similar expressions for $\tilde{v}$, $\tilde{w}$ and the pressure perturbation $\tilde{p}$. We expand the streamwise and azimuthal wavenumbers α and β as

$$\alpha = \alpha_0 + \epsilon\alpha_1 + \dots, \tag{3.2}$$

$$\beta = \beta_0 + \epsilon\beta_1 + \dots. \tag{3.3}$$

Significantly, we see that the disturbances associated with these perturbations are neutrally stable and hence we justify the conditions $\alpha, \beta \in \Re$. Following Hall's argument leads us to observe the existence of two layers, an inviscid layer of thickness $O(\epsilon^3)$ and a viscous layer to incorporate the no-slip condition at the wall, which is found to have thickness $O(\epsilon^4)$, by balancing convection and diffusion terms in the disturbance equations. The velocity and pressure perturbations in the inviscid layer are expanded as

$$u = u_0(\eta) + \epsilon u_1(\eta) + \dots, \tag{3.4}$$

$$v = v_0(\eta) + \epsilon v_1(\eta) + \dots, \tag{3.5}$$

$$w = w_0(\eta) + \epsilon w_1(\eta) + \dots, \tag{3.6}$$

$$p = p_0(\eta) + \epsilon p_1(\eta) + \dots, \tag{3.7}$$

where $\eta = z\epsilon^{-3}$. Here, $\frac{\partial}{\partial x}$ and $\frac{\partial}{\partial \theta}$ are replaced by $\frac{\partial}{\partial x} + \frac{\mathrm{i}}{\epsilon^3}\{\alpha_0 + \epsilon\alpha_1 + \dots,\}$ and $\frac{\mathrm{i}}{\epsilon^3}\{\beta_0 + \epsilon\beta_1 + \dots,\}$, respectively.

3.1 Leading order eigenmodes (cases A and B)

For the situations of a cone in still fluid and a rotating disk in axial flow, we equate terms of $O(\epsilon^{-3})$ in the expansions of (2.46)−(2.49), which leads to

$$\begin{aligned} \mathrm{i}\Big(\alpha_0 u_0 + \frac{\beta_0 v_0}{x\sin\psi}\Big) + w_0^{'} &= 0, && (3.8)\\ \mathrm{i}\overline{\overline{U}}u_0 + xU^{'}w_0 &= -\mathrm{i}\alpha_0 p_0, && (3.9)\\ \mathrm{i}\overline{\overline{U}}v_0 + xV^{'}w_0 &= -\frac{\mathrm{i}\beta_0 p_0}{x\sin\psi}, && (3.10)\\ \mathrm{i}\overline{\overline{U}}w_0 &= -p_0^{'}, && (3.11) \end{aligned}$$

where $\overline{\overline{U}} = \alpha_0 xU + \frac{\beta_0 V}{\sin\psi}$. We now eliminate u_0, v_0, and p_0 from the above equations to yield an equation for w_0 given by

$$\overline{\overline{U}}(w_0^{''} - {\gamma_0}^2 w_0) - \overline{\overline{U}}^{''} w_0 = 0, \tag{3.12}$$

where ${\gamma_0}^2 = {\alpha_0}^2 + \frac{{\beta_0}^2}{x^2\sin^2\psi}$ acts as the effective wavenumber from the streamwise and cross-stream directions, whereas $\overline{\overline{U}}$ is interpreted as the effective velocity profile, as discussed in a similar form by Hall [16] for the rotating disk. However, here $\overline{\overline{U}}$ is in the direction of propagation of the spiral vortices on a rotating cone. We proceed in the same way and subsequently solve Rayleigh's equation for w_0 and obtain γ_0 as an eigenvalue subject to the boundary conditions at the wall and infinity, namely

$$w_0 = 0, \quad \eta = 0, \infty. \tag{3.13}$$

We use the numerical method of central finite differences and choose $\eta = \overline{\eta}$ such that $\overline{\overline{U}}$ and $\overline{\overline{U}}^{''}$ both vanish at this point, known as the location of the critical layer. This

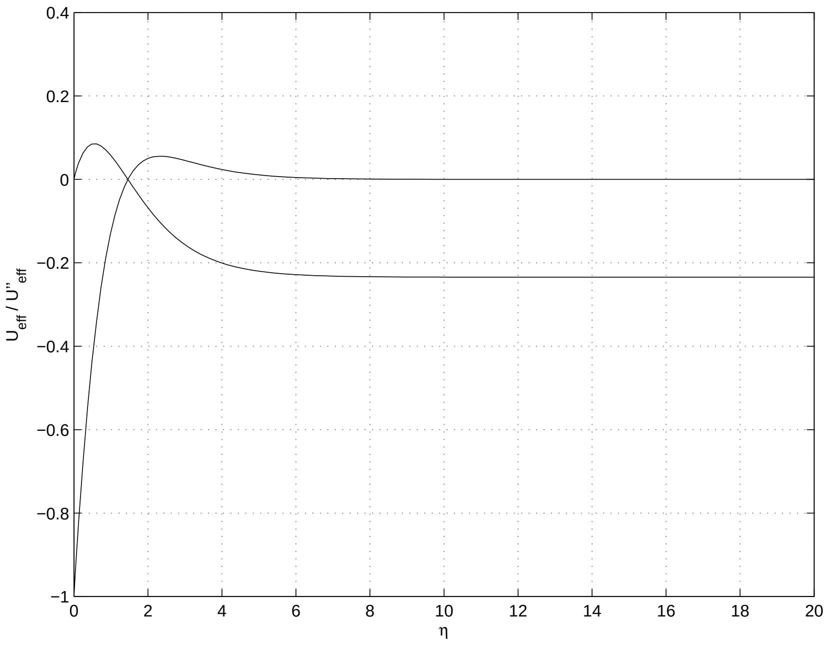

Figure 3.1: Plot of effective velocity $\overline{\overline{U}}$ (lower curve at $\eta = 20$) and its second derivative $\overline{\overline{U}}''$ (upper curve at $\eta = 20$) for $\psi = 70°$, $T_s = 0$.

condition requires that the effective velocity profile has a root and a point of inflexion at the same point, as shown in figure 3.1. In addition, we observe that as $\eta \longrightarrow \overline{\eta}$, u_0 and v_0 behave like $1/(\eta - \overline{\eta})$, but the singularity in their combined profiles, $\alpha_0 u_0 + \frac{\beta_0 v_0}{x \sin\psi}$, is removable. From (3.8), as we require the solution only for w_0, we conclude that we do not need to investigate the critical layer structure of each profile separately.

The solution we obtained for w_0 corresponds to that found by Hall [16] for the stationary instability of a rotating disk. The results are

$$\mu = \frac{\beta_0}{\alpha_0 x \sin\psi} = 0.2350, \tag{3.14}$$

$$\overline{\eta} = 1.458, \tag{3.15}$$

$$\gamma_0 = 1.162. \tag{3.16}$$

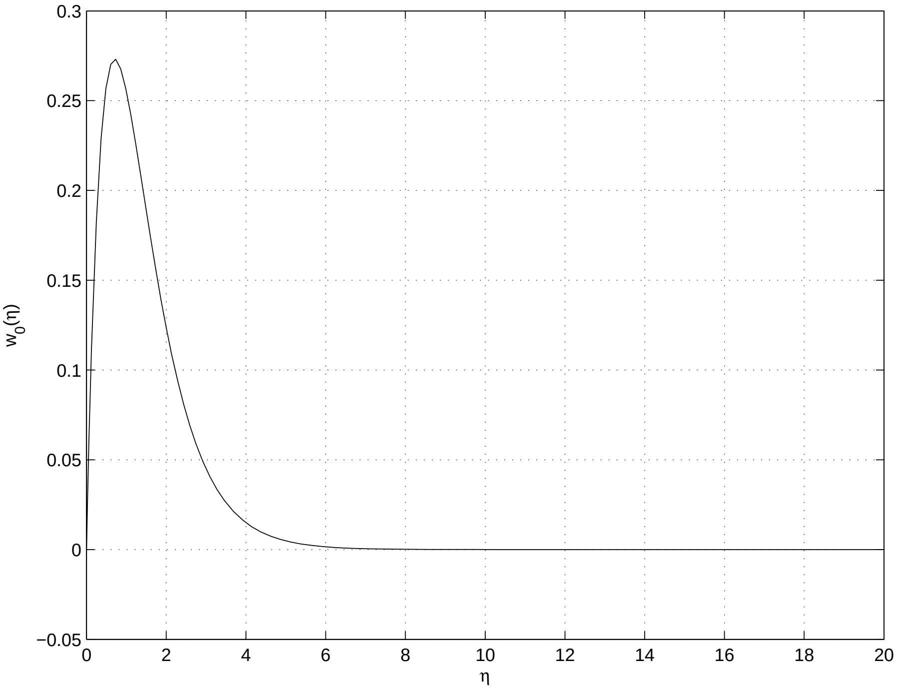

Figure 3.2: Plot of inviscid motion eigenfunction w_0 against η for $\psi = 70°$, $T_s = 0$.

The normalised eigenfunction w_0, with gradient $w_0' = 1$ at $\eta = 0$, is shown in figure 3.2. To interpret these results physically, we consider the rotating cone surface depicted in the image of figure 3.3, noticing that the spiral vortices which wrap around the cone travel at an angle to the cone meridian. The streamwise and cross-stream wavenumbers, α_0 and β_0/r, are shown in the accompanying diagram of figure 3.3, with the normal to the spiral vortices in the direction of the effective velocity, $\overline{\overline{U}}$, making a waveangle, ϕ with the streamwise position vector.

Indeed, our results are related to the spiral angle by the relation

$$\mu \sin\psi = \tan\phi. \tag{3.17}$$

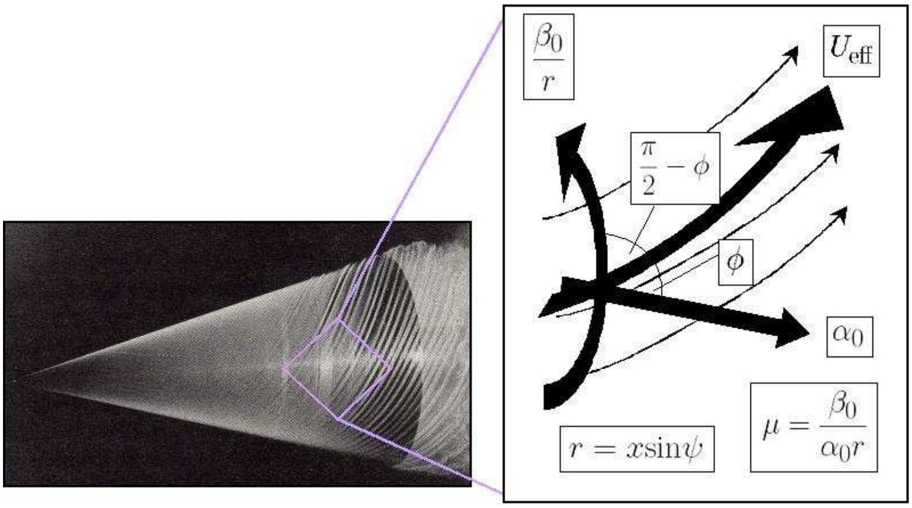

Figure 3.3: Image of primary instability mode of rotating cone (left, Kobayashi *et al.* [25]) and diagram of physical interpretation (right) showing streamwise, azimuthal and effective velocity directions.

The spiral angle ϕ is a physical quantity, which, along with the observed number of spiral vortices (usually denoted by n), has been measured in past experiments (see Kobayashi *et al.* [25] and Kobayashi & Izumi [26]).

We now turn our attention to the leading order inviscid mode solution within the wall layer, where the appropriate surface-normal coordinate takes the form

$$\xi = \epsilon^{-4} z, \tag{3.18}$$

and is related to the previous surface-normal coordinate by $\eta = \epsilon\xi$. Close to the cone wall, the basic flow must satisfy the no-slip condition, with its derivatives being linear in ξ, and having the form

$$U = \epsilon U'(0)\xi, \quad V = \epsilon V'(0)\xi, \quad W = \epsilon W'(0)\xi, \tag{3.19}$$

the last of which is zero from continuity, so $W \approx O(\epsilon^2)$ We subsequently expand the velocity and pressure perturbations within the wall layer as

$$\begin{aligned} u &= U_0(\xi) + \epsilon U_1(\xi) + \dots, && (3.20) \\ v &= V_0(\xi) + \epsilon V_1(\xi) + \dots, && (3.21) \\ w &= \epsilon W_0(\xi) + \epsilon^2 W_1(\xi) + \dots, && (3.22) \\ p &= \epsilon P_0(\xi) + \epsilon^2 P_1(\xi) + \dots, && (3.23) \end{aligned}$$

noting that the surface-normal velocity and pressure have a first order dependence on the small parameter, ϵ, within the wall layer. Upon substituting these expansions into the disturbance equations (2.46)-(2.49), and equating terms of $O(\epsilon^{-3})$, $O(\epsilon^{-2})$, $O(\epsilon^{-2})$ and $O(\epsilon^{-1})$, respectively, we obtain

$$\begin{aligned} \mathrm{i}\Big(\alpha_0 U_0 + \frac{\beta_0 V_0}{x\sin\psi}\Big) + W_0^{'} &= 0, && (3.24) \\ \mathrm{i}\Big(\alpha_0 x U^{'}(0) + \frac{\beta_0 V^{'}(0)}{\sin\psi}\Big)\xi U_0 + xU^{'}(0)W_0 &= -\mathrm{i}\alpha_0 P_0 + U_0^{''}, && (3.25) \\ \mathrm{i}\Big(\alpha_0 x U^{'}(0) + \frac{\beta_0 V^{'}(0)}{\sin\psi}\Big)\xi V_0 + xV^{'}(0)W_0 &= -\frac{\mathrm{i}\beta_0 P_0}{x\sin\psi} + V_0^{''}, && (3.26) \\ \mathrm{i}\Big(\alpha_0 x U^{'}(0) + \frac{\beta_0 V^{'}(0)}{\sin\psi}\Big)\xi W_0^{'} &= -P_2^{'} + W_0^{''}. && (3.27) \end{aligned}$$

Furthermore, equating terms of $O(\epsilon^{-3})$ and $O(\epsilon^{-2})$ in the surface-normal disturbance equation leads to $P_0, P_1 = \text{const.}$, respectively.

We now carry out the manipulation $\alpha_0(3.25)^{'} + \frac{\beta_0}{x\sin\psi}(3.26)^{'}$, which along with (3.24), leads to

$$\Big(\alpha_0 U_0 + \frac{\beta_0 V_0}{x\sin\psi}\Big)^{'''} - \mathrm{i}\xi\Big(\alpha_0 x U^{'}(0) + \frac{\beta_0 V^{'}(0)}{\sin\psi}\Big)\Big(\alpha_0 U_0^{'} + \frac{\beta_0 V_0^{'}}{x\sin\psi}\Big) = 0. \qquad (3.28)$$

From (3.24), the solution of this equation satisfies $\alpha_0 U_0 + \frac{\beta_0 V_0}{x \sin\psi} = 0$ at $\xi = 0$.

Now, if we make the substitution

$$\varphi = \Big(\alpha_0 U_0 + \frac{\beta_0 V_0}{x \sin\psi}\Big)', \tag{3.29}$$

and let $\tau = \gamma\xi$, where $\gamma = (\mathrm{i}(\alpha_0 x U'(0) + \frac{\beta_0 V'(0)}{\sin\psi}))^{\frac{1}{3}}$, then (3.28) becomes

$$\varphi_{\tau\tau} - \tau\varphi = 0, \tag{3.30}$$

indicating that the wall layer eigenfunction behaviour is characterized by a familiar Airy function decay for φ. Use of the condition at $\xi = 0$ and (3.24) yields

$$W_0' = \frac{w_0'(0)\int_0^{\xi}\mathrm{Ai}(\gamma s)\mathrm{d}s}{\int_0^{\infty}\mathrm{Ai}(\gamma s)\mathrm{d}s}, \tag{3.31}$$

where $\mathrm{Ai}(\tau)$ is the required exponentially decaying solution of Airy's equation (3.30). The next step is to use integration by parts, substitute the Airy equation (3.30) to simplify the resulting integrand and subsequently apply $\mathrm{Ai}'(\infty) = 0$. We consider the case of asymptotically large ξ at the outer edge of the wall layer, which corresponds to the inner edge of the inviscid later as $\eta \to 0$. This enables us to obtain

$$W_0 \approx w_0'(0)\xi + \frac{w_0'(0)\mathrm{Ai}'(0)}{\gamma\int_0^{\infty}\mathrm{Ai}(s)\mathrm{d}s}. \tag{3.32}$$

Finally, we match the normal perturbation at the outer edge of the wall layer to the corresponding value at the inner edge of the inviscid layer, by applying the Prandtl matching criterion in the form

$$\lim_{\xi\uparrow\infty} w(\xi) = \lim_{\eta\downarrow 0} w(\eta) \tag{3.33}$$

and use $w_0(0) = 0$ to produce an expression for the order ϵ inviscid zone surface-normal velocity component, which is given by

$$w_1\Big|_{\eta\to 0} = \frac{w_0^{'}(0)\mathrm{Ai}^{'}(0)}{\gamma\int_0^\infty \mathrm{Ai}(s)\mathrm{d}s}. \tag{3.34}$$

3.2 First order eigenmodes

3.2.1 Case A: Rotating cone in still fluid

We now consider the next-order problem in the inviscid zone. We expand the perturbation equations (2.46)−(2.49) to $O(\epsilon^{-2})$ to obtain

$$\mathrm{i}\Big(\alpha_0 u_1 + \alpha_1 u_0 + \frac{\beta_0 v_1 + \beta_1 v_0}{x\sin\psi}\Big) + w_1^{'} = 0, \tag{3.35}$$

$$\mathrm{i}\overline{\overline{U}}u_1 + \mathrm{i}\Big(\alpha_1 U x + \frac{\beta_1 V}{\sin\psi}\Big)u_0 + xU^{'}w_1 = -\mathrm{i}(\alpha_0 p_1 + \alpha_1 p_0), \tag{3.36}$$

$$\mathrm{i}\overline{\overline{U}}v_1 + \mathrm{i}\Big(\alpha_1 U x + \frac{\beta_1 V}{\sin\psi}\Big)v_0 + xV^{'}w_1 = -\mathrm{i}\frac{(\beta_0 p_1 + \beta_1 p_0)}{x\sin\psi}, \tag{3.37}$$

$$\mathrm{i}\overline{\overline{U}}w_1 + \mathrm{i}\Big(\alpha_1 U x + \frac{\beta_1 V}{\sin\psi}\Big)w_0 = -p_1^{'}. \tag{3.38}$$

This system of equations is comparable to the equations (3.8)−(3.11) in terms of the disturbance quantities (u_1, v_1, w_1, p_1) corresponding to (u_0, v_0, w_0, p_0). However, we now observe the appearance of inhomogeneous cross-terms. The quantities u_1, v_1, and p_1 are eliminated in a similar fashion to the leading order problem above. In addition, we also use the leading order continuity equation (3.8) to eliminate u_0 and the next order continuity equation (3.35) to eliminate v_0. This leads to the governing equation for the next order inviscid motion eigenfunction, w_1, given by

$$\overline{\overline{U}}(w_1'' - \gamma_0^2 w_1) - \overline{\overline{U}}'' w_1 = \Big[2\overline{\overline{U}}\Big(\alpha_0\alpha_1 + \frac{\beta_0\beta_1}{x^2\sin^2\psi}\Big) + \Big(\alpha_1 - \frac{\beta_1\alpha_0}{\beta_0}\Big)\Big(U'' - \frac{\overline{\overline{U}}''}{\overline{\overline{U}}}U\Big)x\Big]w_0. \tag{3.39}$$

It is important to note that at the point $\eta = \overline{\eta}$, the second term on the right-hand side of (3.39) causes w_1 to have a logarithmic singularity, which is removable by including a critical layer at this location. To find the solution for w_1 we observe that the Rayleigh differential operator on the left-hand side of (3.39) is the same as the operator acting on w_0 in (3.12). Therefore, a solution for the complementary function is $w_1^{(1)} = w_0$. We now apply the method of reduction of order, producing the second solution

$$w_1^{(2)} = w_0(\eta)\int^{\eta} \frac{\mathrm{d}\zeta}{w_0^2(\zeta)}. \tag{3.40}$$

To obtain the particular integral solution of w_1, taking account of the inhomogeneous terms on the right-hand side of (3.39), we apply the method of variation of parameters on one of the complementary function solutions for w_1, namely $w_1^{(1)}$, in the form $w_1 = t_1 w_1 - t_2 w_1$. Following Hall [16], this leads to

$$\begin{aligned} t_1 &= \int^{\zeta} 2\Big(\alpha_0\alpha_1 + \frac{\beta_0\beta_1}{x^2\sin^2\psi}\Big)w_0^2(t)\mathrm{d}t, \\ t_2 &= \int^{\zeta} \Big(\alpha_1 - \frac{\beta_1\alpha_0}{\beta_0}\Big)x\Big(\frac{U''(t)\overline{\overline{U}}(t) - \overline{\overline{U}}''(t)U(t)}{\overline{\overline{U}}^2(t)}\Big)w_0^2(t)\mathrm{d}t, \end{aligned} \tag{3.41}$$

and upon substituting the expression for $w_1^{(2)}$, we yield the particular integral solution

$$\begin{aligned} w_1 &= 2\Big(\alpha_0\alpha_1 + \frac{\beta_0\beta_1}{x^2\sin^2\psi}\Big)w_0(\eta)\int_{\overline{\overline{\eta}}}^{\eta}\frac{\mathrm{d}\zeta}{w_0^2(\zeta)}\int_{\infty}^{\zeta}w_0^2(\theta)\mathrm{d}\theta \\ &+ \Big(\alpha_1 - \frac{\beta_1\alpha_0}{\beta_0}\Big)xw_0(\eta)\int_{\overline{\overline{\eta}}}^{\eta}\frac{\mathrm{d}\zeta}{w_0^2(\zeta)}\int_{\infty}^{\zeta}w_0^2(\theta)\Big(\frac{U''(\theta)\overline{\overline{U}}(\theta) - \overline{\overline{U}}''(\theta)U(\theta)}{\overline{\overline{U}}(\theta)^2}\Big)\mathrm{d}\theta, \end{aligned} \tag{3.42}$$

where $\overline{\overline{\eta}} > \overline{\eta}$. This expression is very similar to that obtained by Hall [16] for the rotating disk, with the important differences being the transformation of his radial distance, r, to our streamwise co-ordinate, x and the azimuthal wavenumbers transforming as $(\beta_0, \beta_1) \rightarrow (\frac{\beta_0}{\sin\psi}, \frac{\beta_1}{\sin\psi})$. We notice that the solution is only valid for $\eta > \overline{\overline{\eta}}$. Expanding $w_0(\zeta)$ as a Taylor series for ζ close to zero and noticing that we must have $w_0(0) = 0$ at the wall, we obtain the same eigenrelation to Hall [16] (up to scale factors of $\sin\psi$),

$$w_1(0) = 2\Big(\alpha_0\alpha_1 + \frac{\beta_0\beta_1}{x^2\sin^2\psi}\Big)\frac{I_1}{w_0'(0)} + \Big(\frac{\alpha_1}{\beta_0} - \frac{\beta_1\alpha_0}{\beta_0^2}\Big)\frac{\sin\psi x I_2}{w_0'(0)}, \tag{3.43}$$

where

$$I_1 = \int_0^{\infty} w_0^2(\theta)\mathrm{d}\theta, \tag{3.44}$$

$$I_2 = \int_0^{\infty}\frac{\beta_0}{\sin\psi}w_0^2(\theta)\Big(\frac{U''(\theta)\overline{\overline{U}}(\theta) - \overline{\overline{U}}''(\theta)U(\theta)}{\overline{\overline{U}}(\theta)^2}\Big)\mathrm{d}\theta. \tag{3.45}$$

We calculated the value for I_1 in (3.44) by using a fixed-step Simpson's rule numerical integration approximation. However, for I_2, we note that (3.45) is singular at $\eta = \overline{\eta}$. Therefore, we must deform the path of integration above the singularity in order to be consistent with a viscous critical layer calculation. To obtain the correct value for I_2, we deform the integration path above the singularity as long as $\overline{\overline{U}}'(\overline{\eta}) < 0$ (and below if this quantity is positive). Using the original definition for $\overline{\overline{U}}$ we can express the integrand of

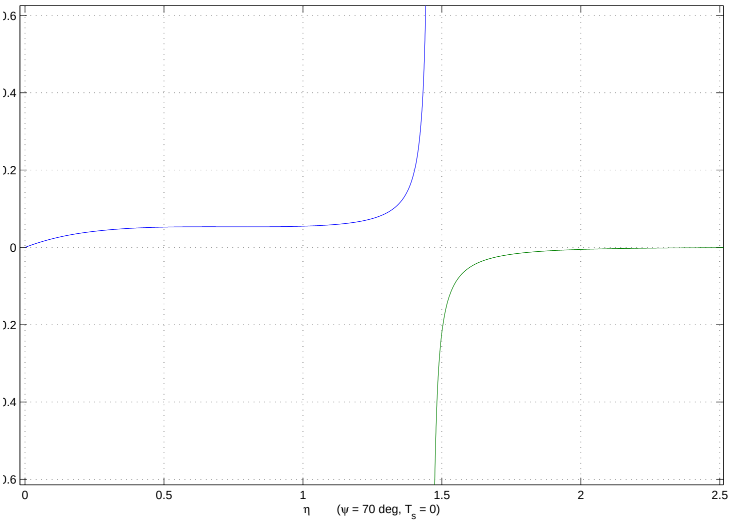

Figure 3.4: Plot of integrand of I_2, $f_2(\eta)$, showing location of singularity at $\eta = \overline{\eta}$.

I_2 in the form

$$f_2(\theta) = \mu^2 w_0^2(\theta) \frac{U''(\theta)V(\theta) - V''(\theta)U(\theta)}{(U(\theta) + \mu V(\theta))^2}, \tag{3.46}$$

so that I_2 is actually independent of ψ. Figure 3.4 shows a plot of f_2 in the $\mathrm{Re}(\eta)$ plane. We see the appearance of the singularity at $\eta = \overline{\eta} = 1.458$. We estimate this integral again using a fixed step Simpson's rule numerical integration approximation, taking into account of the singularity by integrating from $\eta = 0$ to just below the singularity, $\overline{\eta} - \eta_\delta$, and from just above the singularity, $\overline{\eta} + \eta_\delta$, to infinity.

We used $\eta_\delta = 0.124$ to calculate the real part of I_2, whereas for the imaginary part, we evaluate half the complex residue, noting that the integrand of I_2 has a simple pole at $\eta = \overline{\eta}$. Therefore, we expand in terms of Taylor series and use the criteria of $\overline{\overline{U}} = \overline{\overline{U}}'' = 0$

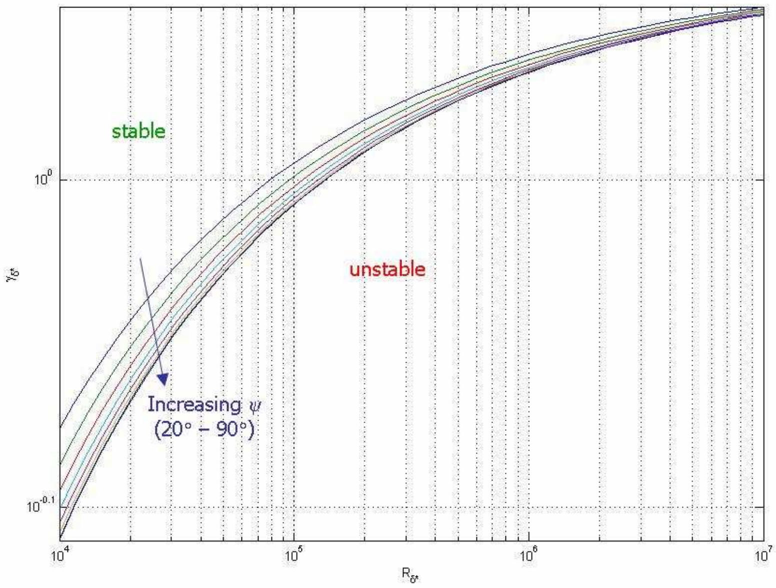

Figure 3.5: Plot of asymptotic neutral wavenumber predictions γ_{δ^*} against R_{δ^*} for inviscid modes for $T_s = 0$, $\psi = 20° - 90°$. Increasing ψ stabilizes the flow.

at the singularity to obtain

$$\mathrm{Im}(I_2) = -\pi\mu^2\Big[w_0^2\frac{U'''V - V'''U + U''V' - V''U'}{(U' + \mu V')^2}\Big]\Big|_{\eta=\overline{\eta}}. \tag{3.47}$$

Upon evaluating both integrals, for the case of the rotating disk ($\psi = 90°$), we obtained

$$I_1 = 0.09656, \tag{3.48}$$

$$I_2 = 0.05824 + 0.03152\mathrm{i}. \tag{3.49}$$

We notice a slight difference between our values and those obtained by Hall [16] for the rotating disk in still fluid and, more recently, Gajjar [6], who has investigated nonlinear effects on the stationary crossflow modes. Hall obtained $I_1 = 0.094$ and $I_2 = 0.058 - 0.029\mathrm{i}$, whereas Gajjar's calculations reveal $I_1 = 0.091$ and $\mathrm{Re}(I_2) = 0.0596$. Furthermore, the value of $\mathrm{Im}(I_2)$ in Hall [16] has been corrected by Gajjar [6]. We will discuss some possible reasons for the differences in these estimates later in §9.1.1, where we draw comparisons between our current results and existing studies on the rotating disk. However, continuing to follow through with the analysis, we use our calculated values for I_1 and I_2 to asymptotically match with the leading order normal velocity solution in the wall layer, (3.34), resulting in the eigenrelation

$$\frac{w_0'(0)^2\mathrm{Ai}'(0)}{\gamma\int_0^\infty \mathrm{Ai}(s)\mathrm{d}s} = 2\Big(\alpha_0\alpha_1 + \frac{\beta_0\beta_1}{x^2\sin^2\psi}\Big)I_1 + \Big(\frac{\alpha_1}{\beta_0} - \frac{\beta_1\alpha_0}{\beta_0^2}\Big)\sin\psi x I_2. \tag{3.50}$$

Using the standard results $\mathrm{Ai}'(0) = -1/(3^{1/3}\Gamma(\frac{1}{3}))$ and $\int_0^\infty \mathrm{Ai}(s)\mathrm{d}s = \frac{1}{3}$, we have

$$\alpha_0\alpha_1 + \frac{\beta_0\beta_1}{x^2\sin^2\psi} = -8.314\gamma_0 x^{-\frac{1}{3}}, \tag{3.51}$$

$$\Big(\frac{\alpha_1}{\beta_0} - \frac{\beta_1\alpha_0}{\beta_0^2}\Big)\sin\psi x = 16.54x^{-\frac{1}{3}}. \tag{3.52}$$

These expressions allow us to calculate the leading order and first order corrections to the effective wavenumber

$$\begin{aligned}\Big(\alpha^2 + \frac{\beta^2}{x^2\sin^2\psi}\Big)^{\frac{1}{2}} &= \gamma_0 + \Big(\alpha_0\alpha_1 + \frac{\beta_0\beta_1}{x^2\sin^2\psi}\Big)\epsilon/\gamma_0 + \ldots, \\ &= 1.162 - 8.314\frac{x^{-1/3}}{\mathrm{R}^{1/6}} + \ldots,\end{aligned} \tag{3.53}$$

as well as the spiral wave angle, ϕ, which has the expansion

$$\begin{aligned}\tan\Big(\frac{\pi}{2} - \phi\Big) &= \frac{\alpha_0 x}{\beta_0} + \Big(\frac{\alpha_1}{\beta_0} - \frac{\beta_1\alpha_0}{\beta_0^2}\Big)x\epsilon + \ldots, \\ &= \frac{4.256}{\sin\psi} + \frac{16.54x^{-1/3}}{\sin\psi\mathrm{R}^{1/6}} + \ldots.\end{aligned} \tag{3.54}$$

We notice here that our leading order estimates agree well with those of Hall [16] when $\psi = 90^\circ$ for the case of a rotating disk. Finally, following Hall [16], we can re-scale these results, expressing the wavenumber and waveangle in terms of the Reynolds number based on boundary layer thickness

$$\delta^* = \left(\frac{\nu^*}{\Omega^*}\right)^{\frac{1}{2}}, \tag{3.55}$$

given by

$$\mathrm{R}_{\delta^*} = \mathrm{R}^{\frac{1}{2}} x (\sin\psi)^{\frac{1}{2}}. \tag{3.56}$$

This leads to expressions for the inviscid mode local wavenumber

$$\gamma_{\delta^*} = 1.162 - 8.314 \mathrm{R}_{\delta^*}^{-1/3} (\sin\psi)^{1/6} + \ldots, \tag{3.57}$$

and the expansion for the inviscid mode local waveangle

$$\tan\left(\frac{\pi}{2} - \phi\right) = \frac{4.256}{\sin\psi} + 16.54 \mathrm{R}_{\delta^*}^{-1/3} (\sin\psi)^{-\frac{5}{6}} + \ldots. \tag{3.58}$$

Therefore, we see that expressing the wavenumber and waveangle in terms of the displacement-thickness Reynolds number eliminates their dependence on the streamwise coordinate, x. Figures 3.5 and 3.6 show the inviscid branches of the asymptotic wavenumber and waveangle predictions, where we have used log-log and semi-log scales for the wavenumber and waveangle plots, respectively. We see that increasing the cone half-angle has the effect of stabilizing the flow by rendering less wavenumbers which are susceptible to the crossflow instability. In the case of the waveangle, increasing the cone half-angle towards that of a rotating disk has the effect of deviating the spiral vortices more from the streamwise

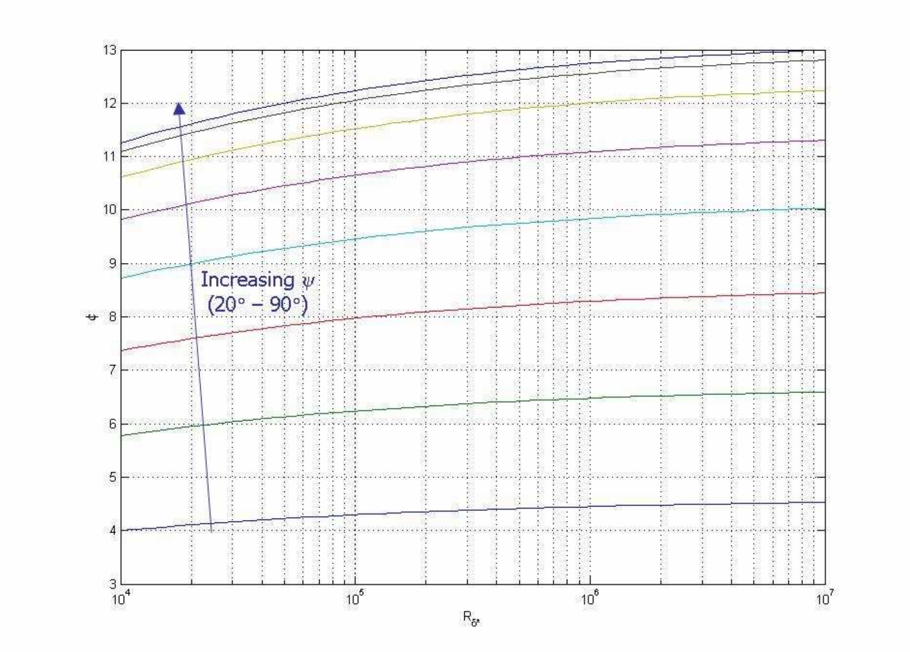

Figure 3.6: Plot of asymptotic neutral waveangle predictions ϕ against R_{δ^*} for inviscid modes for $T_s = 0$, $\psi = 20° - 90°$. Increasing ψ gives a larger vortex waveangle.

direction, reasons for which will be discussed later in §4.

3.2.2 Case B: Rotating disk in axial flow

We now turn our attention to the situation of a rotating disk with an oncoming axial flow (case B). We build on the analysis for the previous case and use modified values for the relevant stability parameters. In our results below, we fix the cone angle at $\psi = 90°$, whereas now the axial flow parameter T_s is varied to represent the introduction of a small amount of streamwise flow onto the rotating cone, for example $T_s = 0.00 - 0.25$, which gives the parameter values investigated by Garrett & Peake [10]. We use the mean flow profiles shown in figures 2.4−2.6 and perturb about these in the same way as for case A. The results for inviscid type I spiral modes are shown in table 3.1 giving the important parameter values for $T_s = 0.00 - 0.25$, $\psi = 90°$. These are the streamwise and azimuthal

T_s	$U'(0)$	$V'(0)$	μ	$\overline{\eta}$	γ_0	I_1	I_2
0.00	0.5102	−0.6159	0.2350	1.458	1.162	0.0966	0.0582 + 0.0315i
0.05	0.5132	−0.6270	0.2543	1.394	1.224	0.0868	0.0710 + 0.0408i
0.10	0.5225	−0.6429	0.2808	1.326	1.294	0.0765	0.0902 + 0.0546i
0.15	0.5380	−0.6626	0.3122	1.260	1.369	0.0669	0.1153 + 0.0735i
0.20	0.5599	−0.6851	0.3473	1.198	1.445	0.0584	0.1466 + 0.0982i
0.25	0.5879	−0.7097	0.3852	1.140	1.522	0.0509	0.1843 + 0.1296i

Table 3.1: Stability parameter values for a rotating disk in axial flow.

velocity gradients at the wall, $\mu-$values for the effective velocity profile, the location of the critical layer, the effective wavenumber as well as the integrals I_1 and I_2 defined in (3.44) and (3.45). We include the case of a rotating disk in still fluid to show how the figures compare with the previously calculated values for a cone in still fluid.

We notice that the $\mu-$values increase with increasing axial flow, as the greater streamwise forced flow is diverted by the perpendicular geometry of the rotating disk and is swept along the disk surface, causing the ratio of azimuthal to radial wavenumbers to increase, as the flow naturally is swept around along the disk surface. From the definition (3.14), this has the effect of increasing μ. As a result of the increased flow onto the disk, the wavenumber in the effective velocity direction, γ_0, also increases and the location of the critical layer for inviscid mode disturbances moves closer to the wall, as the disk boundary layer experiences a larger oncoming flow. Using these calculations, we proceed to evaluate asymptotic estimates for the inviscid mode wavenumber and waveangles at large Reynolds number for varying cases of the axial flow, T_s. These are shown in figures 3.7 and 3.8, respectively. From these inviscid type I results, we see that the introduction of a streamwise axial flow has a slight de-stabilising effect on the asymptotic neutral wavenumber, whereas it has a strongly stabilising effect on the asymptotic neutral waveangle. More generally, in §4 we present the type I and type II combined neutral curves for the rotating disk with varying axial flow strengths. In brief, we find that the introduction of axial flow overall has a stabilizing effect on the inviscid dominated modes for flow over a rotating

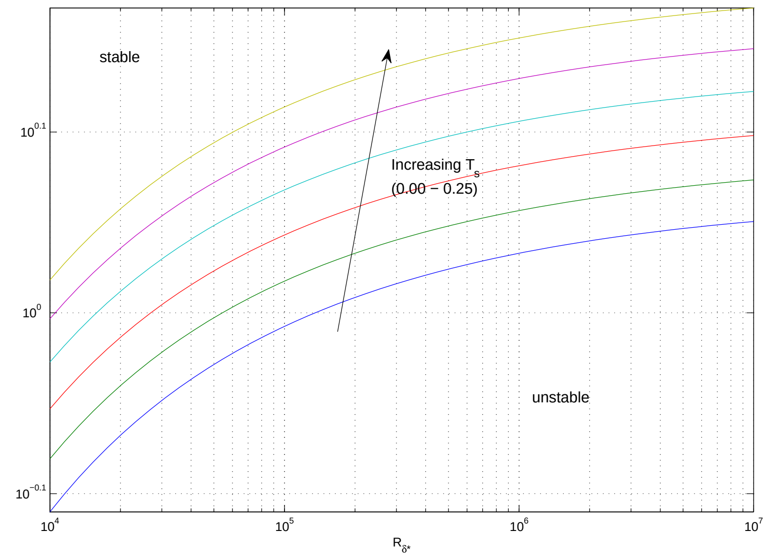

Figure 3.7: Plot of asymptotic neutral wavenumber predictions γ_{δ^*} against R_{δ^*} for inviscid type I modes for $T_s = 0.00 - 0.25$, $\psi = 90°$. Increasing T_s shifts the curves vertically upwards.

disk.

3.3 Leading order eigenmodes (case C)

For the situation of a cone rotating in an axial flow, we again proceed to follow the stability analysis of Hall [16] closely, with the important deviations arising at stages where information about the basic flow quantities is required. This is because, our mean flow setup in §2.3 for a rotating cone in axial flow (case C) is inherently different to the still fluid setup (case A). We proceed to equate terms of $O(\epsilon^{-3})$ in the expansions of

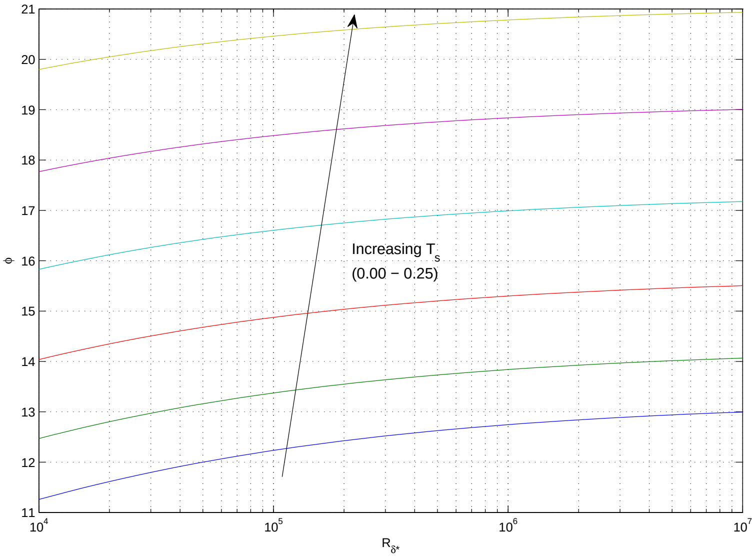

Figure 3.8: Plot of asymptotic neutral waveangle predictions ϕ against R_{δ^*} for inviscid type I modes for $T_s = 0.00 - 0.25$, $\psi = 90°$. Increasing T_s shifts the curves vertically upwards.

(2.53)−(2.56), which leads to

$$\begin{aligned} \mathrm{i}\Big(\alpha_0 u_0 + \frac{\beta_0 v_0}{x\sin\psi}\Big) + w_0^{'} &= 0, && (3.59)\\ \mathrm{i}\overline{\overline{U}}u_0 + U^{'}w_0 &= -\mathrm{i}\alpha_0 p_0, && (3.60)\\ \mathrm{i}\overline{\overline{U}}v_0 + V^{'}w_0 &= -\frac{\mathrm{i}\beta_0 p_0}{x\sin\psi}, && (3.61)\\ \mathrm{i}\overline{\overline{U}}w_0 &= -p_0^{'}, && (3.62) \end{aligned}$$

whereas now in case C, $\overline{\overline{U}} = \alpha_0 U + \frac{\beta_0 V}{x\sin\psi}$. We now eliminate u_0, v_0 and p_0 from the above equations to yield an equation for w_0 given by

$$\overline{\overline{U}}(w_0^{''} - {\gamma_0}^2 w_0) - \overline{\overline{U}}^{''} w_0 = 0, \tag{3.63}$$

where, as in cases A and B, ${\gamma_0}^2 = {\alpha_0}^2 + \frac{{\beta_0}^2}{x^2\sin^2\psi}$ acts as the 'effective' wavenumber from the streamwise and cross-stream directions, and $\overline{\overline{U}}$ is interpreted as the 'effective' velocity profile in the direction of propagation of the spiral vortices on the cone. Therefore we solve Rayleigh's equation once more for w_0 and obtain γ_0 as an eigenvalue subject to the boundary conditions at the wall and infinity, namely

$$w_0 = 0, \quad \eta = 0, \infty. \tag{3.64}$$

Now, again for inviscid instability, we have to solve for the two conditions $\overline{\overline{U}} = 0$ and $\overline{\overline{U}}'' = 0$, where $'$ represents differentiation with respect to η. In order to express these conditions in terms of conditions dependent on the basic flow functions f' and g we notice that in this case $'$ means differentiation with respect to η_1. From the definitions (2.12) and (2.31) we see that η depends on z and η_1 depends on $\overline{z}$. Furthermore, from (2.23) we see that the Mangler surface-normal coordinate depends on z in the form

$$\overline{z} = zx^* \sin\psi. \tag{3.65}$$

This leads to the corresponding relation for the re-scaled surface-normal coordinates based on their respective displacement thicknesses, written in terms of the velocity parameter, m, and the $s-$coordinate,

$$\eta_1 = \left(\frac{m+3}{2s^{\frac{1}{2}}}\right)^{\frac{1}{2}} \eta. \tag{3.66}$$

Using this relation as well as (2.32) to non-dimensionalise the velocities back in terms of $\overline{U}_e^*$, $\overline{V}_w^*$ and s, the conditions for inviscid instability in case C become

$$\begin{aligned} \overline{\overline{U}}_1 = f'(s,\eta_1) + \mu s^{1/2} g(s,\eta_1) &= 0 & (3.67)\\ \text{and} \quad \overline{\overline{U}}_1'' = f'''(s,\eta_1) + \mu s^{1/2} g''(s,\eta_1) &= 0, & \\ \text{at} \quad \eta_1 = \overline{\eta}_1, \mu &= \overline{\mu}, & (3.68) \end{aligned}$$

where $'$ now denotes differentiation with respect to η_1 and as before in cases A and B

$$\mu = \frac{\beta_0}{\alpha_0 x \sin\psi} \tag{3.69}$$

represents the tangent ratio of the observed spiral vortices on the rotating disk or cone. Figure 3.9 shows the inflexional effective velocity profile of most interest in terms of the flow stability and its second derivative, giving a value of $\mu = 1.485$ for the case of $s = 0.3$, with the critical layer being located at $\eta_1 = 1.704$. As in cases A and B, we find the value of μ and $\overline{\eta_1}$ using a Newton-Raphson searching routine. In obtaining the solutions, we require the f''' and g'' profiles, which we calculate using the method of finite differences from the f' and g profiles respectively. In terms of accuracy, this gives an error of $O(h^2)$, where we have used a step length $h = 0.0001$. It is worth noting that these conditions for the location of the onset of inviscid instability at leading order do not include the limiting case of $s = 0$ ($T_s \to \infty$) corresponding to an infinite oncoming flow or no rotation at all, for which the notion of instability is physically meaningless in the (s, η_1)-coordinate setup. The case of the stability of solely streamwise flow onto a non-rotating cone has been studied in the literature by making alternative Mangler transformations. Nevertheless, we require initial profiles for the case $s = 0$ in order to obtain meaningful results for the flow stability in the case $s \neq 0$.

It is important at this stage to note a specific property of the effective velocity profile, $\overline{\overline{U_1}}$, which restricts the scope of our analysis to certain values of s. For a standard Rayleigh critical layer calculation, we seek the location where $\overline{\overline{U}}_1 = \overline{\overline{U}}_1'' = 0$. However, the existence

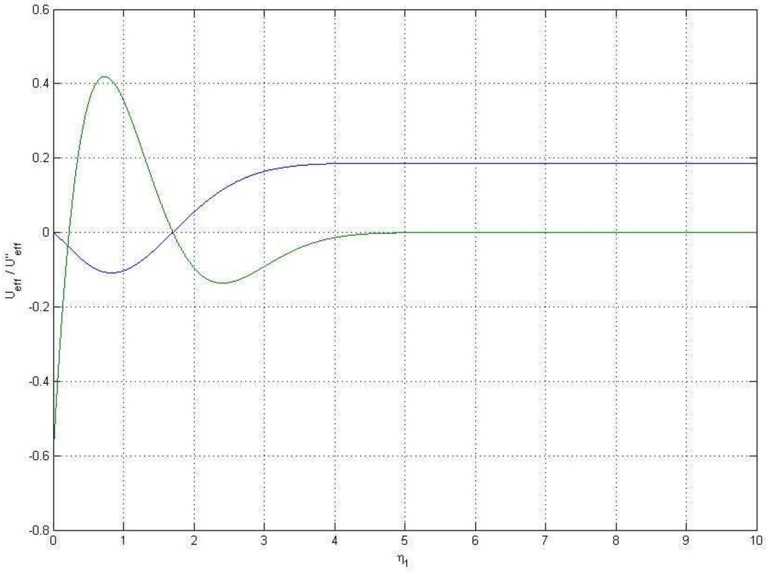

Figure 3.9: Plot of effective velocity $\overline{\overline{U}}_1$ (upper curve at $\eta_1 = 10$) and its second derivative $\overline{\overline{U}}_1''$ (lower curve at $\eta_1 = 10$) for $\psi = 70°$, $s = 0.3$.

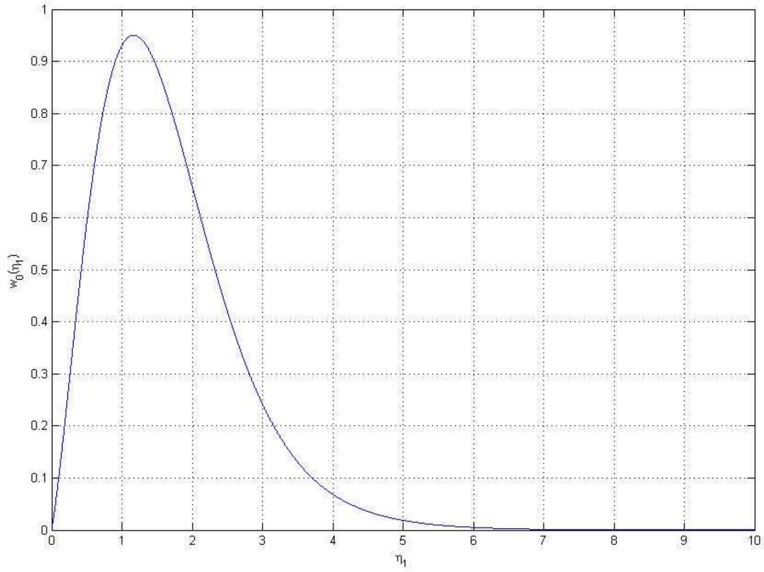

Figure 3.10: Plot of inviscid motion eigenfunction w_0 against η_1 for $\psi = 70°$, $s = 0.3$.

of a location where $\overline{\overline{U}}_1 = 0$ separately raises the case of an additional critical layer. This presents a problem later on in the evaluation of the integral estimate $\mathrm{Re}(I_2)$, which is given in (3.76). We are required to take account of the contribution from this singularity as well as that from the inviscid Rayleigh calculation. For the range $s \geqslant 0.7$ we find that the effective velocity profile, which satisfies the Rayleigh condition, has an additional zero reasonably close to the wall. Figure 3.11 below shows the effective velocity profile for $\mu = 0.8, 0.9, 1.0069, 1.1$ and 1.2 in order of increasing μ. We see that the profile satisfying $\overline{\overline{U}}_1 = \overline{\overline{U}}_1'' = 0$, shown as $\overline{\mu} = 1.0069$, has an extra zero at $\eta_1 = 0.0628$, because it has a positive gradient at the wall; this is in addition to the zero at $\overline{\eta}_1 = 1.6943$. We require the gradient at the wall to be negative, in which case $\overline{\overline{U}}_1$ would only exhibit one zero overall (that obtained at $\overline{\eta}_1 = 1.6943$). Therefore, the turning point for our analysis is at

$$\mu_{crit}(s) = -\frac{f''(s,0)}{s^{\frac{1}{2}} g'(s,0)} \tag{3.70}$$

and we require $\overline{\mu} > \mu_{crit}$ for the standard critical layer calculation to hold. If this condition is satisfied, then μ is sufficiently large at $\mu = \overline{\mu}$ such that the effective velocity profile has a negative gradient at the wall and a second critical layer does not exist. Table 3.2 shows the corresponding values of the stability parameter, $\overline{\mu}$, and the critical value, μ_{crit}, for a zero effective velocity gradient at the wall. We see there is a change between $s = 0.6$ and $s = 0.7$. The results mean that the current inviscid stability analysis is valid for $s \leqslant 0.6$, whereas for $s \geqslant 0.7$ we must include the contribution from the extra critical layer near the wall. Here, we do not include the details of this calculation and present only the results in the region $s \leqslant 0.6$.

s	$\overline{\mu}$	μ_{crit}	s	$\overline{\mu}$	μ_{crit}
0.1	2.5166	1.7973	0.6	1.0790	1.0774
0.2	1.7997	1.4050	0.7	1.0069	1.0517
0.3	1.4849	1.2497	0.8	0.9490	1.0324
0.4	1.2985	1.1655	0.9	0.9011	1.0175
0.5	1.1720	1.1131	1.0	0.86043	1.0057

Table 3.2: Inviscid stability $\overline{\mu}$ and μ_{crit} values for different values of s ($\psi = 70°$).

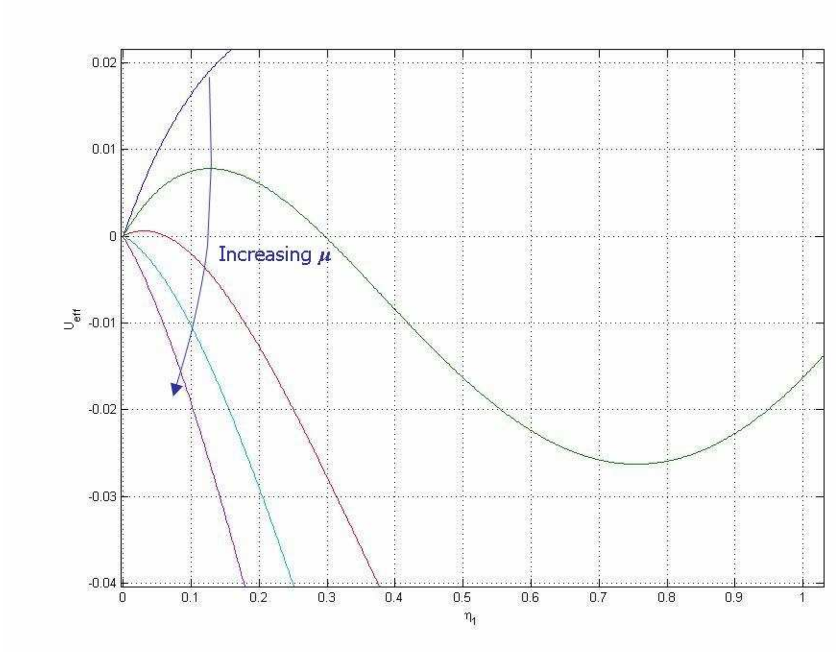

Figure 3.11: Plot of effective velocity profile $\overline{\overline{U}}_1$ for varying μ-values, with $\mu = 0.8, 0.9, 1.0069, 1.1$ and 1.2 in order of increasing μ ($s = 0.7, \psi = 70°$).

We proceed by substituting the expressions (3.68) into (3.63), which yields a modified effective wavenumber

$$\gamma_{01} = \left(\frac{2s^{\frac{1}{2}}}{m+3}\right)^{\frac{1}{2}} \gamma_0 \tag{3.71}$$

as an eigenvalue to the Rayleigh equation, with unchanged boundary conditions requiring the surface-normal eigenfunction to vanish at the wall as well as at the edge of the boundary layer. The requirement that the eigenfunction has unit gradient at the wall in the η_1 setup transfers in η setup to the condition

$$w_0'|_{\eta=0} = \left(\frac{2s^{\frac{1}{2}}}{m+3}\right)^{\frac{1}{2}}. \tag{3.72}$$

In figure 3.10 we see the solution to the corresponding inviscid Rayleigh equation, for the case $\psi = 70°$ and $s = 0.3$. The surface-normal eigenfunction is obtained using the same method of central finite differences, but this time using a fixed mesh size for the η_1 coordinate, and it has similar form to that for cases A and B. We continue to follow the analysis for cases A and B for the leading order inviscid mode solution in the wall layer, which produces very similar solutions except we have $U \to U/x$ and $V \to V/x$ in the basic flow terms.

3.4 First order eigenmodes (case C)

We continue to modify the previous analysis for the situation of a cone rotating in axial flow and follow the work of Hall [16], where possible. The governing equations and solutions for w_1 are much the same, including the eigenrelation, which has the same form as in (3.50), requiring the calculation of two integrals

$$I_1 = \int_0^\infty w_0(\theta)^2 \mathrm{d}\theta, \tag{3.73}$$

$$I_2 = \int_0^\infty \frac{\beta_0}{x \sin\psi} w_0^2(\theta) \Big(\frac{U''(\theta)\overline{\overline{U}}(\theta) - \overline{\overline{U}}^{''}(\theta) U(\theta)}{\overline{\overline{U}}(\theta)^2} \Big) \mathrm{d}\theta, \tag{3.74}$$

where we notice that the integrand of I_2 has an extra term in x present in the present in the denominator as a result of the modified analysis. However, we are able to write f_2, the integrand function of I_2, in the same basic form as in cases A and B due to our modified definition of the effective velocity profile $\overline{\overline{U}}$. We again take account of the singularity at the location of the critical layer, given by $\eta_1 = \overline{\eta_1}$, by evaluating the complex residue at this point, which produces the value of the imaginary part

$$\mathrm{Im}(I_2) = \pi \mu^2 \Big(\frac{(m+3)s^{1/2}}{2} \Big)^{1/2} \Big[w_0^2(\eta) \frac{(f^{''''} g - g^{'''} f' + f^{'''} g^{'} - g^{''} f^{''})}{(f'' + \mu s^{1/2} g^{'})^2} \Big] \Big|_{\eta_1 = \overline{\eta_1}}. \tag{3.75}$$

The terms in $f^{''''}$ and $g^{'''}$ are estimated again using a finite difference approach from the $f^{''}$ and $g^{'}$ profiles. The real part

$$\mathrm{Re}(I_2) = \int_0^\infty \mu^2 \Big(\frac{m+3}{2} \Big) w_0^2(\eta) \frac{f^{'''}(s,\eta_1) g(s,\eta_1) - g''(s,\eta_1) f'(s,\eta_1)}{(f^{'}(s,\eta_1) + \mu s^{1/2} g(s,\eta_1))^2} \mathrm{d}\eta_1, \tag{3.76}$$

and the value of I_1 are again estimated using a fixed step Simpson's rule numerical integration approach. Here, we have not included the full steps, but outline the calculation of those parameters, which are important to the stability analysis. We see that the form of the integrand function of I_2 is shown in figure 3.12, for the case $\psi = 70°$ and $s = 0.3$, with the singularity clearly shown at $\eta_1 = \overline{\eta_1} = 1.704$. The form of f_2 is different from the cases A and B, as the underlying velocity profiles differ due to the changes in the problem formulation. The next order corrections to the effective wavenumber and spiral

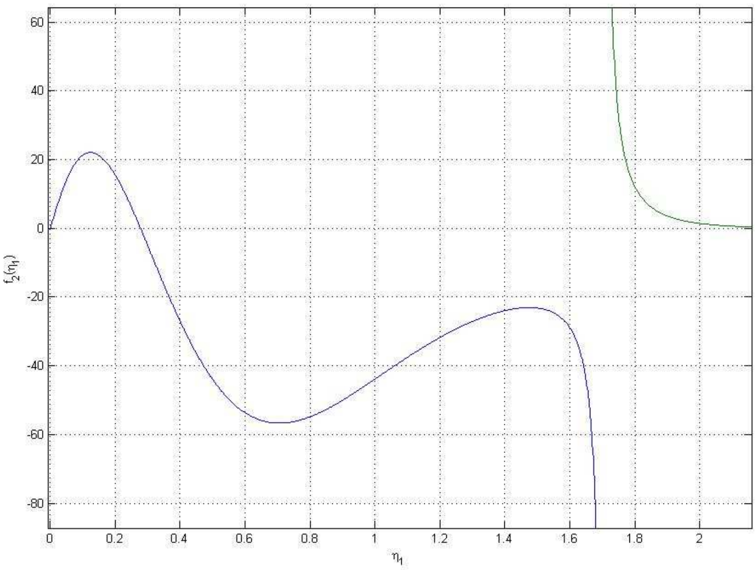

Figure 3.12: Plot of integrand of I_2, $f_2(s,\eta_1)$, showing location of singularity at $\eta_1 = \overline{\eta_1}$ for $\psi = 70°$, $s = 0.3$.

waveangle expansions become

$$\alpha_0\alpha_1 + \frac{\beta_0\beta_1}{x^2\sin^2\psi} = \frac{3\overline{\zeta_0}\left(\sqrt{3}+\frac{\mathrm{Re}(I_2)}{\mathrm{Im}(I_2)}\right)}{4I_1}x^{-\frac{1}{3}}, \tag{3.77}$$

$$\left(\frac{\alpha_1}{\beta_0} - \frac{\beta_1\alpha_0}{\beta_0^2}\right)\sin\psi x = -\frac{3\overline{\zeta_0}}{2\mathrm{Im}(I_2)}x^{-\frac{1}{3}}, \tag{3.78}$$

where we have used $\int_0^\infty \mathrm{Ai}(s)\mathrm{d}s = \frac{1}{3}$ and, for convenience, we define the parameter

$$\overline{\zeta_0}(s) = \frac{w_0'(0)^2\mathrm{Ai}'(0)}{\left(\frac{\gamma_0^2}{1+\mu^2}\right)^{\frac{1}{6}}\left(\frac{m+3}{2s^{3/2}}\right)^{\frac{1}{6}}\left(f''(s,0)+\mu s^{1/2}g'(s,0)\right)^{\frac{1}{3}}}. \tag{3.79}$$

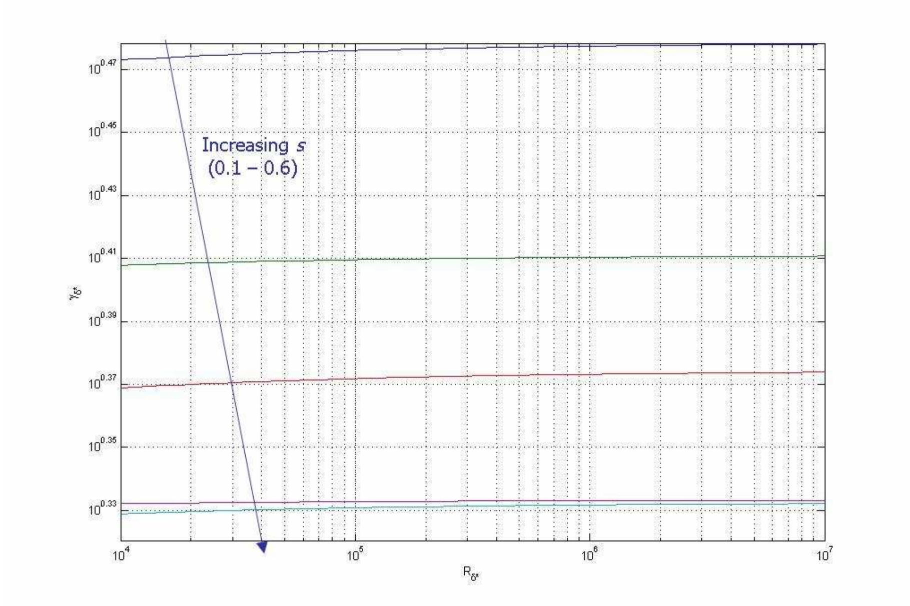

Figure 3.13: Plot of asymptotic neutral wavenumber predictions γ_{δ^*} against R_{δ^*} for inviscid modes for $\psi = 70°$, $s = 0.1 - 0.6$. Increasing s stabilizes the flow.

Furthermore, we are able to write the Reynolds number based on boundary layer thickness in terms of the non-dimensional streamwise coordinate, in the form

$$\mathrm{R}_{\delta^*} \quad = \quad \mathrm{R}^{\frac{1}{2}} x (\sin\psi)^{\frac{1}{2}}. \tag{3.80}$$

If we use this definition, we find the inviscid mode wavenumber and waveangle estimates may be written in terms of the displacement-thickness Reynolds number, and thereby eliminate any dependence on the streamwise coordinate, in the form

$$\gamma_{\delta^*} \quad = \quad \gamma_0 + \frac{3\overline{\zeta_0}\Big(\sqrt{3} + \frac{\mathrm{Re}(I_2)}{\mathrm{Im}(I_2)}\Big)\mathrm{R}_{\delta^*}^{-1/3}(\sin\psi)^{\frac{1}{6}}}{4I_1\gamma_0} + \ldots, \tag{3.81}$$

$$\tan\left(\frac{\pi}{2} - \phi\right) \quad = \quad \frac{1}{\mu\sin\psi} - \frac{3\overline{\zeta_0}\mathrm{R}_{\delta^*}^{-1/3}(\sin\psi)^{-\frac{5}{6}}}{2\mathrm{Im}(I_2)} + \ldots. \tag{3.82}$$

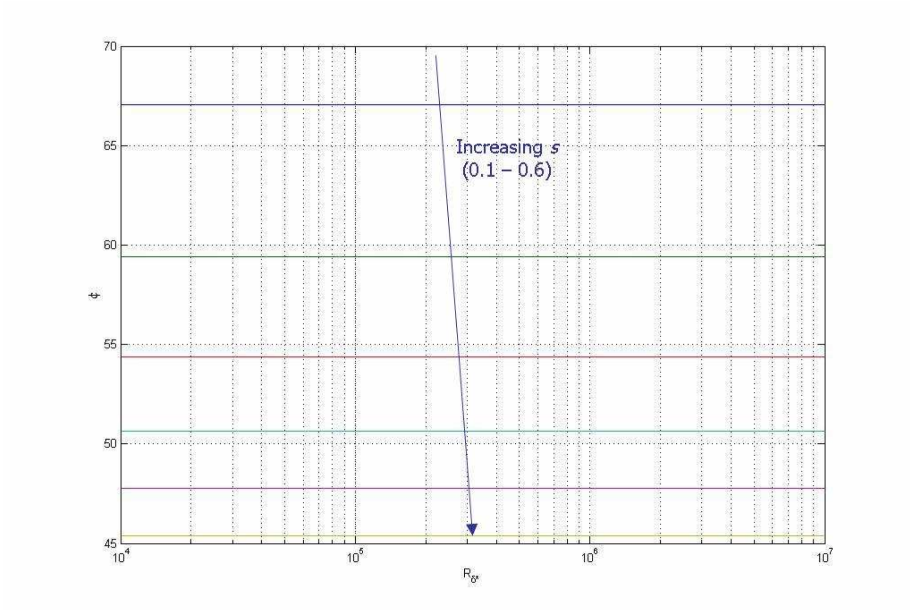

Figure 3.14: Plot of asymptotic neutral waveangle predictions ϕ against R_{δ^*} for inviscid modes for $\psi = 70°$, $s = 0.1 - 0.6$. Increasing s gives a smaller vortex waveangle.

The results for the inviscid mode wavenumber and waveangles are shown in figures 3.13 and 3.14 for different strengths of oncoming flows varying from $s = 0.1 - 0.6$. We see from the wavenumber plot that, in general, as s is increased (or T_s decreased), the type I wavenumber curve is shifted down, effectively reducing the unstable area bounded by the neutral curve, which has the result of stabilizing the flow. The exception is from $s = 0.4$ to $s = 0.5$, where the curve shifts upwards by a small amount. This shows the type I wavenumber exhibits a slight sensitivity to changes in the axial flow. Furthermore, we see that changes in the control parameter s lead to a greater variation in the wavenumber than in case A, where changes in the cone angle ψ are only manifested in the next order correction terms and not the more dominant leading order estimates. In case C, as in case B, we see that changing the axial flow control parameter s (corresponding to changing T_s in case B) results in alterations in both the leading order and next order terms, producing a greater change in the overall wavenumber estimates. Physically, the stronger oncoming flow for smaller s-values causes fluid to be swept along the rotating cone, resulting in the effective number of spiral vortices wrapping around the cone surface to increase once the boundary layer has undergone the first primary instability.

This effect is seen further in the waveangle plot, where increasing the s parameter leads to a reduction in the angle at which the spiral vortices are shed. This would imply that increasing the axial flow parameter, T_s, would increase the vortex waveangle. Physically, the stronger oncoming axial flow would effectively sweep more fluid in the θ-coordinate direction, causing the spiral vortices to undergo a stronger azimuthal shear effect. This results in an increased waveangle for larger values of T_s (or smaller s-values).

A further observation for both curves (especially for the waveangle) is there seems to be less dependence on the next order correction terms, and the leading order terms appear to dominate in the wavenumber and waveangle estimates for larger Reynolds numbers. This is shown by the almost horizontal waveangle neutral curves as R_{δ^*} varies.

Chapter 4

The Viscous Type II Modes

In this section, we consider the stability of stationary viscous modes to lower branch disturbances scaled using a familiar triple-deck structure analogous to that found for Blasius flow over a flat-plate (see Smith [42]). The condition for time-independent stationary modes to be investigated is that the effective wall shear, $\alpha U' x \sin\psi + \beta V'$, is zero at leading order. This is in contrast to the conditions of the earlier inviscid stability analysis of §3, which required the effective velocity, $\overline{\overline{U}}$, and its second derivative, $\overline{\overline{U}}''$, to vanish at the location of the critical layer, $\eta = \overline{\eta}$. We proceed to build our triple-deck structure using the convenient small parameter, now given by

$$\epsilon = \mathrm{R}^{-\frac{1}{16}},$$

with the lower, main and upper decks typically having thicknesses of order ϵ^9, ϵ^8 and ϵ^4, respectively. The triple-deck arrangement, which was used by Hall [16] to successfully identify the viscous wall modes on a rotating disk is shown schematically in figure 4.1. We have defined the inner variables ξ, ζ, and Z to represent $O(1)$ variation within the lower, main and upper decks, respectively. Using Hall's setup, the streamwise and azimuthal wavenumbers, α and β, are now scaled upon a viscous length-scale, so that the velocity perturbation becomes

$$\tilde{u} = u(z)\mathrm{exp}\Big(\frac{\mathrm{i}}{\epsilon^4}\Big\{\int^x \alpha(x,\epsilon)\mathrm{d}x + \beta(\epsilon)\theta\Big\}\Big), \tag{4.1}$$

with similar expressions for $\tilde{v}$, $\tilde{w}$ and the pressure perturbation, $\tilde{p}$. We expand the streamwise and azimuthal wavenumbers as

$$\alpha = \alpha_0 + \epsilon^2\alpha_1 + \epsilon^3\alpha_2 + \dots, \tag{4.2}$$

$$\beta = \beta_0 + \epsilon^2\beta_1 + \epsilon^3\beta_2 + \dots, \tag{4.3}$$

noting that the order ϵ terms are zero. The requirement of stationary modes means that we wish to obtain $\alpha_i \in \Re$ and $\beta_i \in \Re$ such that at the location x the flow is neutrally stable. Importantly, much of the analysis for the wall-dominated type II modes for the rotating cone transpires to be very similar to the rotating disk wall modes studied by Hall [16]. For cases A and B (SS4.1 and 4.2), there are some additional terms in the upper deck disturbance equations pertaining to the introduction of an axial flow and, in addition, a scale factor of $\sin\psi$ is introduced, as was the case with the type I modes investigation. For the case C (§§4.4 and 4.5), the analysis and method follows Hall [16], but the derived equations and calculated results differ much more in their form. This is again due to the input from the basic flow terms, and so we must be careful when calculating such quantities involving the basic flow variables.

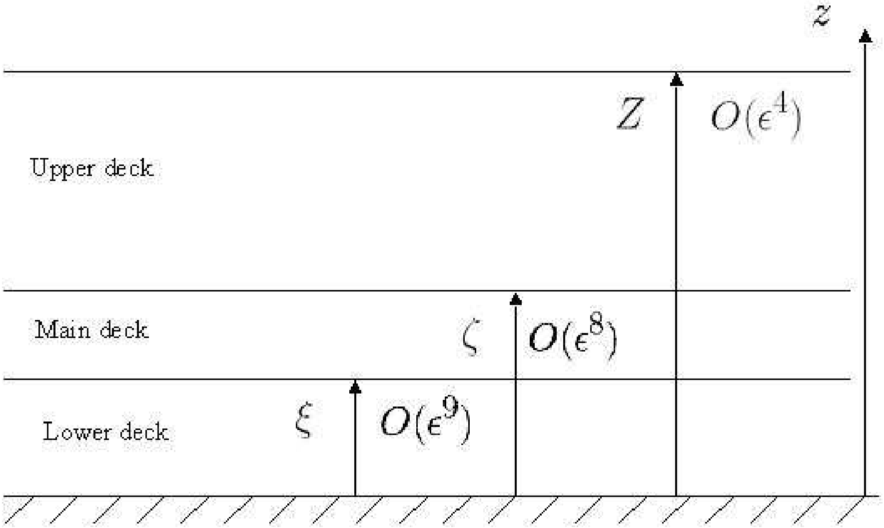

Figure 4.1: Schematic diagram of the triple-deck structure for a rotating cone.

4.1 Leading order triple-deck solution (cases A and B)

In the upper deck, the basic flow expands as $U = T_s$, $V = -1$, whereas the disturbance fields have expansions of the form

$$u = \epsilon^3 u_0^U(Z) + \epsilon^4 u_1^U(Z) + \dots, \tag{4.4}$$

$$v = \epsilon^3 v_0^U(Z) + \epsilon^4 v_1^U(Z) + \dots, \tag{4.5}$$

$$w = \epsilon^3 w_0^U(Z) + \epsilon^4 w_1^U(Z) + \dots, \tag{4.6}$$

$$p = \epsilon^3 p_0^U(Z) + \epsilon^4 p_1^U(Z) + \dots. \tag{4.7}$$

The leading equations obtained by balancing terms of $O(\epsilon^{-1})$ in (2.46)−(2.49) are given by

$$\begin{aligned}
\mathrm{i}\Big(\alpha_0 u_0^U + \frac{\beta_0 v_0^U}{x\sin\psi}\Big) + \frac{\mathrm{d}w_0^U}{\mathrm{d}Z} &= 0, && (4.8)\\
\Big(\frac{\beta_0}{\sin\psi} - \alpha_0 x T_s\Big) u_0^U &= \alpha_0 p_0^U, && (4.9)\\
\Big(\frac{\beta_0}{\sin\psi} - \alpha_0 x T_s\Big) v_0^U &= \frac{\beta_0 p_0^U}{x\sin\psi}, && (4.10)\\
\mathrm{i}\Big(\frac{\beta_0}{\sin\psi} - \alpha_0 x T_s\Big) w_0^U &= \frac{\mathrm{d}p_0^U}{\mathrm{d}Z}. && (4.11)
\end{aligned}$$

Substituting for u_0^U and v_0^U from (4.9) and (4.10) into (4.8), then using (4.11) leads to

$$\frac{\mathrm{d}^2 w_0^U}{\mathrm{d}Z^2} - \gamma_0^2 w_0^U = 0, \qquad (4.12)$$

where the leading order wavenumber is $\gamma_0 = \sqrt{(\alpha_0^2 + \frac{\beta_0^2}{x^2\sin^2\psi})}$. This excludes the case

$$\Big(\frac{\beta_0}{\sin\psi} - \alpha_0 x T_s\Big) = 0 \qquad (4.13)$$

at which $T_s = T_{sc}$. The solutions to this system of equations must decay to zero as $z \longrightarrow \infty$. Therefore, we obtain similar solutions to Hall [16], given by

$$\begin{aligned}
u_0^U &= \frac{\alpha_0 C}{(\frac{\beta_0}{\sin\psi} - \alpha_0 x T_s)} e^{-\gamma_0 Z}, && (4.14)\\
v_0^U &= \frac{\beta_0 C}{x\sin\psi(\frac{\beta_0}{\sin\psi} - \alpha_0 x T_s)} e^{-\gamma_0 Z}, && (4.15)\\
w_0^U &= \frac{\mathrm{i}\gamma_0 C}{(\frac{\beta_0}{\sin\psi} - \alpha_0 x T_s)} e^{-\gamma_0 Z}, && (4.16)\\
p_0^U &= C e^{-\gamma_0 Z}, && (4.17)
\end{aligned}$$

where $C = \text{const.}$

In the main deck, we scale the streamwise and azimuthal disturbance velocity expansions by the difference in powers of ϵ between the upper and main deck, but keep the surface-normal and pressure disturbance expansions at the same leading order to match with the upper deck. This gives

$$\begin{aligned} u &= \epsilon^{-1}u_0^M(\zeta) + u_1^M(\zeta) + \ldots, && (4.18)\\ v &= \epsilon^{-1}v_0^M(\zeta) + v_1^M(\zeta) + \ldots, && (4.19)\\ w &= \epsilon^{3}w_0^M(\zeta) + \epsilon^{4}w_1^M(\zeta) + \ldots, && (4.20)\\ p &= \epsilon^{3}p_0^M(\zeta) + \epsilon^{4}p_1^M(\zeta) + \ldots. && (4.21) \end{aligned}$$

We note that as $Z \to 0$, $p_0^U \to C$, and also by Prandtl matching that

$$\lim_{\zeta\to\infty} p_0^M(\zeta) = \lim_{Z\to 0} p_0^U(Z) = C. \qquad (4.22)$$

Expanding the disturbance equations (2.46)$-$(2.49) and equating terms of $O(\epsilon^{-5})$ leads to

$$\begin{aligned} \mathrm{i}\alpha_0 u_0^M + \frac{\mathrm{i}\beta_0 v_0^M}{x\sin\psi} + \frac{\mathrm{d}w_0^M}{\mathrm{d}\zeta} &= 0, && (4.23)\\ \mathrm{i}\Big(\alpha_0 xU + \frac{\beta_0 V}{\sin\psi}\Big)u_0^M + xU'w_0^M &= 0, && (4.24)\\ \mathrm{i}\Big(\alpha_0 xU + \frac{\beta_0 V}{\sin\psi}\Big)v_0^M + xV'w_0^M &= 0, && (4.25)\\ \frac{\mathrm{d}p_0^M}{\mathrm{d}\zeta} &= 0. && (4.26) \end{aligned}$$

From (4.26) we see that $p_0^M(\zeta) = \text{const.}$ and so use of (4.22) gives $p_0^M(\zeta) = C$. Subsequently, eliminating u_0^M and v_0^M from (4.23), before integrating the resulting expression with respect to ζ, gives the disturbance field in the main deck, which is similar to that obtained by Hall [16] and matches with the previous upper deck solutions

$$\begin{aligned} u_0^M &= \frac{Cx\gamma_0 U^{'}}{(\frac{\beta_0}{\sin\psi} - \alpha_0 x T_s)^2}, && (4.27)\\ v_0^M &= \frac{Cx\gamma_0 V^{'}}{(\frac{\beta_0}{\sin\psi} - \alpha_0 x T_s)^2}, && (4.28)\\ w_0^M &= -\frac{\mathrm{i}C\gamma_0}{(\frac{\beta_0}{\sin\psi} - \alpha_0 x T_s)^2}\Big(\alpha_0 x U + \frac{\beta_0 V}{\sin\psi}\Big). && (4.29) \end{aligned}$$

This gives us that w_0^M satisfies the no-slip condition as $\zeta \to 0$, with the effective wall shear decaying to zero, namely

$$\alpha x U^{'} + \frac{\beta}{\sin\psi} V^{'} \to 0, \tag{4.30}$$

as $\zeta \to 0$. Now, if we choose the leading order streamwise and azimuthal wavenumbers such that

$$\alpha_0 U^{'}(0) + \frac{\beta_0}{x\sin\psi} V^{'}(0) = 0, \tag{4.31}$$

then we have $\alpha_0 u_0^M + \frac{\beta_0}{x\sin\psi} v_0^M \to 0$ as $\zeta \to 0$. The constraint (4.31) is exactly the condition which forces us to consider only neutral, or stationary, disturbances, and in our rotating coordinate system, these modes remain fixed on the cone surface. For the case of the rotating disk in still fluid (with $\psi = 90°$), we have the well-known values $U^{'}(0) = 0.5102$ and $V^{'}(0) = -0.6159$ (see Malik [33]), which gives $\alpha_0 x \sin\psi/\beta_0 = 1.207$. It is important to note from this relation that when

$$T_s = T_{sc} = \Big|\frac{U^{'}(0)}{V^{'}(0)}\Big|, \tag{4.32}$$

T_s	$U^{'}(0)$	$V^{'}(0)$	$\lvert U^{'}(0)/V^{'}(0)\rvert$
0.00	0.5102	-0.6159	0.828
0.05	0.5132	-0.6270	0.819
0.10	0.5225	-0.6429	0.813
0.15	0.5380	-0.6626	0.812
0.20	0.5599	-0.6851	0.817
0.25	0.5879	-0.7097	0.828

Table 4.1: Investigating whether $T_{sc} = |U^{'}(0)/V^{'}(0)|$ for case B.

the analysis breaks down. However, we observe from table 4.1 that for the range of axial flow parameters we have investigated for case B ($T_s = 0.00 - 0.25$), this is not the case, and, therefore, the analysis remains valid within this region.

Next, we expand the basic flow for small ζ and express the main deck stretched coordinate in terms of the lower deck coordinate, $\xi = \zeta/\epsilon$, so we have

$$U = \epsilon U_0\xi + \epsilon^2 U_1\xi^2 + \epsilon^3 U_2\xi^3 + \dots, \tag{4.33}$$

$$V = \epsilon V_0\xi + \epsilon^2 V_1\xi^2 + \epsilon^3 V_2\xi^3 + \dots, \tag{4.34}$$

where $U_{j-1} = U^{(j)}(0)/j!$ and $V_{j-1} = V^{(j)}(0)/j!$ for $j = 1, 2, \dots$.

The corresponding lower deck disturbance fields are expressed in the form $u = \epsilon^{-1}u^L_{-1}(\xi) + u^L_0(\xi)$, with a similar expression for v. However, as before, for the surface-normal and pressure perturbations, we take $w = \epsilon^3 w^L_0(\xi) + \epsilon^4 w^L_1(\xi)$ and $p = \epsilon^3 p^L_0(\xi) + \epsilon^4 p^L_1(\xi)$ to match with the main deck solution. Taking these expansions and substituting the basic flow expansions (4.33),(4.34) to match with the leading order terms from the main deck solutions (4.27)−(4.29) written in terms of ξ, leads us to the lower deck disturbance field expansions having a very similar form to those outlined in Hall [16], namely

$$
\begin{aligned}
u &= \frac{x\gamma_0 C}{\epsilon(\frac{\beta_0}{\sin\psi} - \alpha_0 x T_s)^2}[U_0 + 2\epsilon U_1\xi + \ldots] + \frac{u^L_{-1}(\xi)}{\epsilon} + u^L_0(\xi) + \epsilon u^L_1(\xi) + \ldots, \quad (4.35)\\
v &= \frac{x\gamma_0 C}{\epsilon(\frac{\beta_0}{\sin\psi} - \alpha_0 x T_s)^2}[V_0 + 2\epsilon V_1\xi + \ldots] + \frac{v^L_{-1}(\xi)}{\epsilon} + v^L_0(\xi) + \epsilon v^L_1(\xi) + \ldots, \quad (4.36)\\
w &= -\frac{\mathrm{i}\gamma_0\epsilon^5}{(\frac{\beta_0}{\sin\psi} - \alpha_0 x T_s)^2}\Big[\Big(\alpha_0 U_1 x + \frac{\beta_0 V_1}{\sin\psi}\Big)\xi^2 + \epsilon\Big(\alpha_0 x U_2 + \frac{\beta_0 V_2}{\sin\psi}\Big)\xi^3 + \ldots\Big]\\
&+ \epsilon^6 w^L_1(\xi) + \ldots, \quad (4.37)\\
p &= \epsilon^3 p^L_1(\xi) + \ldots. \quad (4.38)
\end{aligned}
$$

To obtain the solutions in the lower deck, we substitute these expansions into the disturbance equations (2.46)$-$(2.49) and solve for (u^L_{-1}, v^L_{-1}),(u^L_0, v^L_0),$(u^L_1, v^L_1, w^L_1, p^L_1)$. Equating terms of $O(\epsilon^{-5})$ and $O(\epsilon^{-4})$, we obtain the relations

$$
\begin{aligned}
v^L_{-1}(\xi) &= -\frac{\alpha_0 x\sin\psi}{\beta_0}u^L_{-1}(\xi), \quad (4.39)\\
v^L_0(\xi) &= -\frac{\alpha_0 x\sin\psi}{\beta_0}u^L_0(\xi). \quad (4.40)
\end{aligned}
$$

It is worth noting here that from (4.31) we have $\frac{\alpha_0 x\sin\psi}{\beta_0} = -\frac{V'(0)}{U'(0)}$. Next, we turn to the streamwise momentum disturbance equation, equating terms of $O(\epsilon^{-3})$ and $O(\epsilon^{-2})$ to give us the governing differential equation for $u^L_{-1}(\xi)$, as well as an equation for $u^L_0(\xi)$ and $w^L_1(\xi)$, resulting in

$$
\begin{aligned}
\frac{\mathrm{d}^2 u^L_{-1}}{\mathrm{d}\xi^2} - \mathrm{i}\Big(\alpha_0 x U_1 + \frac{\beta_0 V_1}{\sin\psi}\Big)\xi^2 u^L_{-1} &= 0, \quad (4.41)\\
-\mathrm{i}\Big(\alpha_0 x U_1 + \frac{\beta_0}{\sin\psi}V_1\Big)\xi^2 u^L_0 + \frac{\mathrm{d}^2 u^L_0}{\mathrm{d}\xi^2} &= xU_0 w^L_1 + \mathrm{i}\Big(\alpha_0 x U_2 + \frac{\beta_0}{\sin\psi}V_2\Big)\xi^3 u^L_{-1}\\
&+ \mathrm{i}\Big(\alpha_1 U_0 x + \frac{\beta_1}{\sin\psi}V_0\Big)\xi\Big[\frac{x\gamma_0 C U_0}{(\frac{\beta_0}{\sin\psi} - \alpha_0 x T_s)^2} + u^L_{-1}\Big]. \quad (4.42)
\end{aligned}
$$

The corresponding boundary conditions from the no-slip condition at the wall and matching with the main deck away from the wall at $O(\epsilon^{-1})$ and $O(1)$ lead to

$$u^L_{-1} = -\frac{x\gamma_0 C U_0}{(\frac{\beta_0}{\sin\psi} - \alpha_0 x T_s)^2}, \quad u^L_0 = 0, \quad \text{on} \quad \xi = 0, \tag{4.43}$$

$$u^L_{-1} \to 0, \quad u^L_0 \to \frac{x\gamma_0 D U_0}{(\frac{\beta_0}{\sin\psi} - \alpha_0 x T_s)^2}, \quad \text{as} \quad \xi \to \infty, \tag{4.44}$$

for some constant D. If we make the substitution

$$\rho = \sqrt{2}\Delta^{\frac{1}{4}}\xi, \quad \text{where} \quad \Delta = \mathrm{i}\Big(\alpha_0 x U_1 + \frac{\beta_0}{\sin\psi} V_1\Big), \tag{4.45}$$

then we are required to solve the parabolic cylinder equation for u^L_{-1}, given by

$$\frac{\mathrm{d}^2 u^L_{-1}}{\mathrm{d}\rho^2} - \frac{\rho^2}{4} u^L_{-1} = 0. \tag{4.46}$$

We use the boundary condition on $\xi = 0$ to eliminate the constant of integration, and the condition as $\xi \to \infty$ to justify ignoring the exponentially growing solution, $V(0,\rho)$. This results in the following solution, closely related to that given in Hall [16],

$$u^L_{-1}(\xi) = -\frac{U_0 \gamma_0 C x}{(\frac{\beta_0}{\sin\psi} - \alpha_0 x T_s)^2} \frac{U(0, \sqrt{2}\Delta^{\frac{1}{4}}\xi)}{U(0,0)}, \tag{4.47}$$

where $U(0, \sqrt{2}\Delta^{\frac{1}{4}}\xi)$ is a parabolic cylinder function (see Abramowitz & Stegun [1]).

4.2 First order lower-deck solution

4.2.1 Case A: Rotating cone in still fluid

To find $u^L_0(\xi)$ and $v^L_0(\xi)$, we must first solve for $w^L_1(\xi)$, which requires considering the next order approximation to the disturbance equations. At $O(\epsilon^{-3})$ in the continuity equation and $O(\epsilon^{-6})$ in the surface-normal component of the linearised disturbance equations, we obtain

$$\begin{aligned}
\mathrm{i}\Big(\alpha_0 u_1^L + \frac{\beta_0 v_1^L}{x\sin\psi}\Big) + \frac{\mathrm{d}w_1^L}{\mathrm{d}\xi} &= -\frac{\mathrm{i}x\gamma_0 C}{(\frac{\beta_0}{\sin\psi} - \alpha_0 x T_s)^2}\Big(\alpha_1 U_0 + \frac{\beta_1 V_0}{x\sin\psi}\Big) - \mathrm{i}\Big(\alpha_1 u_{-1}^L + \frac{\beta_1 v_{-1}^L}{x\sin\psi}\Big), \qquad (4.48)\\
\frac{\mathrm{d}p_1^L}{\mathrm{d}\xi} &= 0 \Rightarrow p_1^L(\xi) = C. \qquad (4.49)
\end{aligned}$$

Our next task is to expand the streamwise and azimuthal disturbance equations to $O(\epsilon^{-1})$. For the rotating disk in still fluid, Hall [16] made the important observation that it is at this order where terms due to the Coriolis effect from the choice of rotating co-ordinate system balance with the viscous terms and, physically, this is the case for the rotating cone boundary layer. Importantly, this observation allows us to analyse the lower branch viscous mode. Following Hall's idea, we eliminate the terms in W by expanding the continuity equation (2.18) in terms of ϵ and noting that $W = O(\epsilon^2)$, and so does not play a role in the equations at $O(\epsilon^{-1})$. Our equations are similar to those in Hall [16]

$$\begin{aligned}
&\mathrm{i}u_1^L\Big(\alpha_0 x U_1 + \frac{\beta_0}{\sin\psi}V_1\Big)\xi^2 + 2xw_1^L U_1\xi - 2\Big(v_{-1}^L + \frac{x\gamma_0 C V_0}{(\frac{\beta_0}{\sin\psi} - \alpha_0 x T_s)^2}\Big)\\
&\quad + \mathrm{i}\xi\Big(\alpha_1 U_0 x + \frac{\beta_1 V_0}{\sin\psi}\Big)\Big(u_0^L + \frac{2U_1\xi x\gamma_0 C}{(\frac{\beta_0}{\sin\psi} - \alpha_0 x T_s)^2}\Big)\\
&\quad + \mathrm{i}\xi^2\Big(\alpha_1 U_1 x + \frac{\beta_1 V_1}{\sin\psi}\Big)\Big(u_{-1}^L + \frac{U_0 x\gamma_0 C}{(\frac{\beta_0}{\sin\psi} - \alpha_0 x T_s)^2}\Big)\\
&\quad + \mathrm{i}\xi\Big(\alpha_2 U_0 x + \frac{\beta_2 V_0}{\sin\psi}\Big)\Big(u_{-1}^L + \frac{U_0 x\gamma_0 C}{(\frac{\beta_0}{\sin\psi} - \alpha_0 x T_s)^2}\Big) + \mathrm{i}\xi^3\Big(\alpha_0 x U_2 + \frac{\beta_0 V_2}{\sin\psi}\Big)u_0^L\\
&\quad = -\mathrm{i}\alpha_0 p_1^L + \frac{\mathrm{d}^2 u_1^L}{\mathrm{d}\xi^2} + \frac{6U_2 x\gamma_0 C}{(\frac{\beta_0}{\sin\psi} - \alpha_0 x T_s)^2}, \qquad (4.50)
\end{aligned}$$

$$
\begin{aligned}
\mathrm{i}v_1^L\Big(\alpha_0 x U_1 + \frac{\beta_0}{\sin\psi}V_1\Big)\xi^2 + 2xw_1^L V_1\xi + 2\Big(u_{-1}^L + \frac{x\gamma_0 C U_0}{(\frac{\beta_0}{\sin\psi}-\alpha_0 x T_s)^2}\Big)& \\
+\mathrm{i}\xi\Big(\alpha_1 U_0 x + \frac{\beta_1 V_0}{\sin\psi}\Big)\Big(v_0^L + \frac{2V_1\xi x\gamma_0 C}{(\frac{\beta_0}{\sin\psi}-\alpha_0 x T_s)^2}\Big)& \\
+\mathrm{i}\xi^2\Big(\alpha_1 U_1 x + \frac{\beta_1 V_1}{\sin\psi}\Big)\Big(v_{-1}^L + \frac{V_0 x\gamma_0 C}{(\frac{\beta_0}{\sin\psi}-\alpha_0 x T_s)^2}\Big)& \\
+\mathrm{i}\xi\Big(\alpha_2 U_0 x + \frac{\beta_2 V_0}{\sin\psi}\Big)\Big(v_{-1}^L + \frac{V_0 x\gamma_0 C}{(\frac{\beta_0}{\sin\psi}-\alpha_0 x T_s)^2}\Big) + \mathrm{i}\xi^3\Big(\alpha_0 x U_2 + \frac{\beta_0 V_2}{\sin\psi}\Big)v_0^L& \\
= -\frac{\mathrm{i}\beta_0 p_1^L}{x\sin\psi} + \frac{\mathrm{d}^2 v_1^L}{\mathrm{d}\xi^2} + \frac{6V_2 x\gamma_0 C}{(\frac{\beta_0}{\sin\psi}-\alpha_0 x T_s)^2}.& \qquad (4.51)
\end{aligned}
$$

To simplify these expressions, we carry out the manipulation $\mathrm{i}\alpha_0(4.50) + \frac{\mathrm{i}\beta_0}{x\sin\psi}(4.51)$. We also expand the streamwise and azimuthal basic flow equations (2.19),(2.20) in powers of ϵ to obtain the values

$$
\begin{aligned}
U_1 = \frac{U''(0)}{2!} &= -\frac{1+mT_s^2}{2}, &\qquad (4.52)\\
V_1 = \frac{V''(0)}{2!} &= 0, &\qquad (4.53)
\end{aligned}
$$

as well as expanding their derivatives with respect to η to obtain the values

$$
\begin{aligned}
U_2 = \frac{U'''(0)}{3!} &= -\frac{V_0}{3}, &\qquad (4.54)\\
V_2 = \frac{V'''(0)}{3!} &= \frac{U_0}{3}, &\qquad (4.55)
\end{aligned}
$$

which help us to eliminate the Coriolis terms in V_0, U_0 in (4.50), (4.51), respectively. This leads us to the equation, similar to that presented in Hall [16],

$$\begin{aligned}
&\mathrm{i}\Big(\alpha_0\frac{\mathrm{d}^2u_1^L}{\mathrm{d}\xi^2}+\frac{\beta_0}{x\sin\psi}\frac{\mathrm{d}^2v_1^L}{\mathrm{d}\xi^2}\Big)+\gamma_0^2p_1^L+2\mathrm{i}\alpha_0v_{-1}^L-\frac{2\mathrm{i}\beta_0}{x\sin\psi}u_{-1}^L\\
&=-\xi^2\Big(\alpha_0xU_1+\frac{\beta_0V_1}{\sin\psi}\Big)\Big(\alpha_0u_1^L+\frac{\beta_0v_1^L}{x\sin\psi}\Big)+2\mathrm{i}\xi\Big(\alpha_0xU_1+\frac{\beta_0V_1}{\sin\psi}\Big)w_1^L\\
&\quad-\frac{2x\gamma_0C\xi^2}{(\frac{\beta_0}{\sin\psi}-\alpha_0xT_s)^2}\Big(\alpha_1xU_0+\frac{\beta_1V_0}{\sin\psi}\Big)\Big(\alpha_0U_1+\frac{\beta_0V_1}{x\sin\psi}\Big).
\end{aligned}\tag{4.56}$$

It is important to note that the Coriolis effects which survive are manifested by the terms in u_{-1}^L, v_{-1}^L, and at this order, this effect plays the most significant role in balancing the effects of viscosity. This implies that the structure of the neutral curve for stationary small-wavenumber disturbances involves a dominant balance of viscous and Coriolis terms. We can eliminate u_1^L and v_1^L from this system, by the operation $\frac{\mathrm{d}^2}{\mathrm{d}\xi^2}$ (4.48)+(4.56), which, upon simplification and using (4.39), (4.41) and (4.48) leads us to the governing equation for w_1^L, similar to that in Hall [16], given by

$$\begin{aligned}
&\frac{\mathrm{d}^3w_1^L}{\mathrm{d}\xi^3}-\mathrm{i}\alpha_0xU_1\xi^2\frac{\mathrm{d}w_1^L}{\mathrm{d}\xi}+2\mathrm{i}\xi\alpha_0xU_1w_1^L=\gamma_0^2C\\
&\quad+\Big(\alpha_1xU_0+\frac{\beta_1V_0}{\sin\psi}\Big)\frac{x\gamma_0\xi^2C\alpha_0U_1}{(\frac{\beta_0}{\sin\psi}-\alpha_0xT_s)^2}\\
&\quad+\frac{2\mathrm{i}\gamma_0\beta_0C}{\sin\psi(\frac{\beta_0}{\sin\psi}-\alpha_0xT_s)^2}\Big(1+\frac{V_0^2}{U_0^2}\Big)U_0\frac{U(0,\sqrt{2}s)}{U(0,0)},
\end{aligned}\tag{4.57}$$

where $s=\Delta^{\frac{1}{4}}\xi$.

To solve this equation for w_1^L, we pose the complementary function and particular integral form $w_1^L = w_1^{\text{C.F.}} + w_1^{\text{P.I.}}$, finding that

$$w_1^L = \Delta^{-\frac{3}{4}}\Big(\gamma_0^2 C F_1(s) + \frac{2\mathrm{i}\gamma_0\beta_0 C}{\sin\psi(\frac{\beta_0}{\sin\psi} - \alpha_0 x T_s)^2}\Big[1 + \frac{V_0^2}{U_0^2}\Big]\frac{U_0}{U(0,0)}F_2(s)\Big)$$
$$+k_1\xi^2 - \mathrm{i}\Big(\alpha_1 x U_0 + \frac{\beta_1 V_0}{\sin\psi}\Big)\frac{\gamma_0 C}{(\frac{\beta_0}{\sin\psi} - \alpha_0 x T_s)^2}\xi, \tag{4.58}$$

where $k_1 = $ const. and the independent solutions F_1 and F_2, presented in Hall [16], satisfy

$$F_1^{'''} - s^2 F_1^{'} + 2sF_1 = 1, \qquad F_1(0) = F_1(\infty) = 0, \tag{4.59}$$

$$F_2^{'''} - s^2 F_2^{'} + 2sF_2 = U(0, \sqrt{2}s), \qquad F_2(0) = F_2(\infty) = 0, \tag{4.60}$$

respectively. Together with this solution, we now return to the continuity equation (4.48) and substitute $\xi = 0$, using the no-slip condition $u_1^L(0) = v_1^L(0) = 0$ to obtain the eigenrelation

$$\gamma_0^2 I_3 + \frac{i\gamma_0\beta_0 U_0}{\sin\psi(\frac{\beta_0}{\sin\psi} - \alpha_0 x T_s)^2}\Big(1 + \frac{V_0^2}{U_0^2}\Big)I_4 = \frac{\mathrm{i}\Delta^{\frac{1}{2}}\gamma_0}{(\frac{\beta_0}{\sin\psi} - \alpha_0 x T_s)^2}\Big(\alpha_1 x U_0 + \frac{\beta_1 V_0}{\sin\psi}\Big), \tag{4.61}$$

where $I_3 = F_1^{'}(0)$ and $I_4 = \frac{2F_2^{'}(0)}{U(0,0)}$, and they can be expressed in terms of definite integrals involving parabolic cylinder functions. This is achieved by making a series of substitutions, which was initially derived by Hall [16] for the rotating disk in still fluid. Following his method, the eventual aim is to transform (4.59) and (4.60) so they maybe solved in terms of parabolic cylinder functions. For F_1, we first let $F_1 = s^2 G$, which leads to

$$s^2 G^{'''} + 6sG^{''} + (6 - s^4)G^{'} = 1. \tag{4.62}$$

Now, suppose we let $H = G^{'}$. Then this equation becomes

$$s^2 H^{''} + 6sH^{'} + (6 - s^4)H = 1. \tag{4.63}$$

Next, we make the change of variable $H = \frac{K}{s^3}$, followed by $u = \sqrt{2}s$, so we obtain an analogous parabolic cylinder equation with inhomogeneous right-hand side, given by

$$K^{''}(u) - \frac{u^2}{4}K(u) = \frac{u}{2\sqrt{2}}. \tag{4.64}$$

To scale out the parabolic cylinder function, we let $K(u) = R(u)U(0,u)$, leading to a first order equation for $R^{'}$, given by

$$R^{''}U + 2R^{'}U^{'} = \frac{u}{2\sqrt{2}}, \tag{4.65}$$

which is solved using the method of integrating factors to obtain

$$R^{'} = \frac{1}{2\sqrt{2}} \frac{\int_{\infty}^{u} u^{'}U(0,u^{'})\mathrm{d}u^{'}}{U(0,u)^2}. \tag{4.66}$$

Now, if we re-express this solution back in terms of F_1, then we obtain

$$uF_1^{'}(u) - 2F_1(u) = R(u)U(0,u). \tag{4.67}$$

Setting $u = 0$ and using $F_1|_{u=0} = 0$ gives $R(0) = 0$, as $U(0,0) \neq 0$. We subsequently differentiate (4.67) and substitute $u = 0$, noting the change of variable back to s from u, to obtain

$$I_3 = F_1^{'}|_{s=0} = \frac{\int_0^{\infty} \theta U(0,\theta)\mathrm{d}\theta}{2U(0,0)} = 0.5984. \tag{4.68}$$

Carrying out a similar series of substitutions for F_2, taking into account of the difference in the right-hand side, leads us to the corresponding result for I_4, given by

$$I_4 = \frac{2F_2^{'}|_{s=0}}{U(0,0)} = \frac{\int_0^{\infty} \theta U(0,\theta)^2\mathrm{d}\theta}{U(0,0)^2} = 0.4570. \tag{4.69}$$

The values of I_3, I_4 are estimated using a Simpson's rule method with fixed steps of 0.1 from $\theta = 0.0$ to 5.0, noting that $U(0,\theta)$ decays exponentially. We can now solve (4.61) making use of (4.31) to obtain the leading order wavenumber and waveangle estimates, similar to those outlined in Hall [16] for the rotating disk, and given by

$$\gamma_0 = \frac{\beta_0 U_0}{\sin\psi(\frac{\beta_0}{\sin\psi} - \alpha_0 x T_s)^2}\Big(1 + \frac{V_0^2}{U_0^2}\Big)\frac{I_4}{I_3} = \frac{\Big(1+\frac{V_0^2}{U_0^2}\Big)^{\frac{3}{4}}}{\Big|1+\frac{V_0 T_s}{U_0}\Big|}\Big(\frac{U_0 I_4}{I_3}\Big)^{\frac{1}{2}} x^{-\frac{1}{2}} \quad = \quad 1.225x^{-\frac{1}{2}}, \tag{4.70}$$

$$\sin\psi\Big(\frac{\alpha_1}{\beta_0} - \frac{\beta_1\alpha_0}{\beta_0^2}\Big) = \frac{2\gamma_0^{\frac{3}{2}}\Big(1+\frac{V_0^2}{U_0^2}\Big)^{-\frac{1}{4}}\Big(1+\frac{V_0T_s}{U_0}\Big)^2 I_3}{|U_0V_0(1+mT_s^2)|^{\frac{1}{2}}x^{\frac{1}{2}}} \quad = \quad 2.312x^{-\frac{5}{4}}, \tag{4.71}$$

where we have given the numerical calculations for a cone rotating in still fluid ($U_0 = 0.5102, V_0 = -0.6159, T_s = 0$). It is important to note here that it is not possible to find α_1 and β_1 independently. Nor do we have to obtain $u_0(\xi)$ or $v_0(\xi)$ explicitly, as, for the purposes of our analysis, they would not produce any additional useful information. Instead we turn our attention to the combination of α_1 and β_1, in terms of the waveangle ϕ between the streamwise vector and the normal to the spiral vortices. We have

$$\begin{aligned} \tan\Big(\frac{\pi}{2} - \phi\Big) = \frac{\alpha x}{\beta} &= \frac{(\alpha_0 + \epsilon^2\alpha_1 + \ldots)x}{(\beta_0 + \epsilon^2\beta_1 + \ldots)}, \\ &= \frac{\alpha_0 x}{\beta_0} + \epsilon^2\Big(\frac{\alpha_1}{\beta_0} - \frac{\beta_1\alpha_0}{\beta_0^2}\Big)x, \\ &= \frac{1.207}{\sin\psi} + \frac{2.312\epsilon^2 x^{-\frac{1}{4}}}{\sin\psi}. \end{aligned} \tag{4.72}$$

We note that the total wavenumber, scaled appropriately on the viscous mode wavelength, is given by

$$\epsilon^4\gamma = 1.225\epsilon^4 x^{-\frac{1}{2}} + \ldots. \tag{4.73}$$

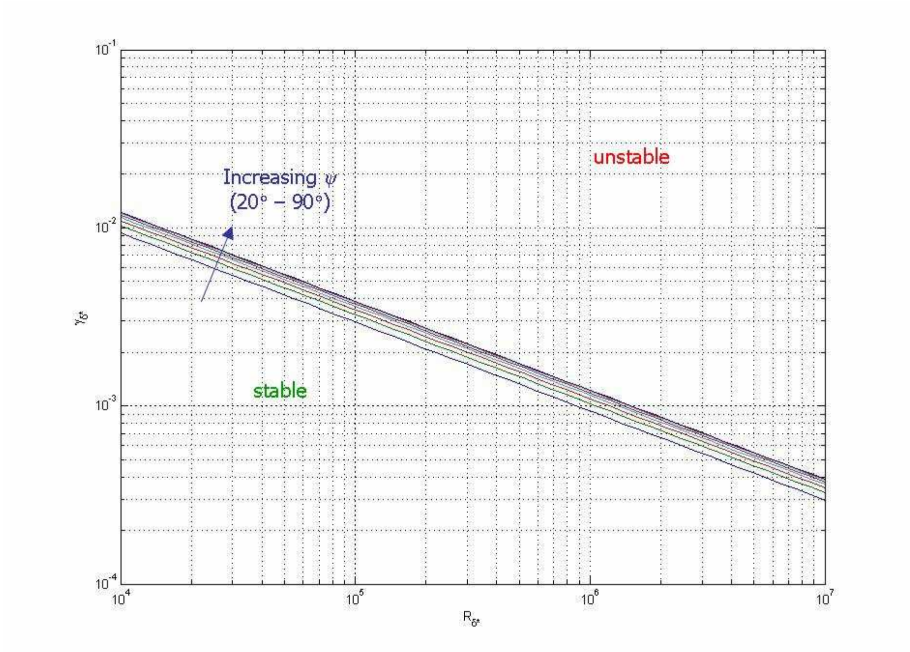

Figure 4.2: Plot of asymptotic neutral wavenumber predictions γ_{δ^*} against R_{δ^*} for viscous modes for $T_s = 0$, $\psi = 20^\circ - 90^\circ$. Increasing ψ stabilizes the flow.

As in §3 for the inviscid modes, we follow Hall [16] and define the Reynolds number based on boundary layer thickness δ^*, given by

$$\mathrm{R}_{\delta^*} = \mathrm{R}^{\frac{1}{2}} x (\sin\psi)^{\frac{1}{2}}, \tag{4.74}$$

where, in this useful notation, the local wavenumber on the lower branch is given by

$$\gamma_{\delta^*} = 1.225 \mathrm{R}_{\delta^*}^{-\frac{1}{2}} (\sin\psi)^{\frac{1}{4}} + \ldots, \tag{4.75}$$

and the local viscous mode waveangle expands as

$$\tan\left(\frac{\pi}{2} - \phi\right) = \frac{1.207}{\sin\psi} + 2.312 \mathrm{R}_{\delta^*}^{-\frac{1}{4}} (\sin\psi)^{-\frac{7}{8}} + \ldots. \tag{4.76}$$

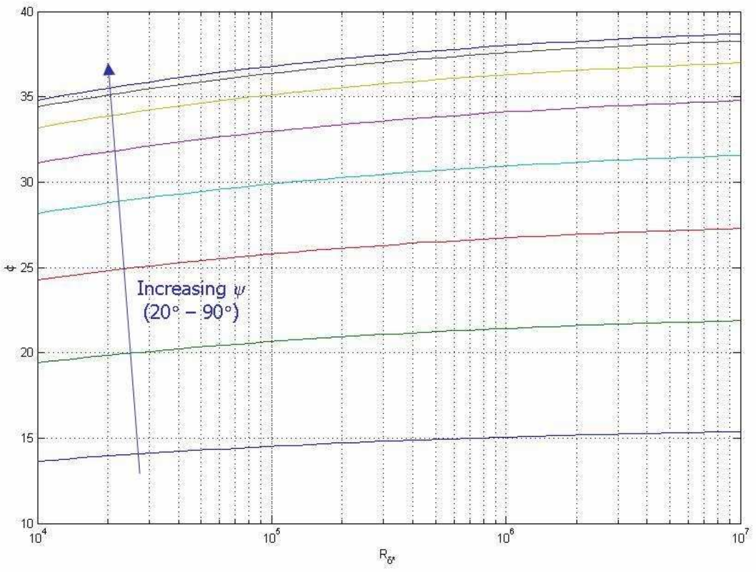

Figure 4.3: Plot of asymptotic neutral waveangle predictions ϕ against R_{δ^*} for viscous modes for $T_s = 0$, $\psi = 20^\circ - 90^\circ$. Increasing ψ gives a larger vortex waveangle.

As in the previous section, we notice that these expressions in terms of the displacement-thickness Reynolds number are independent of the streamwise location, x. Figures 4.2 and 4.3 show the lower branches of the asymptotic neutral wavenumber and waveangle predictions, where we have again used log-log and semi-log scales for the wavenumber and waveangle plots, respectively. In a similar fashion to the inviscid branch, we see that increasing the cone half-angle has the effect of stabilizing the flow by reducing the available wavenumbers which are susceptible to the crossflow instability. Furthermore, in the case of the waveangle, increasing the cone half-angle towards that of a rotating disk still has the effect of increasing the waveangle.

Physically, this seems acceptable, as we should expect the deviation angle of the spiral vortices from the streamwise vector to increase as the cone half-angle is increased, say from 20°. This is because, there is an increased 'rotational shear' force on each vortex spiral, and so they are deviated more from the streamwise direction. Interpreting the results in terms of energy transfer, in the case of the rotating disk ($\psi = 90°$) the vortices do not carry as much kinetic energy in the radial direction. When added to their kinetic energy in the azimuthal direction, due to the purely rotational effect of the disk, the resulting deviation waveangle is relatively large. However, in the case of a rotating cone (e.g. of a moderate to slender half-angle), the streamline curvature effect of the cone surface causes the spiral vortices to carry more energy in the streamwise direction, which aligns the effective velocity propagation direction more with the streamwise vector, resulting in a reduction in the observed waveangle. However, this is not the case for the wavenumber, as for varying cone half-angles, the effective vorticity shed from the cone boundary layer does not change a great deal, which means the number of vortices that are observed to roll-up and wrap around the cone surface or spiral around the disk are roughly the same. For large Reynolds numbers, these wavenumbers are observed to asymptote to the same values as for the rotating disk case.

4.2.2 Case B: Rotating disk in axial flow

We now turn our attention to the problem of a rotating disk in axial flow (case B), proceeding to estimate the local wavenumber and waveangle for the type II lower branch disturbance modes, setting $\psi = 90°$, $m = 1$ and varying $T_s = 0.00 - 0.25$, say. We follow the previous first order analysis. In this case, the value of the integrals I_3 and I_4 remain as in (4.68) and (4.69). Combining the measurements from table 3.1 and substituting into the viscous eigenrelation (4.61), we obtain the corresponding viscous mode type II wavenumber and waveangle estimates for a disk rotating in axial flow, which are shown in figures 4.4 and 4.5. We see that the introduction of axial flow results in shifting the wavenumber curves vertically upwards, effectively stabilizing the flow. However, for the

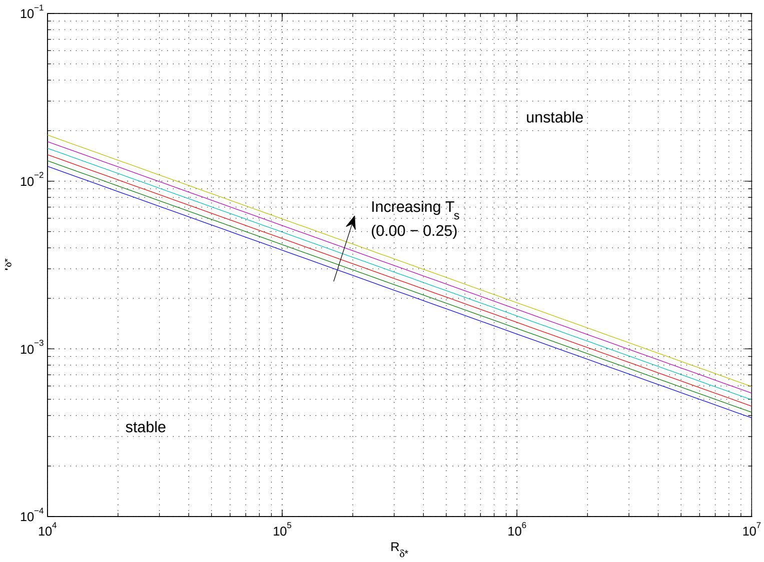

Figure 4.4: Plot of asymptotic neutral wavenumber predictions γ_{δ^*} against R_{δ^*} for lower-branch modes for $T_s = 0.00 - 0.25$, $\psi = 90°$. Increasing T_s shifts the curves vertically upwards.

waveangle, the type II branches are shifted down and subsequently back upwards, but overall remaining close together within the region of around 39°.

4.3 Discussion of type I/type II neutral curves (cases A and B)

Figures 4.6 and 4.7 show the combined inviscid and lower branches for the wavenumber and waveangle, plotted against displacement thickness Reynolds number for still fluid ($T_s = 0$). The curves show the asymptotic results for $\psi = 20° - 90°$ in $10°$ increments. From the wall mode results, together with those for the inviscid modes in §3, we see that as we change ψ, we observe a greater variation in the asymptotic curves for the waveangle ϕ, than we do for the corresponding wavenumber γ_{δ^*}. The rightmost wavenumber curves

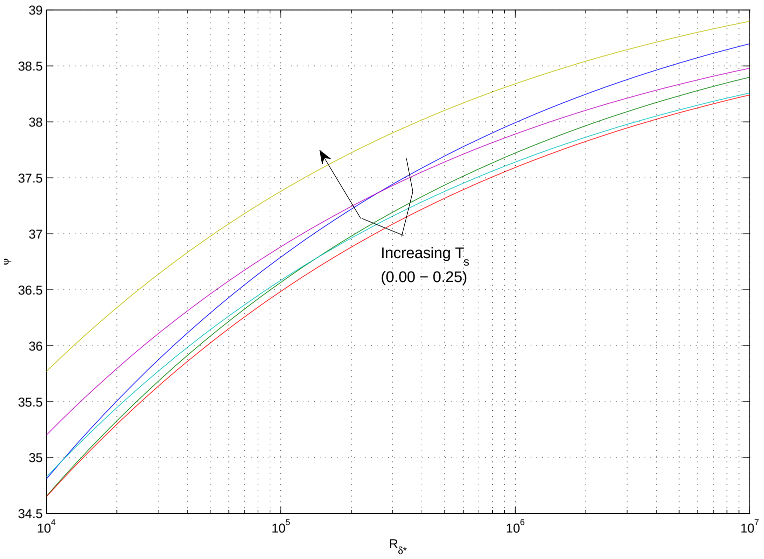

Figure 4.5: Plot of asymptotic neutral waveangle predictions ϕ against $\mathrm{R}_{\delta*}$ for lower-branch modes for $T_s = 0.00 - 0.25$, $\psi = 90°$. Increasing T_s shifts the branch as shown.

and uppermost waveangle curves correspond to $\psi = 90°$ and agree with the measurements of Hall [16], as well as with the numerical results of Malik [33] for a rotating disk. The interested reader is referred to the study of Garrett *et al.* [8], where we develop comparisons between the wavenumber and waveangle neutral curves at large Reynolds for a family of rotating cones in still fluid.

In case B the value of the integrals I_3 and I_4 remain as in (4.68) and (4.69). Combining the measurements from table 3.1 and substituting into the inviscid and viscous eigenrelations (3.50) and (4.61), we obtain the combined asymptotic local wavenumber and waveangle estimates for large Reynolds numbers, which are shown in figures 4.8 and 4.9.

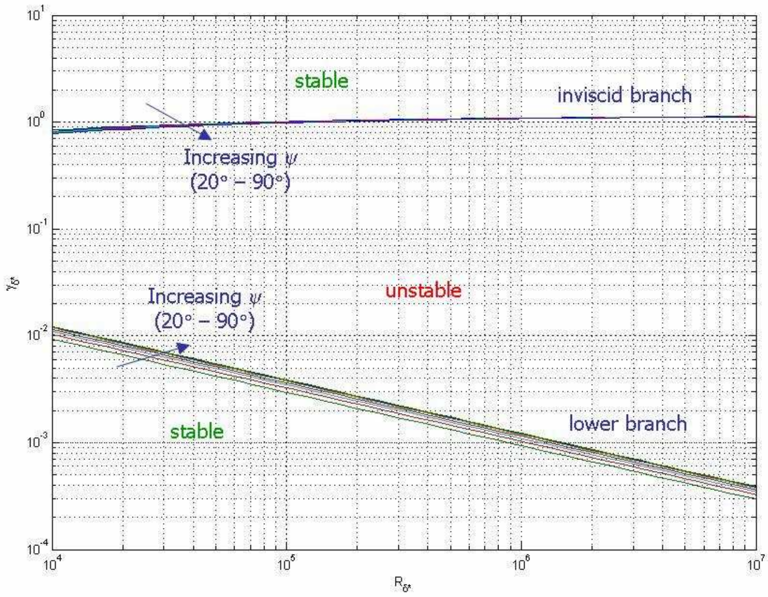

Figure 4.6: Plot of asymptotic neutral wavenumber predictions γ_{δ^*} against R_{δ^*} for inviscid and lower-branch modes for $T_s = 0$, $\psi = 20^\circ - 90^\circ$. Increasing ψ shifts the curves to the right.

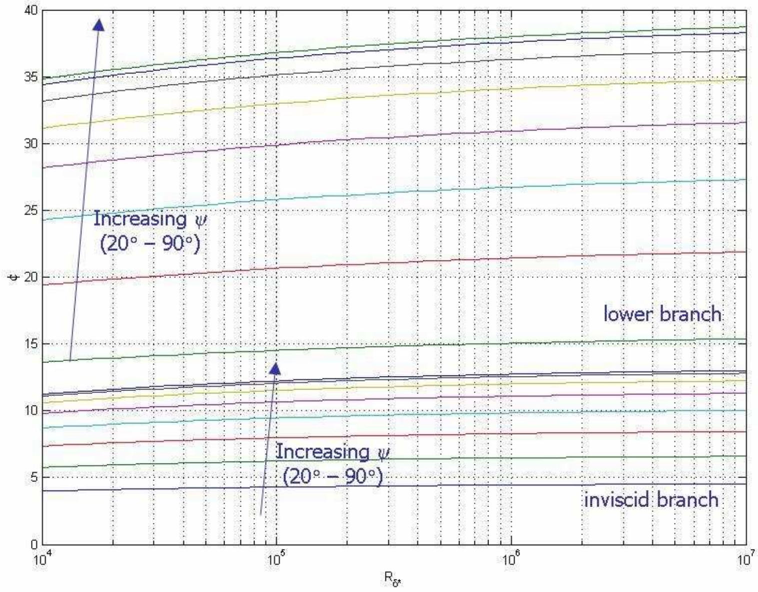

Figure 4.7: Plot of asymptotic neutral waveangle predictions ϕ against R_{δ^*} for inviscid and lower-branch modes for $T_s = 0$, $\psi = 20^\circ - 90^\circ$. Increasing ψ gives a larger vortex waveangle.

In the case of the inviscid type I mode local wavenumber, we notice that the introduction of axial flow shifts the curves further vertically upwards. The shift is approximately by an equal amount for all the curves using the log-log scales shown. This leads us to conclude that switching on an axial flow has the qualitative effect of altering the spiral vortex wavenumbers in an exponential manner. In the inviscid case, the overall effect is to increase the quantity of wavenumbers for which the onset of an unstable mode is observed. This is the opposite for the type II modes. Therefore, we conclude increasing T_s to a non-zero positive value destabilizes the type I modes and stabilizes the type II modes for flow over a rotating disk. In the case of the waveangle branches, the inviscid type I curve exhibits uniformly increasing waveangles with the introduction of axial flow. The oncoming streamwise forced flow is deflected by the disk surface and contributes to increasing the azimuthal shear effect on the flow. Therefore, when the boundary layer eventually separates the spiral vortices are shed at larger waveangles. However, for type II viscous modes, the dominant effect on the waveangle estimates come from the ratio of streamwise and azimuthal velocity gradients at the wall, U_0 and V_0. This is because the viscous stability analysis is related to the wall shear. The leading order waveangle initially decreases as T_s increases, but eventually the ratio of azimuthal to streamwise wall shear decreases back close to its initial value, causing the waveangle curve to increase back up towards the neutral curve for a disk in still fluid. In conclusion, generating an axial flow onto the disk causes a wider variation in the inviscid upper branch waveangles (increasing from 13° to 21°) than for the type II viscous mode waveangles, which remain close to the asymptotic values of around $35^\circ - 39^\circ$ for large Reynolds numbers.

At this stage, it is important to note that both the inviscid type I and viscous type II expansion procedures both provide the capacity to take non-parallel effects into account. As Hall [16] mentioned for the rotating disk, the asymptotic expansion found for the inviscid type I modes includes viscous effects, but while the effects of non-parallel terms

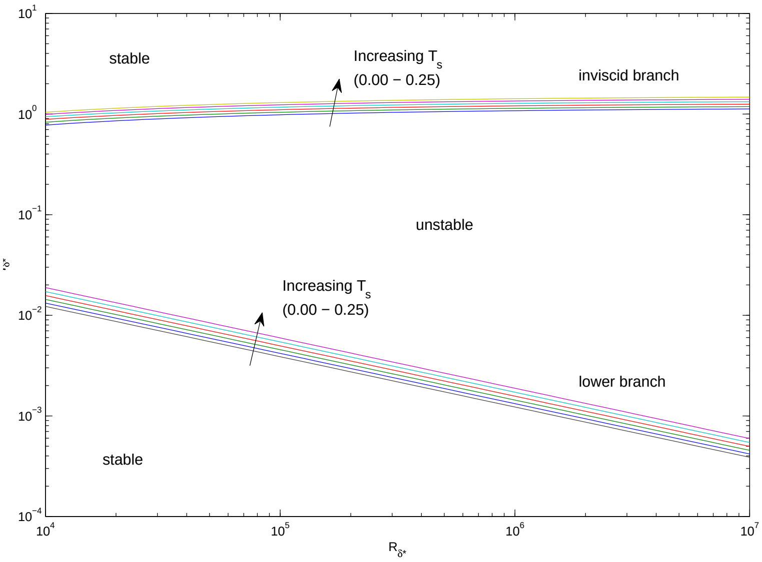

Figure 4.8: Plot of asymptotic neutral wavenumber predictions γ_{δ^*} against R_{δ^*} for inviscid and lower-branch modes for $T_s = 0.00 - 0.25$, $\psi = 90°$. Increasing T_s shifts the curves vertically upwards.

have not been ignored, they do not appear in the leading order and next order correction terms. However, if we continue the asymptotic expansion procedure outlined in §§3.1 and 3.2 in a self-consistent manner, then terms containing non-parallel flow effects will appear. Similarly, for the viscous type II modes found in SS4.1 and 4.2, Hall [16] mentions for the rotating disk that the triple-deck theory applied would yield additional terms at further orders to enable non-parallel effects to be taken into account. Indeed Smith [42] uses a triple-deck structure for the Blasius boundary layer to account for non-parallel effects.

We now proceed to investigate the Type II viscous stability modes for the situation of a cone rotating within an axial flow (case C). As mentioned in §2, we follow the basic flow transformation where $U \rightarrow U/x$ and $V \rightarrow V/x$ in the perturbation equations. We again

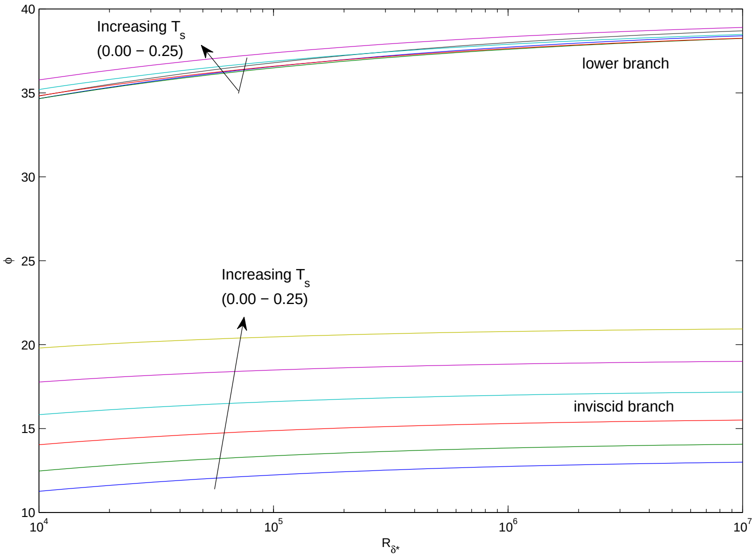

Figure 4.9: Plot of asymptotic neutral waveangle predictions ϕ against R_{δ^*} for inviscid and lower-branch modes for $T_s = 0.00 - 0.25$, $\psi = 90°$. Increasing T_s shifts the inviscid/viscous branches as shown.

follow the viscous stability analysis of Hall [16], with modifications in terms involving the basic flow, in order to take account of the change in coordinate setup for case C. The effective wall shear now becomes $\alpha U' \sin\psi + \beta V'/x$, whereas the perturbation quantities, streamwise and azimuthal wavenumbers remain as in (4.1)−(4.3).

4.4 Leading order triple-deck solution (case C)

In the upper deck, we begin with the boundary conditions at the edge of the boundary layer, $f' \to 1$ and $g \to -1$, which lead to the previous conditions $U = T_s$ and $V = -1$, where here $U = U(x, \eta)$ and $V = V(x, \eta)$ are the modified basic flow velocities for case C. Here $'$ denotes differentiation with respect to η. We follow the analysis as in §4.1, which results in very similar leading order equations. The solutions in the upper deck are

$$
\begin{aligned}
u_0^U &= \frac{\alpha_0 C}{(\frac{\beta_0}{x\sin\psi} - \alpha_0 T_s)} e^{-\gamma_0 Z}, && (4.77)\\
v_0^U &= \frac{\beta_0 C}{x\sin\psi(\frac{\beta_0}{x\sin\psi} - \alpha_0 T_s)} e^{-\gamma_0 Z}, && (4.78)\\
w_0^U &= \frac{\mathrm{i}\gamma_0 C}{(\frac{\beta_0}{x\sin\psi} - \alpha_0 T_s)} e^{-\gamma_0 Z}, && (4.79)\\
p_0^U &= Ce^{-\gamma_0 Z}, && (4.80)
\end{aligned}
$$

where again $C = \text{const}$.

Upon expanding the perturbation equations in the main deck and matching with these upper deck solutions, we obtain the leading order disturbance field in the main deck, given by

$$
\begin{aligned}
u_0^M &= \frac{C\gamma_0 U'}{(\frac{\beta_0}{x\sin\psi} - \alpha_0 T_s)^2}, && (4.81)\\
v_0^M &= \frac{C\gamma_0 V'}{(\frac{\beta_0}{x\sin\psi} - \alpha_0 T_s)^2}, && (4.82)\\
w_0^M &= -\frac{\mathrm{i}C\gamma_0}{(\frac{\beta_0}{x\sin\psi} - \alpha_0 T_s)^2}\Big(\alpha_0 U + \frac{\beta_0 V}{x\sin\psi}\Big). && (4.83)
\end{aligned}
$$

More importantly, the resulting zero effective wall shear condition (4.31) remains the same, allowing us to justify the consideration of stationary disturbances, which remain fixed on the cone surface as it rotates. The analysis in the lower deck follows a similar pattern to that for cases A and B. Here, we will not include all the details, but the resulting leading order term in the lower deck, which is not fixed by matching with the main deck solutions, is given by

$$
u_{-1}^L(\xi) = -\frac{U_0\gamma_0 C}{(\frac{\beta_0}{x\sin\psi} - \alpha_0 T_s)^2}\frac{\widehat{U}(0,\sqrt{2}\Delta^{\frac{1}{4}}\xi)}{\widehat{U}(0,0)}, \tag{4.84}
$$

where

$$\Delta = \mathrm{i}\Big(\alpha_0 U_1 + \frac{\beta_0}{x \sin\psi} V_1\Big), \tag{4.85}$$

and, as previously, $\widehat{U}(0, \sqrt{2}\Delta^{\frac{1}{4}}\xi)$ is the parabolic cylinder function (with alternative notation introduced to distinguish it from the streamwise basic flow velocity).

4.5 First order lower-deck solution (case C)

We proceed to find the next order approximation to the disturbance equations. At $O(\epsilon^{-1})$ in the streamwise and azimuthal disturbance equations, there is a balance between the type II viscous terms and Coriolis terms, which is obtained in the resulting equations analogous to (4.50) and (4.51) by using the relations (4.54) and (4.55) depending on the basic flow. Due to the new coordinate setup for case C, using the basic flow equations (2.33) and (2.34), these expressions are now given as

$$\begin{aligned} U_2 &= \frac{U'''(x,0)}{3!} = \frac{1}{6}\Big(\frac{m+3}{2s^{\frac{1}{2}}}\Big)^{\frac{3}{2}} \frac{xf''''(s,0)}{s^{\frac{1}{2}}}, && (4.86)\\ V_2 &= \frac{V'''(x,0)}{3!} = \frac{1}{6}\Big(\frac{m+3}{2s^{\frac{1}{2}}}\Big)^{\frac{3}{2}} xg'''(s,0). && (4.87) \end{aligned}$$

The leading order terms in the basic flow expansions are

$$\begin{aligned} U_0 &= \Big(\frac{m+3}{2s^{\frac{1}{2}}}\Big)^{\frac{1}{2}} \frac{xf''(s,0)}{s^{\frac{1}{2}}}, && (4.88)\\ V_0 &= \Big(\frac{m+3}{2s^{\frac{1}{2}}}\Big)^{\frac{1}{2}} xg'(s,0). && (4.89) \end{aligned}$$

Importantly, the process still leads to the same relations as (4.54) and (4.55), namely

$$\begin{aligned} U_2 &= -\frac{V_0}{3}, & (4.90)\\ V_2 &= \frac{U_0}{3}, & (4.91) \end{aligned}$$

which means the underlying Coriolis-viscous force balance holds for the type II rotating cone modes despite the change of setup and non-dimensionalisation apparent in case C. Following §4.2 with these changes in hand, we arrive at the equation satisfied by the next order surface-normal perturbation, w_1^L, given by

$$\begin{aligned} \frac{\mathrm{d}^3 w_1^L}{\mathrm{d}\xi^3} - \mathrm{i}\alpha_0 U_1 \xi^2 \frac{\mathrm{d}w_1^L}{\mathrm{d}\xi} + 2\mathrm{i}\xi\alpha_0 U_1 w_1^L &= \gamma_0^2 C \\ +\Big(\alpha_1 U_0 + \frac{\beta_1 V_0}{x\sin\psi}\Big)&\frac{\gamma_0 \xi^2 C \alpha_0 U_1}{(\frac{\beta_0}{x\sin\psi} - \alpha_0 T_s)^2} \\ +\frac{2\mathrm{i}\gamma_0\beta_0 C}{x\sin\psi(\frac{\beta_0}{x\sin\psi} - \alpha_0 T_s)^2}\Big(1 + \frac{V_0^2}{U_0^2}\Big)U_0 &\frac{\widehat{U}(0,\sqrt{2}\tau)}{\widehat{U}(0,0)}, \end{aligned} \tag{4.92}$$

where $\tau = \Delta^{\frac{1}{4}}\xi$. Here, the terms from the basic flow expansion are given by

$$\begin{aligned} U_1 &= \frac{U''(x,0)}{2!} = \Big(\frac{m+3}{4s}\Big)x f'''(s,0), & (4.93)\\ V_1 &= \frac{V''(x,0)}{2!} = \Big(\frac{m+3}{4s^{\frac{1}{2}}}\Big)x g''(s,0). & (4.94) \end{aligned}$$

Eventually, this results in a corresponding eigenrelation for the case C type II modes

$$\gamma_0^2 I_3 + \frac{\mathrm{i}\gamma_0\beta_0 U_0}{x\sin\psi(\frac{\beta_0}{x\sin\psi} - \alpha_0 s^{-\frac{1}{2}})^2}\Big(1 + \frac{V_0^2}{U_0^2}\Big)I_4 = \frac{\mathrm{i}\Delta^{\frac{1}{2}}\gamma_0}{(\frac{\beta_0}{x\sin\psi} - \alpha_0 s^{-\frac{1}{2}})^2}\Big(\alpha_1 U_0 + \frac{\beta_1 V_0}{x\sin\psi}\Big), \tag{4.95}$$

where, upon using (4.93) and (4.94), we now have

$$\Delta = -\mathrm{i}\frac{\alpha_0 x(m+3)|f'''(s,0)|}{4s}. \tag{4.96}$$

We are able to estimate the integrals $I_3 = 0.5984$ and $I_4 = 0.4570$ using the same series of transformations on the governing equations we obtain for the functions F_1 and F_2. Upon solving the eigenrelation (4.95) by equating real and imaginary parts, we arrive at the leading order wavenumber estimate for case C type II modes

$$\begin{aligned} \gamma_0 &= \frac{\beta_0 U_0}{x \sin\psi(\frac{\beta_0}{x\sin\psi} - \alpha_0 T_s)^2}\Big(1 + \frac{V_0^2}{U_0^2}\Big)\frac{I_4}{I_3}, \\ &= \overline{\gamma_0} x^{\frac{1}{2}}, \end{aligned} \tag{4.97}$$

where

$$\overline{\gamma_0}(s) = \frac{\left(1 + \frac{sg'(s,0)^2}{f''(s,0)^2}\right)^{\frac{3}{4}} \left(\left[\frac{m+3}{2s^{\frac{3}{2}}}\right]^{\frac{1}{2}} f''(s,0)\frac{I_4}{I_3}\right)^{\frac{1}{2}}}{\left|1 + \frac{g'(s,0)}{f''(s,0)}\right|}. \tag{4.98}$$

The corresponding wave angle estimate is

$$\begin{aligned} \sin\psi\Big(\frac{\alpha_1}{\beta_0} - \frac{\beta_1\alpha_0}{\beta_0^2}\Big) &= \frac{\sqrt{2}\gamma_0^{\frac{3}{2}}\left(1 + \frac{V_0^2}{U_0^2}\right)^{-\frac{1}{4}}\left(1 + \frac{V_0 T_s}{U_0}\right)^2 I_3}{|U_0 V_0|^{\frac{1}{2}}\left(\frac{(m+3)|f'''(s,0)|}{4s}\right)^{\frac{1}{2}} x^{\frac{3}{2}}}, \\ &= \overline{\phi_0} x^{-\frac{7}{4}}, \end{aligned} \tag{4.99}$$

where

$$\overline{\phi_0}(s) = \frac{4\overline{\gamma_0}^{\frac{3}{2}}\left(1 + \frac{sg'(s,0)^2}{f''(s,0)^2}\right)^{-\frac{1}{4}}\left(1 + \frac{g'(s,0)}{f''(s,0)}\right)^2 I_3}{\left(\frac{m+3}{s}\right)|f''(s,0)g'(s,0)f'''(s,0)|^{\frac{1}{2}}}. \tag{4.100}$$

It is useful to note that the stability parameters $\overline{\gamma_0}$ and $\overline{\phi_0}$ may be calculated from the basic flow profiles alone. However, importantly, the basic flow profiles, and hence both parameters, will depend inherently on s. Also, higher derivative wall estimates of f and g are estimated using a finite difference approach. Now, we may express the wavenumber and waveangle in terms of the Reynolds number based on displacement thickness scaled on a power of x, which is given by

$$\mathrm{R}^{*}_{\delta^*} = \mathrm{R}^{\frac{1}{2}} x^{3} (\sin\psi)^{\frac{1}{2}}. \tag{4.101}$$

Following this transformation, we acquire the subsequent representations for the leading order case C wavenumber and wave angle estimates

$$\begin{aligned}
\epsilon^{4}\gamma x^{-1} &= \gamma_{\delta^*} x^{-1} \\
&= \overline{\gamma_0}(\sin\psi)^{\frac{1}{4}} \mathrm{R}_{\delta^*}^{-\frac{1}{2}} + \ldots, \qquad (4.102)\\
\tan\left(\frac{\pi}{2} - \phi\right) &= \overline{\phi_{00}} + \frac{\overline{\phi_0}}{(\sin\psi)^{\frac{7}{8}}} \mathrm{R}_{\delta^*}^{*-\frac{1}{4}} + \ldots, \qquad (4.103)
\end{aligned}$$

where the first term in (4.103) is $\overline{\phi_{00}}(s) = -\frac{s^{\frac{1}{2}} g'(s,0)}{f''(s,0)\sin\psi}$ and is calculated from the zero wall shear condition analogous to (4.31). We notice this depends on s and the velocity gradients at the wall, which themselves depend inherently on s through the basic flow profiles for case C. In addition, we have re-expressed the wavenumber expansion in terms of the Reynolds number R_{δ^*} given for the inviscid mode analysis in (3.80) in order to compare the upper and lower branch wavenumbers later in figure 4.14 for $\psi = 70^\circ$, as well as in the Appendix for $\psi = 50^\circ$ (see figure 8). However, for the wave angle our results are given in terms of $\mathrm{R}^{*}_{\delta^*}$ for the type II modes, as we do not compare directly with the type I waveangle presented earlier in §3.4.

Furthermore, from expression (4.102), we see that for the type II modes, we must scale the wavenumber on a factor of x^{-1}, in order to obtain the appropriate relationship with the displacement thickness Reynolds number. Some of the important stability parameters for a cone of half-angle 70° are shown in table 4.2, including the velocity wall gradients and the wavenumber/wave angle estimates. From the third column and the denominator

s	$f^{''}(s,0)$	$g^{'}(s,0)$	$\frac{f^{''}(s,0)}{g^{'}(s,0)}$	$f^{'''}(s,0)$	$\overline{\gamma_0}(s)$	$\overline{\phi_{00}}(s)$	$\overline{\phi_0}(s)$
0.1	0.5442	-0.9575	< 1	-0.1997	2.8499	0.5564	0.5379
0.2	0.6156	-0.9796	< 1	-0.3993	3.3345	0.7116	0.5238
0.3	0.6844	-0.9999	< 1	-0.5989	4.1291	0.8002	0.4938
0.4	0.7510	-1.0188	< 1	-0.7986	5.2381	0.8580	0.4545
0.5	0.8157	-1.0364	< 1	-0.9982	6.8193	0.8984	0.4093
0.6	0.8787	-1.0529	< 1	-1.1978	9.2238	0.9282	0.3594
1.0	1.1174	-1.1111	> 1	-1.9961	317.3367	0.9944	0.0643
5.0	2.9984	-1.4343	> 1	-9.9748	3.2509	1.0696	0.6730
10.0	4.8718	-1.6511	> 1	-19.9421	2.5253	1.0717	0.7650

Table 4.2: Stability parameter values for a rotating cone with $\psi = 70°$ in axial flow.

of (4.98), we see there is a special case $s_{crit} = 0.99$ (to 2 d.p.), where the viscous analysis breaks down. This is because, $g'(s,0)/f''(s,0) = -1$ and from equation (4.98), the value of $\overline{\gamma_0}(s)$ becomes undefined. Physically, we interpret this as the value close to $s = 1$ where there is a change in the dominant external component of the flow, with the oncoming free-stream flow being stronger for $s < 1$ and the azimuthal rotating flow dominating for $s > 1$. Koh & Price [27] referred to these distinct regimes as 'slowly rotating' and 'rapidly rotating' cones, respectively.

Despite this critical 'transitional' value of s, we are still able to obtain representations for type II wavenumbers and wave angles at values $s < 1.0$ and $s > 1.0$. Figures 4.10 and 4.11 show the effect of varying s on the corresponding lower branch curves, in the order $s = 0.1 - 0.6$ in increments of 0.1 followed by $s = 1.0, 5.0$ and 10.0. For $s < 1.0$ we see that increasing s has the effect of shifting the curves vertically upwards, in effect stabilizing the flow, and the opposite for $s > 1.0$. This is the same as our case C type I results for $s = 0.1 - 0.6$, where increasing s had a stabilizing effect in general. Physically, this regime for 'slowly' rotating cones corresponds to large values of the axial flow parameter

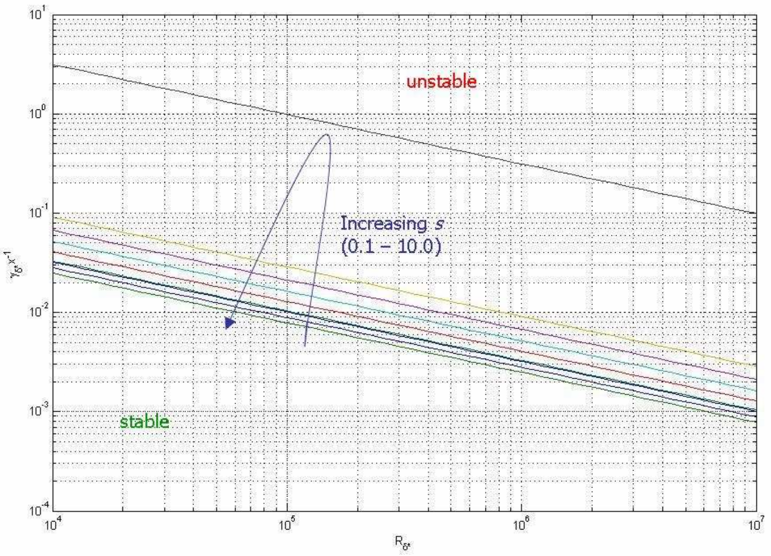

Figure 4.10: Plot of asymptotic neutral wavenumber predictions $\gamma_{\delta*}x^{-1}$ against R$_{\delta*}$ for viscous modes for $\psi = 70°$, $s = 0.1 - 10.0$. Increasing s shifts the curves as shown $(s = 1istheuppermostcurve)$.

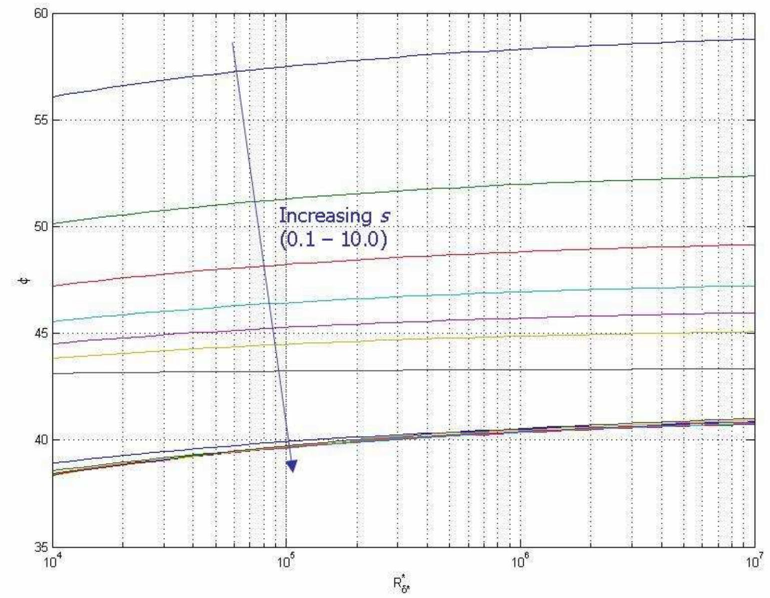

Figure 4.11: Plot of asymptotic neutral waveangle predictions ϕ against R$^*_{\delta*}$ for viscous modes for $\psi = 70°$, $s = 0.1 - 10.0$. Increasing s gives a smaller vortex waveangle.

s	T_s	$f''(s,0)$	$g'(s,0)$	$f'''(s,0)$
16	0.25	6.834	-1.8286	-31.8974
25	0.20	9.4648	-2.0221	-49.8227
44.44	0.15	14.4609	$-2.311\ 1$	-88.5287
100	0.10	26.4014	-2.8035	-199.0174
400	0.05	74.321	-3.9308	-794.4932

Table 4.3: Wall shear velocities and gradients for a rotating cone with $\psi = 70°$ in axial flow with $s > 1$.

$T_s > 1.0$. Therefore, both the type I and II results would suggest that in this region, increasing T_s would have an overall de-stabilizing effect on the flow. Conversely, if we consider the results for $s > 1.0$ we see that increasing s de-stabilizes the flow. It is within this parameter regime which Salzberg & Kezios [39] found that increasing the peripheral speed whilst keeping the mainstream velocity constant resulted in the advancement of the transition location towards the cone apex. Therefore, our results seem to suggest that increasing the axial flow component T_s has a stabilizing effect, as the laminar mass-transfer effect of the mainstream velocity transfers unstable perturbations downstream along the cone surface. From these results, we pose that the introduction of axial flow is most stabilizing when the ratio of the peripheral to axial velocities is close to 1. The flow is essentially a battle between these two velocity scales and when one dominates, either the crossflow instability or the centrifugal instability due to the streamline curvature seems to be most apparent. Physically, we interpret the situation where these two ratios balance as the case where the underlying instabilities cancel each other out most and produce the least amount of unstable wavenumbers. This is clearly seen for the type II modes.

In terms of the wave angle plot, we see that increasing s reduces the deviation angle of the spiral vortices, and so increasing T_s will have the adverse effect. We seek to compare the results for the type II case C wavenumber and wave angle curves for $s-$values, which correspond to the equivalent axial flow parameter values $T_s = 0.05, 0.1, 0.15, 0.2$ and 0.25.

This 'rapidly rotating' parameter range corresponds to the setup already studied in

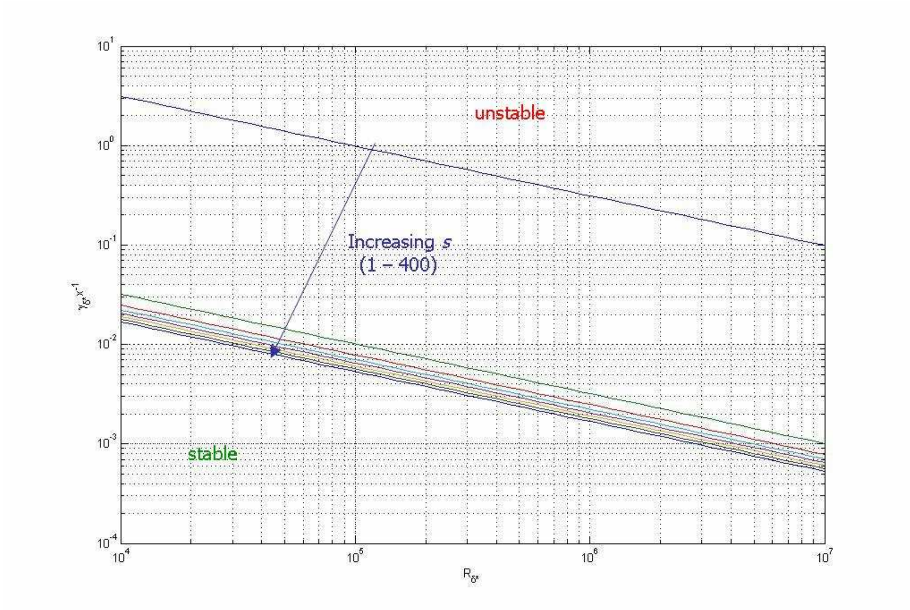

Figure 4.12: Plot of asymptotic neutral wavenumber predictions $\gamma_{\delta*}x^{-1}$ against $\mathrm{R}_{\delta*}$ for viscous modes for $\psi = 70°$, $s = 1.0 - 400.0$. Increasing s shifts the curves vertically downwards.

case B for the rotating disk, and the important stability values are presented in table 4.3.

Figures 4.12 and 4.13 show the lower branch wavenumber and wave angle neutral curve plots for the values $s = 1.0, 5.0, 10.0, 16.0, 25.0, 44.4, 100.0$ and 400.0. The last five values correspond to the T_s values previously studied from $0.05 - 0.25$ in increments of 0.05. From the wavenumber curve, we clearly see that increasing T_s has a stabilizing effect on the spiral vortices. Indeed for large s-values (or small T_s) the wavenumber curves shown for $\psi = 70°$ closely approach the 70° curve shown in figure 4.2 for a cone rotating in still fluid ($T_s = 0$). We notice however that the corresponding agreement for the wave angles is not as accurate, with the case A still fluid results for $\psi = 70°$ predicting a leading order wave angle of around 37.5° (see figure 4.3), whereas the current case C setup for $T_s = 0.05$

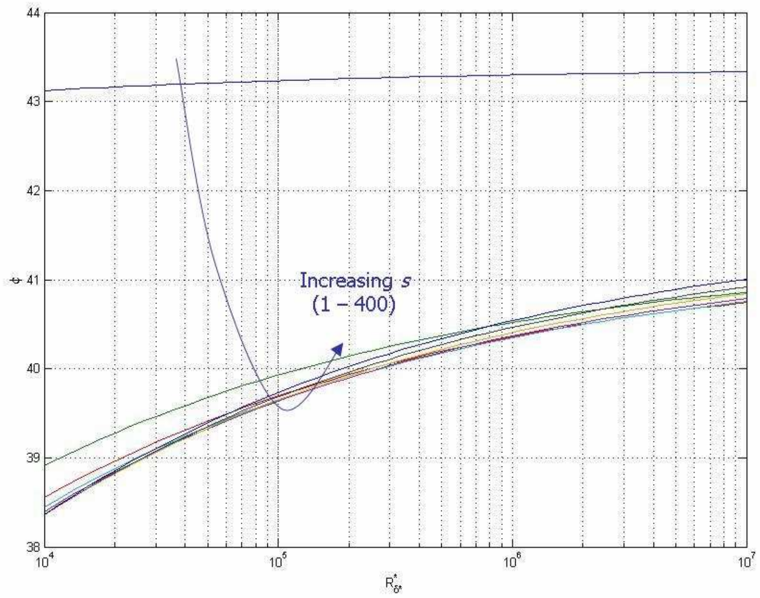

Figure 4.13: Plot of asymptotic neutral waveangle predictions ϕ against $\mathrm{R}^*_{\delta^*}$ for viscous modes for $\psi = 70°$, $s = 1.0 - 400.0$. Increasing s shifts the curves as shown.

predicts $\phi = 41°$. Nevertheless, we see that in the case of an oncoming axial flow, the viscous type II branch of the wave angle is not as stable as the type I branch. This was seen previously in figure 4.9 for axial flow onto a rotating disk (case B). Uniform changes in the axial flow strength did not produce smooth changes in the leading order estimate for ϕ. As was eluded to earlier, the reason for this seems to be that the lower branch stability results depend much more closely on events near the wall. The leading order wave angle estimate turns out to be very sensitive to small changes in the streamwise/azimuthal wall shear ratios.

4.6 Discussion of type I/type II neutral curves (case C)

We now proceed to combine the neutral curve wavenumber estimates for the inviscid upper branch modes found in §3 and the currently obtained viscous lower branch modes.

Figure 4.14 shows both type I and type II modes for a 70° cone in varying axial flow strengths. Due to limitations on the type I analysis, pertaining to the presence of an extra critical layer for larger s-values, we are only able to show wavenumber curves for $s = 0.1 - 0.6$. For the type II wavenumber, we see clearly the change in the stabilizing effect of the introduced axial flow as s moves from $s < 0.99$ to $s > 0.99$. This lends further credence to the suggestion that a change in the dominant external velocity (either rotational or tangential) leads to a physical transition through the most stabilizing flow setup, namely when the ratio of both external velocities is close to unity. We propose that further investigation of the type I modes for $s > 1$ may possibly reveal a similar type of behaviour, where the most stable inviscid mode wavenumber would arise for $s \approx 1$, and either side of this special case would lead to a strong destabilizing effect on the flow. However, this is purely an intuitive prediction, and a rigorous analysis involving the resolution of the extra critical layer would be required to confirm or disprove this suggestion.

We now refer to the Appendix, where we have provided neutral curves for the type I and type II local wavenumbers and waveangles, as well as a combined wavenumber plot, for a cone of half-angle $\psi = 50°$. In general, the results are very similar to those for $\psi = 70°$, with most notably the boundary layer developing an additional critical layer for $s \geqslant 0.7$ associated with the type I modes. Comparisons of the results as ψ increased from 50° to 70° show that the correction term in the type I wavenumber reduces, whereas the leading order estimate for the waveangle increases. This is in agreement with the calculations observed for increasing ψ in our case A results for a cone rotating in still fluid, as shown in figures 3.5 and 3.6. This illustrates that the inviscid mode spiral vortices on a rotating cone follow the same trends for changing cone half-angle when shed in an axial flow as well as in an otherwise stagnant fluid. Furthermore, in terms of the viscous type II modes, we

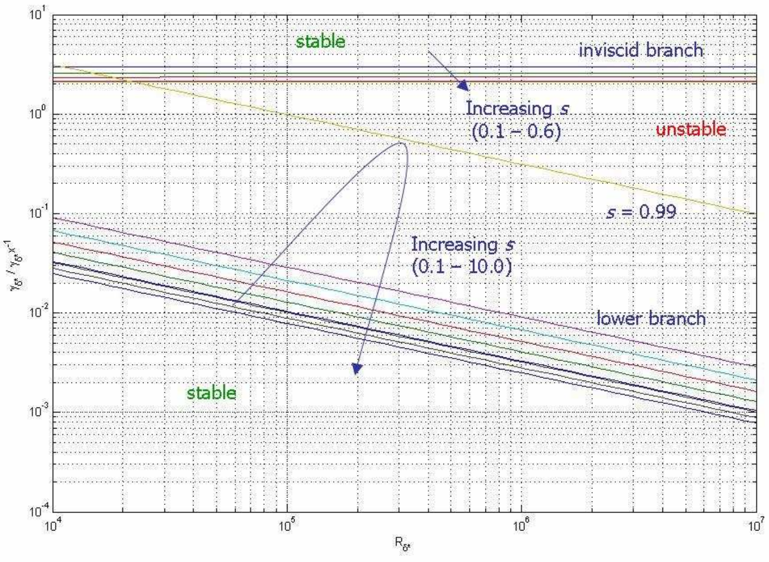

Figure 4.14: Plot of asymptotic neutral wavenumber predictions $\gamma_{\delta^*}, \gamma_{\delta^*} x^{-1}$ against R_{δ^*} for inviscid type I and viscous type II modes for $\psi = 70^\circ$, $s = 0.1 - 0.6$ (type I), $s = 0.1 - 10.0$ (type II). Increasing s shifts the curves as shown.

again find that the results depend closely on events near the wall, with the case $s = 1.0$ producing the most stable flow setup. Detailed observation of the results for a 50° cone when compared with a 70° cone in axial flow reveal similar trends as for the still fluid case, as found in figures 4.2 and 4.3. We notice that both the local wavenumber and waveangle estimates increase as ψ is increased, lending further credence to our claim that for two distinct axial flow strength setups, altering the cone half-angle will result in very similar qualitative effects on the nature of the observed spiral vortices.

As in §4.3, we note that both the inviscid type I and viscous type II expansion procedures again both provide the capacity to take non-parallel effects into account, as mentioned by Hall [16] for the rotating disk. Despite the fact that the case C problem takes into account the effect of an oncoming axial flow, the effect of this physical parameter is captured in the basic flow terms and in the quantities T_s and s, which appear in the governing equations and hence in the leading order and next order corrections. Therefore, following the argument of Hall [16], the type I and type II asymptotic expansions outlined in §§3.3, 3.4 and §§4.4, 4.5 maybe extended in a self-consistent manner in order to take account of non-parallel flow effects. It is important to stress that these non-parallel effects have not been ignored; their effect merely does not appear in the leading order and next order terms of the expansions.

Chapter 5

Problem formulation for the centrifugal instability

We now consider a rotating cone setup where the half-angle ψ is sufficiently small ($\psi < 40^\circ - 50^\circ$) for the dominant mechanism governing the primary instability to arise from centrifugal forces in the mean flow, due to the curvature of the cone surface. In particular, flow visualisation of the instability is distinguished by the existence of two physical cases: the existence circular and spiral waves, where the waveangle satisfies $\phi = 0^\circ$ and $\phi > 0$, respectively. Both circular and spiral waves are observed in still fluid as well as in axial flow (see Kobayashi *et al.* [25] and Kobayashi & Izumi [26]). In the former case, the circular waves are observed in still fluid for $\psi \leqslant 15^\circ$, and in axial flow at $\psi = 15^\circ$ for $s \geqslant 5$. In order to model these circular rings, we use the streamwise, azimuthal and surface-normal coordinate setup (x, θ, z), which we introduced in §2. However, for the parameter regimes $\psi > 15^\circ$ and $s < 5$ at $\psi = 15^\circ$, logarithmic spiral streaks are observed and to model these spirals, we use a coordinate transformation similar to Kobayashi [23]. Here, we introduce $\widehat{x}^*$- and y^*-axes to represent logarithmic spirals that coincide with the direction of propagation of the spiral vortices and the tangent curve to the spiral vortices, whereas the z^*-axis is normal to the cone surface. In this case, we focus on a new origin O' on the cone surface, which has local cone radius $r_0^* = x_0^* \sin\psi$. Importantly, the logarithmic spirals are directed such that the y^*-axis coincides with the direction of rotation of the cone, in order to remain consistent with the position of the origin O'. This requires that the $\widehat{x}^*$-axis spiral propagates outwards and the y^*-axis spiral propagate in towards the origin. The spiral vortices are shed at a waveangle ϕ, and the familiar coordinates (r^*, θ) are transformed to

$$\widehat{x}^* = r_0^*(\cos\phi \ln\Big(\frac{r^*}{r_0^*}\Big) + \theta \sin\psi \sin\phi), \tag{5.1}$$

$$y^* = -r_0^*(\sin\phi \ln\Big(\frac{r^*}{r_0^*}\Big) - \theta \sin\psi \cos\phi), \tag{5.2}$$

which leads to

$$r^* = r_0^* \exp\Big(\frac{1}{r_0^*}(\widehat{x}^* \cos\phi - y^* \sin\phi)\Big), \tag{5.3}$$

$$\theta = \frac{1}{r_0^* \sin\psi}(\widehat{x}^* \sin\phi + y^* \cos\phi). \tag{5.4}$$

We now proceed to investigate the formulation for each problem of a slender rotating cone in still fluid, with circular and spiral waves, as well as a slender rotating cone in axial flow, outlining the differences between the different setups.

5.1 Case A: Slender rotating cone in still fluid (circular waves)

As a preliminary investigation into the slender cone problem, we shall consider the special case where circular waves have been observed experimentally for a rotating cone of half-angle $\psi \leqslant 15°$, where it has been observed experimentally by Kobayashi & Izumi [26] that $\phi = 0°$. In still fluid, these waves are aligned with the azimuthal axis (θ), and as such are periodic in the streamwise direction (x). Hence, a linear stability analysis incorporating curvature effects may be developed from the still fluid disturbance equations (2.46)–(2.49). For completeness, we include the time-dependent term, scaling the time variable t on $1/(\Omega^* \sin\psi)$. Furthermore, we scale the streamwise and normal coordinates on boundary layer thickness, in the form

$$\eta = \mathrm{R}^{\frac{1}{2}} z, \quad \overline{x} = \mathrm{R}^{\frac{1}{2}} x. \tag{5.5}$$

Next we use the fact that the circular waves are periodic in the streamwise direction to introduce periodicity into the perturbation quantities of vortex wavenumber a and azimuthal wavenumber b. Our basic flow quantities remain unchanged, whereas we scale the perturbation velocities on boundary layer thickness, leading to

$$\tilde{\mathbf{u}}^* = \Omega^* l^* \sin\psi[\{xU(\eta), xV(\eta), \mathrm{R}^{-\frac{1}{2}} W\} + \mathrm{R}^{-\frac{1}{2}}\{\tilde{u}(\eta), \tilde{v}(\eta), \tilde{w}(\eta)\}\mathrm{exp}(\mathrm{i}a\overline{x} + \mathrm{i}b\theta)], \tag{5.6}$$

The pressure perturbation term scales as

$$p^* = (\rho^* \Omega^{*2} l^{*2} \sin^2\psi)\mathrm{R}^{-1}\tilde{p}(\eta)\mathrm{exp}(\mathrm{i}a\overline{x} + \mathrm{i}b\theta). \tag{5.7}$$

5.1.1 Linear disturbance equations

As a result, these scalings lead to the following linearised disturbance equations

$$\mathrm{i}a\tilde{u} + \frac{\tilde{u}\mathrm{sin}\psi + \tilde{w}\mathrm{cos}\psi}{\overline{h}} + \frac{\mathrm{i}b}{\overline{h}}\tilde{v} + \frac{\partial \tilde{w}}{\partial \eta} = 0, \tag{5.8}$$

$$\frac{\partial \tilde{u}}{\partial t} + \mathrm{i}a\overline{x}U\tilde{u} + \mathrm{i}\frac{b\overline{x}V}{\overline{h}}\tilde{u} + W\frac{\partial \tilde{u}}{\partial \eta} + U\tilde{u} + \overline{x}\tilde{w}U' - 2\Big(\frac{\overline{x}V\mathrm{sin}\psi}{\overline{h}} + 1\Big)\tilde{v}$$
$$= -\mathrm{i}a\tilde{p} + \Big(\overline{\nabla}^2\tilde{u} - \frac{(\tilde{u}\mathrm{sin}\psi + \tilde{w}\mathrm{cos}\psi)\mathrm{sin}\psi}{\overline{h}^2} - 2\mathrm{i}\frac{b\mathrm{sin}\psi}{\overline{h}^3}v\Big), \tag{5.9}$$

$$\frac{\partial \tilde{v}}{\partial t} + \mathrm{i}a\overline{x}U\tilde{v} + \mathrm{i}\frac{b\overline{x}V}{\overline{h}}\tilde{v} + W\frac{\partial \tilde{v}}{\partial \eta} + V\tilde{u}$$
$$+\overline{x}\tilde{w}V' + \Big(\frac{\overline{x}V\mathrm{sin}\psi}{\overline{h}} + 2\Big)(\tilde{u} + \tilde{w}\mathrm{cot}\psi) + \frac{(\overline{x}U\mathrm{sin}\psi + W\mathrm{cos}\psi)\tilde{v}}{\overline{h}}$$
$$= -\mathrm{i}\frac{b}{\overline{h}}\tilde{p} + \Big(\overline{\nabla}^2\tilde{v} + 2\mathrm{i}\frac{b\mathrm{sin}\psi}{\overline{h}^3}\tilde{u} + 2\mathrm{i}\frac{b\mathrm{cos}\psi}{\overline{h}^3}\tilde{w} - \frac{\tilde{v}}{\overline{h}^2}\Big), \tag{5.10}$$

$$\frac{\partial \tilde{w}}{\partial t} + \mathrm{i}a\overline{x}U\tilde{w} + \mathrm{i}\frac{b\overline{x}V}{\overline{h}}\tilde{w} + W\frac{\partial \tilde{w}}{\partial \eta} + \tilde{w}W' - 2\Big(\frac{\overline{x}V\mathrm{sin}\psi}{\overline{h}} + 1\Big)\tilde{v}\mathrm{cot}\psi$$
$$= -\frac{\partial \tilde{p}}{\partial \eta} + \Big(\overline{\nabla}^2\tilde{w} - \frac{(\tilde{u}\mathrm{sin}\psi + \tilde{w}\mathrm{cos}\psi)\mathrm{cos}\psi}{\overline{h}^2} - 2\mathrm{i}\frac{\mathrm{cos}\psi}{\overline{h}^3}\tilde{v}\Big), \tag{5.11}$$

where $\overline{h} = \mathrm{R}^{\frac{1}{2}}h$ and $\overline{\nabla}^2 = \mathrm{R}^{-1}\nabla^2$ is the non-dimensional re-scaled Laplacian operator, which may be expressed as

$$\overline{\nabla}^2 = \frac{\partial^2}{\partial \eta^2} - (a^2 + b^2) + \mathrm{i}a\frac{\mathrm{sin}\psi}{\overline{h}} + \frac{\mathrm{cos}\psi}{\overline{h}}\frac{\partial}{\partial \eta}. \tag{5.12}$$

We wish to investigate the short-wavelength asymptotic structure of the centrifugal instability and hence identify the spiral vortex wavenumber as $a = \epsilon^{-1}$, where ϵ is a small parameter which forms the basis of our asymptotic analysis. Here, $b = O(1)$. After substituting into (5.8)–(5.11), we differentiate (5.9) with respect to η and use (5.11) to arrive at the following system of equations

$$\mathrm{i}\tilde{u} + \epsilon\Big(\frac{\tilde{u}\sin\psi + \tilde{w}\cos\psi}{\overline{h}}\Big) + \mathrm{i}\frac{b\epsilon\tilde{v}}{\overline{h}} + \epsilon\frac{\partial \tilde{w}}{\partial \eta} = 0, \tag{5.13}$$

$$
\begin{aligned}
\Big(\epsilon^2\frac{\partial^2}{\partial\eta^2}-1\Big)^2\tilde{w} &= 2\epsilon^2\Big(\frac{\overline{x}V\sin\psi}{\overline{h}}+1\Big)\tilde{v}\cot\psi \\
&-\mathrm{i}\epsilon^3\frac{\partial^2\tilde{u}}{\partial t\partial\eta}+\frac{\partial}{\partial\eta}\Big(\epsilon^2\overline{x}U\tilde{u}+\frac{b\epsilon^3\overline{x}V}{\overline{h}}\tilde{u}-\mathrm{i}\epsilon^3W\frac{\partial\tilde{u}}{\partial\eta} \\
&-\mathrm{i}\epsilon^3U\tilde{u}-\mathrm{i}\epsilon^3\tilde{w}\overline{x}U'+2\mathrm{i}\epsilon^3\Big[\frac{\overline{x}V\sin\psi}{\overline{h}}+1\Big]\tilde{v}\Big) \\
&-\Big(\epsilon^2\frac{\partial\tilde{w}}{\partial t}+\mathrm{i}\epsilon\overline{x}U\tilde{w}+\mathrm{i}\frac{b\epsilon^2\overline{x}V}{\overline{h}}\tilde{w}+\epsilon^2W\frac{\partial\tilde{w}}{\partial\eta} \\
&-2\epsilon^2\Big[\frac{\overline{x}V\sin\psi}{\overline{h}}+1\Big]\tilde{v}\cot\psi+\frac{b^2\epsilon^2}{\overline{h}^2}\tilde{w}-\mathrm{i}\frac{\epsilon\sin\psi}{\overline{h}}\tilde{w} \\
&-\frac{\epsilon^2\cos\psi}{\overline{h}}\frac{\partial\tilde{w}}{\partial\eta}+\frac{\epsilon^2(\tilde{u}\sin\psi+\tilde{w}\cos\psi)}{\overline{h}^2}\cos\psi+2\mathrm{i}\frac{b\epsilon^2\cos\psi}{\overline{h}^3}\tilde{v}\Big) \\
&+\epsilon^2\frac{\partial}{\partial\eta}\Big(\frac{\tilde{u}\sin\psi+\mathrm{i}b\tilde{v}+\tilde{w}\cos\psi}{\overline{h}}\Big) \\
&-\epsilon^4\frac{\partial^3}{\partial\eta^3}\Big(\frac{\tilde{u}\sin\psi+\mathrm{i}b\tilde{v}+\tilde{w}\cos\psi}{\overline{h}}\Big) \\
&-\mathrm{i}\Big(\frac{\epsilon^3b^2}{\overline{h}^2}\frac{\partial\tilde{u}}{\partial\eta}-\mathrm{i}\frac{\epsilon^2\sin\psi}{\overline{h}}\frac{\partial\tilde{u}}{\partial\eta} \\
&-\frac{\epsilon^3\cos\psi}{\overline{h}}\frac{\partial^2\tilde{u}}{\partial\eta^2}+\frac{\epsilon^3}{\overline{h}^2}\Big[\frac{\partial\tilde{u}}{\partial\eta}\sin\psi+\frac{\partial\tilde{w}}{\partial\eta}\cos\psi\Big]\sin\psi\Big),
\end{aligned}
\tag{5.14}
$$

$$
\begin{aligned}
\Big(\epsilon^2\frac{\partial^2}{\partial\eta^2}-1\Big)\tilde{v} &= \epsilon^2\overline{x}\tilde{w}V'+\epsilon^2\frac{\partial\tilde{v}}{\partial t} \\
&+\mathrm{i}\epsilon\overline{x}U\tilde{v}+\mathrm{i}\frac{b\epsilon^2\overline{x}V}{\overline{h}}\tilde{v}+\epsilon^2W\frac{\partial\tilde{v}}{\partial\eta}+\epsilon^2V\tilde{u} \\
&+\frac{\epsilon^2}{\sin\psi}\Big(\frac{\overline{x}V\sin\psi}{\overline{h}}+2\Big)(\tilde{u}\sin\psi+\tilde{w}\cos\psi)+\epsilon^2\Big(\frac{\overline{x}U\sin\psi+W\cos\psi}{\overline{h}}\Big)\tilde{v} \\
&+\mathrm{i}\frac{b\epsilon^2}{\overline{h}}\tilde{p}+\frac{(b^2+1)\epsilon^2}{\overline{h}^2}\tilde{v}-\mathrm{i}\frac{\epsilon\sin\psi}{\overline{h}}\tilde{v}-\frac{\epsilon^2\cos\psi}{\overline{h}}\frac{\partial\tilde{v}}{\partial\eta} \\
&-2\mathrm{i}\frac{b\epsilon^2\sin\psi}{\overline{h}^3}\tilde{u}-2\mathrm{i}\frac{b\epsilon^2\cos\psi}{\overline{h}^3}\tilde{w},
\end{aligned}
\tag{5.15}
$$

subject to the boundary conditions

$$
\tilde{u}=\tilde{v}=\tilde{w}=0, \quad \text{on} \quad \eta=0,\infty. \tag{5.16}
$$

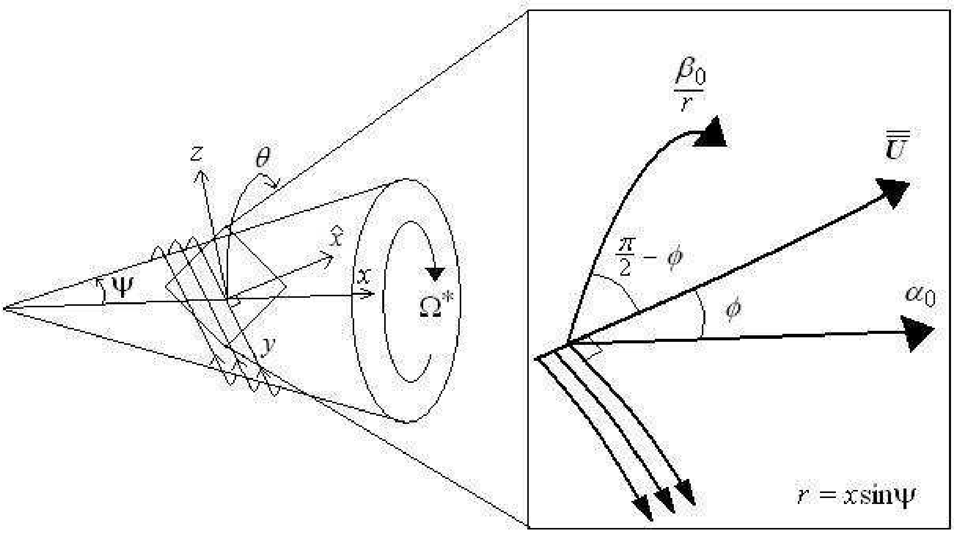

Figure 5.1: Schematic diagram of spiral vortex instability of a rotating cone (left) and the detailed physical interpretation (right) showing streamwise, azimuthal and effective velocity directions. Note the cone is rotating anticlockwise when viewed from the nose tip.

5.2 Case A: Slender rotating cone in still fluid (spiral waves)

We now focus our attention on the case of a slender rotating cone in still fluid, where the cone half-angle lies in the range $\psi = 15^\circ - 45^\circ$.

The problem setup for a cone rotating in otherwise still fluid is shown in figure 5.1, where for consistency with our existing setup in §2, we consider an anti-clockwise rotating cone. Our model differs from that of Kobayashi [23] by a sign of the Coriolis terms in the momentum equations, as we have the transformation $\Omega^* \rightarrow -\Omega^*$. We observe that the logarithmic coordinates $(\widehat{x}^*, y^*)$ emanating from the shifted origin O', which propagate in the direction of the normal to the vortices and inwards towards the cone apex along the spiral vortices, respectively. The shifted basic flow velocities in these directions are $\overline{U}$

and $\overline{V}$, and are related to the basic flow setup in the previous (x^*, θ) formulation by the equations

$$\overline{U} = x(U(\eta)\cos\phi + V(\eta)\sin\phi) = x\tilde{U}(\eta), \tag{5.17}$$

$$\overline{V} = x(U(\eta)\sin\phi + V(\eta)\cos\phi) = x\tilde{V}(\eta). \tag{5.18}$$

From figures 5.2 and 5.3, we see that for increasing waveangles ϕ, there is a minor increase in the velocity in the y-direction. However, for the $\widehat{x}$-direction, we observe a greater change, with the velocity decreasing and becoming negative as the waveangle increases. We note that physically, increasing ϕ corresponds to an increasing cone half angle ψ. Hence, in the case where $\psi = 15°, \phi = 0°$, we recover the previous basic flow velocities $(xU(\eta), xV(\eta))$ in the streamwise and azimuthal directions, respectively. Now, the standard Cartesian coordinates may be written in terms of $(\widehat{x}^*, y^*, z^*)$,

$$X^* = r^* \cot\psi - z^* \sin\psi, \tag{5.19}$$

$$Y^* = (r^* + z^* \cos\psi)\cos\theta, \tag{5.20}$$

$$Z^* = (r^* + z^* \cos\psi)\sin\theta, \tag{5.21}$$

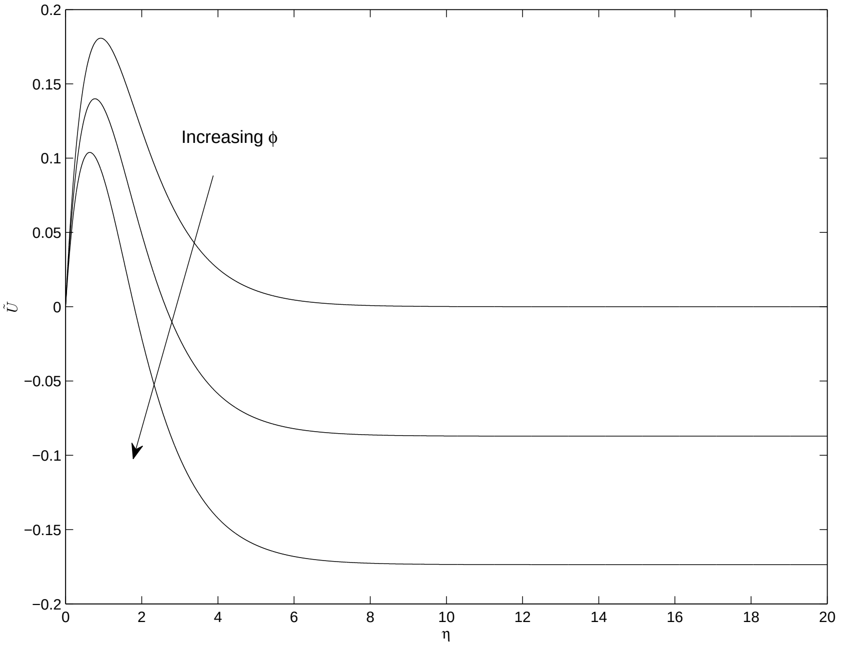

Figure 5.2: Velocity profiles $\tilde{U}(\eta)$ in the $\widehat{x}$-direction for phase angles $\phi = 0°, 5°, 10°$.

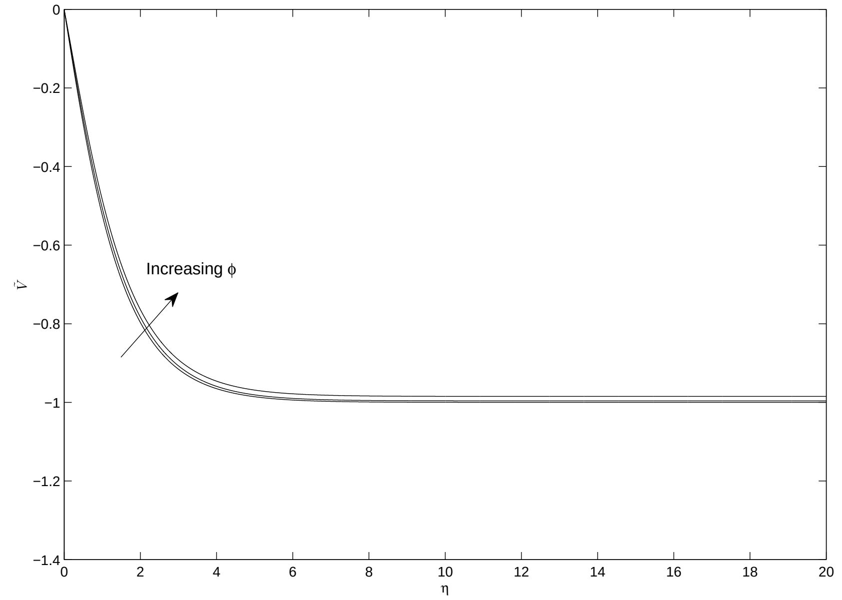

Figure 5.3: Velocity profiles $\tilde{V}(\eta)$ in the y-direction for phase angles $\phi = 0°, 5°, 10°$.

where r^* and θ are given by equations (5.3),(5.4). This enables us to calculate the scale factors of the new curvilinear coordinate system,

$$\begin{aligned}
h_1 &= \frac{r^*}{r_0^*\sin\psi}\Big(1+2\frac{z^*}{r^*}\cos\psi\sin^2\phi+\frac{z^{*2}}{r^{*2}}\cos^2\psi\sin^2\phi\Big)^{\frac{1}{2}} \\
&\approx \frac{r^*}{r_0^*\sin\psi}\Big(1+\frac{z^*}{r^*}\cos\psi\sin^2\phi\Big) \\
&= \frac{x}{x_0\sin\psi}\Big(1+\frac{\mathrm{R}^{-\frac{1}{2}}\eta}{x}\cot\psi\sin^2\phi\Big), \qquad (5.22) \\
h_2 &= \frac{r^*}{r_0^*\sin\psi}\Big(1+2\frac{z^*}{r^*}\cos\psi\cos^2\phi+\frac{z^{*2}}{r^{*2}}\cos^2\psi\cos^2\phi\Big)^{\frac{1}{2}}, \\
&\approx \frac{r^*}{r_0^*\sin\psi}\Big(1+\frac{z^*}{r^*}\cos\psi\cos^2\phi\Big) \\
&= \frac{x}{x_0\sin\psi}\Big(1+\frac{\mathrm{R}^{-\frac{1}{2}}\eta}{x}\cot\psi\cos^2\phi\Big), \qquad (5.23) \\
h_3 &= 1, \qquad (5.24)
\end{aligned}$$

where η and x are defined in (2.12). If we suppose the velocities in the new coordinate system $(\widehat{x}^*, y^*, z^*)$ are $\underline{\mathbf{u}} = (u^*, v^*, w^*)$, then we eventually arrive at the governing Navier-

Stokes equations in a rotating frame

$$
\begin{aligned}
\frac{1}{h_1}\frac{\partial u^*}{\partial \widehat{x}^*} \quad &+ \quad \frac{1}{h_2}\frac{\partial v^*}{\partial y^*} + \frac{\partial w^*}{\partial z^*} + \frac{1}{h_1 h_2}\Big[\frac{\partial h_2}{\partial \widehat{x}^*}u^* + \frac{\partial h_1}{\partial y^*}v^* + \Big(h_1\frac{\partial h_2}{\partial z^*} + h_2\frac{\partial h_1}{\partial z^*}\Big)w^*\Big] = 0,
\end{aligned}
\tag{5.25}
$$

$$
\begin{aligned}
\frac{u^*}{h_1}\frac{\partial u^*}{\partial \widehat{x}^*} \quad &+ \quad \frac{v^*}{h_2}\frac{\partial u^*}{\partial y^*} + w^*\frac{\partial u^*}{\partial z^*} + \frac{u^* v^*}{h_1 h_2}\frac{\partial h_1}{\partial y^*} + \frac{u^* w^*}{h_1}\frac{\partial h_1}{\partial z^*} - \frac{v^{*2}}{h_1 h_2}\frac{\partial h_2}{\partial \widehat{x}^*} \\
&- \quad 2\Omega^*(w^*\cos\psi\sin\phi + v^*\sin\psi) + (\underline{\Omega}\times\underline{\Omega}\times\underline{r})_{\widehat{x}^*} \\
&= \quad -\frac{1}{\rho^* h_1}\frac{\partial p^*}{\partial \widehat{x}^*} + \nu^*\Big[\nabla^{*2}u^* + \Big\{\frac{\partial}{\partial \widehat{x}^*}\Big(\frac{1}{h_1 h_2}\frac{\partial}{\partial \widehat{x}^*}(h_1 h_2)\Big)u^* - \frac{2}{h_2^2}\frac{\partial h_2}{\partial \widehat{x}^*}\frac{\partial v^*}{\partial y^*} \\
&- \quad \Big(\frac{1}{h_2^3}\frac{\partial h_2}{\partial y^*}\frac{\partial h_2}{\partial \widehat{x}^*} + \frac{1}{h_1^2 h_2}\frac{\partial h_1}{\partial y^*}\frac{\partial h_1}{\partial \widehat{x}^*}\Big)v^* - \Big(\frac{1}{h_1^3}\frac{\partial h_1}{\partial z^*}\frac{\partial h_1}{\partial \widehat{x}^*} + \frac{1}{h_1 h_2^2}\frac{\partial h_2}{\partial z^*}\frac{\partial h_2}{\partial \widehat{x}^*}\Big)w^*\Big\}\Big],
\end{aligned}
\tag{5.26}
$$

$$
\begin{aligned}
\frac{u^*}{h_1}\frac{\partial v^*}{\partial \widehat{x}^*} \quad &+ \quad \frac{v^*}{h_2}\frac{\partial v^*}{\partial y^*} + w^*\frac{\partial v^*}{\partial z^*} + \frac{u^* v^*}{h_1 h_2}\frac{\partial h_2}{\partial \widehat{x}^*} + \frac{v^* w^*}{h_2}\frac{\partial h_2}{\partial z^*} - \frac{u^{*2}}{h_1 h_2}\frac{\partial h_1}{\partial y^*} \\
&+ \quad 2\Omega^*(w^*\cos\psi\cos\phi + u^*\sin\psi) + (\underline{\Omega}\times\underline{\Omega}\times\underline{r})_{y^*} \\
&= \quad -\frac{1}{\rho^* h_2}\frac{\partial p^*}{\partial y^*} + \nu^*\Big[\nabla^{*2}v^* - \Big\{\Big(\frac{1}{h_2^3}\frac{\partial h_2}{\partial \widehat{x}^*}\frac{\partial h_2}{\partial y^*} + \frac{1}{h_1^2 h_2}\frac{\partial h_1}{\partial \widehat{x}^*}\frac{\partial h_1}{\partial y^*}\Big)u^* + \frac{1}{h_2^2}v^* \\
&- \quad \Big(\frac{1}{h_1^3}\frac{\partial h_1}{\partial z^*}\frac{\partial h_1}{\partial y^*} + \frac{1}{h_1 h_2^2}\frac{\partial h_2}{\partial z^*}\frac{\partial h_2}{\partial y^*}\Big)w^* - 2\Big(\frac{1}{h_2^2}\frac{\partial h_2}{\partial \widehat{x}^*}\frac{\partial u^*}{\partial y^*} + \frac{1}{h_2^2}\frac{\partial h_2}{\partial z^*}\frac{\partial w^*}{\partial y^*}\Big)\Big\}\Big],
\end{aligned}
\tag{5.27}
$$

$$
\begin{aligned}
\frac{u^*}{h_1}\frac{\partial w^*}{\partial \widehat{x}^*} \quad &+ \quad \frac{v^*}{h_2}\frac{\partial w^*}{\partial y^*} + w^*\frac{\partial w^*}{\partial z^*} - \frac{u^{*2}}{h_1}\frac{\partial h_1}{\partial z^*} - \frac{v^{*2}}{h_2}\frac{\partial h_2}{\partial z^*} \\
&- \quad 2\Omega^*(v^*\cos\psi\cos\phi - u^*\cos\psi\sin\phi) + (\underline{\Omega}\times\underline{\Omega}\times\underline{r})_{z^*} \\
&= \quad -\frac{1}{\rho^*}\frac{\partial p^*}{\partial z^*} + \nu^*\Big[\nabla^{*2}w^* - \Big\{\Big(\frac{1}{h_1^3}\frac{\partial h_1}{\partial \widehat{x}^*}\frac{\partial h_1}{\partial z^*} + \frac{1}{h_1 h_2^2}\frac{\partial h_2}{\partial \widehat{x}^*}\frac{\partial h_2}{\partial z^*}\Big)u^* \\
&+ \quad \Big(\frac{1}{h_2^3}\frac{\partial h_2}{\partial y^*}\frac{\partial h_2}{\partial z^*} + \frac{1}{h_1^2 h_2}\frac{\partial h_1}{\partial y^*}\frac{\partial h_1}{\partial z^*}\Big)v^* + 2\Big(\frac{1}{h_1^2}\frac{\partial h_1}{\partial z^*}\frac{\partial u^*}{\partial \widehat{x}^*} + \frac{1}{h_2^2}\frac{\partial h_2}{\partial z^*}\frac{\partial v^*}{\partial y^*}\Big) \\
&- \quad \frac{\partial}{\partial z^*}\Big(\frac{1}{h_1 h_2}\frac{\partial}{\partial z^*}(h_1 h_2)\Big)w^*\Big\}\Big],
\end{aligned}
\tag{5.28}
$$

where the dimensional Laplacian operator is

$$
\nabla^{*2} = \frac{1}{h_1^2}\frac{\partial^2}{\partial \widehat{x}^{*2}} + \frac{1}{h_2^2}\frac{\partial^2}{\partial y^{*2}} + \frac{\partial^2}{\partial z^{*2}} + \frac{1}{h_1 h_2}\Big[\frac{\partial}{\partial \widehat{x}^*}\Big(\frac{h_2}{h_1}\Big)\frac{\partial}{\partial \widehat{x}^*} + \frac{\partial}{\partial y^*}\Big(\frac{h_1}{h_2}\Big)\frac{\partial}{\partial y^*} + \frac{\partial}{\partial z^*}(h_1 h_2)\frac{\partial}{\partial z^*}\Big].
\tag{5.29}
$$

In this setup, we non-dimensionalise lengths with distance along the cone l^*, so $\widehat{x}^* = l^*\widehat{x}$ and $y^* = l^*y$. Secondly, we scale both logarithmic coordinates $\widehat{x}$ and y on boundary layer thickness as well as the normal coordinate z, in the form

$$\eta = \mathrm{R}^{\frac{1}{2}}z, \quad \breve{x} = \mathrm{R}^{\frac{1}{2}}\widehat{x}, \quad \overline{y} = \mathrm{R}^{\frac{1}{2}}y. \tag{5.30}$$

The enables the vortex structure in both logarithmic directions to be analysed on the same level as the smallest length scale in the surface-normal direction. As in §5.1, usually a Görtler mode analysis requires lengths normal to the surface and spanwise to the vortices to be scaled on boundary layer thickness (see Hall [14] and Denier *et al.* [3]). However, in the current spiral wave analysis, the counter-rotating vortices are characterised by both logarithmic coordinates. This may be seen from the expressions for the Lamé coefficients in (5.22) and (5.23), where the relationship between x and both logarithmic coordinates is introduced. Next we use the fact that the spiral waves are periodic in the effective velocity direction to introduce periodicity into the perturbation quantities of vortex wavenumber a and wavenumber b in the $\overline{y}$-direction. Our shifted basic flow quantities remain unchanged, whereas we scale the perturbation velocities again on boundary layer thickness, leading to

$$\tilde{\mathbf{u}}^* = \Omega^* l^* \sin\psi[\{x\tilde{U}(\eta), x\tilde{V}(\eta), \mathrm{R}^{-\frac{1}{2}}W\} + \mathrm{R}^{-\frac{1}{2}}\{\tilde{u}(\overline{y},\eta), \tilde{v}(\overline{y},\eta), \tilde{w}(\overline{y},\eta)\}\mathrm{exp}(\mathrm{i}a\breve{x} + \mathrm{i}b\overline{y})], \tag{5.31}$$

Similarly with the circular wave case, the pressure perturbation term scales as

$$p^* = (\rho^*\Omega^{*2}l^{*2}\sin^2\psi)\mathrm{R}^{-1}\tilde{p}(\eta)\mathrm{exp}(\mathrm{i}a\breve{x} + \mathrm{i}b\overline{y}). \tag{5.32}$$

Now, before we continue to derive the resulting disturbance equations in the spiral wave setup, we first notice from equations (5.22),(5.23) that the quantities h_1 and h_2 both depend on the streamwise coordinate x. However, our current setup is based on the outwardly propagating logarithmic coordinate $\widehat{x}$. Hence, we must obtain a suitable relationship between these two coordinates, which is given by (5.3). Furthermore, we recall our analysis is based on a large Reynolds number setup, which allows us to expand the exponential quantity in (5.3) in powers of $\mathrm{R}^{-\frac{1}{2}}$ to arrive at

$$x = x_0 + \frac{\mathrm{R}^{-\frac{1}{2}}}{\sin\psi}(\check{x}\cos\phi - \overline{y}\sin\phi) + O(\mathrm{R}^{-1}). \tag{5.33}$$

This results in the following expressions for the Lamé scale factors

$$h_1 = \frac{1}{\sin\psi} + \frac{\mathrm{R}^{-\frac{1}{2}}}{r_0}\Big(\check{x}\cos\phi - \overline{y}\sin\phi + \eta\cos\psi\sin^2\phi\Big) + O(\mathrm{R}^{-1}), \tag{5.34}$$

$$h_2 = \frac{1}{\sin\psi} + \frac{\mathrm{R}^{-\frac{1}{2}}}{r_0}\Big(\check{x}\cos\phi - \overline{y}\sin\phi + \eta\cos\psi\cos^2\phi\Big) + O(\mathrm{R}^{-1}). \tag{5.35}$$

Importantly, we notice the difference between the current setup and that for the case of circular waves, where ($\phi = 0°$), is the location of the new origin O' resulting in the term containing x_0. However, we also note that in the current analysis, whilst the spirals are propagating at a non-zero waveangle ϕ, they are still very close to circular waves. This is seen from the experimental results of Kobayashi & Izumi [26] where for $15° \leqslant \psi \leqslant 30°$, the experimental waveangle actually varies from $0° - 2.7°$, whereas their theoretical estimate varies from $0° - 1°$. Hence, ϕ is considerably small and, as a result, we deduce the boundary layer becomes unstable and admits spiral vortices from close to the cone nose. Therefore, the location x_0 of the new origin is very close to the nose and we are able to maintain a consistent formulation by introducing the assumption of writing $x_0 = O(\mathrm{R}^{-\frac{1}{2}})$

for large R, in the form

$$r_0 = \mu \mathrm{R}^{-\frac{1}{2}}. \tag{5.36}$$

Here, without loss of generality, we may write $\mu = 1$. Now, as a result of applying this assumption, we may write the Lamé scale factors as

$$h_1 = \frac{\overline{h}_1}{\sin\psi} + O(\mathrm{R}^{-\frac{1}{2}}), \tag{5.37}$$

$$h_2 = \frac{\overline{h}_2}{\sin\psi} + O(\mathrm{R}^{-\frac{1}{2}}), \tag{5.38}$$

where

$$\overline{h}_1 = 1 + \check{x}\cos\phi - \overline{y}\sin\phi + \eta\cos\psi\sin^2\phi, \tag{5.39}$$

$$\overline{h}_2 = 1 + \check{x}\cos\phi - \overline{y}\sin\phi + \eta\cos\psi\cos^2\phi. \tag{5.40}$$

5.2.1 Linear disturbance equations

Application of these modified scalings and assumptions leads us to the following linearised perturbation equations

$$\mathrm{i}a\frac{\sin\psi}{\overline{h}_1}\tilde{u} + \frac{\sin\psi(\tilde{u}\cos\phi + \tilde{v}\sin\phi)}{\overline{h}_1\overline{h}_2} + \mathrm{i}b\frac{\sin\psi}{\overline{h}_2}\tilde{v} + \frac{\partial\tilde{w}}{\partial\eta} + \Big(\frac{\cos\psi\cos^2\phi}{\overline{h}_2} + \frac{\cos\psi\sin^2\phi}{\overline{h}_1}\Big)\tilde{w} = 0, \tag{5.41}$$

$$
\begin{array}{rcl}
\Big(\mathrm{i}a\dfrac{(1+\check{x}\cos\phi-\overline{y}\sin\phi)}{\overline{h}_1}\tilde{U} & + & \mathrm{i}b\dfrac{(1+\check{x}\cos\phi-\overline{y}\sin\phi)}{\overline{h}_2}\tilde{V}+W\dfrac{\partial}{\partial\eta}\Big)\tilde{u} \\
+\dfrac{\tilde{U}\cos\phi}{\overline{h_1}}\tilde{u}-\dfrac{\tilde{U}\sin\phi}{\overline{h}_2}\tilde{v} & + & \dfrac{(1+\check{x}\cos\phi-\overline{y}\sin\phi)}{\sin\psi}\dfrac{\partial\tilde{U}}{\partial\eta}\tilde{w} \\
+\dfrac{(1+\check{x}\cos\phi-\overline{y}\sin\phi)}{\overline{h}_1\overline{h}_2}(\tilde{U}\tilde{v} & + & \tilde{V}\tilde{u})\sin\phi \\
+\Big(\dfrac{(1+\check{x}\cos\phi-\overline{y}\sin\phi)}{\overline{h}_1}\tilde{U}\tilde{w} & + & \dfrac{\sin\psi}{\overline{h}_1}W\tilde{u}\Big)\cot\psi\sin^2\phi \\
-2\dfrac{(1+\check{x}\cos\phi-\overline{y}\sin\phi)}{\overline{h}_1\overline{h}_2}\tilde{V}\tilde{v}\cos\phi & - & 2(\tilde{w}\cot\psi\sin\phi+\tilde{v}) \\
=-\mathrm{i}a\dfrac{\sin\psi}{\overline{h}_1}\tilde{p}+\overline{\nabla}^2\tilde{u} & + & \Big[\dfrac{\partial}{\partial\check{x}}\Big(\dfrac{1}{\overline{h}_1\overline{h}_2}\dfrac{\partial(\overline{h}_1\overline{h}_2)}{\partial\check{x}}\Big)\tilde{u}-2\mathrm{i}b\dfrac{\sin\psi}{\overline{h}_2^2}\dfrac{\partial\overline{h}_2}{\partial\check{x}}\tilde{v} \\
-\Big(\dfrac{\sin\psi}{\overline{h}_2^3}\dfrac{\partial\overline{h}_2}{\partial\overline{y}}\dfrac{\partial\overline{h}_2}{\partial\check{x}}+\dfrac{\sin\psi}{\overline{h}_1^2\overline{h}_2}\dfrac{\partial\overline{h}_1}{\partial\overline{y}}\dfrac{\partial\overline{h}_1}{\partial\check{x}}\Big)\tilde{v} & - & \Big(\dfrac{\sin\psi}{\overline{h}_1^3}\dfrac{\partial\overline{h}_1}{\partial\overline{\eta}}\dfrac{\partial\overline{h}_1}{\partial\check{x}}+\dfrac{\sin\psi}{\overline{h}_1\overline{h}_2^2}\dfrac{\partial\overline{h}_2}{\partial\overline{\eta}}\dfrac{\partial\overline{h}_2}{\partial\check{x}}\Big)\tilde{w}\Big],
\end{array}
\tag{5.42}
$$

$$
\begin{array}{rcl}
\Big(\mathrm{i}a\dfrac{(1+\check{x}\cos\phi-\overline{y}\sin\phi)}{\overline{h}_1}\tilde{U} & + & \mathrm{i}b\dfrac{(1+\check{x}\cos\phi-\overline{y}\sin\phi)}{\overline{h}_2}\tilde{V}+W\dfrac{\partial}{\partial\eta}\Big)\tilde{v} \\
+\dfrac{\tilde{V}\cos\phi}{\overline{h_1}}\tilde{u}-\dfrac{\tilde{V}\sin\phi}{\overline{h}_2}\tilde{v} & + & \dfrac{(1+\check{x}\cos\phi-\overline{y}\sin\phi)}{\sin\psi}\dfrac{\partial\tilde{V}}{\partial\eta}\tilde{w} \\
+\dfrac{(1+\check{x}\cos\phi-\overline{y}\sin\phi)}{\overline{h}_1\overline{h}_2}(\tilde{U}\tilde{v} & + & \tilde{V}\tilde{u})\cos\phi \\
+\Big(\dfrac{(1+\check{x}\cos\phi-\overline{y}\sin\phi)}{\overline{h}_2}\tilde{V}\tilde{w} & + & \dfrac{\sin\psi}{\overline{h}_2}W\tilde{v}\Big)\cot\psi\cos^2\phi \\
-2\dfrac{(1+\check{x}\cos\phi-\overline{y}\sin\phi)}{\overline{h}_1\overline{h}_2}\tilde{U}\tilde{u}\sin\phi & + & 2(\tilde{w}\cot\psi\cos\phi+\tilde{u}) \\
=-\mathrm{i}b\dfrac{\sin\psi}{\overline{h}_2}\tilde{p}+\overline{\nabla}^2\tilde{v} & + & \Big[\Big(\dfrac{\sin\psi}{\overline{h}_2^3}\dfrac{\partial\overline{h}_2}{\partial\check{x}}\dfrac{\partial\overline{h}_2}{\partial\overline{y}}+\dfrac{\sin\psi}{\overline{h}_1^2\overline{h}_2}\dfrac{\partial\overline{h}_1}{\partial\check{x}}\dfrac{\partial\overline{h}_1}{\partial\overline{y}}\Big)\tilde{u} \\
+\dfrac{\sin^2\psi}{\overline{h}_2^2}\tilde{v} & - & 2\mathrm{i}b\dfrac{\sin\psi}{\overline{h}_2^2}\Big(\dfrac{\partial\overline{h}_2}{\partial\check{x}}\tilde{u}+\dfrac{\partial\overline{h}_2}{\partial\overline{\eta}}\tilde{w}\Big) \\
-\Big(\dfrac{\sin\psi}{\overline{h}_1^3}\dfrac{\partial\overline{h}_1}{\partial\overline{\eta}}\dfrac{\partial\overline{h}_1}{\partial\overline{y}} & + & \dfrac{\sin\psi}{\overline{h}_1\overline{h}_2^2}\dfrac{\partial\overline{h}_2}{\partial\overline{\eta}}\dfrac{\partial\overline{h}_2}{\partial\overline{y}}\Big)\tilde{w}\Big],
\end{array}
\tag{5.43}
$$

$$
\begin{aligned}
\Big(\mathrm{i}a\frac{(1+\check{x}\cos\phi-\overline{y}\sin\phi)}{\overline{h}_1}\tilde{U} \quad &+ \quad \mathrm{i}b\frac{(1+\check{x}\cos\phi-\overline{y}\sin\phi)}{\overline{h}_2}\tilde{V}+W\frac{\partial}{\partial\eta}\Big)\tilde{w}+\frac{\partial W}{\partial\eta}\tilde{w} \\
-2\frac{(1+\check{x}\cos\phi-\overline{y}\sin\phi)}{\overline{h}_1}\tilde{U}\tilde{u}\cot\psi\sin^2\phi \quad &- \quad 2\frac{(1+\check{x}\cos\phi-\overline{y}\sin\phi)}{\overline{h}_2}\tilde{V}\tilde{v}\cot\psi\cos^2\phi \\
-2(\tilde{v}\cot\psi\cos\phi \quad &- \quad \tilde{u}\cot\psi\sin\phi)=-\frac{\partial\tilde{p}}{\partial\eta}+\overline{\nabla}^2\tilde{w} \\
-\Big(\frac{\sin\psi}{\overline{h}_1^3}\frac{\partial\overline{h}_1}{\partial\check{x}}\frac{\partial\overline{h}_1}{\partial\eta} \quad &+ \quad \frac{\sin\psi}{\overline{h}_1\overline{h}_2^2}\frac{\partial\overline{h}_2}{\partial\check{x}}\frac{\partial\overline{h}_2}{\partial\overline{\eta}}\Big)\tilde{u} \\
+\Big(\frac{\sin\psi}{\overline{h}_2^3}\frac{\partial\overline{h}_2}{\partial\overline{y}}\frac{\partial\overline{h}_2}{\partial\overline{\eta}} \quad &+ \quad \frac{\sin\psi}{\overline{h}_1^2\overline{h}_2}\frac{\partial\overline{h}_1}{\partial\overline{y}}\frac{\partial\overline{h}_1}{\partial\eta}\Big)\tilde{v} \\
+2\Big(\frac{\sin\psi}{\overline{h}_1^2}\frac{\partial\overline{h}_1}{\partial\eta}\frac{\partial\tilde{u}}{\partial\check{x}} \quad &+ \quad \frac{\sin\psi}{\overline{h}_2^2}\frac{\partial\overline{h}_2}{\partial\eta}\frac{\partial\tilde{v}}{\partial\overline{y}}\Big)-\frac{\partial}{\partial\eta}\Big(\frac{1}{\overline{h}_1\overline{h}_2}\frac{\partial(\overline{h}_1\overline{h}_2)}{\partial\eta}\Big)\tilde{w},
\end{aligned}
\tag{5.44}
$$

where $\overline{\nabla}^2=\mathrm{R}^{-1}\nabla^2$ is now the non-dimensional re-scaled Laplacian operator in the logarithmic spiral wave coordinate setup, which may be expressed as

$$
\overline{\nabla}^2=\frac{\partial^2}{\partial\eta^2}-\Big(a^2\frac{\sin^2\psi}{\overline{h}_1^2}+b^2\frac{\sin^2\psi}{\overline{h}_2^2}\Big)+\frac{\sin^2\psi}{\overline{h}_1\overline{h}_2}\Big[\mathrm{i}a\frac{\partial}{\partial\check{x}}\Big(\frac{\overline{h}_2}{\overline{h}_1}\Big)+\mathrm{i}b\frac{\partial}{\partial\overline{y}}\Big(\frac{\overline{h}_1}{\overline{h}_2}\Big)+\frac{\partial}{\partial\eta}(\overline{h}_1\overline{h}_2)\frac{\partial}{\partial\eta}\Big).\Big]
\tag{5.45}
$$

We omit the time-dependent terms in this case because, as we have seen in §5.1, introducing the unsteady perturbations constitutes the inclusion of an extra term in each momentum equation, which is relatively straightforward to deal with. We again wish to investigate the short-wavelength asymptotic structure of the centrifugal instability and hence identify the spiral vortex wavenumber in the $\check{x}$-direction as $a=\epsilon^{-1}$, where ϵ is a small parameter which forms the basis of our asymptotic analysis. Here, $b=O(1)$ is the wavenumber in the $\overline{y}$-direction. After substituting into (5.41)–(5.44), we differentiate (5.42) with respect to η and use (5.44) to arrive at the system of equations (1)–(3) in the

Appendix, which are subject to the boundary conditions

$$\tilde{u} = \tilde{v} = \tilde{w} = 0, \quad \text{on} \quad \eta = 0, \infty. \tag{5.46}$$

5.3 Case C: Slender rotating cone in axial flow (circular and spiral waves)

We now turn our attention to the case of a slender rotating cone placed in an oncoming axial flow, which has been investigated experimentally and numerically by Kobayashi *et al.* [25] and Kobayashi [23] respectively, both for a cone with $\psi = 15^\circ$ for a range of values of the rotational flow parameter, s. We notice from these experimental studies that for different parameter values of s, both circular waves $\phi = 0^\circ$ and spiral vortices $\phi > 0^\circ$ may exist on the surface of a cone with $\psi = 15^\circ$. Indeed, Kobayashi *et al.* conclude that for $s > 5$, the waveangle reduces to 0° and the spiral vortices change into Taylor vortices.

As a result, we shall develop our analysis to include spiral and circular vortices in the case of axial flow, which may be dealt with by using a single formulation and altering the control parameter s accordingly. We follow the setup described above in §5.2, with logarithmic coordinates $(\widehat{x}^*, y^*)$ and express the shifted basic flow quantities in these directions as $(\overline{U}, \overline{V})$, which are now functions of the streamwise and surface-normal coordinates (x, η). Hence, the basic flows are written in the form

$$\overline{U}(x,\eta) = U(x,\eta)\cos\phi + V(x,\eta)\sin\phi, \tag{5.47}$$

$$\overline{V}(x,\eta) = U(x,\eta)\sin\phi + V(x,\eta)\cos\phi. \tag{5.48}$$

Importantly, these quantities may be expressed in terms of the basic flow solutions found in §2 for case C by making use of the relation $s^{-1/2} = T_s$, which leads us to

$$\overline{U} = \frac{\overline{U}_e^*}{\Omega^* l^* \sin\psi}\Big(f'(s,\eta_1)\cos\phi + s^{\frac{1}{2}} g(s,\eta_1)\sin\phi\Big) = \frac{\overline{U}_e^*}{\Omega^* l^* \sin\psi}\widehat{U}(s,\eta_1) \qquad (5.49)$$

$$\overline{V} = \frac{\overline{U}_e^*}{\Omega^* l^* \sin\psi}\Big(f'(s,\eta_1)\sin\phi + s^{\frac{1}{2}} g(s,\eta_1)\cos\phi\Big) = \frac{\overline{U}_e^*}{\Omega^* l^* \sin\psi}\widehat{V}(s,\eta_1). \qquad (5.50)$$

Figures 5.4 and 5.5 show the basic flow components in both directions of the logarithmic spirals $(\widehat{x}, y)$. Importantly, we see that for $s \geqslant 5$ we have $\phi = 0°$, and hence $\widehat{U}$ recovers the streamwise basic flow quantity f'. For $s < 5$, the basic flow quantities are shifted downwards, converging to a smaller value at the edge of the boundary layer. However, the y-component $\widehat{V}$ exhibits a uniform shear and is reduced as s is increased. Furthermore, for $s \geqslant 5$, $\widehat{V}$ still differs from g by a scale factor of $s^{1/2}$. Subsequently, to obtain the linearised equations of motion, we follow the setup used for the still fluid spiral wave case §5.2, except we replace instances of $(x\tilde{U}(\eta), x\tilde{V}(\eta))$ in the still fluid formulation with quantities in the new setup $(\overline{U}(x,\eta), \overline{V}(x,\eta))$. Now, the governing dimensional Navier-Stokes equations in the logarithmic spiral setup remain (5.25)–(5.28) and we scale the normal coordinate η as well as both logarithmic coordinates $\widehat{x}$ and y on boundary layer thickness, in the form

$$\eta = \mathrm{R}^{\frac{1}{2}} z, \quad \check{x} = \mathrm{R}^{\frac{1}{2}} \widehat{x}, \quad \overline{y} = \mathrm{R}^{\frac{1}{2}} y. \qquad (5.51)$$

Similar to §5.2, we express the mean flow and perturbation quantities in the form

$$\tilde{\mathbf{u}}^* = \Omega^* l^* \sin\psi[\{\overline{U}(x,\eta), \overline{V}(x,\eta), \mathrm{R}^{-\frac{1}{2}} W\} + \mathrm{R}^{-\frac{1}{2}}\{\tilde{u}(\overline{y},\eta), \tilde{v}(\overline{y},\eta), \tilde{w}(\overline{y},\eta)\}\exp(\mathrm{i}a\check{x} + \mathrm{i}b\overline{y})], \qquad (5.52)$$

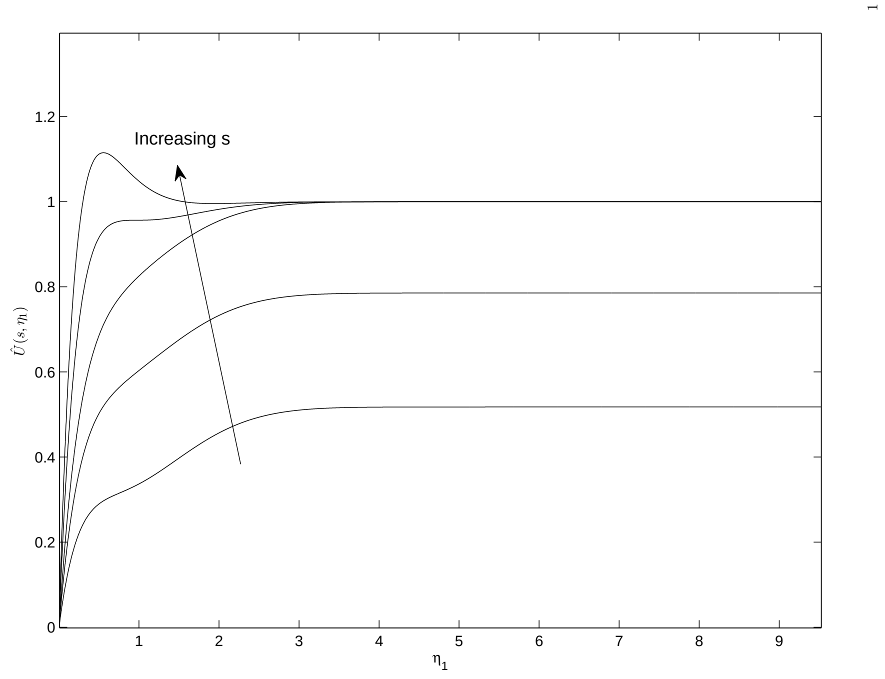

Figure 5.4: Velocity profiles $\widehat{U}(s,\eta_1)$ in the $\widehat{x}$-direction at $\psi = 15°$ for $s = 3, 4, 5, 10, 16$ and $\phi = 13.6°, 6°, 0°, 0°, 0°$.

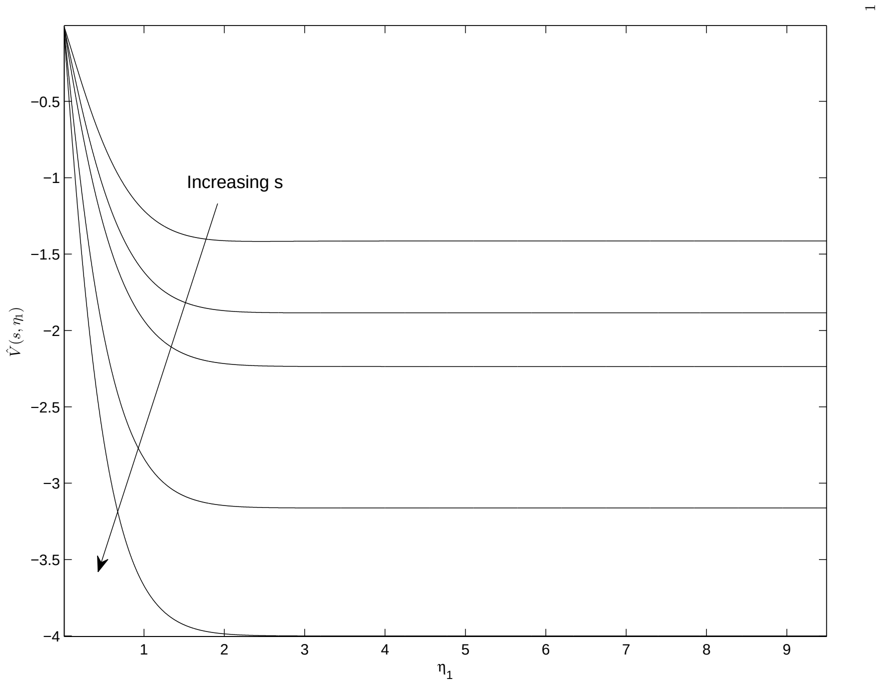

Figure 5.5: Velocity profiles $\widehat{V}(s,\eta_1)$ in the y-direction at $\psi = 15°$ for $s = 3, 4, 5, 10, 16$ and $\phi = 13.6°, 6°, 0°, 0°, 0°$.

In addition, the pressure perturbation term scales as

$$p^* = (\rho^* \Omega^{*2} l^{*2} \sin^2 \psi) \mathrm{R}^{-1} \tilde{p}(\eta) \exp(\mathrm{i} a \check{x} + \mathrm{i} b \overline{y}). \tag{5.53}$$

However, we notice from (5.33) and (5.36) that $x = O(\mathrm{R}^{-\frac{1}{2}})$, but the problem now has x-dependence embedded in the more general shifted basic flow quantities $(\overline{U}(x, \eta), \overline{V}(x, \eta))$. Hence, it is possible to expand the basic flow quantities in powers of $\mathrm{R}^{-\frac{1}{2}}$, which we do so about the location of vortex activity, namely at $\eta = 0$. The reasons for this are elaborated upon in §6.1, but briefly, we observe that the setup is similar to the Taylor problem investigated by Hall [14], where the vortex activity is confined to a thin layer near the wall. This is because, for the range of s we are considering, this location is consistent with small ϕ, which is a necessary requirement from the experiments of Kobayashi *et al.* [25] and Kobayashi [23]. Furthermore, it is also consistent with our still fluid spiral wave analysis, where we have used the condition $x = O(\mathrm{R}^{-\frac{1}{2}})$. It is worth noting that from (5.33), x depends on both the logarithmic spiral coordinates after they have been re-scaled on the boundary layer thickness, namely $\check{x}$ and $\overline{y}$. Hence, both $\overline{U}$ and $\overline{V}$ actually depend on these logarithmic coordinates, and so we may write $\overline{U} = \overline{U}(\check{x}, \overline{y}, \eta)$ and $\overline{V} = \overline{V}(\check{x}, \overline{y}, \eta)$. Therefore, expansion of the basic flow quantities leads to

$$\overline{U}(\check{x}, \overline{y}, \eta) = \mathrm{R}^{-\frac{1}{2}} \eta \frac{\partial \overline{U}}{\partial \eta}(\check{x}, \overline{y}, 0) + O(\mathrm{R}^{-1}), \tag{5.54}$$

$$\overline{V}(\check{x}, \overline{y}, \eta) = \mathrm{R}^{-\frac{1}{2}} \eta \frac{\partial \overline{V}}{\partial \eta}(\check{x}, \overline{y}, 0) + O(\mathrm{R}^{-1}), \tag{5.55}$$

noting that $\overline{U}(\check{x}, \overline{y}, 0) = \overline{V}(\check{x}, \overline{y}, 0) = 0$.

5.3.1 Linear disturbance equations

In the axial flow formulation with spiral waves, we apply the modified scalings and assumptions above, which leads us to the following linearised perturbation equations

$$\mathrm{i}a\frac{\sin\psi}{\overline{h}_1}\tilde{u}+\frac{\sin\psi(\tilde{u}\cos\phi+\tilde{v}\sin\phi)}{\overline{h}_1\overline{h}_2}+\mathrm{i}b\frac{\sin\psi}{\overline{h}_2}\tilde{v}+\frac{\partial\tilde{w}}{\partial\eta}+\Big(\frac{\cos\psi\cos^2\phi}{\overline{h}_2}+\frac{\cos\psi\sin^2\phi}{\overline{h}_1}\Big)\tilde{w}=0, \tag{5.56}$$

$$\begin{aligned}
&\Big(\mathrm{i}a\frac{\sin\psi}{\overline{h}_1}\eta\frac{\partial\overline{U}}{\partial\eta}(\check{x},\overline{y},0) &+&\quad \mathrm{i}b\frac{\sin\psi}{\overline{h}_2}\eta\frac{\partial\overline{V}}{\partial\eta}(\check{x},\overline{y},0)+W\frac{\partial}{\partial\eta}\Big)\tilde{u}\\
+\frac{\sin\psi}{\overline{h_1}}\eta\frac{\partial^2\overline{U}}{\partial\check{x}\partial\eta}(\check{x},\overline{y},0)\tilde{u}-&\frac{\sin\psi}{\overline{h}_2}\eta\frac{\partial^2\overline{U}}{\partial\overline{y}\partial\eta}(\check{x},\overline{y},0)\tilde{v} &+&\quad \frac{\partial\overline{U}}{\partial\eta}(\check{x},\overline{y},0)\tilde{w}\\
&+\frac{\sin\psi}{\overline{h}_1\overline{h}_2}[\eta\frac{\partial\overline{U}}{\partial\eta}(\check{x},\overline{y},0)\tilde{v} &+&\quad \eta\frac{\partial\overline{V}}{\partial\eta}(\check{x},\overline{y},0)\tilde{u}]\sin\phi\\
&+\Big(\frac{\sin\psi}{\overline{h}_1}\eta\frac{\partial\overline{U}}{\partial\eta}(\check{x},\overline{y},0)\tilde{w} &+&\quad \frac{\sin\psi}{\overline{h}_1}W\tilde{u}\Big)\cot\psi\sin^2\phi\\
&-2\frac{\sin\psi}{\overline{h}_1\overline{h}_2}\eta\frac{\partial\overline{V}}{\partial\eta}(\check{x},\overline{y},0)\tilde{v}\cos\phi &-&\quad 2(\tilde{w}\cot\psi\sin\phi+\tilde{v})+O(\mathrm{R}^{-\frac{1}{2}})\\
&=-\mathrm{i}a\frac{\sin\psi}{\overline{h}_1}\tilde{p}+\overline{\nabla}^2\tilde{u} &+&\quad \Big[\frac{\partial}{\partial\check{x}}\Big(\frac{1}{\overline{h}_1\overline{h}_2}\frac{\partial(\overline{h}_1\overline{h}_2)}{\partial\check{x}}\Big)\tilde{u}-2\mathrm{i}b\frac{\sin\psi}{\overline{h}_2^2}\frac{\partial\overline{h}_2}{\partial\check{x}}\tilde{v}\\
-\Big(&\frac{\sin\psi}{\overline{h}_2^3}\frac{\partial\overline{h}_2}{\partial\overline{y}}\frac{\partial\overline{h}_2}{\partial\check{x}}+\frac{\sin\psi}{\overline{h}_1^2\overline{h}_2}\frac{\partial\overline{h}_1}{\partial\overline{y}}\frac{\partial\overline{h}_1}{\partial\check{x}}\Big)\tilde{v} &-&\quad \Big(\frac{\sin\psi}{\overline{h}_1^3}\frac{\partial\overline{h}_1}{\partial\overline{\eta}}\frac{\partial\overline{h}_1}{\partial\check{x}}+\frac{\sin\psi}{\overline{h}_1\overline{h}_2^2}\frac{\partial\overline{h}_2}{\partial\overline{\eta}}\frac{\partial\overline{h}_2}{\partial\check{x}}\Big)\tilde{w}\Big],
\end{aligned} \tag{5.57}$$

$$\begin{aligned}
\Big(\mathrm{i}a\frac{\sin\psi}{\overline{h}_1}\eta\frac{\partial\overline{U}}{\partial\eta}(\check{x},\overline{y},0) &\;+\; \mathrm{i}b\frac{\sin\psi}{\overline{h}_2}\eta\frac{\partial\overline{V}}{\partial\eta}(\check{x},\overline{y},0)+W\frac{\partial}{\partial\eta}\Big)\tilde{v} \\
+\frac{\sin\psi}{\overline{h}_1}\eta\frac{\partial^2\overline{V}}{\partial\check{x}\partial\eta}(\check{x},\overline{y},0)\tilde{u}-\frac{\sin\psi}{\overline{h}_2}\eta\frac{\partial^2\overline{V}}{\partial\overline{y}\partial\eta}(\check{x},\overline{y},0)\tilde{v} &\;+\; \frac{\partial\overline{V}}{\partial\eta}(\check{x},\overline{y},0)\tilde{w} \\
+\frac{\sin\psi}{\overline{h}_1\overline{h}_2}[\eta\frac{\partial\overline{U}}{\partial\eta}(\check{x},\overline{y},0)\tilde{v} &\;+\; \eta\frac{\partial\overline{V}}{\partial\eta}(\check{x},\overline{y},0)\tilde{u}]\cos\phi \\
+\Big(\frac{\sin\psi}{\overline{h}_2}\eta\frac{\partial\overline{V}}{\partial\eta}(\check{x},\overline{y},0)\tilde{w} &\;+\; \frac{\sin\psi}{\overline{h}_2}W\tilde{v}\Big)\cot\psi\cos^2\phi \\
-2\frac{\sin\psi}{\overline{h}_1\overline{h}_2}\eta\frac{\partial\overline{U}}{\partial\eta}(\check{x},\overline{y},0)\tilde{u}\sin\phi &\;+\; 2(\tilde{w}\cot\psi\cos\phi+\tilde{u})+O(\mathrm{R}^{-\frac{1}{2}}) \\
=-\mathrm{i}b\frac{\sin\psi}{\overline{h}_2}\tilde{p}+\overline{\nabla}^2\tilde{v} &\;+\; \Big[\Big(\frac{\sin\psi}{\overline{h}_2^3}\frac{\partial\overline{h}_2}{\partial\check{x}}\frac{\partial\overline{h}_2}{\partial\overline{y}}+\frac{\sin\psi}{\overline{h}_1^2\overline{h}_2}\frac{\partial\overline{h}_1}{\partial\check{x}}\frac{\partial\overline{h}_1}{\partial\overline{y}}\Big)\tilde{u} \\
+\frac{\sin^2\psi}{\overline{h}_2^2}\tilde{v} &\;-\; 2\mathrm{i}b\frac{\sin\psi}{\overline{h}_2^2}\Big(\frac{\partial\overline{h}_2}{\partial\check{x}}\tilde{u}+\frac{\partial\overline{h}_2}{\partial\overline{\eta}}\tilde{w}\Big) \\
-\Big(\frac{\sin\psi}{\overline{h}_1^3}\frac{\partial\overline{h}_1}{\partial\overline{\eta}}\frac{\partial\overline{h}_1}{\partial\overline{y}} &\;+\; \frac{\sin\psi}{\overline{h}_1\overline{h}_2^2}\frac{\partial\overline{h}_2}{\partial\overline{\eta}}\frac{\partial\overline{h}_2}{\partial\overline{y}}\Big)\tilde{w}\Big],
\end{aligned} \tag{5.58}$$

$$\begin{aligned}
\Big(\mathrm{i}a\frac{\sin\psi}{\overline{h}_1}\eta\frac{\partial\overline{U}}{\partial\eta}(\check{x},\overline{y},0) &\;+\; \mathrm{i}b\frac{\sin\psi}{\overline{h}_2}\eta\frac{\partial\overline{V}}{\partial\eta}(\check{x},\overline{y},0)+W\frac{\partial}{\partial\eta}\Big)\tilde{w}+\frac{\partial W}{\partial\eta}\tilde{w} \\
-2\frac{\sin\psi}{\overline{h}_1}\eta\frac{\partial\overline{U}}{\partial\eta}(\check{x},\overline{y},0)\tilde{u}\cot\psi\sin^2\phi &\;-\; 2\frac{\sin\psi}{\overline{h}_2}\eta\frac{\partial\overline{V}}{\partial\eta}(\check{x},\overline{y},0)\tilde{v}\cot\psi\cos^2\phi \\
-2(\tilde{v}\cot\psi\cos\phi &\;-\; \tilde{u}\cot\psi\sin\phi)+O(\mathrm{R}^{-\frac{1}{2}})=-\frac{\partial\tilde{p}}{\partial\eta}+\overline{\nabla}^2\tilde{w} \\
-\Big(\frac{\sin\psi}{\overline{h}_1^3}\frac{\partial\overline{h}_1}{\partial\check{x}}\frac{\partial\overline{h}_1}{\partial\eta} &\;+\; \frac{\sin\psi}{\overline{h}_1\overline{h}_2^2}\frac{\partial\overline{h}_2}{\partial\check{x}}\frac{\partial\overline{h}_2}{\partial\overline{\eta}}\Big)\tilde{u} \\
+\Big(\frac{\sin\psi}{\overline{h}_2^3}\frac{\partial\overline{h}_2}{\partial\overline{y}}\frac{\partial\overline{h}_2}{\partial\overline{\eta}} &\;+\; \frac{\sin\psi}{\overline{h}_1^2\overline{h}_2}\frac{\partial\overline{h}_1}{\partial\overline{y}}\frac{\partial\overline{h}_1}{\partial\eta}\Big)\tilde{v} \\
+2\Big(\frac{\sin\psi}{\overline{h}_1^2}\frac{\partial\overline{h}_1}{\partial\eta}\frac{\partial\tilde{u}}{\partial\check{x}} &\;+\; \frac{\sin\psi}{\overline{h}_2^2}\frac{\partial\overline{h}_2}{\partial\eta}\frac{\partial\tilde{v}}{\partial\overline{y}}\Big)-\frac{\partial}{\partial\eta}\Big(\frac{1}{\overline{h}_1\overline{h}_2}\frac{\partial(\overline{h}_1\overline{h}_2)}{\partial\eta}\Big)\tilde{w},
\end{aligned} \tag{5.59}$$

where $\overline{\nabla}^2 = \mathrm{R}^{-1}\nabla^2$ is now the non-dimensional re-scaled Laplacian operator in the logarithmic spiral wave coordinate setup, which may be expressed as

$$\overline{\nabla}^2 = \frac{\partial^2}{\partial \eta^2} - \Big(a^2 \frac{\sin^2\psi}{\overline{h}_1^2} + b^2 \frac{\sin^2\psi}{\overline{h}_2^2}\Big) + \frac{\sin^2\psi}{\overline{h}_1\overline{h}_2}\Big[\mathrm{i}a\frac{\partial}{\partial \check{x}}\Big(\frac{\overline{h}_2}{\overline{h}_1}\Big) + \mathrm{i}b\frac{\partial}{\partial \overline{y}}\Big(\frac{\overline{h}_1}{\overline{h}_2}\Big) + \frac{\partial}{\partial \eta}(\overline{h}_1\overline{h}_2)\frac{\partial}{\partial \eta}\Big).\Big] \tag{5.60}$$

As in §5.2, we do not include the time-dependent terms for similar reasons. We again wish to investigate the short-wavelength asymptotic structure of the centrifugal instability and hence identify the spiral vortex wavenumber in the $\check{x}$-direction as $a = \epsilon^{-1}$, where ϵ is a small parameter which forms the basis of our asymptotic analysis. Here, $b = O(1)$ is the wavenumber in the $\overline{y}$-direction. Importantly, in the axial flow setup, both spiral and circular waves are observed by Kobayashi *et al.* [25] for varying values of s. After substituting into (5.56)–(5.59), we differentiate (5.57) with respect to η and use (5.59) to obtain the system of equations (4)–(6) in the Appendix subject to the boundary conditions

$$\tilde{u} = \tilde{v} = \tilde{w} = 0, \quad \text{on} \quad \eta = 0, \infty. \tag{5.61}$$

Chapter 6

Neutral modes for still fluid (case A: circular waves)

6.1 Leading order solution

We now proceed to analyse the neutrally stable perturbations, so that there is no growth appearing in the governing equations (5.13)–(5.15). We observe that the steady flow problem setup is similar to the investigation of Hall [14] for the Taylor problem of flow between concentric rotating cylinders. Indeed, for slender rotating cones, the cone half-angle is sufficiently small, such that the physical flow setup resembles that for flow moving axially over a rotating cylinder. We follow the analysis of Hall [14] by expanding the perturbation quantities and the Taylor number, which we define as $T = 2\cot\psi$, given by the balance of centrifugal forces from the cone rotation and viscous forces. We notice the Taylor number appears in similar terms in the disturbance equations for both the Taylor problem and the circular wave analysis for the rotating cone with $\psi = 15°$. Furthermore, as we seek to develop an asymptotic analysis for large Taylor number, we see that the quantity $2\cot\psi$ becomes large for a slender cone, where ψ is small. Now, in a similar way to Hall [14] for the Taylor problem, we follow Meksyn [34] and seek a WKB solution for small values of ϵ, corresponding to the right-hand branches of the neutral curves. Hence, we consider $\epsilon \to 0$. We find that the dominant terms in these equations balance if we scale $T \sim \epsilon^{-4}$ and $W/V \sim O(\epsilon^{-2})$, resulting in

$$\begin{aligned}
\tilde{u} &= E(u_0(\eta) + \epsilon u_1(\eta) + \epsilon^2 u_2(\eta) + \ldots), \\
\tilde{v} &= \epsilon^2 E(v_0(\eta) + \epsilon v_1(\eta) + \epsilon^2 v_2(\eta) + \ldots), \\
\tilde{w} &= E(w_0(\eta) + \epsilon w_1(\eta) + \epsilon^2 w_2(\eta) + \ldots), \\
T &= \epsilon^{-4}(\lambda_0 + \lambda_1 \epsilon + \lambda_2 \epsilon^2 + \ldots), \qquad (6.1)
\end{aligned}$$

where

$$E = \exp \frac{\mathrm{i}}{\epsilon} \int^{\eta} K(\tau) \mathrm{d}\tau. \qquad (6.2)$$

Here, we note that w_0, w_1, K etc. are to be determined. Now, after substituting the above expressions into (5.14),(5.15) and equating terms of $O(1)$ and $O(\epsilon^2)$ respectively, we arrive at the following eigenrelation at leading order

$$(K^2 + 1)^3 = -\frac{\lambda_0 \overline{h}}{\sin \psi} \Big(\frac{\overline{x} V \sin \psi}{\overline{h}} + 1 \Big) \frac{\overline{x} \sin \psi}{\overline{h}} V'. \qquad (6.3)$$

In the similar Taylor problem studied by Hall [14], the vortex activity is located at the wall at $\eta = 0$, where in our problem we have $V = 0$. Also, the azimuthal wavenumber b is $O(1)$ and we are able fix it as

$$\mathrm{i} b \sin \psi = \overline{h}^3 \qquad (6.4)$$

in order to account for the additional perturbation terms in (5.15). In the Taylor problem, Hall [14] argues that in the WKB solution, the roots of the eigenrelation correspond to eigenfunctions, which lead to only real values of K. This can also be seen from the findings of Meksyn [34], where only real values of the growth rate are obtained for the flow between rotating cylinders. Now, in the first approximation, the structure of the WKB solution is the same as that for the Taylor problem, up to real factors introduced by the change in physical geometry. As a result, we proceed in similar fashion to Hall [14] and consider the most general case of K, seeking to retain only those solutions, which are not growing. A comparison of the eigenrelation (6.3) with that obtained by Hall [14] reveals that there is a difference only in real factors on the right-hand side of the equation. In addition, the structure of the corresponding eigenfunctions of the six roots of (6.3) is affected only through the real factors arising from the terms on the right-hand side, and so the findings of Meksyn [34] apply. Hence, the values of K, which lead to stable non-growing solutions in the stability equations correspond to real values; it is these real roots for K, which are the only physically acceptable roots due to the behaviour of the corresponding eigenfunctions. Therefore, we argue as in Hall [14] that these real values of K can only occur in regions where the right-hand side of (6.3) is positive and has its greatest magnitude. After re-scaling the eigenvalue in the form $\overline{\lambda} = \lambda\overline{x}$, this results in the leading order eigenvalue estimate having the form

$$\overline{\lambda} = -V'^{-1}_{\min}, \tag{6.5}$$

where $V'_{\min}$ denotes the minimum value of V', which occurs at the wall where $\eta = 0$, and is $V'(0) = -0.6159$. Therefore, for a slender cone with $\psi \leqslant 15°$, where purely circular waves are observed in still fluid, our leading order eigenvalue estimate is $\overline{\lambda} = 1.6236$.

6.2 First order solution

Our next task is to investigate the asymptotic structure of the effective scaled Taylor number, $\overline{T} = T\overline{x}$, for the special case when $\overline{\lambda} = -V'(0)^{-1}$. We apply the differential operator $(\epsilon^2\partial^2/\partial\eta^2 - 1)$ to (5.14) and use equation (5.15) to simplify by eliminating relevant terms in $\tilde{v}$, leading to (7) in the Appendix, subject to the boundary conditions

$$\tilde{w} = \frac{\partial^2 \tilde{w}}{\partial \eta^2} = \frac{\partial}{\partial \eta}\Big(\epsilon^2 \frac{\partial^2}{\partial \eta^2} - 1\Big)\tilde{w} = 0, \qquad \eta = 0, \infty. \tag{6.6}$$

The second and third boundary conditions arise due to the differential operation $(\epsilon^2\partial^2/\partial\eta^2 - 1)$, which we applied earlier to the equation (5.14). We apply this operation to the normal perturbation $\tilde{w}$, noting that $\tilde{w} = 0$ at $\eta = 0, \infty$ to obtain the second boundary condition. Subsequently, we apply the same operation to the normal perturbation gradient $\partial\tilde{w}/\partial\eta$ to obtain the third boundary condition.

We now follow the scalings used by Hall [14] for the Taylor problem and expand the Taylor number using a modified expansion to (6.1). In order to take account of terms of the same order as the thickness of the $\epsilon^{\frac{2}{3}}$ layer, we express the Taylor number in the form

$$T = \epsilon^{-4}(\lambda_0 + \lambda_1 \epsilon^{\frac{2}{3}} + \ldots) \tag{6.7}$$

followed by the re-scaled normal variable

$$\xi = \frac{\eta}{3^{\frac{1}{3}}\epsilon^{\frac{2}{3}}}. \tag{6.8}$$

We subsequently expand the normal perturbation velocity as

$$\tilde{w} = w_0(\xi) + \epsilon^{\frac{2}{3}} w_1(\xi) + \ldots, \tag{6.9}$$

with $\tilde{u} = O(1)$ and $\tilde{v} = O(\epsilon^2)$ as previously in the special case above. After substituting these expressions into (7) in the Appendix, we use the condition $V(0) = 0$ and (6.4) to eliminate additional perturbation terms. Now, we equate terms of $O(\epsilon^{\frac{2}{3}})$, noticing that we may write terms in η in terms of ϵ and ξ, which leads to a similar equation derived by Hall [14], given by

$$\frac{\partial^2 w_0}{\partial \xi^2} + \xi V'(0) w_0 - \lambda_1 \overline{x} 3^{-\frac{1}{3}} V'(0) w_0 = 0. \tag{6.10}$$

The solution of this equation, which remains bounded as $\xi \to \infty$ is given by

$$w_0 = C\mathrm{Ai}\Big(\frac{\xi - \lambda_1 \overline{x} 3^{-\frac{1}{3}}}{|V'(0)|}\Big), \tag{6.11}$$

where C is an arbitrary constant. Now, as this solution does not satisfy the boundary condition at $\eta = 0$, we seek another boundary layer embedded inside the $\epsilon^{\frac{2}{3}}$ layer, which is of thickness ϵ. We follow Hall [14] and define the inner variable Y as

$$Y = \frac{\eta}{\epsilon}, \tag{6.12}$$

where within this layer, the normal velocity $\tilde{w}$ may be expanded in the form

$$\tilde{w} = \epsilon^{\frac{1}{3}} W_0(Y) + \epsilon^{\frac{2}{3}} W_1(Y) + \dots . \tag{6.13}$$

We now substitute this expression into (7) in the Appendix and equate terms of $O(\epsilon^{\frac{1}{3}})$, which leads to

$$\Big(\frac{\mathrm{d}^2}{\mathrm{d}Y^2} - 1\Big)^3 W_0 = -W_0, \tag{6.14}$$

subject to the boundary conditions

$$W_0 = \frac{\mathrm{d}^2 W_0}{\mathrm{d}Y^2} = \frac{\mathrm{d}^3 W_0}{\mathrm{d}Y^3} - \frac{\mathrm{d}W_0}{\mathrm{d}Y} = 0, \quad Y = 0. \tag{6.15}$$

As previously, the second and third boundary conditions arise due to the differential operation $(\epsilon^2\partial^2/\partial\eta^2 - 1)$, which has been applied earlier to the equation (5.14). We use this operation on the normal perturbation W_0, noting that $W_0(0) = 0$ to obtain the second boundary condition. Then as before, we apply the same operation to the normal perturbation gradient $\mathrm{d}W_0/\mathrm{d}Y$ to obtain the third boundary condition. The bounded solution to this equation has the following form, presented in Hall [14],

$$W_0 = a_0 + a_1 Y + \exp[-(3^{\frac{1}{4}} \cos\frac{\pi}{12})Y]\{a_2 \sin(3^{\frac{1}{4}} \sin\frac{\pi}{12})Y + a_3 \cos(3^{\frac{1}{4}} \sin\frac{\pi}{12})Y\}, \tag{6.16}$$

where it is possible to choose a_1, a_2 and a_3 in terms of a_0 such that the required boundary conditions at $Y = 0$ remain satisfied. Now, for large Y, we see that $W_0 \sim Y$, and hence matching with the outer boundary-layer solution for w_0 is possible if

$$\mathrm{Ai}\Big(-\frac{\lambda_1 \overline{x} 3^{-\frac{1}{3}}}{|V'(0)|}\Big) = 0. \tag{6.17}$$

This results in an infinite sequence of eigenvalues $\{\lambda_{1n}\}$, which correspond to the zeros of the Airy function on the negative real axis. Subsequently, the most dangerous mode of instability has a re-scaled effective Taylor number expansion given by

$$\begin{aligned} \overline{T} &= T\overline{x} \\ &= \epsilon^{-4}\Big(\frac{1}{|V'(0)|} + 2.3381|V'(0)|3^{\frac{1}{3}}\epsilon^{\frac{2}{3}} + \dots\Big), \\ &= \epsilon^{-4}\Big(1.6236 + 2.0769\epsilon^{\frac{2}{3}} + \dots\Big). \end{aligned} \tag{6.18}$$

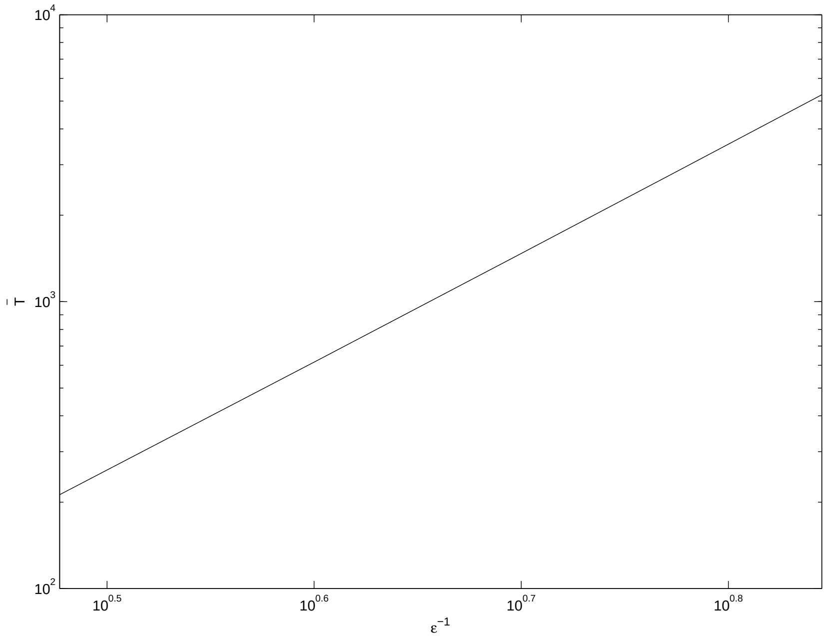

Figure 6.1: Scaled effective asymptotic Taylor number $\overline{T}$ as a function of non-dimensional wavenumber ϵ^{-1} for $\psi \leqslant 15^\circ, \phi = 0^\circ$.

6.3 Results and physical interpretation

Figure 6.1 shows a plot of the re-scaled effective Taylor number for the most dangerous mode as a function of the non-dimensional vortex wavenumber ϵ^{-1}, which corresponds to the right-hand branch of the neutral curve. Now, for large n the eigenvalues may be approximated by

$$2\Big(\frac{\overline{\lambda_{1n}}}{3|V'(0)|^3}\Big)^{\frac{3}{2}} \sim \pi(n-\frac{1}{4}), \tag{6.19}$$

in which case the re-scaled effective Taylor number has the form

$$\overline{T}_n \;=\; \epsilon^{-4}\Big(\frac{1}{|V'(0)|}+3[\epsilon|V'(0)|^3\frac{\pi}{2}(n-\frac{1}{4})]^{\frac{2}{3}}+\dots\Big). \tag{6.20}$$

Qualitatively, this asymptotic estimate of the effective Taylor number represents cones of half-angle $\psi \leqslant 15^\circ$ in still fluid, which admit circular waves with waveangle $\phi = 0$. Hence, the result we have derived does actually apply within a specific parameter regime to a small family of cones.

Physically, we observe that an increase in the vortex wavenumber of the circular waves is achieved by an increase in the Taylor number, which governs the flow, so we move further up the right-hand branch of the neutral curve. Our assumptions in the analysis require that the boundary layer instability develops from close to the cone nose and grows in the streamwise direction. As the vortex streaks remain circular in nature, we propose that there is no growth along the azimuthal direction. Hence, for a cone of half-angle $\psi = 15^\circ$, the vortices are visualised as circular rings and, in terms of the centrifugal instability, the resulting flow structure is one of the most stable configurations. Whereas the rotational shear effect of the spinning cone sheds vorticity in the azimuthal direction, the cone half-angle is sufficiently small such that the streamwise forcing of the mean flow causes vorticity to be shed along the cone. The result is the appearance of counter-rotating vortices, which form each individual streak on the cone surface as the instability develops. Now, the cone half-angle $\psi = 15^\circ$ is a special case as it exhibits a flow arrangement where these counter-rotating Görtler vortex streaks remain aligned with each other as circular rings. Indeed, these rings are observed for a 15° cone for a range of axial flows and are termed ‘Taylor’ vortices by Kobayashi *et al.* [25] for the region $s \geqslant 5$.

Chapter 7

Neutral modes for still fluid (case A: spiral waves)

7.1 Leading order solution

In the case of spiral waves for a rotating cone in still fluid, we proceed to expand the perturbation quantities and the modified Taylor number, which arises through a balance between the centrifugal and viscous forces, and is given by

$$T = \frac{2 \cot \psi \cos \phi}{\sin^5 \psi}. \tag{7.1}$$

This quantity differs from the corresponding expression for circular waves, but remains large for small ϕ and ψ close to 15°. Following the setup of §6 for circular waves in still fluid and the analysis of Hall [14], we consider a WKB solution for small values of ϵ, corresponding to $\epsilon \to 0$. We find that the dominant terms in these equations balance if we scale $T \sim \epsilon^{-4}$ and $W/V \sim O(\epsilon^{-2})$, resulting in

$$\begin{aligned} \tilde{u} &= E(u_0(\eta) + \epsilon u_1(\eta) + \epsilon^2 u_2(\eta) + \ldots), \\ \tilde{v} &= \epsilon^2 E(v_0(\eta) + \epsilon v_1(\eta) + \epsilon^2 v_2(\eta) + \ldots), \\ \tilde{w} &= E(w_0(\eta) + \epsilon w_1(\eta) + \epsilon^2 w_2(\eta) + \ldots), \\ T &= \epsilon^{-4}(\lambda_0 + \lambda_1 \epsilon + \lambda_2 \epsilon^2 + \ldots), \end{aligned} \tag{7.2}$$

where $\lambda = \lambda_0 + \lambda_1 \epsilon + \lambda_2 \epsilon^2 + \ldots$,

$$E = \exp \frac{\mathrm{i}}{\epsilon} \int^{\varphi} K(\tau) \mathrm{d}\tau, \tag{7.3}$$

and

$$\varphi = \frac{\sin \psi}{\overline{h}_1} \eta. \tag{7.4}$$

Therefore, we substitute the above expressions into (2),(3). Importantly, we notice that in the region of a slender cone, which we are considering where $\psi = 15° - 45°$, the waveangle is small and from the results of Kobayashi & Izumi $\phi = 0° - 10°$. We are able to identify that in this case $\sin^2 \phi \ll \cos^2 \phi$. Hence, the terms in (3) containing $\sin^2 \phi$ may be neglected. Upon equating terms of $O(\epsilon^2)$ and $O(1)$ respectively, and making use of (1) in the Appendix, we arrive at the following eigenrelation at leading order

$$(K^2 + 1)^3 = -\lambda_0 \overline{h}_1^{4} (1 + \check{x} \cos \phi - \overline{y} \sin \phi) \Big(\tilde{V} \cos \phi + 1 \Big) \frac{\partial \tilde{V}}{\partial \eta}. \tag{7.5}$$

Here, we have noticed that, as the spirals have small wave angles, the problem is similar to the circular wave case. Therefore, as in the Taylor problem investigated by Hall [14],

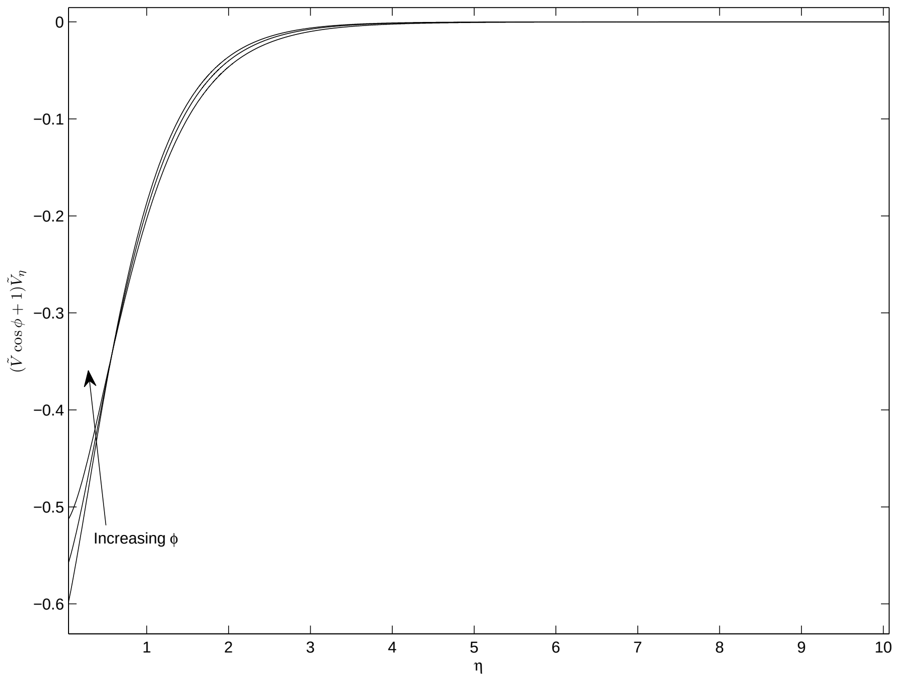

Figure 7.1: Plots of $(\tilde{V}\cos\phi+1)\frac{\partial\tilde{V}}{\partial\eta}$ for waveangles $\phi=0°,5°,10°$.

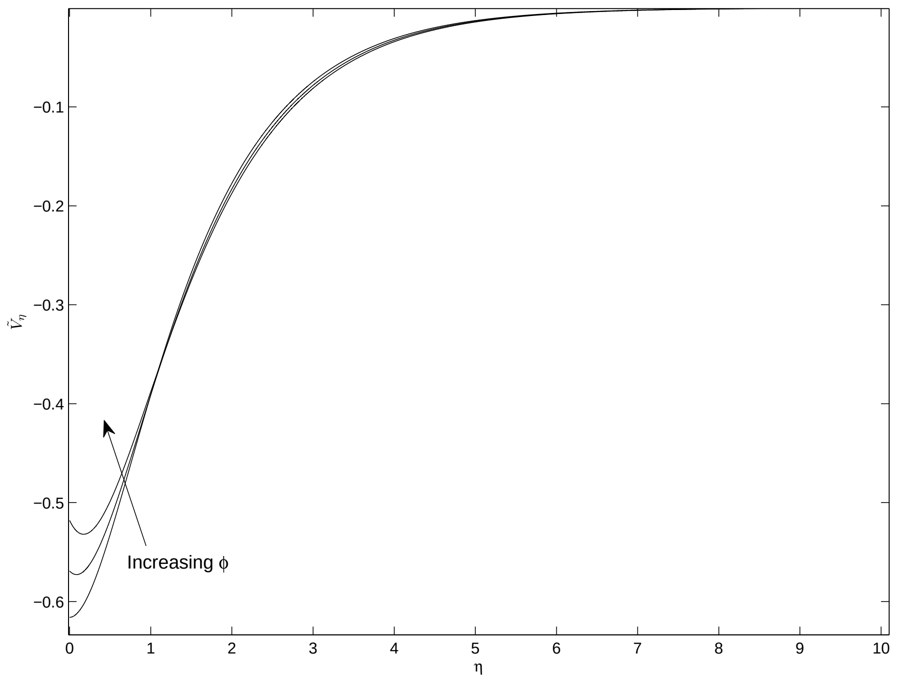

Figure 7.2: Plots of $\frac{\partial\tilde{V}}{\partial\eta}$ for waveangles $\phi=0°,5°,10°$.

we identify that for small ϕ, the vortex activity will be located at the wall, $\eta = O(\epsilon)$, and hence we write $\eta = \epsilon\xi$. Therefore, the term in (3) in the Appendix, which remains containing a factor of $\overline{h}_2$ in the denominator may be dealt with by expanding this quantity using the definition for $\overline{h}_2$ to obtain

$$\begin{aligned} \frac{(1 + \check{x}\cos\phi - \overline{y}\sin\phi)}{\overline{h}_2} &= \frac{1}{1 + \frac{\epsilon\xi\cos\psi\cos^2\phi}{(1+\check{x}\cos\phi - \overline{y}\sin\phi)}} \\ &= 1 + O(\epsilon). \end{aligned} \tag{7.6}$$

Furthermore, as in the circular wave case, the wavenumber b in the $\overline{y}$-direction is $O(1)$ and we are able express it as

$$\mathrm{i}b\frac{\sin\psi}{\overline{h}_2^2}\frac{\partial\overline{h}_2}{\partial\check{x}} = -1 - \frac{1}{2}\Big(\frac{\sin\psi}{\overline{h}_2^3}\frac{\partial\overline{h}_2}{\partial\check{x}}\frac{\partial\overline{h}_2}{\partial\overline{y}} + \frac{\sin\psi}{\overline{h}_1^2\overline{h}_2}\frac{\partial\overline{h}_1}{\partial\check{x}}\frac{\partial\overline{h}_1}{\partial\overline{y}}\Big) \tag{7.7}$$

in order to account for the additional perturbation terms in (2) in the Appendix. Again, we argue that from (7.5) only real values of K result in acceptable solutions to the stability equations. These occur in regions where the right-hand side of (7.5) is negative and has its greatest magnitude. After re-scaling the eigenvalue in the form $\overline{\lambda} = \lambda\overline{h}_1^4(1 + \check{x}\cos\phi - \overline{y}\sin\phi)$, we obtain the leading order eigenvalue estimate in the form

$$\overline{\lambda}_0 = -\frac{1}{\Big[(\tilde{V}\cos\phi + 1)\frac{\partial\tilde{V}}{\partial\eta}\Big]_{min}}, \tag{7.8}$$

where the minimum value of the denominator occurs at the wall where $\eta = 0$. Hence, our analysis is consistent with the assumptions we have made earlier with the vortex activity being located at the wall. This is seen in figure 7.1, where the minimum value of $(\tilde{V}\cos\phi + 1)\frac{\partial\tilde{V}}{\partial\eta}$ occurs at the wall in the range of small wave angles, which correspond to our slender cone parameter regime of $\psi = 15° - 45°$. In order to calculate this quantity for the leading order eigenvalue estimate, we note that $\tilde{V}(0) = 0$ for all of the observed waveangles (see figure 5.3). Therefore, we are required to evaluate $\frac{\partial \tilde{V}}{\partial \eta}(0)$ for varying ϕ. A plot of this quantity is shown in figure 7.2, with its magnitude decreasing as ϕ is increased. Hence, our leading order eigenvalue estimate will increase in magnitude as the waveangle ϕ, or equivalently the cone half-angle ψ, is increased. Finally, we notice that in the case where $\phi = 0°$ and $\psi = 15°$, we recover the circular wave results of §6, with $\overline{\lambda}_0 = 1.6236$.

7.2 First order solution

We now proceed to investigate the asymptotic structure of the modified scaled Taylor number in the spiral wave problem, $\overline{T} = T\overline{h}_1^4(1 + \check{x}\cos\phi - \overline{y}\sin\phi)$. Here, we apply the differential operator $(\epsilon^2\partial^2/\partial\varphi^2 - 1)$ to (3) and use equation (2) to simplify by eliminating relevant terms in $\tilde{v}$, which leads to (8) in the Appendix, subject to the boundary conditions

$$\tilde{w} = \frac{\partial^2 \tilde{w}}{\partial \varphi^2} = \frac{\partial}{\partial \varphi}\Big(\epsilon^2 \frac{\partial^2}{\partial \varphi^2} - 1\Big)\tilde{w} = 0, \quad \varphi = 0, \infty. \tag{7.9}$$

As in §6, the second and third boundary conditions arise due to the differential operation $(\epsilon^2\partial^2/\partial\varphi^2 - 1)$, which we applied earlier to the equation (3) in the Appendix. We apply this operation to the normal perturbation $\tilde{w}$, noting that $\tilde{w} = 0$ at $\varphi = 0, \infty$ to obtain the second boundary condition. Subsequently, we apply the same operation to the normal perturbation gradient $\partial\tilde{w}/\partial\varphi$ to obtain the third boundary condition.

We proceed in a similar direction to the analysis of circular waves in §6, but make appropriate modifications to account for the spiral nature of the vortices. Furthermore, we also note that the nature of our asymptotic analysis assumes ϕ is small, as we have used $\sin^2\phi \ll \cos^2\phi$. We expand the Taylor number in the form

$$T = \epsilon^{-4}(\lambda_0 + \lambda_1\epsilon^{\frac{2}{3}} + \ldots) \tag{7.10}$$

followed by the re-scaled normal variable based on the thickness established by Hall [14] for the Taylor problem

$$\xi = \frac{\varphi}{3^{\frac{1}{3}}\epsilon^{\frac{2}{3}}}. \tag{7.11}$$

We subsequently expand the normal perturbation velocity as

$$\tilde{w} = w_0(\xi) + \epsilon^{\frac{2}{3}} w_1(\xi) + \dots, \tag{7.12}$$

with $\tilde{u} = O(1)$ and $\tilde{v} = O(\epsilon^2)$ as previously in the special case above. After substituting these expressions into (8) in the Appendix, we use the condition $\tilde{V}(0) = 0$ and (7.7) to eliminate additional perturbation terms. Now, we equate terms of $O(\epsilon^{\frac{2}{3}})$, noticing that we may write terms in φ in terms of ϵ and ξ, which leads to

$$\frac{\partial^2 w_0}{\partial \xi^2} + \xi\Big(\frac{\tilde{V}''(0)}{\tilde{V}'(0)} + \tilde{V}'(0)\cos\phi\Big)w_0 - \lambda_1 \overline{h}_1^{4}(1 + \check{x}\cos\phi - \overline{y}\sin\phi)3^{-\frac{1}{3}}\tilde{V}'(0)w_0 = 0, \tag{7.13}$$

where $'$ denotes differentiation of the shifted basic flow terms with respect to their argument η. The solution of this equation, which remains bounded as $\xi \to \infty$ is given by

$$w_0 = C\mathrm{Ai}\left(\zeta - \lambda_1 \overline{h}_1^{4}(1 + \check{x}\cos\phi - \overline{y}\sin\phi)\frac{3^{-\frac{1}{3}}\tilde{V}'(0)}{\left[\frac{\tilde{V}''(0)}{\tilde{V}'(0)} + \tilde{V}'(0)\cos\phi\right]^2}\right), \tag{7.14}$$

where C is an arbitrary constant and

$$\zeta = \xi\Big(-\Big[\frac{\tilde{V}''(0)}{\tilde{V}'(0)} + \tilde{V}'(0)\cos\phi\Big]^{-1}\Big). \tag{7.15}$$

Now, as this solution does not satisfy the boundary condition at $\varphi = 0$, we seek the solution in an interior layer embedded inside the $\epsilon^{\frac{2}{3}}$ layer, which is of thickness ϵ. We define the inner variable Y as

$$Y = \frac{\varphi}{\epsilon}, \tag{7.16}$$

and expand the normal velocity $\tilde{w}$ as

$$\tilde{w} = \epsilon^{\frac{1}{3}} W_0(Y) + \epsilon^{\frac{2}{3}} W_1(Y) + \dots. \tag{7.17}$$

As in §6, we substitute this expression into (8) in the Appendix and equate terms of $O(\epsilon^{\frac{1}{3}})$, which reduces to

$$\left(\frac{\mathrm{d}^2}{\mathrm{d}Y^2} - 1\right)^3 W_0 = -W_0, \tag{7.18}$$

subject to the boundary conditions

$$W_0 = \frac{\mathrm{d}^2 W_0}{\mathrm{d}Y^2} = \frac{\mathrm{d}^3 W_0}{\mathrm{d}Y^3} - \frac{\mathrm{d}W_0}{\mathrm{d}Y} = 0, \quad Y = 0. \tag{7.19}$$

As previously in §6, we notice the second and third boundary conditions arise due to the differential operation $(\epsilon^2 \partial^2/\partial\varphi^2 - 1)$, which has been applied earlier to the equation (3) in the Appendix. The normal perturbation W_0 is used, noting that $W_0(0) = 0$ to obtain the second boundary condition. We then apply the same operation to the normal perturbation gradient $\mathrm{d}W_0/\mathrm{d}Y$ to obtain the third boundary condition.

We have solved this problem in §6 and the bounded solution has the form given in (6.16). However, for large Y, $W_0 \sim Y$, and so we match with our new outer boundary-layer solution for w_0 leading to the condition

$$\mathrm{Ai}\left(- \frac{\lambda_1 \overline{h}_1^{-4} (1 + \check{x} \cos\phi - \overline{y} \sin\phi) 3^{-\frac{1}{3}} \tilde{V}'(0)}{\left[\frac{\tilde{V}''(0)}{\tilde{V}'(0)} + \tilde{V}'(0) \cos\phi\right]^2} \right) = 0. \tag{7.20}$$

Hence, the first order estimate of our Taylor number eigenvalue is given by

$$\overline{\lambda}_1 = \frac{2.3381 \times 3^{\frac{1}{3}}}{|\tilde{V}'(0)|}\Big[\frac{\tilde{V}''(0)}{\tilde{V}'(0)} + \tilde{V}'(0)\cos\phi\Big]^2. \tag{7.21}$$

As previously, we obtain an infinite sequence of eigenvalues $\{\lambda_{1n}\}$, corresponding to the zeros of the Airy function on the negative real axis. After noting that $\tilde{V}(0) = 0$ in the spiral wave problem, the most dangerous instability mode has a modified Taylor number expansion given by

$$\begin{aligned} \overline{T} &= T\overline{h}_1^{-4}(1 + \check{x}\cos\phi - \overline{y}\sin\phi) \\ &= \epsilon^{-4}\Big(\frac{1}{|\tilde{V}'(0)|} + \frac{2.3381 \times 3^{\frac{1}{3}}\epsilon^{\frac{2}{3}}}{|\tilde{V}'(0)|}\Big[\frac{\tilde{V}''(0)}{\tilde{V}'(0)} + \tilde{V}'(0)\cos\phi\Big]^2 + \ldots\Big). \end{aligned} \tag{7.22}$$

For large n, the eigenvalues may be approximated by

$$2\Big(\frac{\overline{\lambda}_{1n}}{3|\tilde{V}'(0)|^3}\Big[\frac{\tilde{V}''(0)}{\tilde{V}'(0)} + \tilde{V}'(0)\cos\phi\Big]^6\Big)^{\frac{3}{2}} \sim \pi(n - \frac{1}{4}), \tag{7.23}$$

and so the re-scaled still fluid spiral wave Taylor number estimate has the form

$$\begin{aligned} \overline{T}_n &= T\overline{h}_1^{-4}(1 + \check{x}\cos\phi - \overline{y}\sin\phi), \\ &= \epsilon^{-4}\left[\frac{1}{|\tilde{V}'(0)|} + 3\left(\frac{\epsilon|\tilde{V}'(0)|^3}{\Big[\frac{\tilde{V}''(0)}{\tilde{V}'(0)} + \tilde{V}'(0)\cos\phi\Big]^6}\frac{\pi}{2}(n - \frac{1}{4})\right)^{\frac{2}{3}} + \ldots\right]. \end{aligned} \tag{7.24}$$

7.3 Results and physical interpretation

Estimates of the leading order and first order eigenvalues corresponding to the modified Taylor number developed in the previous two subsections are shown in table 7.1. We have presented results in the parameter regime $\psi = 15° - 45°$, using both experimental (ψ_E) and theoretical (ψ_T) cone half-angle data referenced from Kobayashi & Izumi [26] for the

ψ	ϕ	$\overline{\lambda}_0$	$\overline{\lambda}_1$
$\psi_E = \psi_T = 15°$	0°	1.6236	2.0769
$\psi_E = 30°$	1°	1.6477	1.8567
	2°	1.6731	1.6389
$\psi_T = 30°$	2.7°	1.6915	1.4887
	4°	1.7277	1.2162
	5°	1.7572	1.0146
	6°	1.7883	0.8221
	8°	1.8556	0.4747
$\psi_T = 45$	8.5°	1.8735	0.3979
$\psi_E = 45$	10°	1.9305	0.1991

Table 7.1: Leading order and first order eigenvalue estimates of the Taylor number, $\overline{\lambda}_0, \overline{\lambda}_1$, for a range of slender rotating cones in still fluid.

respective waveangles, as well as some intermediate values of ϕ.

Importantly, we notice from the data of Kobayashi & Izumi [26] that for a wide range of slender cone half-angles, such as $\psi = 15° - 30°$, there is almost no variation in the waveangle, which changes by $1-2°$ or so. Therefore, the assumption we have made in our analysis of $\sin^{\phi} \ll \cos^2\phi$ is acceptable in this region. Furthermore, the condition holds reasonably well for less slender cones, such as $\psi = 30° - 45°$. A logarithmic plot of the scaled effective Taylor number for spiral waves in still fluid is shown for a range of slender cone half-angles in figure 7.3. As the cone half-angle is increased, we see that although there is a small increase in the leading order estimate, the reduction in the first order term results in an overall decrease in the asymptotic neutral curve. There is a smooth change in the Taylor number for varying cone half-angles. We have presented results for $\phi = 0° - 10°$ in increments of 2.5°.

Physically, we claim that the most stable case in the underlying centrifugal instability, which governs the flow for slender cones, is the circular wave case of $\psi = 15°$ or less. Firstly, as the cone half-angle is increased from this critical value, we see from the

1

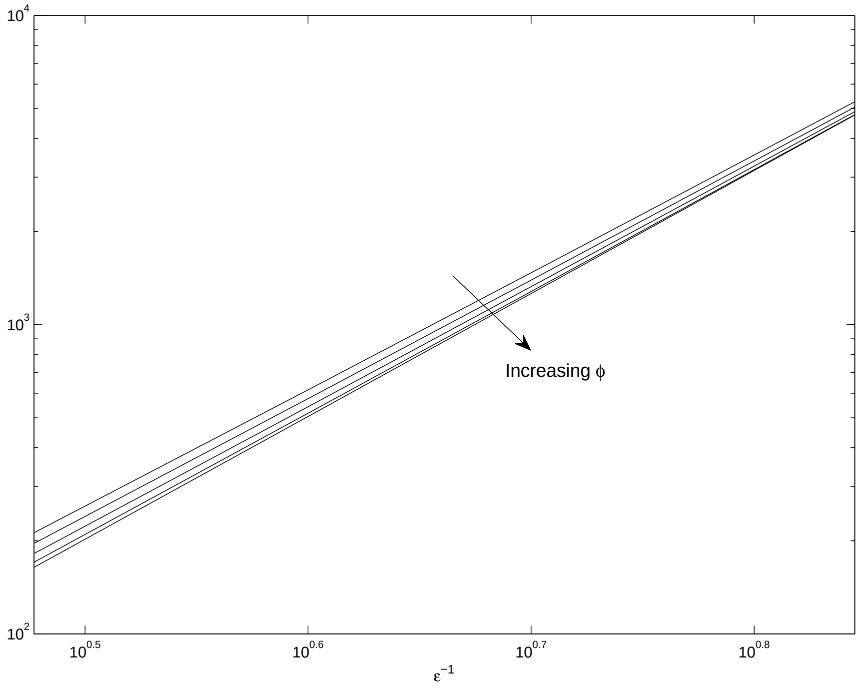

Figure 7.3: Scaled effective asymptotic Taylor number $\overline{T}$ as a function of non-dimensional vortex wavenumber ϵ^{-1} for $\psi = 15^\circ - 45^\circ, \phi = 0^\circ - 10^\circ$ in increments of 2.5°.

experiments of Kobayashi & Izumi [26] that the vortices develop in a spiral nature and eventually exhibit growth in the negative $\overline{y}$-direction. In contrast, the case of $\psi = 15^\circ$ exhibits only circular waves, which do not appear to grow azimuthally. Furthermore, our Taylor number neutral curves in figure 7.3 show that the circular wave case of $\psi = 15^\circ$ results in more stable flow by minimising the unstable region above the neutral curve. Therefore, we conclude that decreasing the cone half-angle, or equivalently the waveangle, results in the centrifugal instability approaching its most stable flow conditions. Qualitatively, this is similar to the extreme case of $\psi = 90^\circ$ resulting in the most stable flow setup for the crossflow instability studied previously for wider cones. As ψ is decreased from such a large value, there is a gradual and continuous change in the underlying governing instability, with the centrifugal effect of the mean flow beginning to dominate. This has been observed by Kobayashi & Izumi [26] in their experiments, where it was found there was a continuous change from co-rotating to counter-rotating vortices as the cone half-angle was reduced. Once ψ reaches the circular wave arrangement and ϕ reduces to zero, it is not possible to further stabilise the flow through the centrifugal forcing of the mean flow alone. Hence, this critical value of $\psi = 15^\circ$ leads to the most stable slender cone flow arrangement in still fluid. It is observed by Kobayashi [24] that for cone half-angles $\psi > 15^\circ$ the 'Taylor-vortex-like counter rotating pairs of vortices' eventually lead to the existence of co-rotating vortices. Indeed, they find that for a cone with $\psi = 30^\circ$, both co-rotating and counter-rotating vortices coexist on the surface. Hence, we propose that there may not exist a specific critical cone half-angle where the change of instabilities occurs. Instead, this change is a gradual continuous change from one dominant instability to the next.

Chapter 8

Neutral modes for axial flow (case C: circular and spiral waves)

8.1 Leading order solution

We now turn our attention to the case of a slender rotating cone in axial flow. Numerical and experimental studies by Kobayashi [23] and Kobayashi *et al.* [25] have been conducted for a 15° cone in a range of axial flow strengths. Their results show the existence of both spiral and circular waves for different values of the rotational flow parameter, s. We shall begin by considering the more general case of spiral waves and extend the analysis of §7 accordingly by taking into account modifications to the basic flow quantities. Subsequently, we shall treat $\phi = 0^\circ$ as a special case of this model, recovering the circular wave setup. Firstly, the governing Taylor number for the axial flow problem has the form

$$T = \frac{2\cot\psi\cos\phi}{\sin^4\psi}. \tag{8.1}$$

Following §§6 and 7, we develop a WKB solution for small values of our expansion parameter ϵ, corresponding to $\epsilon \to 0$. We again find a dominant balance if we scale $T \sim \epsilon^{-4}$

and $W/V \sim O(\epsilon^{-2})$, leading to

$$\begin{aligned} \tilde{u} &= E(u_0(\eta) + \epsilon u_1(\eta) + \epsilon^2 u_2(\eta) + \ldots), \\ \tilde{v} &= \epsilon^2 E(v_0(\eta) + \epsilon v_1(\eta) + \epsilon^2 v_2(\eta) + \ldots), \\ \tilde{w} &= E(w_0(\eta) + \epsilon w_1(\eta) + \epsilon^2 w_2(\eta) + \ldots), \\ T &= \epsilon^{-4}(\lambda_0 + \lambda_1 \epsilon + \lambda_2 \epsilon^2 + \ldots), \end{aligned} \tag{8.2}$$

where $\lambda = \lambda_0 + \lambda_1 \epsilon + \lambda_2 \epsilon^2 + \ldots$,

$$E = \exp \frac{\mathrm{i}}{\epsilon} \int^{\varphi} K(\tau) \mathrm{d}\tau, \tag{8.3}$$

and

$$\varphi = \frac{\sin \psi}{\overline{h}_1} \eta \tag{8.4}$$

We now substitute the above expressions into (5),(6) in the Appendix. Furthermore, in the problem of a slender cone, we are investigating $\psi = 15^\circ$ and a varying axial flow strength with $s \geqslant 3$. The resulting waveangle in this parameter regime is small and from the results of Kobayashi *et al.* [25], $\phi = 0^\circ - 13.6^\circ$. Hence, we are able to make use of the assumption $\sin^2 \phi \ll \cos^2 \phi$ in (6) in the Appendix and neglect terms containing $\sin^2 \phi$ accordingly. Upon equating terms of $O(\epsilon^2)$ and $O(1)$ respectively, and making use of (4), we arrive at the following eigenrelation at leading order

$$(K^2 + 1)^3 = -\lambda_0 \overline{h}_1^4 \frac{\partial \overline{V}}{\partial \eta}(\check{x}, \overline{y}, 0). \tag{8.5}$$

As in §§6 and 7, we identify that for small ϕ, the vortex activity will be located at the wall, so $\eta = O(\epsilon)$, and hence we write $\eta = \epsilon \xi$. Therefore, the term in (6) in the Appendix,

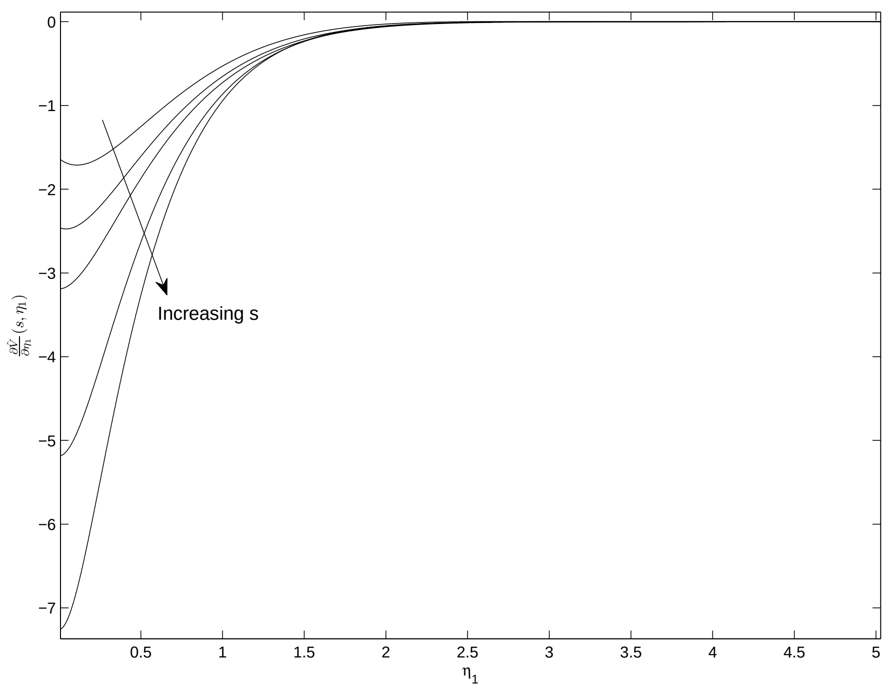

Figure 8.1: Plots of $\frac{\partial \widehat{V}}{\partial \eta_1}(s, \eta_1)$ for a slender rotating cone with $\psi = 15°, s = 3, 4, 5, 10, 16$.

which remains containing a factor of $\overline{h}_2$ in the denominator will be of $O(\epsilon)$, and so is too small at leading order.

Next, we account for the additional perturbation terms in (5) in the Appendix by expressing the $O(1)$ wavenumber b in the $\overline{y}$-direction as

$$\mathrm{i}b\frac{\sin\psi}{\overline{h}_2^2}\frac{\partial \overline{h}_2}{\partial \check{x}} = -1 - \frac{1}{2}\Big(\frac{\sin\psi}{\overline{h}_2^3}\frac{\partial \overline{h}_2}{\partial \check{x}}\frac{\partial \overline{h}_2}{\partial \overline{y}} + \frac{\sin\psi}{\overline{h}_1^2\overline{h}_2}\frac{\partial \overline{h}_1}{\partial \check{x}}\frac{\partial \overline{h}_1}{\partial \overline{y}}\Big). \tag{8.6}$$

Now, as we have already expanded the basic flow terms in the right-hand side of (8.5), our solutions for K become restricted accordingly. However, we require real solutions and so the right-hand side must be negative, which we see is the case from figure 8.1. Therefore, we may proceed to re-write the eigenvalue as

$$\overline{\lambda} = \lambda \overline{h}_1^{4} \frac{\overline{U}_e^*}{\Omega^* l^* \sin\psi} \tag{8.7}$$

and obtain the leading order eigenvalue estimate in the form

$$\overline{\lambda}_0 = -\frac{1}{\left(\frac{m+3}{2s^{\frac{1}{2}}}\right)^{\frac{1}{2}} \frac{\partial \widehat{V}}{\partial \eta_1}(s,0)}, \tag{8.8}$$

where we evaluate the basic flow term at the wall where $\eta = 0$. Figure 8.1 shows our analysis is consistent with the assumptions we have made earlier in §5.3, with the vortex activity being located at the wall. This is the case for the curves $s = 5, 10, 16$. However, for $s = 3, 4$, the curve has a minimum slightly departed from the wall. In this case, the turning point giving the location of vortex activity will not be located at the wall, but to obtain valid real solutions for K we still require

$$\overline{\lambda}_0 > -\frac{1}{\left[\left(\frac{m+3}{2s^{\frac{1}{2}}}\right)^{\frac{1}{2}} \frac{\partial \widehat{V}}{\partial \eta_1}\right]_{min}}, \tag{8.9}$$

which holds for $s = 3, 4$. The exception is that the solutions we obtain are not the most dangerous modes available. Nevertheless, we shall take account of these modes for $s = 3, 4$, as they provide information and results for non-zero waveangles (spiral waves) for a 15° cone in axial flow. Furthermore, the inclusion of results for $s = 3$ will prove useful later in §8.3 where we shall develop comparisons with the numerical results of Kobayashi [23], who has used the parameters $\psi = 15°, s = 3$ to construct a neutral stability curve.

Finally, we notice from figure 8.1 that the magnitude of $\frac{\partial \widehat{V}}{\partial \eta_1}(s, 0)$ increases as s increases. Hence, our leading order eigenvalue estimate in axial flow will decrease in magnitude as s is increased.

8.2 First order solution

For the first order problem in axial flow we use a similar formulation to §7.2 but write the modified Taylor number as

$$\overline{T} = T\overline{h}_1^{4}\frac{\overline{U}_e^*}{\Omega^* l^* \sin\psi}. \tag{8.10}$$

We now apply the differential operator $(\epsilon^2\partial^2/\partial\varphi^2 - 1)$ to (6) in the Appendix and use (5) from the Appendix to substitute for terms in $\tilde{v}$ to obtain (9) in the Appendix, subject to the boundary conditions

$$\tilde{w} = \frac{\partial^2\tilde{w}}{\partial\varphi^2} = \frac{\partial}{\partial\varphi}\Big(\epsilon^2\frac{\partial^2}{\partial\varphi^2} - 1\Big)\tilde{w} = 0, \quad \varphi = 0, \infty. \tag{8.11}$$

Once more following §§6 and 7, taking into account changes to the basic flow terms in the case of axial flow, we are able to develop an asymptotic expansion of this equation. We again assume ϕ is small. Indeed, at most $\phi = 15°$ for a $15°$ cone when $s = 3$. Hence, we may apply the condition $\sin^2\phi \ll \cos^2\phi$ to neglect certain terms. We expand the Taylor number as

$$T = \epsilon^{-4}(\lambda_0 + \lambda_1\epsilon^{\frac{2}{3}} + \dots) \tag{8.12}$$

with the re-scaled normal variable

$$\xi = \frac{\varphi}{3^{\frac{1}{3}}\epsilon^{\frac{2}{3}}}. \tag{8.13}$$

The normal perturbation velocity expands as

$$\tilde{w} = w_0(\xi) + \epsilon^{\frac{2}{3}}w_1(\xi) + \dots, \tag{8.14}$$

with $\tilde{u} = O(1)$ and $\tilde{v} = O(\epsilon^2)$ as previously in the special case above. After substituting these expressions into (9) from the Appendix, we use the condition (8.6) to eliminate additional perturbation terms. Next, we equate terms of $O(\epsilon^{\frac{2}{3}})$, noticing that we may write terms in φ in terms of ϵ and ξ, which leads to

$$\frac{\partial^2 w_0}{\partial\xi^2} + \xi\left(\frac{\frac{\partial^2\overline{V}}{\partial\eta^2}(\check{x},\overline{y},0)}{\frac{\partial\overline{V}}{\partial\eta}(\check{x},\overline{y},0)} + \frac{\partial\overline{V}}{\partial\eta}(\check{x},\overline{y},0)\cos\phi\right)w_0 - \lambda_1\overline{h}_1^4 3^{-\frac{1}{3}}\tilde{V}'(0)w_0 = 0, \tag{8.15}$$

where we have used the relation (8.4) and $\sin^2\phi \ll \cos^2\phi$ to re-write

$$\begin{aligned} \frac{\sin\psi}{\overline{h}_2}\eta &= \frac{\overline{h}_1}{\overline{h}_2} \\ &= 1 + O(\epsilon). \end{aligned} \tag{8.16}$$

The solution of this equation, which remains bounded as $\xi \to \infty$ is given by

$$w_0 = C\mathrm{Ai}\left(\zeta - \frac{\lambda_1\overline{h}_1^4 \times 3^{-\frac{1}{3}}\frac{\partial\overline{V}}{\partial\eta}(\check{x},\overline{y},0)}{\left[\frac{\frac{\partial^2\overline{V}}{\partial\eta^2}(\check{x},\overline{y},0)}{\frac{\partial\overline{V}}{\partial\eta}(\check{x},\overline{y},0)} + \frac{\partial\overline{V}}{\partial\eta}(\check{x},\overline{y},0)\cos\phi\right]^2}\right), \tag{8.17}$$

where C is an arbitrary constant and

$$\zeta = \xi\Big(- \Big[\frac{\frac{\partial^2\overline{V}}{\partial\eta^2}(\check{x},\overline{y},0)}{\frac{\partial\overline{V}}{\partial\eta}(\check{x},\overline{y},0)} + \frac{\partial\overline{V}}{\partial\eta}(\check{x},\overline{y},0)\cos\phi\Big]^{-1}\Big). \tag{8.18}$$

To satisfy the boundary condition at $\varphi = 0$, we seek the solution in an interior layer embedded inside the $\epsilon^{\frac{2}{3}}$ layer, which is of thickness ϵ. As in §§6 and 7, we define the inner variable Y in the form

$$Y = \frac{\varphi}{\epsilon}, \tag{8.19}$$

and expand the normal velocity $\tilde{w}$ as

$$\tilde{w} = \epsilon^{\frac{1}{3}} W_0(Y) + \epsilon^{\frac{2}{3}} W_1(Y) + \dots . \tag{8.20}$$

As previously, the bounded solution has the form given in (6.16). However, for large Y, $W_0 \sim Y$, and we match with outer boundary-layer solution in axial flow for w_0 resulting in the relation

$$\mathrm{Ai}\left(- \frac{\lambda_1 \overline{h}_1^{4} \times 3^{-\frac{1}{3}} \frac{\partial \overline{V}}{\partial \eta}(\check{x}, \overline{y}, 0)}{\left[\frac{\frac{\partial^2 \overline{V}}{\partial \eta^2}(\check{x},\overline{y},0)}{\frac{\partial \overline{V}}{\partial \eta}(\check{x},\overline{y},0)} + \frac{\partial \overline{V}}{\partial \eta}(\check{x}, \overline{y}, 0) \cos\phi \right]^2} \right) = 0. \tag{8.21}$$

Therefore, the first order Taylor number eigenvalue estimate is given by

$$\begin{aligned} \overline{\lambda}_1 &= \frac{2.3381 \times 3^{\frac{1}{3}}}{\left|\frac{\partial \overline{V}}{\partial \eta}(\check{x}, \overline{y}, 0)\right|} \frac{\overline{U}_e^*}{\Omega^* l^* \sin\psi} \left[\frac{\frac{\partial^2 \overline{V}}{\partial \eta^2}(\check{x}, \overline{y}, 0)}{\frac{\partial \overline{V}}{\partial \eta}(\check{x}, \overline{y}, 0)} + \frac{\partial \overline{V}}{\partial \eta}(\check{x}, \overline{y}, 0) \cos\phi \right]^2 . \\ &= \frac{2.3381 \times 3^{\frac{1}{3}} \left(\frac{m+3}{2 s^{\frac{1}{2}}} \right)^{\frac{1}{2}}}{\left|\frac{\partial \widehat{V}}{\partial \eta_1}(s, 0)\right|} \left[\frac{\frac{\partial^2 \widehat{V}}{\partial \eta_1^2}(s, 0)}{\frac{\partial \widehat{V}}{\partial \eta_1}(s, 0)} + s^{-\frac{1}{2}} \frac{\partial \widehat{V}}{\partial \eta_1}(s, 0) \cos\phi \right]^2 , \end{aligned} \tag{8.22}$$

where we have substituted the basic flow quantities from (5.50). For a cone of half-angle 15°, we have $m = 0.03927$. The infinite sequence of eigenvalues corresponding to the zeros of the Airy function on the negative real axis are given by $\{\lambda_{1n}\}$. Hence, the modified

Taylor number expansion may be written as

$$\begin{aligned}
\overline{T} &= T\overline{h}_1^{-4}\frac{\overline{U}_e^*}{\Omega^* l^* \sin\psi}, \\
&= \epsilon^{-4}\frac{\overline{U}_e^*}{\Omega^* l^* \sin\psi}\left(\frac{1}{|\frac{\partial\overline{V}}{\partial\eta}(\check{x},\overline{y},0)|} + \frac{2.3381\times 3^{\frac{1}{3}}\epsilon^{\frac{2}{3}}}{|\frac{\partial\overline{V}}{\partial\eta}(\check{x},\overline{y},0)|}\left[\frac{\frac{\partial^2\overline{V}}{\partial\eta^2}(\check{x},\overline{y},0)}{\frac{\partial\overline{V}}{\partial\eta}(\check{x},\overline{y},0)} + \frac{\partial\overline{V}}{\partial\eta}(\check{x},\overline{y},0)\cos\phi\right]^2 + \dots\right), \\
&= \epsilon^{-4}\left(\frac{1}{\left(\frac{m+3}{2s^{\frac{1}{2}}}\right)^{\frac{1}{2}}|\frac{\partial\widehat{V}}{\partial\eta_1}(s,0)|}\right. \\
&+ \left.\frac{2.3381\times 3^{\frac{1}{3}}\left(\frac{m+3}{2s^{\frac{1}{2}}}\right)^{\frac{1}{2}}\epsilon^{\frac{2}{3}}}{|\frac{\partial\widehat{V}}{\partial\eta_1}(s,0)|}\left[\frac{\frac{\partial^2\widehat{V}}{\partial\eta_1^2}(s,0)}{\frac{\partial\widehat{V}}{\partial\eta_1}(s,0)} + s^{-\frac{1}{2}}\frac{\partial\widehat{V}}{\partial\eta_1}(s,0)\cos\phi\right]^2 + \dots\right).
\end{aligned} \tag{8.23}$$

For large n, it is possible to write the eigenvalues as

$$2\left(\frac{\overline{\lambda}_{1n}\left(\frac{m+3}{2s^{\frac{1}{2}}}\right)^{\frac{3}{2}}}{3|\frac{\partial\widehat{V}}{\partial\eta_1}(s,0)|^3}\left[\frac{\frac{\partial^2\widehat{V}}{\partial\eta_1^2}(s,0)}{\frac{\partial\widehat{V}}{\partial\eta_1}(s,0)} + s^{-\frac{1}{2}}\frac{\partial\widehat{V}}{\partial\eta_1}(s,0)\cos\phi\right]^6\right)^{\frac{3}{2}} \sim \pi(n-\frac{1}{4}), \tag{8.24}$$

and so the re-scaled Taylor number estimate for a slender cone in axial flow has the form

$$\begin{aligned}
\overline{T}_n &= T\overline{h}_1^{-4}\frac{\overline{U}_e^*}{\Omega^* l^* \sin\psi}, \\
&= \epsilon^{-4}\left[\frac{1}{\left(\frac{m+3}{2s^{\frac{1}{2}}}\right)^{\frac{1}{2}}|\frac{\partial\widehat{V}}{\partial\eta_1}(s,0)|}\right. \\
&+ \left. 3\left(\frac{\epsilon|\frac{\partial\widehat{V}}{\partial\eta_1}(s,0)|^3}{\left(\frac{m+3}{2s^{\frac{1}{2}}}\right)^{\frac{3}{2}}\left[\frac{\frac{\partial^2\widehat{V}}{\partial\eta_1^2}(s,0)}{\frac{\partial\widehat{V}}{\partial\eta_1}(s,0)} + s^{-\frac{1}{2}}\frac{\partial\widehat{V}}{\partial\eta_1}(s,0)\cos\phi\right]^6}\frac{\pi}{2}(n-\frac{1}{4})\right)^{\frac{2}{3}} + \dots\right].
\end{aligned} \tag{8.25}$$

8.3 Results and physical interpretation

We present results for the leading order and first order correction terms to the eigenvalue estimates for the modified Taylor number in table 8.1. The data are for a cone of half-angle $\psi = 15^\circ$ in a range of axial flows, where the values for ϕ have been adapted from the study of Kobayashi *et al.* [25]. We vary s from 3 to 16, where beyond $s = 5$, the waveangle reduces to $\phi = 0^\circ$. Our results are plotted in figure 8.2, where we observe that as s is increased, the most noticeable stabilisation occurs when $s = 5$. For this critical value, where the waveangle first reaches $\phi = 0^\circ$, the flow instability exhibits circular waves. As a result, the neutral curve increases for $s = 5$ but is subsequently shifted downwards for $s > 5$, where the vortices retain a circular wave nature. Now, as s is increased further so we reach the regime of large s, or equivalently small T_s, we approach the case of still fluid. As a result, we subsequently recover the case A result for circular waves studies in §6. Hence, for a 15° cone the introduction of an imposed oncoming axial flow of increasing strength acts to reduce the unstable region by increasing the right-hand branch of the neutral curve. The overall result is that increasing T_s or decreasing s has the effect of stabilising the flow up to the most stable value at $T_s = 0.4472$ or $s = 5$. The flow is then destabilised by reducing the Taylor number estimate through an increase in the unstable region above the right-hand branch of the neutral stability curve.

We wish to understand why the experimental observation of Kobayashi *et al.* [25] finding $s = 5$ as exhibiting circular waves, corresponds clearly to our result of $s = 5$ giving a maximum stability estimate for the modified Taylor number. Physically, for a slender cone ($\psi = 15^\circ$), the counter-rotating vortices governed by the centrifugal instability are forced further in the streamwise direction by an increasing oncoming axial flow. Vortices which result the instability being triggered are forced downstream and overall result is a more stable boundary layer flow. Once the circular waves with $\phi = 0^\circ$ are shifted and

s	T_s	ϕ	$\overline{\lambda}_0$	$\overline{\lambda}_1$
3	0.5774	13.6°	0.6288	0.0321
3	0.5774	15°	0.6531	0.0015
4	0.5	6°	0.4668	0.9470
5	0.4472	0°	0.3803	1.7922
10	0.3162	0°	0.2782	1.2277
16	0.25	0°	0.2236	0.9561

Table 8.1: Leading order and first order eigenvalue estimates of the Taylor number, $\overline{\lambda}_0, \overline{\lambda}_1$, for a 15° slender rotating cone in a range of axial flows.

not aligned with each other, causing spiral waves ($\phi > 0°$), we interpret the directions of possible growth of the counter-rotating vortices. Referring to figure 5.1, we see that for circular waves, although there is growth in the streamwise x-direction, there is no growth in the azimuthal θ-direction due to the periodicity of the flow instability in this direction. Once these circular waves shift to spiral waves, the boundary layer instability generates vortices, which are susceptible to growth in both of the logarithmic spiral directions, namely $\widehat{x}$ as well as the negative y-direction. Hence, spiral vortices will exhibit stronger boundary layer growth overall than circular waves.

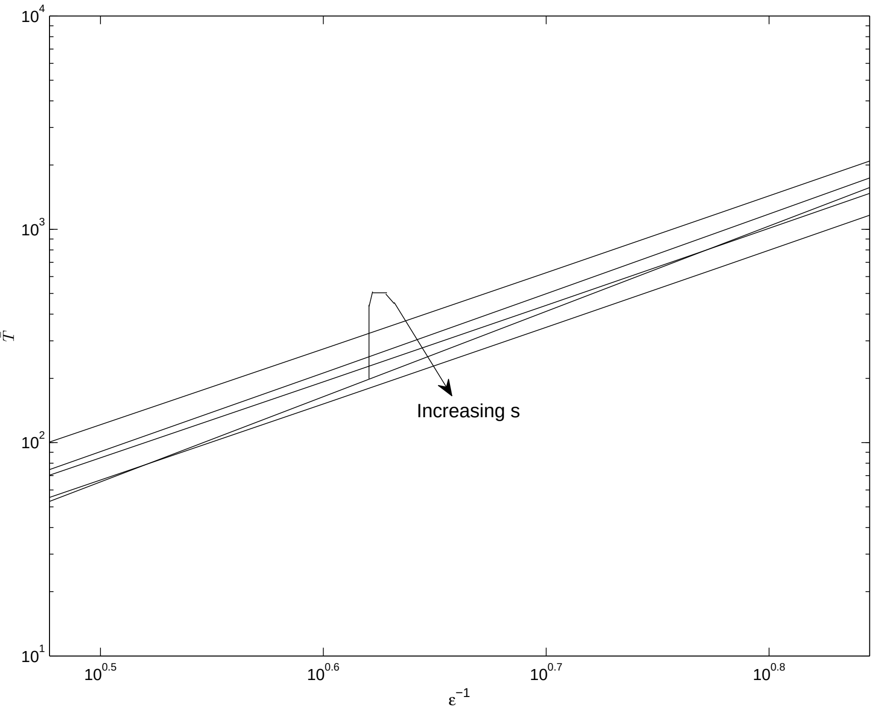

Figure 8.2: Scaled effective asymptotic Taylor number $\overline{T}$ as a function of non-dimensional vortex wavenumber ϵ^{-1} for $\psi = 15°, s = 3, 4, 5$ (uppermost curve), $10, 16$ and $\phi = 13.6°, 6°, 0°, 0°, 0°$.

Chapter 9

Conclusions

This thesis comprises separate stability analyses of three physically different problems: a rotating cone or disk in still fluid, a rotating disk in axial flow and a rotating cone in axial flow, which have been investigated as case A, case B and case C, respectively. The cases A and C are further split into slender and wide angle cones, governed by the centrifugal and crossflow instabilities, respectively. In each case, we have non-dimensionalised the governing Navier-Stokes equations, introduced an appropriate similarity solution for the velocity scales and expanded the equations in terms of our pre-defined large Reynolds number, to obtain the steady basic flow equations governing flow within the boundary layer. Depending on cases A and B or case C, this leads to a fifth-order system of first-order ODEs or a fifth-order system of first-order PDEs, the solutions for which are described in §2.1, §2.2 and §2.3, respectively. We have subsequently linearised the equations about these mean flows by introducing small perturbation velocities. Following Hall [16], using inverse powers of the Reynolds number as our small expansion parameter, we have investigated the occurrence of inviscidly dominated perturbation modes away from the wall, and wall dominated perturbations, which breakdown from a viscous-Coriolis force balance, with a view to describing the spiral vortex streaks, which have been observed experimentally in the literature. The inviscid type I modes have been investigated using a Rayleigh critical layer analysis, whereas the viscous type II modes were described using a tripe-deck structure close to the wall. In each case, we have derived leading order and first order estimates for the wavenumber and waveangles associated with the spiral vortex streaks. We have presented the asymptotic neutral curves in each case for varying cone angles (ψ) and axial flow strengths parameters (T_s and s). Subsequently, for a slender cone, the right-hand branch neutral modes have been constructed using a WKB asymptotic analysis for large Reynolds number and large vortex wavenumber in both still fluid and axial flow. In these cases, we have developed leading order and first order estimates for the Taylor number governing the flow for large vortex wavenumber. Throughout this thesis, it has been our overall aim to describe where the asymptotic results we have obtained link into existing studies in the literature. In §9.1, we combine our results together and show some comparisons with previous experimental and theoretical measurements. Furthermore, where possible, we attempt to explain some of the underlying physical mechanisms at work. For some of the parameter ranges we have studied pertaining to the rotating disk and cone in axial flow there are currently no experimental studies available for quantitative comparison. Instead, here we shall consider the qualitative link between our results, with a view to explaining some of the general trends. Finally, in §9.2, we highlight the limitations of our current research and proceed to outline some possible extension studies, which would provide a more complete description of the body of work on the rotating cone.

9.1 Current work

We have investigated the incompressible boundary layer flow over a rotating cone and rotating disk, placed in both a still fluid and an oncoming streamwise axial flow. We now comment on the results for each of these problems in terms of comparisons with existing studies.

9.1.1 Case A: Rotating cone in still fluid

For the case of a still fluid, we have formulated the basic flow equations by non-dimensionalising lengths with the distance measured along the cone surface, l^*, which effectively scales out the cone half-angle, ψ, from the equations. Therefore, our solutions, which are effectively the von Kármán profiles for a rotating disk, are valid for a range of cone half-angles, which is of practical importance later during the stability analysis when utilising the basic flow values at the critical layer location. This is because, only one set of basic values need to be calculated, as opposed to one set for each cone half-angle. Hence, the efficiency of the overall stability calculation is increased. During the ensuing linear stability analyses, our leading order inviscid mode calculations for the critical layer location ($\overline{\eta} = 1.458$) and the Rayleigh equation eigenvalue ($\gamma_0 = 1.162$) agree closely with those of Hall [16] and, more recently, with the recently corrected estimates of Gajjar [6]. We note there is a slight discrepancy between our inviscid neutral mode wavenumber and waveangle results and those of Hall [16], which seems to arise from the different methods used to obtain the integral estimates I_1 and I_2. For I_1, we have used Simpson's rule with a fixed step of size $h = 0.0005$. We have integrated to the edge of the boundary layer thickness, which was taken to be located at $\eta = 20$, which could possibly account for the difference in I_1. Naturally, this leads to a deviation in the first order type I wavenumber and waveangle estimates. However, this deviation reduces for larger Reynolds numbers, as both estimates approach their leading order values. Comparisons of our asymptotic neutral curve calculations for both type I and type II modes show close agreement with those of Hall [16], and hence with the numerically obtained neutral curves of Malik [33] for the rotating disk. Furthermore, our asymptotic estimates in the range $\psi = 50^\circ - 90^\circ$ have shown to correspond well with the neutral curves of Garrett [7] (as well as private communication for larger Reynolds numbers). For cone angles as slender as $\psi = 20^\circ - 40^\circ$, both upper and lower branches of the spiral waveangle continue to exhibit good agreement with Garrett's calculations.

In figure 9.1, we present a comparison between our predicted inviscid mode calculations of the spiral wave angle for large Reynolds numbers for various cone half-angles and the experimental measurements and linear theory calculations of Kobayashi & Izumi [26], as well as the linear numerical measurements of Garrett [7], corresponding to critical Reynolds numbers. We have used our asymptotic results derived in (3.58), which show a close agreement with Kobayashi & Izumi [26] for moderately large cone half-angles (e.g. $\psi = 45^\circ - 90^\circ$), suggesting that the inflexional nature of the crossflow component plays an important role in the stability of the inviscid upper branch mode. However, for more slender cone half-angles, our results show a discrepancy from the observed experimental results and more closely follow the numerical convective stability analysis measurements of Garrett [7], who used a parallel flow approximation to setup the mean flow system of equations, and actually observed this discrepancy for cone angles $\psi < 50^\circ$ (see Garrett & Peake [10]). This seems understandable, as our length scalings in §3 for the inviscid stability analysis take into account the crossflow component within the boundary layer, and hence the modes we are investigating here break down from an inherent crossflow instability. The conclusions of Kobayashi & Izumi [26] stated that the spiral vortices seem to change from co-rotating to counter-rotating in nature continuously as ψ is decreased. We propose that the change depends on a toppling argument, based on how much momentum the spiral vortices carry as they are shed from the boundary layer. For slender cone half-angles, the centrifugal instability dominates and the boundary layer naturally sheds vorticity in equal and opposite directions, leading to the observed counter-rotating spiral vortices. However, as ψ is increased, the surface slope increases and the boundary layer eventually does not possess sufficient momentum to shed vorticity in both directions. In this case, all the vorticity is shed back in one direction, as the fluid falls back onto itself creating co-rotating crossflow-dominated vortices. We consider intuitively from figure 9.1

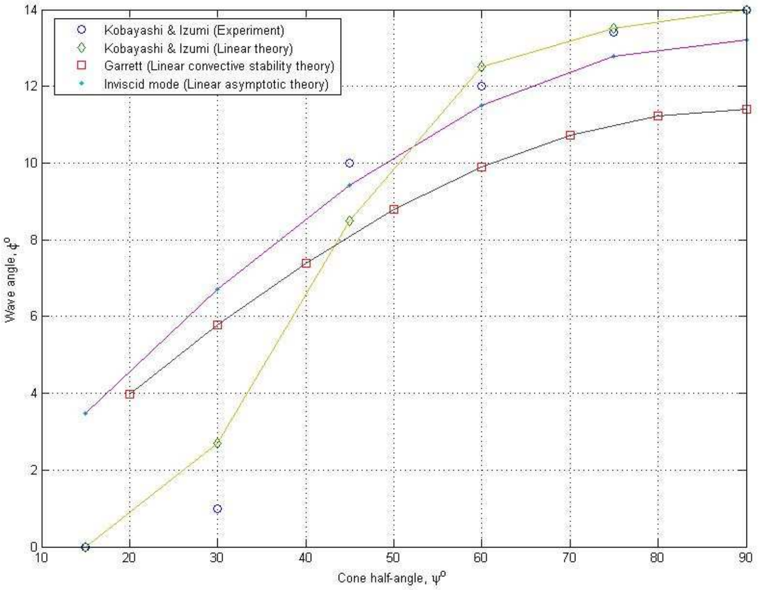

Figure 9.1: Plot comparing predicted waveangle ϕ for various cone angles ψ in still fluid with experimental/theoretical measurements of Kobayashi & Izumi [26] and Garrett [7].

that it is around the region $\psi \approx 45^\circ - 50^\circ$ where this toppling of vorticity occurs and there is a transition from the observation of counter-rotating vortices to purely co-rotating vortices.

Furthermore, the slight discrepancy between our results and those of Garrett [7] arise because his measurements are taken at the critical Reynolds numbers for the onset of convective instability modes, whereas our asymptotic results are valid for large Reynolds numbers further along the neutral curves. Nevertheless, the underlying structure of the spiral vortex modes remains unchanged, which is why they are shed at similar waveangles for increasing cone angles even at vastly differing Reynolds numbers. Indeed, the over-prediction of our waveangle estimates in relation to those of Garrett arise purely because of the larger Reynolds number of our measurements translate into a greater rotational shear velocity, Ω^*, within the boundary layer, which leads to an increase in the spiral

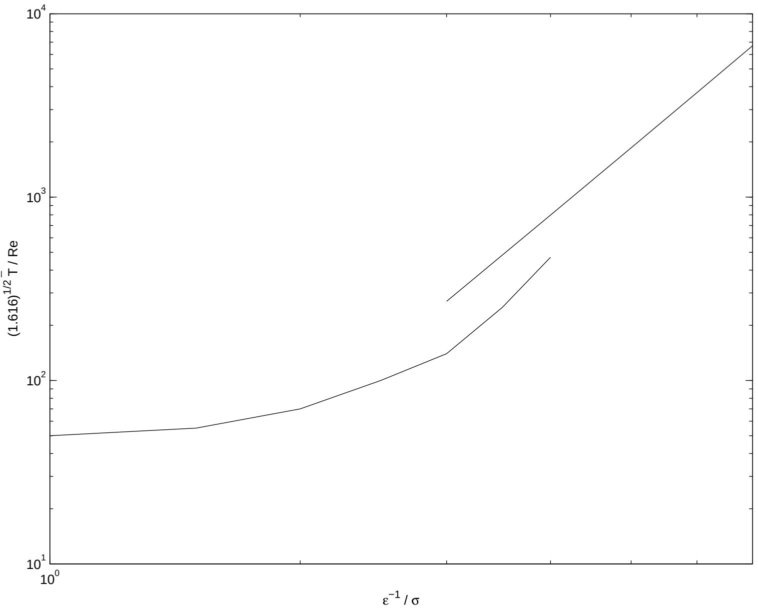

Figure 9.2: Comparison between scaled effective asymptotic Taylor number $\overline{T}$ (right) and Reynolds number Re of Kobayashi & Izumi [26] (left) against vortex wavenumbers ϵ^{-1} and σ for $\psi \leqslant 15°, \phi = 0°$.

waveangle as the vortices are shed, due to the stronger rotational shear effect of the cone. For further comparisons between our inviscid and viscous neutral mode calculations of the wavenumber and waveangle for a range of rotating cones in still fluid, and numerical neutral stability curves, the reader is referred to Garrett *et al.* [8].

In the case of a slender rotating cone in still fluid, we seek to draw a comparison between our effective Taylor number estimate and existing results in the literature. Specifically, our results are compared with the right-hand branch of the neutral curve, which has been calculated by Kobayashi & Izumi [26], in terms of the rotational Reynolds number against the vortex wavenumber, referred to as σ. Now, for slender cones we know that the boundary layer instability is visualised in terms of counter-rotating spiral vortices (see Kobayashi & Izumi [26]), which are often termed Görtler vortices. Furthermore, the study of Hall [14] shows that the Görtler number, G, which describes the governing centrifugal instability maybe written in the form

$$G = 2\mathrm{R}^{\frac{1}{2}}\delta, \tag{9.1}$$

with curvature term δ. Now, Hall [14] shows that $G = O(\epsilon^{-4})$. Our corresponding scaled effective Taylor number estimate gives $\overline{T} = O(\epsilon^{-4})$. Now, we connect the rotational Reynolds number, Re, to the conventional Reynolds number we have defined, R, using equation (8) of Kobayashi & Izumi [26] to re-write the curvature term, which leads us to the relation

$$Re = \mathrm{R}^{\frac{1}{2}}\surd(1.616). \tag{9.2}$$

As a result, we may write the rotational Reynolds number in terms of the effective Taylor number

$$Re = \overline{T}\surd(1.616). \tag{9.3}$$

This allows us to make a direct quantitative comparison between our asymptotic estimate for the scaled effective Taylor number and the numerical Reynolds number calculated by Kobayashi & Izumi [26], which is shown in figure 9.2. Here, both quantities are calculated against the spiral vortex wavenumbers, referred to as ϵ^{-1} and σ, respectively. Kobayashi's data is displayed for low Reynolds number Re and low σ, whereas our results are valid for large Taylor number and large vortex wavenumber. Now, our model employs the assumption of large Reynolds number. Hence, we see our comparisons with Kobayashi & Izumi [26], for which data exists up to $Re \sim 500$, improve as the Reynolds number increases. We conclude the current asymptotic setup closely models the right-hand branch of the neutral curve for Reynolds numbers of $O(10^4)$ and above.

9.1.2 Case B: Rotating disk in axial flow

For the case of a disk rotating in an axial flow, we have used a formulation consistent with case A, this time switching on the non-zero axial flow parameter, T_s. Mathematically, the solutions we obtain appear only to be valid convergent profiles for a rotating disk ($m = 1$). The type I and type II stability analyses have been shown to be very close in structure to the analysis for case A, with the most important change being manifested in the basic flow profiles, as a result of the introduction of a non-zero T_s. In the literature, the work of Garrett [7] provides an opportunity to compare both the type I and type II neutral curve estimates for the spiral vortex wavenumbers and waveangles in the case of axial flow onto a rotating disk. Through private communication, we have managed to observe close agreement for both wavenumber branches and the type II waveangle branch up to $T_s = 0.25$. However, the type I waveangle branch begins to develop a slight discrepancy for increasing T_s. Nevertheless, the comparisons appear to be promising for the investigated range of axial flow parameters. However, in this thesis, we present in figure 9.3 a comparison between our leading-order inviscid crossflow mode waveangle estimates at large Reynolds number and linear convective stability measurements at critical Reynolds number; the latter have been adapted from Garrett's 2002 PhD thesis [7] for a rotating disk in axial flow. As with case A, there is favourable comparison between our results across the whole axial flow parameter-range studied. We note that with increasing T_s, both studies predict that the spiral vortex waves will be shed from the boundary layer at larger waveangles to the radial vector. For further comparisons between our neutral mode wavenumber and waveangle calculations for a rotating disk in axial flow and the numerical neutral stability curves obtained by Garrett, the reader is referred to Hussain *et al.* [20].

Physically, as was mentioned previously, the stronger oncoming flow forces more fluid onto the rotating disk surface, which is entrained into the boundary layer before being swept out radially. The increased strength of the oncoming flow results in the fluid having greater energy as it enters the boundary layer, and so it carries an increased flux of energy as it is redirected into the azimuthal direction once the spiral vortices are shed. This causes the vortices to propagate along an effective velocity direction, which subtends a larger angle with the radial vector, producing a greater vortex waveangle from our definition of ϕ. Once more, we account for the slight over-prediction ($\sim 1^\circ$) of our measurements when compared with Garrett's due to the locations along the neutral curve where the calculations have been made. Garrett's results are related to the smaller critical Reynolds numbers, at the location of onset of the primary instability, whereas our calculations refer to Reynolds numbers of $O(10^6)$ and larger. The increased rotational shear velocity component of the cone surface therefore has the effect of sweeping the spiral vortices through a greater angle as they are shed from the boundary layer, leading to a larger estimate for the waveangle. However, as previously for the still fluid case, the governing instability mechanisms we have described are at work in a similar nature for both sets of results. This is further seen from the experimental studies by Kobayashi *et al.* [25] (see figure 4) and Kobayashi & Izumi [26] (see figure 8(a)), when comparing cross-sectional images of the spiral vortices for a cone in still fluid and in axial flow. Importantly, we are only able to make comparisons between their results for slender cone angles, and hence we see the counter-rotating nature of the spiral vortex pairs. A closer examination reveals that the vortices in the axial flow case are forced much more strongly in the streamwise direction, with the right vortex core is well defined and is clearly seen to roll over onto the cone surface, whereas the left vortex core appears elongated, forced towards the wall, and is only just seen to roll back onto itself to create the counter-rotating pair. In contrast, both vortex cores in the case of still fluid appear well defined and develop

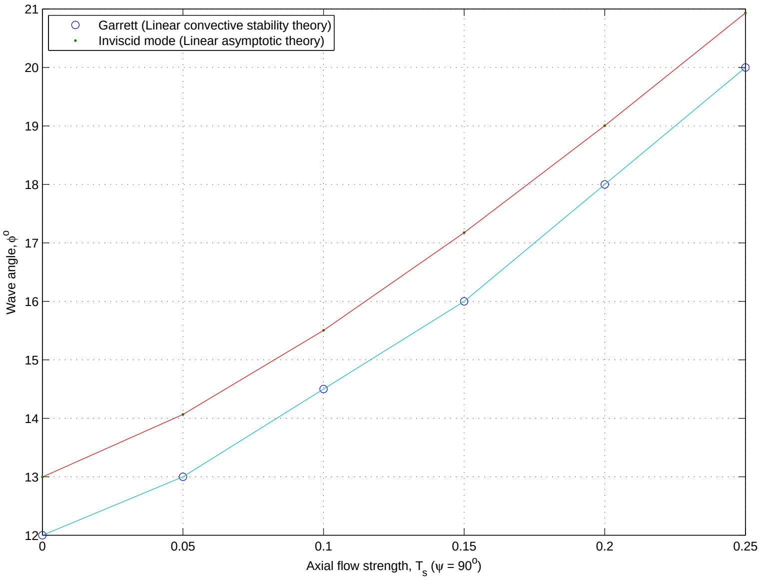

Figure 9.3: Plot comparing predicted waveangle ϕ in varying axial flow strengths T_s for a rotating disk in axial flow with theoretical measurements of Garrett [7].

over a similar length scale. These observations suggest for the rotating cone that a viscous wall-dominated streamwise instability, such as the Tollmien-Schlichting instability, is also at work, as well as the centrifugal Görtler instability. We therefore argue, in theory, that when a strong enough axial flow is introduced, this streamwise physical mechanism should also be present for the case of larger cone half-angles, namely, in this situation, for a rotating disk.

Indeed, we propose that the spiral vortices, which are radially ejected from the rotating disk boundary layer, undergo a strong forcing in the oncoming axial direction, which effectively pushes them against the disk wall. This has the result of decreasing their wavelengths and effectively increasing the numbers of vortex waves which are observed spiralling around the disk surface. This lends an explanation for the increase in both type I and type II wavenumber estimates we find for our asymptotic neutral curves when an axial flow is introduced onto a rotating disk.

9.1.3 Case C: Rotating cone in axial flow

We have investigated the more general problem of a cone rotating in an axial flow using an alternative formulation for the basic flow profiles. By converting to Mangler coordinates, followed by the use of a similarity-type transformation, we have successfully obtained convergent boundary layer profiles for a cone rotating within a varying strength axial flow. Our profiles are solved for the rotating frame case and have been found to be in good agreement with those of Koh & Price [27] for the fixed frame, taking into account the relative Coriolis terms. Furthermore, application of our basic flow solutions to wide cones may be found in the proceedings of Garrett *et al.* [9]. In terms of the type I and type II linear stability analyses for case C, we have attempted to follow the setup for case A as close as possible. Due to the stability coordinates η and x differing from the mean flow coordinates η_1 and s, we have derived relevant conditions to enable quantities relating to the basic flow to be expressed suitably in terms of the appropriate coordinates. For the inviscid type I modes, our parameter range is restricted to $s = 0.1 - 0.6$, due to the presence of an additional critical layer for $s \geqslant 0.7$. However, for the viscous type II modes, our results depend a great deal on the basic flow velocity gradients near the wall. Hence, there is a wider solution range in s available for the lower branch modes.

The two major studies with which we attempt to make comparisons with for our case C results are the works of Salzberg & Kezios [39] and Kobayashi *et al.* [25], both of which are experimental, with $\psi = 15°$. We note, therefore, it is only possible to compare our calculations for $\psi = 70°$ qualitatively with these studies. This is because, our case A findings have already shown that there exists a discrepancy in the waveangle for $\psi < 45°$ between our results and those of Kobayashi *et al.* Indeed, compiling our code for $\psi = 15°$ would not be useful, as we are modelling the crossflow instability modes, as opposed to the Görtler modes, which are governed by a centrifugal instability. This remains the case despite the introduction of axial flow. We begin with the concluding remarks of Salzberg & Kezios [39], who found, '...the advancement of the location of transition toward the apex as the peripheral speed increases.' This means the flow becomes more unstable as the ratio of peripheral to tangential speed, s, is increased. Their experiments were conducted in the range $1.5 < s < 7$ and provide favourable comparisons with our type II results for this range, as we have found increasing s has a destabilizing effect on the flow. Furthermore, the work of Kobayashi *et al.* [25] found for a similar range $1.5 < s < 3$, increasing s reduced the waveangle from 30.2° to 13.6° as well as the most unstable wavenumber from 1.60 to 1.10. Furthermore, the large values of these waveangles seem to suggest that the study of Kobayashi *et al.* [25] for small ψ may have observed viscous wall-dominated modes. Indeed, comparisons with our type II results for $\psi = 70°$ again show a similar qualitative trend in this range for s. The waveangle, ϕ, is reduced over the range $0.1 < s < 10$, and only subsequently increases slightly for $s > 10$. However, the results of Kobayashi *et al.* [25] state that the spiral vortices become counter-rotating in nature for $s > 5$, which is a result of the cone half-angle being so small. Therefore, at this stage, it is not possible to make any further quantitative comparisons.

Physically, we mentioned earlier a streamwise forcing effect which occurs as a result of the introduction of axial flow onto the cone, and identified this as a possible Tollmien-Schlichting instability which acts on the spiral vortices, along with the centrifugal instability in the work by Kobayashi *et al.* [25]. In terms of wider cone half-angles, which we have studied, from our case A results, we are able to consider the combination of the Tollmien-Schlichting instability and the crossflow instability. We propose that for applications such as flow over relatively wide propeller nose cones ($\psi > 50°$ or so), these two instabilities act as the two dominant battling forces which govern whether the flow is stable or unstable. The Tollmien-Schlichting instability acts to force fluid in the tangential direction and effectively sweeps any arising instabilities in the boundary layer, say from surface roughness etc., further downstream causing the location of transition to retreat downstream also. Therefore, overall, it has a stabilizing effect. In contrast, the rotational forcing of the crossflow instability promotes vorticity from the boundary layer to be shed in the azimuthal direction and hence create the observed co-rotating crossflow vortices. The net effect is for these vortices to propagate in the effective velocity direction. It is precisely when these battling streamwise and rotational velocities balance each other that we observe a sharp stabilizing effect in the flow, which we identify with the case $s = 0.99$ from our viscous mode type II results. We pose that, physically, this value is indeed $s = 1$, with a slight error being introduced from our numerical results for the basic flow. It is suggested that this result is physically significant in applications, such as high speed flow onto the nose of a spinning propeller during the flight of an aeroplane. Here, the oncoming axial flow varies naturally with oncoming winds or at different altitudes. Therefore, the rotational angular speed, corresponding to engine thrust, may be altered accordingly to achieve an axial to rotational velocity ratio close to 1, thereby producing a more stable flow setup.

We now proceed to develop a comparison between our effective Taylor number estimate for a 15° cone in axial flow and the right-hand branch of the neutral stability curve obtained numerically by Kobayashi [23] for the parameters $\psi = 15^\circ, s = 3, \phi = 15^\circ$. We must compare with the rotational Reynolds number plotted against vortex wavenumber, σ. As for still fluid, we consider the Görtler number, G, which governs the centrifugal instability, written in the form

$$G = 2\mathrm{R}^{\frac{1}{2}}\delta, \tag{9.4}$$

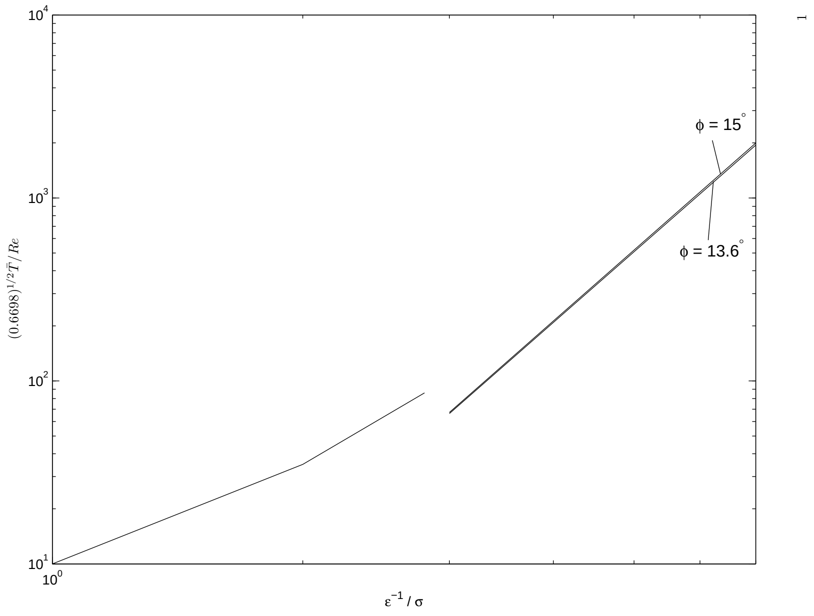

Figure 9.4: Comparison between scaled effective asymptotic Taylor number $\overline{T}$ (right plots) and Reynolds number Re of Kobayashi [23] (left) against vortex wavenumbers ϵ^{-1} and σ for $\psi = 15°,\ s = 3$ (Kobayashi uses $\phi = 15°$).

with curvature δ. Following this argument, we connect the rotational Reynolds number, Re, to the conventional Reynolds number we have defined, R, using equation (45) of Kobayashi [23] to re-write the curvature term, which leads to the relation

$$Re = \mathrm{R}^{\frac{1}{2}}\surd(0.6698). \tag{9.5}$$

As a result, we may write the rotational Reynolds number in terms of the effective Taylor number

$$Re = \overline{T}\surd(0.6698). \tag{9.6}$$

We can subsequently make a direct quantitative comparison between our asymptotic estimate for the scaled effective Taylor number and the numerical Reynolds number calculated by Kobayashi [23], which is shown in figure 9.4. These are plotted against the spiral vortex wavenumbers ϵ^{-1} and σ. Once again, Kobayashi's data is displayed for low Re and low σ, whereas our results are plotted for large Taylor number and large vortex wavenumber. Through the assumption of large Reynolds number, our comparisons with Kobayashi [23] improve as the Reynolds number increases beyond $Re \sim 100$. From the data plot, we conclude our asymptotic setup in axial flow closely models the right-hand branch of the neutral stability curve for Reynolds numbers of $O(10^4)$ and above.

Importantly, we note that these comparisons are for $s = 3$, for which our analysis does not cover the most dangerous mode. Nevertheless, when extended to large Reynolds number, the stability curve of Kobayashi [23] agrees well with both neutral mode estimates we have constructed. Physically, we interpret this as the mode we have calculated is one which is close to the most dangerous mode. Furthermore, we notice that data from the numerical stability curve of Kobayashi [23] is available for $\phi = 15°$. Therefore, we have plotted our neutral mode estimates both for $\phi = 13.6°$ (corresponding to the data from Kobayashi *et al.* [26]) and $\phi = 15°$. As a result, we see that the $\phi = 15°$ plot would more closer model the numerical results of Kobayashi [23] for large Reynolds number beyond $O(10^4)$.

It is important to clarify a general point with regard to all three physical flow régimes. In all cases A, B and C, the basic flow equations do not use a parallel flow approximation, but in fact cover both spatial streamwise and surface-normal variation. With regard to the crossflow instability, both the type I and type II mode asymptotic expansions do not neglect non-parallel flow effects. The expansion procedures may be continued to higher order terms at which non-parallel effects will actually come into play. Nevertheless, for both the crossflow and centrifugal instabilities, the stability analyses presented are local in that the perturbation expansions focus about a specific streamwise location x. For the crossflow instability, this streamwise location is related to the Reynolds number R and we therefore re-scale using the Reynolds number based on boundary layer thickness R_{δ^*}. Hence, as the Reynolds number is varied, our results are valid for varying streamwise locations, x. Similarly, with regard to the centrifugal instability, we notice that for circular waves in still fluid (§6), spiral waves in still fluid (§7) and circular/spiral waves in axial flow (§8), while the stability analyses are local, they are carried out at varying streamwise or re-scaled logarithmic coordinates along the cone surface. This variation is taken into account in the re-scaled Taylor number, $\overline{T}$, which allows our neutral stability curves to be valid for varying streamwise locations along the cone surface. The main difference to notice with the centrifugal instability is that it is established relatively early in the analyses that the vortex activity is located close to the wall for both circular and spiral waves in still fluid and in axial flow. This is used in a non-trivial way in §8 where we consider the case of circular/spiral waves for a slender cone in axial flow and expand the basic flow at the wall. In this case, although the stability analysis recovers variations in the spatial logarithmic coordinate propagating along the cone surface, it is restricted to the wall in the normal direction, in order to fully capture the counter-rotating vortex activity of the centrifugal instability. Furthermore, it is important to note that the asymptotic expansions presented in §6-8 contain leading order and next order correction terms to the re-scaled neutrally stable Taylor number $\overline{T}$ in terms of the non-dimensional vortex wavenumber ϵ^{-1}. These expansions can be continued in a self-consistent way to calculate higher order terms, at which point non-parallel effects in the flow appear and maybe taken into account.

9.2 Future work

The current research work comprises an incompressible high Reynolds number linear asymptotic model of two distinct instability modes, which may be observed on the surface of the rotating cone. Some important limitations have been found in terms of certain parameter ranges where our theory breaks down.

Firstly, for a rotating cone in still fluid (case A), the possibility to analyse the setup for more slender cone half-angles ($\psi < 45^\circ - 50^\circ$ or so) remains open. In order to make progress here, we must use appropriate length scalings in our problem formulation to take account of the slender surface curvature of the cone surface and hence investigate the centrifugal instability, which would yield modes that have been visualised as counter-rotating spiral vortices by Kobayashi & Izumi [26] in the literature. This would seem to suggest the possibility of a viscous mode dominated structure at work, perhaps pertaining to the onset of the centrifugal Görtler instability mechanism.

Secondly, our type I results for case C are so far limited to small s, as the existence of an extra zero in the effective velocity profile, and hence an extra critical layer in the inviscid mode analysis, requires closer attention. When calculating the integral estimate I_2 we must take account of the logarithmic contribution from the additional singularity at this critical layer location. This would enable us to verify the correctness, or otherwise, of our assertion, which claims the case $s = 1$ is the most stabilizing flow setup for inviscid type I modes, as well as for the lower-branch viscous modes.

Thirdly, an alternative method rather than an extension would involve obtaining greater accuracy in our solutions for case C. In equation (3.68), we obtain the double-derivative of the effective velocity $\overline{\overline{U}}_1$ in order to establish the critical layer location. We estimate the profiles $f^{'''}(s, \eta_1)$ and $g^{''}(s, \eta_1)$ using a finite difference approach, which is accurate for our choice of small step-length, h. However, it is possible to differentiate the basic flow equations and obtain expressions for $f^{'''}$ and $g^{''}$, which, most notably, will include terms involving $\frac{\partial U}{\partial s}$, where the solution vector $U = (f, f^{'}, f^{''}, g, g^{'})$. Importantly, our current setup for obtaining the case C basic flow using the NAG routine D03PEF is unable to provide s-derivatives of the solution vector. These are required at each integration step, in order to obtain the complete profiles $f^{'''}$ and $g^{''}$. Investigations have begun on using the alternative NAG routine D03PKF, which allows a set of ODEs in s to be defined, the solutions of which we choose to be precisely the s-derivatives of our main solution vector. As with D03PEF, the routine employs the method of lines, but, in this case, it solves and passes back both the PDE solutions and the new ODE solution at each step in the so-called 'time integration' for s. This is achieved through defining a set of coupling points, at which the solutions for the ODEs are required, and these points are chosen to coincide with the spatial (i.e. η_1) mesh points. However, as the profiles are required at each mesh point and the system to be solved is fifth-order in size, this requires the overall solution of a total number of ODEs, which is equal to five times the number of spatial mesh points. Given that the η_1-mesh is already well refined from the initial solution for $s = 0$, this creates a much more complex and computationally challenging problem. Nevertheless, in theory, the solutions obtained would be more accurate than the existing profiles found using finite differences.

Lastly, in terms of natural extensions to the current work, we focus on §5 and the resulting stability analyses of the following chapters where we have calculated large Reynolds number estimates to the right-hand branch of the neutral curve. The next step in all the relevant cases of circular and spiral waves in still fluid and axial flow would be to investigate the occurrence of the most unstable Görtler vortex modes. In similar fashion to the study of Denier *et al.* [3], who extended the work of Hall [14] for a Blasius boundary layer. We would concentrate the neighbourhood of the neutral mode and seek spatially amplified modes close to the right-hand branch of neutral curve, which we have obtained for a range of slender cones in still fluid and axial flow. Such an analysis would involved calculation of the thickness of a layer centered on the location of vortex activity, which admit growing spatial modes, most likely in the streamwise direction. Subsequently, it would be possible to numerically solve for the spatial growth rate and location of the critical layer, which may move away from the wall, in the neighbourhood of the neutral modes on the stability curve. However, before such a study to obtain the structure of the most unstable vortex in still fluid may be conducted, it would be useful to draw comparisons between our right-hand branch neutral curve estimates for the Taylor number and the Reynolds number stability curve for a range of slender cones in still fluid. At present, such comparisons are only possible for $\psi \leqslant 15^\circ$ (see figure 9.2). We have developed Taylor number estimates for $\psi = 15^\circ - 45^\circ$ in this thesis, but stability curves do not yet exist for these larger cone half-angles. Hence, there is scope for additional numerical or experimental studies to be conducted in order to allow us to make further progress on the still fluid problem pertaining to the investigation the most unstable Görtler modes.

A more general extension to this thesis would involve a study of convex or concave nosed cones, where the surface would be prescribed by some function involving its curvature. Ogive nose cones more closely model the nose of spinning missiles used, for example, in military applications. Studies by Mueller *et al.* [35] and also Kohama [30] have experimentally observed the existence of spiral vortices during the instability. Kohama's work identified horseshoe-like patterns, which appear as a secondary instability before the eventual breakdown to turbulent flow. This maybe interpreted as a potential method of delaying the onset of transition, which suggests ogive nose cones appear to be more stabilizing than the standard linear vertex nose cone we have studied in this thesis. A further study could investigate the stabilizing or destabilizing effect of changing the curvature parameter to perhaps obtain an optimum surface curvature, which would correspond to the flow being most stable.

In terms of modelling the problem using a more realistic setup, closer to physical flow in applications, such as spinning missiles and rotating propeller nose cones, we propose that our assumptions of linear theory and incompressible flow be extended to consider nonlinear effects and flow within a compressible free stream. Considering that much of our work here has stemmed from extensions of linear rotating disk flow studies by Gregory, Stuart & Walker [13] and Hall [16], it would seem sensible to seek to develop the nonlinear rotating disk analyses carried out by MacKerrell [32] for type II modes and, more recently, Gajjar [6], who has studied the upper-branch type I modes. Furthermore, for the case of compressible flow, Gajjar [5] has also investigated the evolution of growing modes using the properties of unsteady nonlinear critical layers.

In conclusion, throughout this thesis we have attempted to identify the instability modes of oscillation present on the surface of a rotating cone. Using asymptotic theory for large Reynolds number to model the observed spiral vortices, we have been able to draw some useful comparisons with existing experimental work. However, we have also obtained additional results (for example for a rotating cone in axial flow of relatively large cone half-angle), where there are not currently any direct experimental results in the literature with which to make suitable comparisons with. In addition, there are certain ranges of the inverse axial flow parameter, s, which are yet to be investigated experimentally, most notably $s < 1$. Furthermore, in the case of still fluid for varying slender cone half-angles, we have developed estimates for the right-hand branch of the neutral stability curve. However, there are currently no corresponding experimental or numerical results to compare with, and so we notice the potential here for further study to draw additional comparisons with our own work. Overall, altering the cone half-angle ψ towards the extreme values of $\psi = 15^\circ$ or $\psi = 90^\circ$ results in flow stabilisation. In addition, in the case of axial flow, we find that for both wide and slender cones, increasing the strength of the oncoming flow has the effect of stabilising both flows.

Appendix

In this appendix we provide the inviscid mode and viscous mode results for a rotating cone with $\psi = 50°$, for varying strengths of the inverse axial flow parameter, s. Figures 1−3 are very similar to those for $\psi = 70°$ and are presented here to illustrate the form of the important stability functions, such as the effective velocity profile, $\overline{\overline{\overline{U}}}_1$, and the inviscid surface-normal eigenfunction, w_0. Furthermore, in figures 4−8, we present asymptotic neutral curves for values ranging from $s = 0.1 - 0.6$ for the type I and type II modes, as well as $s = 1.0, 5.0, 10$ additionally for the type II modes. Discussion of the results for these curves is provided in §4.6. Finally, for brevity in the main text, we use the Appendix here to provide versions of disturbance equations used at various points during the stability analyses in §§5–8. This maybe, for example, when transforming the equations using differential operators in order to reveal the relevant terms in the ensuing perturbation expansions.

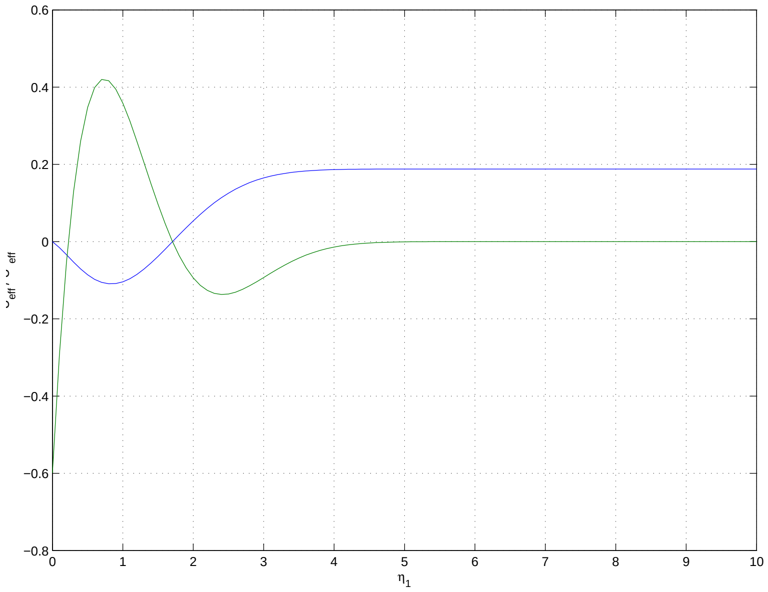

Figure 1: Effective velocity $\overline{\overline{U}}_1$ (upper curve at $\eta_1 = 10$) and its second derivative $\overline{\overline{U}}_1''$ (lower curve at $\eta_1 = 10$) for $\psi = 50°$, $s = 0.3$.

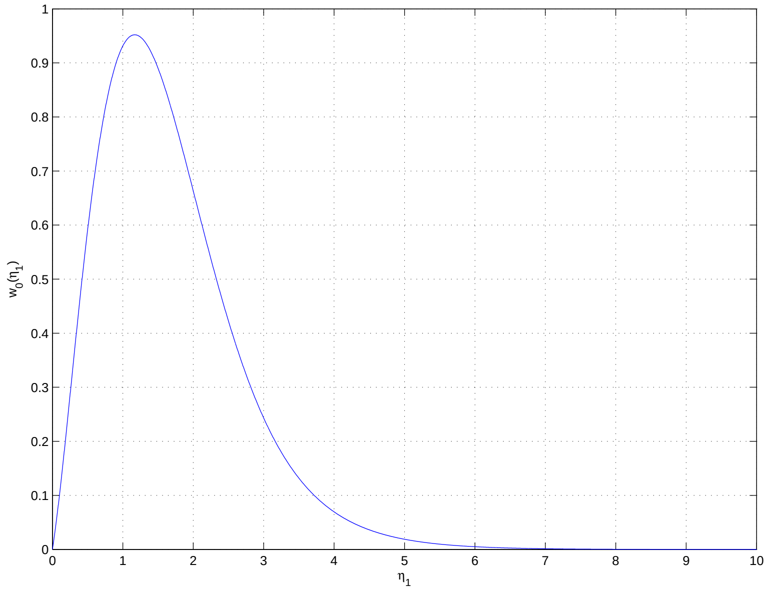

Figure 2: Plot of inviscid motion eigenfunction $w_0(\eta_1)$ for $\psi = 50°$, $s = 0.3$.

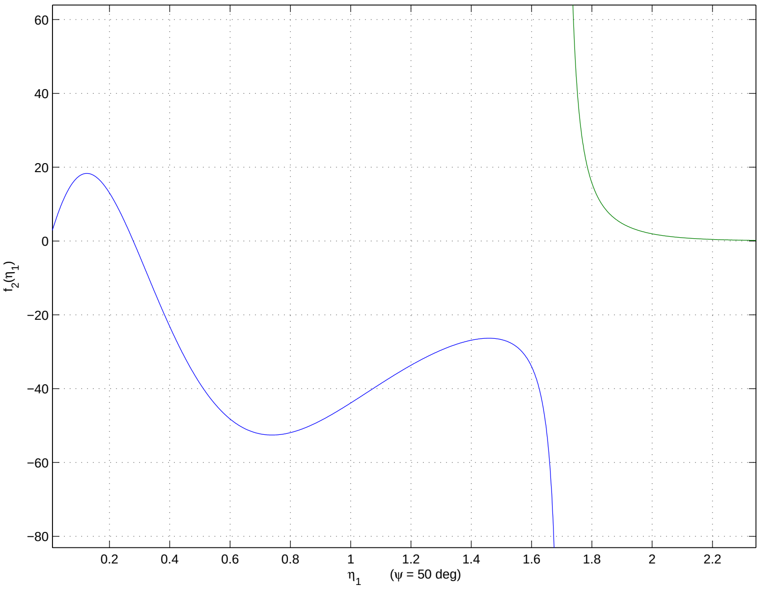

Figure 3: Plot of integrand of I_2, $f_2(s, \eta_1)$, showing location of singularity at $\eta_1 = \overline{\eta_1}$ for $\psi = 50°$, $s = 0.3$.

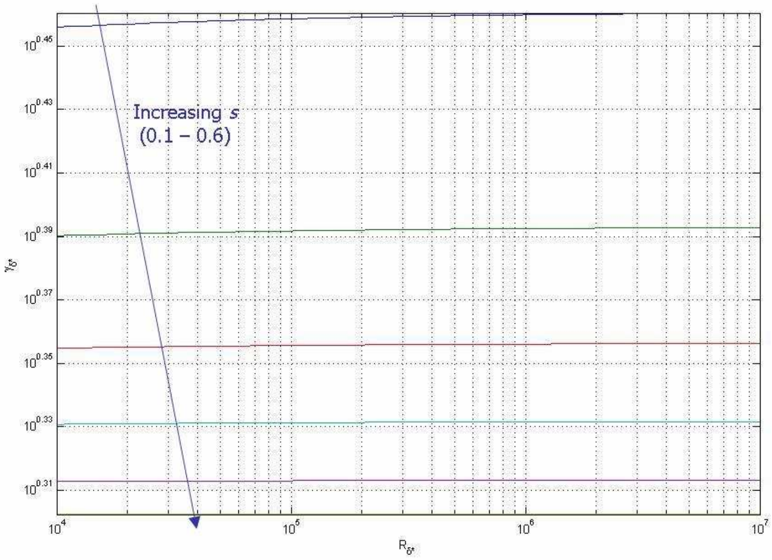

Figure 4: Plot of asymptotic neutral wavenumber predictions $\gamma_{\delta*}$ against $\mathrm{R}_{\delta*}$ for inviscid modes for $\psi = 50°$, $s = 0.1 - 0.6$. Increasing s stabilizes the flow.

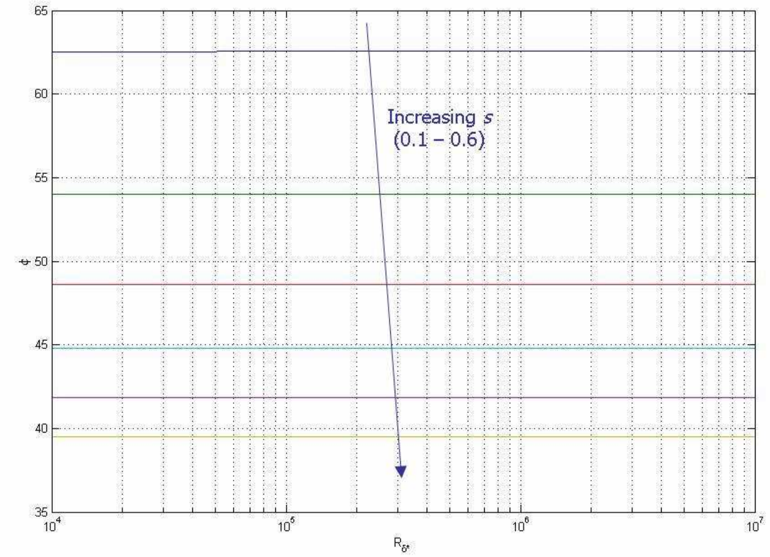

Figure 5: Plot of asymptotic neutral waveangle predictions ϕ against R_{δ^*} for inviscid modes for $\psi = 50°$, $s = 0.1 - 0.6$. Increasing s gives a smaller vortex waveangle.

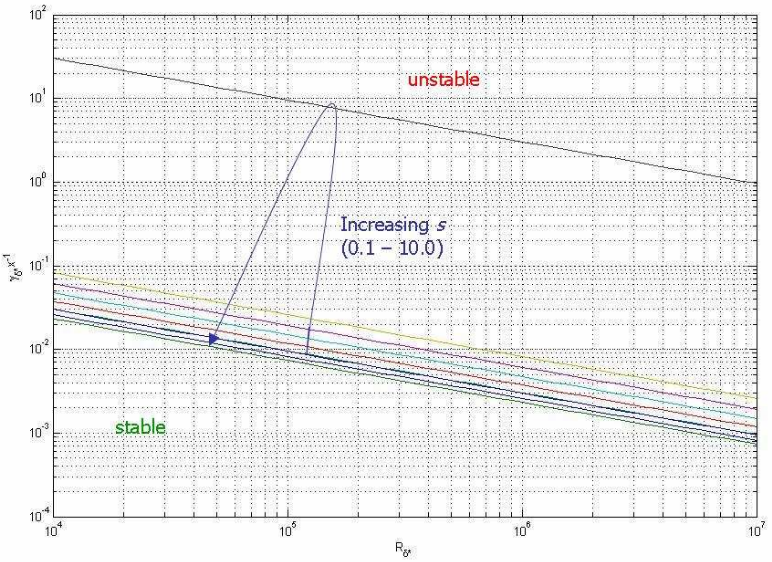

Figure 6: Plot of asymptotic neutral wavenumber predictions $\gamma_{\delta^*} x^{-1}$ against R_{δ^*} for viscous modes for $\psi = 50°$, $s = 0.1 - 10.0$. Increasing s shifts the curves as shown.

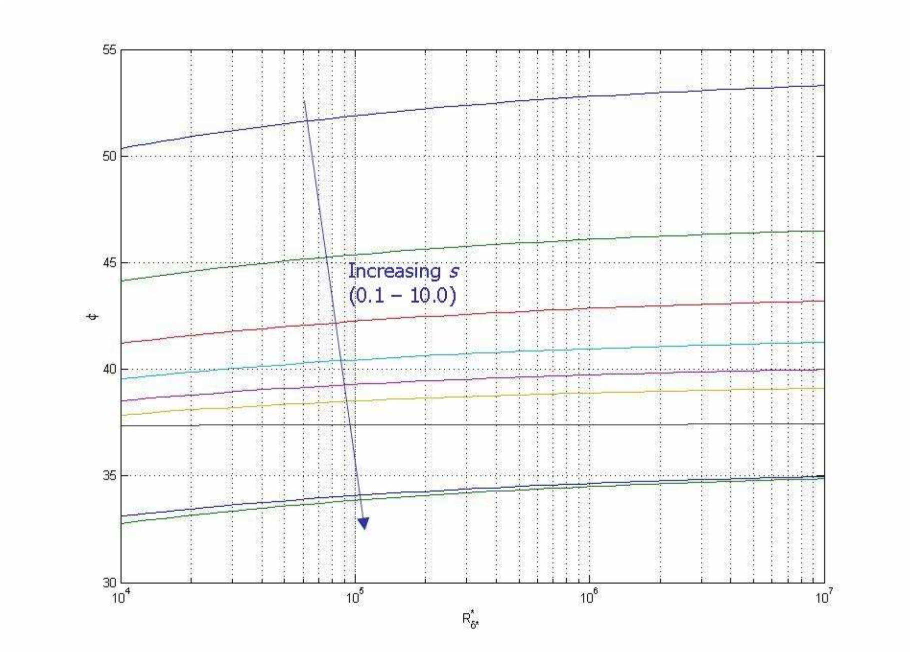

Figure 7: Plot of asymptotic neutral waveangle predictions ϕ against $\mathrm{R}^*_{\delta *}$ for viscous modes for $\psi = 50^\circ$, $s = 0.1 - 10.0$. Increasing s gives a smaller vortex waveangle.

$$
\begin{aligned}
\mathrm{i}\frac{\sin\psi}{\overline{h}_1}\tilde{u} \quad &+ \quad \epsilon\frac{\sin\psi(\tilde{u}\cos\phi + \tilde{v}\sin\phi)}{\overline{h}_1\overline{h}_2} + \mathrm{i}b\epsilon\frac{\sin\psi}{\overline{h}_2}\tilde{v} + \epsilon\frac{\partial\tilde{w}}{\partial\eta} \\
+\epsilon\Big(\frac{\cos\psi\cos^2\phi}{\overline{h}_2} \quad &+ \quad \frac{\cos\psi\sin^2\phi}{\overline{h}_1}\Big)\tilde{w} = 0,
\end{aligned}
\tag{1}
$$

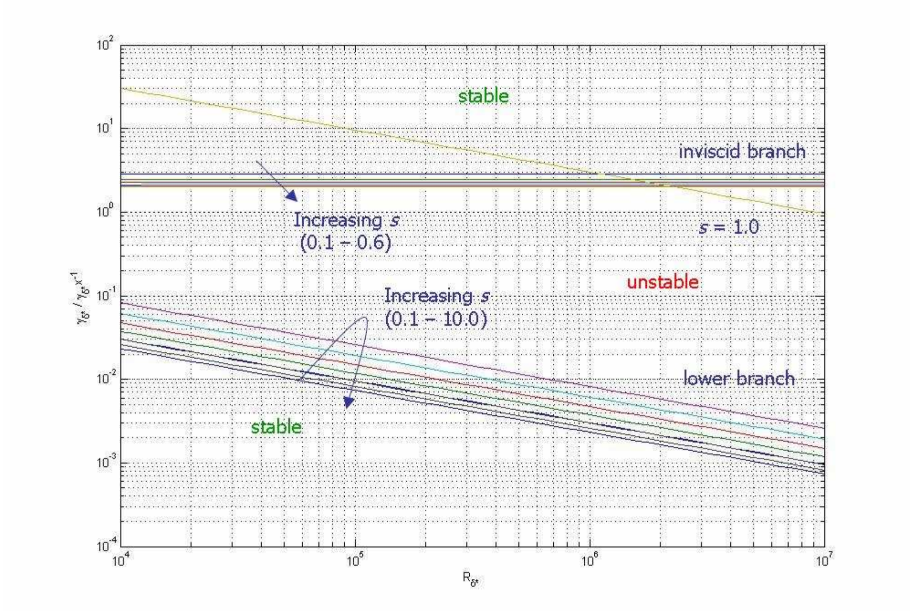

Figure 8: Plot of asymptotic neutral wavenumber predictions $\gamma_{\delta^*}, \gamma_{\delta^*} x^{-1}$ against R_{δ^*} for inviscid type I and viscous type II modes for $\psi = 50°$, $s = 0.1 - 0.6$ (type I), $s = 0.1 - 10.0$ (type II). Increasing s shifts the curves as shown.

$$
\begin{aligned}
\Big(\epsilon^2 \overline{h}_1^2 \frac{\partial^2}{\partial \eta^2} - \sin^2\psi\Big)\tilde{v} &= \epsilon^2 \overline{h}_1^2 \frac{(1 + \check{x}\cos\phi - \overline{y}\sin\phi)}{\sin\psi} \frac{\partial \tilde{V}}{\partial \eta}\tilde{w} \\
+\epsilon \overline{h}_1^2 \Big[\mathrm{i}\frac{(1 + \check{x}\cos\phi - \overline{y}\sin\phi)}{\overline{h}_1}\tilde{U} &+ \mathrm{i}b\epsilon \frac{(1 + \check{x}\cos\phi - \overline{y}\sin\phi)}{\overline{h}_2}\tilde{V} + \epsilon W \frac{\partial}{\partial \eta}\Big]\tilde{v} \\
&+ \epsilon^2 \overline{h}_1 \tilde{V}\cos\phi\,\tilde{u} - \epsilon^2 \overline{h}_1^2 \frac{\tilde{V}\sin\phi}{\overline{h}_2}\tilde{v} \\
&+ \epsilon^2 \frac{\overline{h}_1(1 + \check{x}\cos\phi - \overline{y}\sin\phi)}{\overline{h}_2}(\tilde{U}\tilde{v} + \tilde{V}\tilde{u})\cos\phi \\
&+ \epsilon^2 \overline{h}_1^2 \Big(\frac{(1 + \check{x}\cos\phi - \overline{y}\sin\phi)}{\overline{h}_2}\tilde{V}\tilde{w} + \frac{\sin\psi}{\overline{h}_2}W\tilde{v}\Big)\cot\psi\cos^2\phi \\
-2\epsilon^2 \frac{\overline{h}_1(1 + \check{x}\cos\phi - \overline{y}\sin\phi)}{\overline{h}_2}\tilde{U}\tilde{u}\sin\phi &+ 2\epsilon^2 \frac{\overline{h}_1^2}{\sin\psi}(\tilde{u}\sin\psi + \tilde{w}\cos\psi\cos\phi) \\
+\mathrm{i}b\epsilon^2 \frac{\overline{h}_1^2 \sin\psi}{\overline{h}_2}\tilde{p} + b^2\epsilon^2 \frac{\overline{h}_1^2 \sin^2\psi}{\overline{h}_2^2}\tilde{v} - \frac{\overline{h}_1 \sin^2\psi}{\overline{h}_2}&\Big[\mathrm{i}\epsilon \frac{\partial}{\partial \check{x}}\Big(\frac{\overline{h}_2}{\overline{h}_1}\Big) + \mathrm{i}b\epsilon^2 \frac{\partial}{\partial \overline{y}}\Big(\frac{\overline{h}_1}{\overline{h}_2}\Big) + \epsilon^2 \frac{\partial}{\partial \eta}(\overline{h}_1\overline{h}_2)\frac{\partial}{\partial \eta}\Big]\tilde{v} \\
&+ \epsilon^2 \overline{h}_1^2 \Big[\Big(\frac{\sin\psi}{\overline{h}_2^3}\frac{\partial \overline{h}_2}{\partial \check{x}}\frac{\partial \overline{h}_2}{\partial \overline{y}} + \frac{\sin\psi}{\overline{h}_1^2\overline{h}_2}\frac{\partial \overline{h}_1}{\partial \check{x}}\frac{\partial \overline{h}_1}{\partial \overline{y}}\Big)\tilde{u} - \frac{\sin^2\psi}{\overline{h}_2^2}\tilde{v} \\
&+ 2\mathrm{i}b\frac{\sin\psi}{\overline{h}_2^2}\Big(\frac{\partial \overline{h}_2}{\partial \check{x}}\tilde{u} + \frac{\partial \overline{h}_2}{\partial \eta}\tilde{w}\Big) + \Big(\frac{\sin\psi}{\overline{h}_1^3}\frac{\partial \overline{h}_1}{\partial \eta}\frac{\partial \overline{h}_1}{\partial \overline{y}} + \frac{\sin\psi}{\overline{h}_1\overline{h}_2^2}\frac{\partial \overline{h}_2}{\partial \eta}\frac{\partial \overline{h}_2}{\partial \overline{y}}\Big)\tilde{w}\Big],
\end{aligned}
\tag{2}
$$

$$
\begin{aligned}
\Big(\frac{\epsilon^2\overline{h}_1^2}{\sin\psi}\frac{\partial^2}{\partial\eta^2}-\sin\psi\Big)^2\tilde{w} = {}& \epsilon^2\overline{h}_1^2(2\cot\psi\cos\phi)\Big[\frac{(1+\check{x}\cos\phi-\overline{y}\sin\phi)}{\overline{h}_2}\tilde{V}\cos\phi+1\Big]\tilde{v}\\
&+\epsilon^2\overline{h}_1^2(2\cot\psi\sin\phi)\Big[\frac{(1+\check{x}\cos\phi-\overline{y}\sin\phi)}{\overline{h}_2}\tilde{U}\sin\phi-1\Big]\tilde{u}\\
-\epsilon\overline{h}_1^2\Big(\mathrm{i}\frac{(1+\check{x}\cos\phi-\overline{y}\sin\phi)}{\overline{h}_1}\tilde{U}+\mathrm{i}b\epsilon\frac{(1+\check{x}\cos\phi-\overline{y}\sin\phi)}{\overline{h}_2}\tilde{V}+\epsilon W\frac{\partial}{\partial\eta}\Big)\tilde{w}-\epsilon^2\overline{h}_1^2\frac{\partial W}{\partial\eta}\tilde{w}&\\
-\mathrm{i}\frac{\epsilon^2\overline{h}_1^2}{\sin\psi}\frac{\partial}{\partial\eta}\Big(\Big[\mathrm{i}\frac{(1+\check{x}\cos\phi-\overline{y}\sin\phi)}{\overline{h}_1}\tilde{U}+\mathrm{i}b\epsilon\frac{(1+\check{x}\cos\phi-\overline{y}\sin\phi)}{\overline{h}_2}\tilde{V}+\epsilon W\frac{\partial}{\partial\eta}\Big]\tilde{u}\Big)&\\
&-\mathrm{i}\frac{\epsilon^3\overline{h}_1^3}{\sin\psi}\frac{\partial}{\partial\eta}\Big(\frac{\tilde{u}\tilde{U}\cos\phi}{\overline{h}_1}-\frac{\tilde{v}\tilde{U}\sin\phi}{\overline{h}_2}+\frac{(1+\check{x}\cos\phi-\overline{y}\sin\phi)}{\overline{h}_1}\frac{\partial\tilde{U}}{\partial\eta}\tilde{w}\\
&+\frac{(1+\check{x}\cos\phi-\overline{y}\sin\phi)}{\overline{h}_1\overline{h}_2}(\tilde{U}\tilde{v}+\tilde{V}\tilde{u})\sin\phi\\
&+\Big[\frac{(1+\check{x}\cos\phi-\overline{y}\sin\phi)}{\overline{h}_1}\tilde{U}\tilde{w}+\frac{\sin\psi}{\overline{h}_1}W\tilde{u}\Big]\cot\psi\sin^2\phi\Big)\\
&+\mathrm{i}\frac{\epsilon^3\overline{h}_1^3}{\sin\psi}\frac{\partial}{\partial\eta}\Big[2\frac{(1+\check{x}\cos\phi-\overline{y}\sin\phi)}{\overline{h}_1\overline{h}_2}\tilde{V}\tilde{v}\cos\phi+2(\tilde{w}\cot\psi\sin\phi+\tilde{v})\Big]\\
&-\frac{\epsilon^4\overline{h}_1^4}{\sin^2\psi}\frac{\partial}{\partial\eta}\Big\{\frac{\partial^2}{\partial\eta^2}\Big[\frac{\sin\psi(\tilde{u}\cos\phi+\tilde{v}\sin\phi)}{\overline{h}_1\overline{h}_2}+\mathrm{i}b\frac{\sin\psi}{\overline{h}_2}\tilde{v}+\\
+\Big(\frac{\cos\psi\cos^2\phi}{\overline{h}_2}+\frac{\cos\psi\sin^2\phi}{\overline{h}_1}\Big)\tilde{w}\Big]-\frac{\sin^2\psi}{\epsilon^2\overline{h}_1^2}\Big[\frac{\sin\psi(\tilde{u}\cos\phi+\tilde{v}\sin\phi)}{\overline{h}_1\overline{h}_2}+\mathrm{i}b\frac{\sin\psi}{\overline{h}_2}\tilde{v}+&\\
&+\Big(\frac{\cos\psi\cos^2\phi}{\overline{h}_2}+\frac{\cos\psi\sin^2\phi}{\overline{h}_1}\Big)\tilde{w}\Big]-\frac{b^2\tilde{u}}{\overline{h}_2^2}\\
&+\frac{\sin^2\psi}{\overline{h}_1\overline{h}_2}\Big[\frac{\mathrm{i}}{\epsilon}\frac{\partial}{\partial\check{x}}\Big(\frac{\overline{h}_2}{\overline{h}_1}\Big)+\mathrm{i}b\frac{\partial}{\partial\overline{y}}\Big(\frac{\overline{h}_1}{\overline{h}_2}\Big)+\frac{\overline{h}_1\overline{h}_2}{\sin^2\psi}\frac{\partial}{\partial\eta}\Big]\tilde{u}\Big\}\\
&+\mathrm{i}\frac{\epsilon^3\overline{h}_1^3}{\sin\psi}\frac{\partial}{\partial\eta}\Big\{\frac{\partial}{\partial\check{x}}\Big(\frac{1}{\overline{h}_1\overline{h}_2}\frac{\partial(\overline{h}_1\overline{h}_2)}{\partial\check{x}}\Big)\tilde{u}-2\mathrm{i}b\frac{\sin\psi}{\overline{h}_2^2}\frac{\partial\overline{h}_2}{\partial\check{x}}\tilde{v}\\
-\Big(\frac{\sin\psi}{\overline{h}_2^3}\frac{\partial\overline{h}_2}{\partial\overline{y}}\frac{\partial\overline{h}_2}{\partial\check{x}}+\frac{\sin\psi}{\overline{h}_1^2\overline{h}_2}\frac{\partial\overline{h}_1}{\overline{y}}\frac{\partial\overline{h}_1}{\partial\check{x}}\Big)\tilde{v}-\Big(\frac{\sin\psi}{\overline{h}_1^3}\frac{\partial\overline{h}_1}{\partial\eta}\frac{\partial\overline{h}_1}{\partial\check{x}}+\frac{\sin\psi}{\overline{h}_1\overline{h}_2^2}\frac{\partial\overline{h}_2}{\partial\eta}\frac{\partial\overline{h}_2}{\partial\check{x}}\Big)\tilde{w}\Big\}&\\
&-\epsilon^2\overline{h}_1^2\Big\{\frac{b^2}{\overline{h}_2^2}\tilde{w}-\frac{\sin^2\psi}{\overline{h}_1\overline{h}_2}\Big[\frac{\mathrm{i}}{\epsilon}\frac{\partial}{\partial\check{x}}\Big(\frac{\overline{h}_2}{\overline{h}_1}\Big)+\mathrm{i}b\frac{\partial}{\partial\overline{y}}\Big(\frac{\overline{h}_1}{\overline{h}_2}\Big)+\frac{\overline{h}_1\overline{h}_2}{\sin^2\psi}\frac{\partial}{\partial\eta}\Big]\tilde{w}\Big\}\\
-\epsilon^2\overline{h}_1^2\Big\{\Big(\frac{\sin\psi}{\overline{h}_1^3}\frac{\partial\overline{h}_1}{\partial\check{x}}\frac{\partial\overline{h}_1}{\partial\eta}+\frac{\sin\psi}{\overline{h}_1\overline{h}_2^2}\frac{\partial\overline{h}_2}{\partial\check{x}}\frac{\partial\overline{h}_2}{\partial\eta}\Big)\tilde{u}-\Big(\frac{\sin\psi}{\overline{h}_2^3}\frac{\partial\overline{h}_2}{\partial\overline{y}}\frac{\partial\overline{h}_2}{\partial\eta}+\frac{\sin\psi}{\overline{h}_1^2\overline{h}_2}\frac{\partial\overline{h}_1}{\partial\overline{y}}\frac{\partial\overline{h}_1}{\partial\eta}\Big)\tilde{v}&\\
&-2\Big(\frac{\sin\psi}{\overline{h}_1^2}\frac{\partial\overline{h}_1}{\partial\eta}\frac{\partial\tilde{u}}{\partial\check{x}}+\frac{\sin\psi}{\overline{h}_2^2}\frac{\partial\overline{h}_2}{\partial\eta}\frac{\partial\tilde{v}}{\partial\overline{y}}\Big)+\frac{\partial}{\partial\eta}\Big(\frac{1}{\overline{h}_1\overline{h}_2}\frac{\partial(\overline{h}_1\overline{h}_2)}{\partial\eta}\Big)\tilde{w}\Big\}
\end{aligned}
\tag{3}
$$

$$
\begin{aligned}
\mathrm{i}\frac{\sin\psi}{\overline{h}_1}\tilde{u} &+ \epsilon\frac{\sin\psi(\tilde{u}\cos\phi+\tilde{v}\sin\phi)}{\overline{h}_1\overline{h}_2} + \mathrm{i}b\epsilon\frac{\sin\psi}{\overline{h}_2}\tilde{v} + \epsilon\frac{\partial\tilde{w}}{\partial\eta} \\
+\epsilon\Big(\frac{\cos\psi\cos^2\phi}{\overline{h}_2} &+ \frac{\cos\psi\sin^2\phi}{\overline{h}_1}\Big)\tilde{w} = 0,
\end{aligned}
\tag{4}
$$

$$
\begin{aligned}
\Big(\epsilon^2\overline{h}_1^2\frac{\partial^2}{\partial\eta^2} - \sin^2\psi\Big)\tilde{v} = \epsilon^2\overline{h}_1^2\frac{\partial\overline{V}}{\partial\eta}(\check{x},\overline{y},0)\tilde{w} \\
+\epsilon\overline{h}_1^2\Big[\mathrm{i}\frac{\sin\psi}{\overline{h}_1}\eta\frac{\partial\overline{U}}{\partial\eta}(\check{x},\overline{y},0) + \mathrm{i}b\epsilon\frac{\sin\psi}{\overline{h}_2}\eta\frac{\partial\overline{V}}{\partial\eta}(\check{x},\overline{y},0) + \epsilon W\frac{\partial}{\partial\eta}\Big]\tilde{v} \\
+\epsilon^2\overline{h}_1\eta\sin\psi\frac{\partial^2\overline{V}}{\partial\check{x}\partial\eta}(\check{x},\overline{y},0)\tilde{u} - \epsilon^2\overline{h}_1^2\frac{\sin\psi}{\overline{h}_2}\eta\frac{\partial^2\overline{V}}{\partial\overline{y}\partial\eta}(\check{x},\overline{y},0) \\
+\epsilon^2\frac{\overline{h}_1\sin\psi}{\overline{h}_2}(\eta\frac{\partial\overline{U}}{\partial\eta}(\check{x},\overline{y},0)\tilde{v} + \eta\frac{\partial\overline{V}}{\partial\eta}(\check{x},\overline{y},0)\tilde{u})\cos\phi \\
+\epsilon^2\overline{h}_1^2\Big(\frac{\sin\psi}{\overline{h}_2}\eta\frac{\partial\overline{V}}{\partial\eta}(\check{x},\overline{y},0)\tilde{w} + \frac{\sin\psi}{\overline{h}_2}W\tilde{v}\Big)\cot\psi\cos^2\phi \\
-2\epsilon^2\frac{\overline{h}_1\sin\psi}{\overline{h}_2}\eta\frac{\partial\overline{U}}{\partial\eta}(\check{x},\overline{y},0)\tilde{u}\sin\phi + 2\epsilon^2\frac{\overline{h}_1^2}{\sin\psi}(\tilde{u}\sin\psi + \tilde{w}\cos\psi\cos\phi) + O(\mathrm{R}^{-\frac{1}{2}}) \\
+\mathrm{i}b\epsilon^2\frac{\overline{h}_1^2\sin\psi}{\overline{h}_2}\tilde{p} + b^2\epsilon^2\frac{\overline{h}_1^2\sin^2\psi}{\overline{h}_2^2}\tilde{v} - \frac{\overline{h}_1\sin^2\psi}{\overline{h}_2}\Big[\mathrm{i}\epsilon\frac{\partial}{\partial\check{x}}\Big(\frac{\overline{h}_2}{\overline{h}_1}\Big) + \mathrm{i}b\epsilon^2\frac{\partial}{\partial\overline{y}}\Big(\frac{\overline{h}_1}{\overline{h}_2}\Big) + \epsilon^2\frac{\partial}{\partial\eta}(\overline{h}_1\overline{h}_2)\frac{\partial}{\partial\eta}\Big]\tilde{v} \\
+\epsilon^2\overline{h}_1^2\Big[\Big(\frac{\sin\psi}{\overline{h}_2^3}\frac{\partial\overline{h}_2}{\partial\check{x}}\frac{\partial\overline{h}_2}{\partial\overline{y}} + \frac{\sin\psi}{\overline{h}_1^2\overline{h}_2}\frac{\partial\overline{h}_1}{\partial\check{x}}\frac{\partial\overline{h}_1}{\partial\overline{y}}\Big)\tilde{u} - \frac{\sin^2\psi}{\overline{h}_2^2}\tilde{v} \\
+2\mathrm{i}b\frac{\sin\psi}{\overline{h}_2^2}\Big(\frac{\partial\overline{h}_2}{\partial\check{x}}\tilde{u} + \frac{\partial\overline{h}_2}{\partial\eta}\tilde{w}\Big) + \Big(\frac{\sin\psi}{\overline{h}_1^3}\frac{\partial\overline{h}_1}{\partial\eta}\frac{\partial\overline{h}_1}{\partial\overline{y}} + \frac{\sin\psi}{\overline{h}_1\overline{h}_2^2}\frac{\partial\overline{h}_2}{\partial\eta}\frac{\partial\overline{h}_2}{\partial\overline{y}}\Big)\tilde{w}\Big],
\end{aligned}
\tag{5}
$$

$$
\begin{aligned}
\Big(\frac{\epsilon^2\overline{h}_1^2}{\sin\psi}\frac{\partial^2}{\partial\eta^2}-\sin\psi\Big)^2\tilde{w} = {} & \epsilon^2\overline{h}_1^2(2\cot\psi\cos\phi)\Big[\frac{\sin\psi}{\overline{h}_2}\eta\frac{\partial\overline{V}}{\partial\eta}(\check{x},\overline{y},0)\cos\phi+1\Big]\tilde{v}\\
& +\epsilon^2\overline{h}_1^2(2\cot\psi\sin\phi)\Big[\frac{\sin\psi}{\overline{h}_2}\eta\frac{\partial\overline{U}}{\partial\eta}(\check{x},\overline{y},0)\sin\phi-1\Big]\tilde{u}\\
& -\epsilon\overline{h}_1^2\Big(\mathrm{i}\frac{\sin\psi}{\overline{h}_1}\eta\frac{\partial\overline{U}}{\partial\eta}(\check{x},\overline{y},0)+\mathrm{i}b\epsilon\frac{\sin\psi}{\overline{h}_2}\eta\frac{\partial\overline{V}}{\partial\eta}(\check{x},\overline{y},0)+\epsilon W\frac{\partial}{\partial\eta}\Big)\tilde{w}-\epsilon^2\overline{h}_1^{2}\frac{\partial W}{\partial\eta}\tilde{w}\\
& -\mathrm{i}\frac{\epsilon^2\overline{h}_1^2}{\sin\psi}\frac{\partial}{\partial\eta}\Big(\Big[\mathrm{i}\frac{\sin\psi)}{\overline{h}_1}\eta\frac{\partial\overline{U}}{\partial\eta}(\check{x},\overline{y},0)+\mathrm{i}b\epsilon\frac{\sin\psi}{\overline{h}_2}\eta\frac{\partial\overline{V}}{\partial\eta}(\check{x},\overline{y},0)+\epsilon W\frac{\partial}{\partial\eta}\Big]\tilde{u}\Big)\\
& -\mathrm{i}\frac{\epsilon^3\overline{h}_1^3}{\sin\psi}\frac{\partial}{\partial\eta}\Big(\frac{\sin\psi}{\overline{h}_1}\eta\frac{\partial^2\overline{U}}{\partial\check{x}\partial\eta}(\check{x},\overline{y},0)\tilde{u}-\frac{\sin\psi}{\overline{h}_2}\eta\frac{\partial^2\overline{U}}{\partial\overline{y}\partial\eta}(\check{x},\overline{y},0)\tilde{v}+\frac{\sin\psi}{\overline{h}_1}\frac{\partial\overline{U}}{\partial\eta}(\check{x},\overline{y},0)\tilde{w}\\
& +\frac{\sin\psi}{\overline{h}_1\overline{h}_2}(\eta\frac{\partial\overline{U}}{\partial\eta}(\check{x},\overline{y},0)\tilde{v}+\eta\frac{\partial\overline{V}}{\partial\eta}(\check{x},\overline{y},0)\tilde{u})\sin\phi\\
& +\Big[\frac{\sin\psi}{\overline{h}_1}\eta\frac{\partial\overline{U}}{\partial\eta}(\check{x},\overline{y},0)\tilde{w}+\frac{\sin\psi}{\overline{h}_1}W\tilde{u}\Big]\cot\psi\sin^2\phi\Big)\\
& +\mathrm{i}\frac{\epsilon^3\overline{h}_1^3}{\sin\psi}\frac{\partial}{\partial\eta}\Big[2\frac{\sin\psi}{\overline{h}_1\overline{h}_2}\eta\frac{\partial\overline{V}}{\partial\eta}(\check{x},\overline{y},0)\tilde{v}\cos\phi+2(\tilde{w}\cot\psi\sin\phi+\tilde{v})\Big]+O(\mathrm{R}^{-\frac{1}{2}})\\
& -\frac{\epsilon^4\overline{h}_1^4}{\sin^2\psi}\frac{\partial}{\partial\eta}\Big\{\frac{\partial^2}{\partial\eta^2}\Big[\frac{\sin\psi(\tilde{u}\cos\phi+\tilde{v}\sin\phi)}{\overline{h}_1\overline{h}_2}+\mathrm{i}b\frac{\sin\psi}{\overline{h}_2}\tilde{v}+\\
& +\Big(\frac{\cos\psi\cos^2\phi}{\overline{h}_2}+\frac{\cos\psi\sin^2\phi}{\overline{h}_1}\Big)\tilde{w}\Big]-\frac{\sin^2\psi}{\epsilon^2\overline{h}_1^2}\Big[\frac{\sin\psi(\tilde{u}\cos\phi+\tilde{v}\sin\phi)}{\overline{h}_1\overline{h}_2}+\mathrm{i}b\frac{\sin\psi}{\overline{h}_2}\tilde{v}+\\
& +\Big(\frac{\cos\psi\cos^2\phi}{\overline{h}_2}+\frac{\cos\psi\sin^2\phi}{\overline{h}_1}\Big)\tilde{w}\Big]-\frac{b^2\tilde{u}}{\overline{h}_2^2}\\
& +\frac{\sin^2\psi}{\overline{h}_1\overline{h}_2}\Big[\frac{\mathrm{i}}{\epsilon}\frac{\partial}{\partial\check{x}}\Big(\frac{\overline{h}_2}{\overline{h}_1}\Big)+\mathrm{i}b\frac{\partial}{\partial\overline{y}}\Big(\frac{\overline{h}_1}{\overline{h}_2}\Big)+\frac{\overline{h}_1\overline{h}_2}{\sin^2\psi}\frac{\partial}{\partial\eta}\Big]\tilde{u}\Big\}\\
& +\mathrm{i}\frac{\epsilon^3\overline{h}_1^3}{\sin\psi}\frac{\partial}{\partial\eta}\Big\{\frac{\partial}{\partial\check{x}}\Big(\frac{1}{\overline{h}_1\overline{h}_2}\frac{\partial(\overline{h}_1\overline{h}_2)}{\partial\check{x}}\Big)\tilde{u}-2\mathrm{i}b\frac{\sin\psi}{\overline{h}_2^2}\frac{\partial\overline{h}_2}{\partial\check{x}}\tilde{v}\\
& -\Big(\frac{\sin\psi}{\overline{h}_2^3}\frac{\partial\overline{h}_2}{\partial\overline{y}}\frac{\partial\overline{h}_2}{\partial\check{x}}+\frac{\sin\psi}{\overline{h}_1^2\overline{h}_2}\frac{\partial\overline{h}_1}{\overline{y}}\frac{\partial\overline{h}_1}{\partial\check{x}}\Big)\tilde{v}-\Big(\frac{\sin\psi}{\overline{h}_1^3}\frac{\partial\overline{h}_1}{\partial\eta}\frac{\partial\overline{h}_1}{\partial\check{x}}+\frac{\sin\psi}{\overline{h}_1\overline{h}_2^2}\frac{\partial\overline{h}_2}{\partial\eta}\frac{\partial\overline{h}_2}{\partial\check{x}}\Big)\tilde{w}\Big\}\\
& -\epsilon^2\overline{h}_1^2\Big\{\frac{b^2}{\overline{h}_2^2}\tilde{w}-\frac{\sin^2\psi}{\overline{h}_1\overline{h}_2}\Big[\frac{\mathrm{i}}{\epsilon}\frac{\partial}{\partial\check{x}}\Big(\frac{\overline{h}_2}{\overline{h}_1}\Big)+\mathrm{i}b\frac{\partial}{\partial\overline{y}}\Big(\frac{\overline{h}_1}{\overline{h}_2}\Big)+\frac{\overline{h}_1\overline{h}_2}{\sin^2\psi}\frac{\partial}{\partial\eta}\Big]\tilde{w}\Big\}\\
& -\epsilon^2\overline{h}_1^2\Big\{\Big(\frac{\sin\psi}{\overline{h}_1^3}\frac{\partial\overline{h}_1}{\partial\check{x}}\frac{\partial\overline{h}_1}{\partial\eta}+\frac{\sin\psi}{\overline{h}_1\overline{h}_2^2}\frac{\partial\overline{h}_2}{\partial\check{x}}\frac{\partial\overline{h}_2}{\partial\eta}\Big)\tilde{u}-\Big(\frac{\sin\psi}{\overline{h}_2^3}\frac{\partial\overline{h}_2}{\partial\overline{y}}\frac{\partial\overline{h}_2}{\partial\eta}+\frac{\sin\psi}{\overline{h}_1^2\overline{h}_2}\frac{\partial\overline{h}_1}{\partial\overline{y}}\frac{\partial\overline{h}_1}{\partial\eta}\Big)\tilde{v}\\
& -2\Big(\frac{\sin\psi}{\overline{h}_1^2}\frac{\partial\overline{h}_1}{\partial\eta}\frac{\partial\tilde{u}}{\partial\check{x}}+\frac{\sin\psi}{\overline{h}_2^2}\frac{\partial\overline{h}_2}{\partial\eta}\frac{\partial\tilde{v}}{\partial\overline{y}}\Big)+\frac{\partial}{\partial\eta}\Big(\frac{1}{\overline{h}_1\overline{h}_2}\frac{\partial(\overline{h}_1\overline{h}_2)}{\partial\eta}\Big)\tilde{w}\Big\}
\end{aligned}
\tag{6}
$$

$$
\begin{aligned}
\Big(\epsilon^2\frac{\partial^2}{\partial\eta^2}-1\Big)^3\tilde{w} &= \epsilon^4 T\Big(\frac{\overline{x}V\sin\psi}{\overline{h}}+1\Big)\overline{x}V'\tilde{w} \\
&\quad +\epsilon^2 T\Big(\frac{\overline{x}V\sin\psi}{\overline{h}}+1\Big)\Big[\epsilon^2\frac{\partial\tilde{v}}{\partial t} \\
&\quad +\mathrm{i}\epsilon\overline{x}U\tilde{v}+\mathrm{i}\frac{b\epsilon^2\overline{x}V}{\overline{h}}\tilde{v}+\epsilon^2 W\frac{\partial\tilde{v}}{\partial\eta}+\epsilon^2 V\tilde{u} \\
&\quad +\frac{\epsilon^2}{\sin\psi}\Big(\frac{\overline{x}V\sin\psi}{\overline{h}}+2\Big)(\tilde{u}\sin\psi+\tilde{w}\cos\psi)+\epsilon^2\Big(\frac{\overline{x}U\sin\psi+W\cos\psi}{\overline{h}}\Big)\tilde{v} \\
&\quad +\mathrm{i}\frac{b\epsilon^2}{\overline{h}}\tilde{p}+\frac{(b^2+1)\epsilon^2}{\overline{h}^2}\tilde{v}-\mathrm{i}\frac{\epsilon\sin\psi}{\overline{h}}\tilde{v}-\frac{\epsilon^2\cos\psi}{\overline{h}}\frac{\partial\tilde{v}}{\partial\eta} \\
&\quad -2\mathrm{i}\frac{b\epsilon^2\sin\psi}{\overline{h}^3}\tilde{u}-2\mathrm{i}\frac{b\epsilon^2\cos\psi}{\overline{h}^3}\tilde{w}\Big] \\
&\quad +\Big(\epsilon^2\frac{\partial^2}{\partial\eta^2}-1\Big)\Big[-\mathrm{i}\epsilon^3\frac{\partial^2\tilde{u}}{\partial t\partial\eta}+\frac{\partial}{\partial\eta}\Big(\epsilon^2\overline{x}U\tilde{u}+\frac{b\epsilon^3\overline{x}V}{\overline{h}}\tilde{u}-\mathrm{i}\epsilon^3 W\frac{\partial\tilde{u}}{\partial\eta} \\
&\quad -\mathrm{i}\epsilon^3 U\tilde{u}-\mathrm{i}\epsilon^3\tilde{w}\overline{x}U'+2\mathrm{i}\epsilon^3\Big[\frac{\overline{x}V\sin\psi}{\overline{h}}+1\Big]\tilde{v}\Big) \\
&\quad -\Big(\epsilon^2\frac{\partial\tilde{w}}{\partial t}+\mathrm{i}\epsilon\overline{x}U\tilde{w}+\mathrm{i}\frac{b\epsilon^2\overline{x}V}{\overline{h}}\tilde{w}+\epsilon^2 W\frac{\partial\tilde{w}}{\partial\eta} \\
&\quad -2\epsilon^2\Big[\frac{\overline{x}V\sin\psi}{\overline{h}}+1\Big]\tilde{v}\cot\psi+\frac{b^2\epsilon^2}{\overline{h}^2}\tilde{w}-\mathrm{i}\frac{\epsilon\sin\psi}{\overline{h}}\tilde{w} \\
&\quad -\frac{\epsilon^2\cos\psi}{\overline{h}}\frac{\partial\tilde{w}}{\partial\eta}+\frac{\epsilon^2(\tilde{u}\sin\psi+\tilde{w}\cos\psi)}{\overline{h}^2}\cos\psi+2\mathrm{i}\frac{b\epsilon^2\cos\psi}{\overline{h}^3}\tilde{v}\Big) \\
&\quad +\epsilon^2\frac{\partial}{\partial\eta}\Big(\frac{\tilde{u}\sin\psi+\mathrm{i}b\tilde{v}+\tilde{w}\cos\psi}{\overline{h}}\Big) \\
&\quad -\epsilon^4\frac{\partial^3}{\partial\eta^3}\Big(\frac{\tilde{u}\sin\psi+\mathrm{i}b\tilde{v}+\tilde{w}\cos\psi}{\overline{h}}\Big) \\
&\quad -\mathrm{i}\Big(\frac{\epsilon^3 b^2}{\overline{h}^2}\frac{\partial\tilde{u}}{\partial\eta}-\mathrm{i}\frac{\epsilon^2\sin\psi}{\overline{h}}\frac{\partial\tilde{u}}{\partial\eta} \\
&\quad -\frac{\epsilon^3\cos\psi}{\overline{h}}\frac{\partial^2\tilde{u}}{\partial\eta^2}+\frac{\epsilon^3}{\overline{h}^2}\Big[\frac{\partial\tilde{u}}{\partial\eta}\sin\psi+\frac{\partial\tilde{w}}{\partial\eta}\cos\psi\Big]\sin\psi\Big)\Big],
\end{aligned}
\tag{7}
$$

$$
\begin{aligned}
\Big(\epsilon^2\frac{\partial^2}{\partial\varphi^2}-1\Big)^3\tilde{w} = \epsilon^4\overline{h}_1^4 T\Big(\frac{(1+\check{x}\cos\phi-\overline{y}\sin\phi)}{\overline{h}_2}\tilde{V}\cos\phi+1\Big)(1+\check{x}\cos\phi-\overline{y}\sin\phi)\frac{\partial\tilde{V}}{\partial\eta}\tilde{w} \\
+\epsilon^2\overline{h}_1^{2}\frac{2\cot\psi\cos\phi}{\sin^2\psi}\Big(\epsilon^2\frac{\partial^2}{\partial\varphi^2}-1\Big)\Big[\frac{(1+\check{x}\cos\phi-\overline{y}\sin\phi)}{\overline{h}_2}\tilde{V}\cos\phi\Big]\tilde{v} \\
+\epsilon^2\overline{h}_1^{2}\frac{2\cot\psi\cos\phi}{\sin^2\psi}\Big[\frac{(1+\check{x}\cos\phi-\overline{y}\sin\phi)}{\overline{h}_2}\tilde{V}\cos\phi+1\Big]\Big\{ \\
\epsilon\overline{h}_1^{2}\Big[\mathrm{i}\frac{(1+\check{x}\cos\phi-\overline{y}\sin\phi)}{\overline{h}_1}\tilde{U}+\mathrm{i}b\epsilon\frac{(1+\check{x}\cos\phi-\overline{y}\sin\phi)}{\overline{h}_2}\tilde{V}+\epsilon W\frac{\partial}{\partial\eta}\Big]\tilde{v} \\
+\epsilon^2\overline{h}_1\tilde{V}\cos\phi\tilde{u}-\epsilon^2\overline{h}_1^{2}\frac{\tilde{V}\sin\phi}{\overline{h}_2}\tilde{v} \\
+\epsilon^2\frac{\overline{h}_1(1+\check{x}\cos\phi-\overline{y}\sin\phi)}{\overline{h}_2}(\tilde{U}\tilde{v}+\tilde{V}\tilde{u})\cos\phi \\
+\epsilon^2\overline{h}_1^{2}\Big(\frac{(1+\check{x}\cos\phi-\overline{y}\sin\phi)}{\overline{h}_2}\tilde{V}\tilde{w}+\frac{\sin\psi}{\overline{h}_2}W\tilde{v}\Big)\cot\psi\cos^2\phi \\
-2\epsilon^2\frac{\overline{h}_1(1+\check{x}\cos\phi-\overline{y}\sin\phi)}{\overline{h}_2}\tilde{U}\tilde{u}\sin\phi+2\epsilon^2\frac{\overline{h}_1^{2}}{\sin\psi}(\tilde{u}\sin\psi+\tilde{w}\cos\psi\cos\phi) \\
+\mathrm{i}b\epsilon^2\frac{\overline{h}_1^{2}\sin\psi}{\overline{h}_2}\tilde{p}+b^2\epsilon^2\frac{\overline{h}_1^{2}\sin^2\psi}{\overline{h}_2^{2}}\tilde{v}-\frac{\overline{h}_1\sin^2\psi}{\overline{h}_2}\Big[\mathrm{i}\epsilon\frac{\partial}{\partial\check{x}}\Big(\frac{\overline{h}_2}{\overline{h}_1}\Big)+\mathrm{i}b\epsilon^2\frac{\partial}{\partial\overline{y}}\Big(\frac{\overline{h}_1}{\overline{h}_2}\Big)+\epsilon^2\frac{\partial}{\partial\eta}(\overline{h}_1\overline{h}_2)\frac{\partial}{\partial\eta}\Big]\tilde{v} \\
+\epsilon^2\overline{h}_1^{2}\Big[\Big(\frac{\sin\psi}{\overline{h}_2^{3}}\frac{\partial\overline{h}_2}{\partial\check{x}}\frac{\partial\overline{h}_2}{\partial\overline{y}}+\frac{\sin\psi}{\overline{h}_1^{2}\overline{h}_2}\frac{\partial\overline{h}_1}{\partial\check{x}}\frac{\partial\overline{h}_1}{\partial\overline{y}}\Big)\tilde{u}-\frac{\sin^2\psi}{\overline{h}_2^{2}}\tilde{v} \\
+2\mathrm{i}b\frac{\sin\psi}{\overline{h}_2^{2}}\Big(\frac{\partial\overline{h}_2}{\partial\check{x}}\tilde{u}+\frac{\partial\overline{h}_2}{\partial\eta}\tilde{w}\Big)+\Big(\frac{\sin\psi}{\overline{h}_1^{3}}\frac{\partial\overline{h}_1}{\partial\eta}\frac{\partial\overline{h}_1}{\partial\overline{y}}+\frac{\sin\psi}{\overline{h}_1\overline{h}_2^{2}}\frac{\partial\overline{h}_2}{\partial\eta}\frac{\partial\overline{h}_2}{\partial\overline{y}}\Big)\tilde{w}\Big]\Big\}
\end{aligned}
$$

$$
\begin{aligned}
+\frac{1}{\sin^2\psi}\Big(\epsilon^2\frac{\partial^2}{\partial\varphi^2}-1\Big)\Bigg[\\
\epsilon^2\overline{h}_1^2(2\cot\psi\sin\phi)\Big[\frac{(1+\check{x}\cos\phi-\overline{y}\sin\phi)}{\overline{h}_2}\tilde{U}\sin\phi-1\Big]\tilde{u}\\
-\epsilon\overline{h}_1^2\Big(\mathrm{i}\frac{(1+\check{x}\cos\phi-\overline{y}\sin\phi)}{\overline{h}_1}\tilde{U}+\mathrm{i}b\epsilon\frac{(1+\check{x}\cos\phi-\overline{y}\sin\phi)}{\overline{h}_2}\tilde{V}+\epsilon W\frac{\partial}{\partial\eta}\Big)\tilde{w}-\epsilon^2\overline{h}_1^2\frac{\partial W}{\partial\eta}\tilde{w}\\
-\mathrm{i}\frac{\epsilon^2\overline{h}_1^2}{\sin\psi}\frac{\partial}{\partial\eta}\Big(\Big[\mathrm{i}\frac{(1+\check{x}\cos\phi-\overline{y}\sin\phi)}{\overline{h}_1}\tilde{U}+\mathrm{i}b\epsilon\frac{(1+\check{x}\cos\phi-\overline{y}\sin\phi)}{\overline{h}_2}\tilde{V}+\epsilon W\frac{\partial}{\partial\eta}\Big]\tilde{u}\Big)\\
-\mathrm{i}\frac{\epsilon^3\overline{h}_1^3}{\sin\psi}\frac{\partial}{\partial\eta}\Big(\frac{\tilde{u}\tilde{U}\cos\phi}{\overline{h}_1}-\frac{\tilde{v}\tilde{U}\sin\phi}{\overline{h}_2}+\frac{(1+\check{x}\cos\phi-\overline{y}\sin\phi)}{\overline{h}_1}\frac{\partial\tilde{U}}{\partial\eta}\tilde{w}\\
+\frac{(1+\check{x}\cos\phi-\overline{y}\sin\phi)}{\overline{h}_1\overline{h}_2}(\tilde{U}\tilde{v}+\tilde{V}\tilde{u})\sin\phi\\
+\Big[\frac{(1+\check{x}\cos\phi-\overline{y}\sin\phi)}{\overline{h}_1}\tilde{U}\tilde{w}+\frac{\sin\psi}{\overline{h}_1}W\tilde{u}\Big]\cot\psi\sin^2\phi\Big)\\
+\mathrm{i}\frac{\epsilon^3\overline{h}_1^3}{\sin\psi}\frac{\partial}{\partial\eta}\Big[2\frac{(1+\check{x}\cos\phi-\overline{y}\sin\phi)}{\overline{h}_1\overline{h}_2}\tilde{V}\tilde{v}\cos\phi+2(\tilde{w}\cot\psi\sin\phi+\tilde{v})\Big]\\
-\frac{\epsilon^4\overline{h}_1^4}{\sin^2\psi}\frac{\partial}{\partial\eta}\Big\{\frac{\partial^2}{\partial\eta^2}\Big[\frac{\sin\psi(\tilde{u}\cos\phi+\tilde{v}\sin\phi)}{\overline{h}_1\overline{h}_2}+\mathrm{i}b\frac{\sin\psi}{\overline{h}_2}\tilde{v}+\\
+\Big(\frac{\cos\psi\cos^2\phi}{\overline{h}_2}+\frac{\cos\psi\sin^2\phi}{\overline{h}_1}\Big)\tilde{w}\Big]-\frac{\sin^2\psi}{\epsilon^2\overline{h}_1^2}\Big[\frac{\sin\psi(\tilde{u}\cos\phi+\tilde{v}\sin\phi)}{\overline{h}_1\overline{h}_2}+\mathrm{i}b\frac{\sin\psi}{\overline{h}_2}\tilde{v}+\\
+\Big(\frac{\cos\psi\cos^2\phi}{\overline{h}_2}+\frac{\cos\psi\sin^2\phi}{\overline{h}_1}\Big)\tilde{w}\Big]-\frac{b^2\tilde{u}}{\overline{h}_2^2}\\
+\frac{\sin^2\psi}{\overline{h}_1\overline{h}_2}\Big[\frac{\mathrm{i}}{\epsilon}\frac{\partial}{\partial\check{x}}\Big(\frac{\overline{h}_2}{\overline{h}_1}\Big)+\mathrm{i}b\frac{\partial}{\partial\overline{y}}\Big(\frac{\overline{h}_1}{\overline{h}_2}\Big)+\frac{\overline{h}_1\overline{h}_2}{\sin^2\psi}\frac{\partial}{\partial\eta}\Big]\tilde{u}\Big\}\\
+\mathrm{i}\frac{\epsilon^3\overline{h}_1^3}{\sin\psi}\frac{\partial}{\partial\eta}\Big\{\frac{\partial}{\partial\check{x}}\Big(\frac{1}{\overline{h}_1\overline{h}_2}\frac{\partial(\overline{h}_1\overline{h}_2)}{\partial\check{x}}\Big)\tilde{u}-2\mathrm{i}b\frac{\sin\psi}{\overline{h}_2^2}\frac{\partial\overline{h}_2}{\partial\check{x}}\tilde{v}\\
-\Big(\frac{\sin\psi}{\overline{h}_2^3}\frac{\partial\overline{h}_2}{\partial\overline{y}}\frac{\partial\overline{h}_2}{\partial\check{x}}+\frac{\sin\psi}{\overline{h}_1^2\overline{h}_2}\frac{\partial\overline{h}_1}{\partial\overline{y}}\frac{\partial\overline{h}_1}{\partial\check{x}}\Big)\tilde{v}-\Big(\frac{\sin\psi}{\overline{h}_1^3}\frac{\partial\overline{h}_1}{\partial\eta}\frac{\partial\overline{h}_1}{\partial\check{x}}+\frac{\sin\psi}{\overline{h}_1\overline{h}_2^2}\frac{\partial\overline{h}_2}{\partial\eta}\frac{\partial\overline{h}_2}{\partial\check{x}}\Big)\tilde{w}\Big\}\\
-\epsilon^2\overline{h}_1^2\Big\{\frac{b^2}{\overline{h}_2^2}\tilde{w}-\frac{\sin^2\psi}{\overline{h}_1\overline{h}_2}\Big[\frac{\mathrm{i}}{\epsilon}\frac{\partial}{\partial\check{x}}\Big(\frac{\overline{h}_2}{\overline{h}_1}\Big)+\mathrm{i}b\frac{\partial}{\partial\overline{y}}\Big(\frac{\overline{h}_1}{\overline{h}_2}\Big)+\frac{\overline{h}_1\overline{h}_2}{\sin^2\psi}\frac{\partial}{\partial\eta}\Big]\tilde{w}\Big\}\\
-\epsilon^2\overline{h}_1^2\Big\{\Big(\frac{\sin\psi}{\overline{h}_1^3}\frac{\partial\overline{h}_1}{\partial\check{x}}\frac{\partial\overline{h}_1}{\partial\eta}+\frac{\sin\psi}{\overline{h}_1\overline{h}_2^2}\frac{\partial\overline{h}_2}{\partial\check{x}}\frac{\partial\overline{h}_2}{\partial\eta}\Big)\tilde{u}-\Big(\frac{\sin\psi}{\overline{h}_2^3}\frac{\partial\overline{h}_2}{\partial\overline{y}}\frac{\partial\overline{h}_2}{\partial\eta}+\frac{\sin\psi}{\overline{h}_1^2\overline{h}_2}\frac{\partial\overline{h}_1}{\partial\overline{y}}\frac{\partial\overline{h}_1}{\partial\eta}\Big)\tilde{v}\\
-2\Big(\frac{\sin\psi}{\overline{h}_1^2}\frac{\partial\overline{h}_1}{\partial\eta}\frac{\partial\tilde{u}}{\partial\check{x}}+\frac{\sin\psi}{\overline{h}_2^2}\frac{\partial\overline{h}_2}{\partial\eta}\frac{\partial\tilde{v}}{\partial\overline{y}}\Big)+\frac{\partial}{\partial\eta}\Big(\frac{1}{\overline{h}_1\overline{h}_2}\frac{\partial(\overline{h}_1\overline{h}_2)}{\partial\eta}\Big)\tilde{w}\Big\}\Bigg]
\end{aligned}
\tag{8}
$$

$$
\begin{aligned}
\Big(\epsilon^2\frac{\partial^2}{\partial\varphi^2}-1\Big)^3\tilde{w} &= \epsilon^4\overline{h}_1^4 T\Big(\frac{\sin\psi}{\overline{h}_2}\eta\frac{\partial\overline{V}}{\partial\eta}(\check{x},\overline{y},0)\cos\phi+1\Big)\frac{\partial\overline{V}}{\partial\eta}(\check{x},\overline{y},0)\tilde{w} \\
&+\epsilon^2\overline{h}_1^2\frac{2\cot\psi\cos\phi}{\sin^2\psi}\Big(\epsilon^2\frac{\partial^2}{\partial\varphi^2}-1\Big)\Big[\frac{\sin\psi}{\overline{h}_2}\eta\frac{\partial\overline{V}}{\partial\eta}(\check{x},\overline{y},0)\cos\phi\Big]\tilde{v} \\
&+\epsilon^2\overline{h}_1^2\frac{2\cot\psi\cos\phi}{\sin^2\psi}\Big[\frac{\sin\psi}{\overline{h}_2}\eta\frac{\partial\overline{V}}{\partial\eta}(\check{x},\overline{y},0)\cos\phi+1\Big]\Big\{ \\
&\epsilon\overline{h}_1^2\Big[\mathrm{i}\frac{\sin\psi}{\overline{h}_1}\eta\frac{\partial\overline{U}}{\partial\eta}(\check{x},\overline{y},0)+\mathrm{i}b\epsilon\frac{\sin\psi}{\overline{h}_2}\eta\frac{\partial\overline{V}}{\partial\eta}(\check{x},\overline{y},0)+\epsilon W\frac{\partial}{\partial\eta}\Big]\tilde{v} \\
&+\epsilon^2\overline{h}_1\eta\frac{\partial^2\overline{V}}{\partial\check{x}\partial\eta}(\check{x},\overline{y},0)\tilde{u}-\epsilon^2\frac{\overline{h}_1^2}{\overline{h}_2}\eta\frac{\partial^2\overline{V}}{\partial\overline{y}\partial\eta}(\check{x},\overline{y},0)\tilde{v} \\
&+\epsilon^2\frac{\overline{h}_1\sin\psi}{\overline{h}_2}(\eta\frac{\partial\overline{U}}{\partial\eta}(\check{x},\overline{y},0)\tilde{v}+\eta\frac{\partial\overline{V}}{\partial\eta}(\check{x},\overline{y},0)\tilde{u})\cos\phi \\
&+\epsilon^2\overline{h}_1^2\Big(\frac{\sin\psi}{\overline{h}_2}\eta\frac{\partial\overline{V}}{\partial\eta}(\check{x},\overline{y},0)\tilde{w}+\frac{\sin\psi}{\overline{h}_2}W\tilde{v}\Big)\cot\psi\cos^2\phi \\
&-2\epsilon^2\frac{\overline{h}_1\sin\psi}{\overline{h}_2}\eta\frac{\partial\overline{U}}{\partial\eta}(\check{x},\overline{y},0)\tilde{u}\sin\phi+2\epsilon^2\frac{\overline{h}_1^2}{\sin\psi}(\tilde{u}\sin\psi+\tilde{w}\cos\psi\cos\phi) \\
&+\mathrm{i}b\epsilon^2\frac{\overline{h}_1^2\sin\psi}{\overline{h}_2}\tilde{p}+b^2\epsilon^2\frac{\overline{h}_1^2\sin^2\psi}{\overline{h}_2^2}\tilde{v}-\frac{\overline{h}_1\sin^2\psi}{\overline{h}_2}\Big[\mathrm{i}\epsilon\frac{\partial}{\partial\check{x}}\Big(\frac{\overline{h}_2}{\overline{h}_1}\Big)+\mathrm{i}b\epsilon^2\frac{\partial}{\partial\overline{y}}\Big(\frac{\overline{h}_1}{\overline{h}_2}\Big)+\epsilon^2\frac{\partial}{\partial\eta}(\overline{h}_1\overline{h}_2)\frac{\partial}{\partial\eta}\Big]\tilde{v} \\
&+\epsilon^2\overline{h}_1^2\Big[\Big(\frac{\sin\psi}{\overline{h}_2^3}\frac{\partial\overline{h}_2}{\partial\check{x}}\frac{\partial\overline{h}_2}{\partial\overline{y}}+\frac{\sin\psi}{\overline{h}_1^2\overline{h}_2}\frac{\partial\overline{h}_1}{\partial\check{x}}\frac{\partial\overline{h}_1}{\partial\overline{y}}\Big)\tilde{u}-\frac{\sin^2\psi}{\overline{h}_2^2}\tilde{v} \\
&+2\mathrm{i}b\frac{\sin\psi}{\overline{h}_2^2}\Big(\frac{\partial\overline{h}_2}{\partial\check{x}}\tilde{u}+\frac{\partial\overline{h}_2}{\partial\eta}\tilde{w}\Big)+\Big(\frac{\sin\psi}{\overline{h}_1^3}\frac{\partial\overline{h}_1}{\partial\eta}\frac{\partial\overline{h}_1}{\partial\overline{y}}+\frac{\sin\psi}{\overline{h}_1\overline{h}_2^2}\frac{\partial\overline{h}_2}{\partial\eta}\frac{\partial\overline{h}_2}{\partial\overline{y}}\Big)\tilde{w}\Big]\Big\}
\end{aligned}
$$

$$
\begin{aligned}
&+\frac{1}{\sin^2\psi}\Big(\epsilon^2\frac{\partial^2}{\partial\varphi^2}-1\Big)\Bigg[\\
&\epsilon^2\overline{h}_1^{2}(2\cot\psi\sin\phi)\Big[\frac{\sin\psi}{\overline{h}_2}\eta\frac{\partial\overline{U}}{\partial\eta}(\check{x},\overline{y},0)\sin\phi-1\Big]\tilde{u}\\
&-\epsilon\overline{h}_1^{2}\Big(\mathrm{i}\frac{\sin\psi}{\overline{h}_1}\eta\frac{\partial\overline{U}}{\partial\eta}(\check{x},\overline{y},0)+\mathrm{i}b\epsilon\frac{\sin\psi}{\overline{h}_2}\eta\frac{\partial\overline{V}}{\partial\eta}(\check{x},\overline{y},0)+\epsilon W\frac{\partial}{\partial\eta}\Big)\tilde{w}-\epsilon^2\overline{h}_1^{2}\frac{\partial W}{\partial\eta}\tilde{w}\\
&-\mathrm{i}\frac{\epsilon^2\overline{h}_1^{2}}{\sin\psi}\frac{\partial}{\partial\eta}\Big(\Big[\mathrm{i}\frac{\sin\psi}{\overline{h}_1}\eta\frac{\partial\overline{U}}{\partial\eta}(\check{x},\overline{y},0)+\mathrm{i}b\epsilon\frac{\sin\psi}{\overline{h}_2}\eta\frac{\partial\overline{V}}{\partial\eta}(\check{x},\overline{y},0)+\epsilon W\frac{\partial}{\partial\eta}\Big]\tilde{u}\Big)\\
&-\mathrm{i}\frac{\epsilon^3\overline{h}_1^{3}}{\sin\psi}\frac{\partial}{\partial\eta}\Big(\frac{1}{\overline{h}_1}\frac{\partial^2\overline{U}}{\partial\check{x}\partial\eta}\tilde{u}-\frac{1}{\overline{h}_2}\frac{\partial^2\overline{U}}{\partial\overline{y}\partial\eta}\tilde{v}+\frac{\sin\psi}{\overline{h}_1}\frac{\partial\overline{U}}{\partial\eta}(\check{x},\overline{y},0)\tilde{w}\\
&+\frac{\sin\psi}{\overline{h}_1\overline{h}_2}(\eta\frac{\partial\overline{U}}{\partial\eta}(\check{x},\overline{y},0)\tilde{v}+\eta\frac{\partial\overline{V}}{\partial\eta}(\check{x},\overline{y},0)\tilde{u})\sin\phi\\
&+\Big[\frac{\sin\psi}{\overline{h}_1}\eta\frac{\partial\overline{U}}{\partial\eta}(\check{x},\overline{y},0)\tilde{w}+\frac{\sin\psi}{\overline{h}_1}W\tilde{u}\Big]\cot\psi\sin^2\phi\Big)\\
&+\mathrm{i}\frac{\epsilon^3\overline{h}_1^{3}}{\sin\psi}\frac{\partial}{\partial\eta}\Big[2\frac{\sin\psi}{\overline{h}_1\overline{h}_2}\eta\frac{\partial\overline{V}}{\partial\eta}(\check{x},\overline{y},0)\tilde{v}\cos\phi+2(\tilde{w}\cot\psi\sin\phi+\tilde{v})\Big]\\
&-\frac{\epsilon^4\overline{h}_1^{4}}{\sin^2\psi}\frac{\partial}{\partial\eta}\Big\{\frac{\partial^2}{\partial\eta^2}\Big[\frac{\sin\psi(\tilde{u}\cos\phi+\tilde{v}\sin\phi)}{\overline{h}_1\overline{h}_2}+\mathrm{i}b\frac{\sin\psi}{\overline{h}_2}\tilde{v}+\\
&+\Big(\frac{\cos\psi\cos^2\phi}{\overline{h}_2}+\frac{\cos\psi\sin^2\phi}{\overline{h}_1}\Big)\tilde{w}\Big]-\frac{\sin^2\psi}{\epsilon^2\overline{h}_1^{2}}\Big[\frac{\sin\psi(\tilde{u}\cos\phi+\tilde{v}\sin\phi)}{\overline{h}_1\overline{h}_2}+\mathrm{i}b\frac{\sin\psi}{\overline{h}_2}\tilde{v}+\\
&+\Big(\frac{\cos\psi\cos^2\phi}{\overline{h}_2}+\frac{\cos\psi\sin^2\phi}{\overline{h}_1}\Big)\tilde{w}\Big]-\frac{b^2\tilde{u}}{\overline{h}_2^{2}}\\
&+\frac{\sin^2\psi}{\overline{h}_1\overline{h}_2}\Big[\frac{\mathrm{i}}{\epsilon}\frac{\partial}{\partial\check{x}}\Big(\frac{\overline{h}_2}{\overline{h}_1}\Big)+\mathrm{i}b\frac{\partial}{\partial\overline{y}}\Big(\frac{\overline{h}_1}{\overline{h}_2}\Big)+\frac{\overline{h}_1\overline{h}_2}{\sin^2\psi}\frac{\partial}{\partial\eta}\Big]\tilde{u}\Big\}\\
&+\mathrm{i}\frac{\epsilon^3\overline{h}_1^{3}}{\sin\psi}\frac{\partial}{\partial\eta}\Big\{\frac{\partial}{\partial\check{x}}\Big(\frac{1}{\overline{h}_1\overline{h}_2}\frac{\partial(\overline{h}_1\overline{h}_2)}{\partial\check{x}}\Big)\tilde{u}-2\mathrm{i}b\frac{\sin\psi}{\overline{h}_2^{2}}\frac{\partial\overline{h}_2}{\partial\check{x}}\tilde{v}\\
&-\Big(\frac{\sin\psi}{\overline{h}_2^{3}}\frac{\partial\overline{h}_2}{\partial\overline{y}}\frac{\partial\overline{h}_2}{\partial\check{x}}+\frac{\sin\psi}{\overline{h}_1^{2}\overline{h}_2}\frac{\partial\overline{h}_1}{\partial\overline{y}}\frac{\partial\overline{h}_1}{\partial\check{x}}\Big)\tilde{v}-\Big(\frac{\sin\psi}{\overline{h}_1^{3}}\frac{\partial\overline{h}_1}{\partial\eta}\frac{\partial\overline{h}_1}{\partial\check{x}}+\frac{\sin\psi}{\overline{h}_1\overline{h}_2^{2}}\frac{\partial\overline{h}_2}{\partial\eta}\frac{\partial\overline{h}_2}{\partial\check{x}}\Big)\tilde{w}\Big\}\\
&-\epsilon^2\overline{h}_1^{2}\Big\{\frac{b^2}{\overline{h}_2^{2}}\tilde{w}-\frac{\sin^2\psi}{\overline{h}_1\overline{h}_2}\Big[\frac{\mathrm{i}}{\epsilon}\frac{\partial}{\partial\check{x}}\Big(\frac{\overline{h}_2}{\overline{h}_1}\Big)+\mathrm{i}b\frac{\partial}{\partial\overline{y}}\Big(\frac{\overline{h}_1}{\overline{h}_2}\Big)+\frac{\overline{h}_1\overline{h}_2}{\sin^2\psi}\frac{\partial}{\partial\eta}\Big]\tilde{w}\Big\}\\
&-\epsilon^2\overline{h}_1^{2}\Big\{\Big(\frac{\sin\psi}{\overline{h}_1^{3}}\frac{\partial\overline{h}_1}{\partial\check{x}}\frac{\partial\overline{h}_1}{\partial\eta}+\frac{\sin\psi}{\overline{h}_1\overline{h}_2^{2}}\frac{\partial\overline{h}_2}{\partial\check{x}}\frac{\partial\overline{h}_2}{\partial\eta}\Big)\tilde{u}-\Big(\frac{\sin\psi}{\overline{h}_2^{3}}\frac{\partial\overline{h}_2}{\partial\overline{y}}\frac{\partial\overline{h}_2}{\partial\eta}+\frac{\sin\psi}{\overline{h}_1^{2}\overline{h}_2}\frac{\partial\overline{h}_1}{\partial\overline{y}}\frac{\partial\overline{h}_1}{\partial\eta}\Big)\tilde{v}\\
&-2\Big(\frac{\sin\psi}{\overline{h}_1^{2}}\frac{\partial\overline{h}_1}{\partial\eta}\frac{\partial\tilde{u}}{\partial\check{x}}+\frac{\sin\psi}{\overline{h}_2^{2}}\frac{\partial\overline{h}_2}{\partial\eta}\frac{\partial\tilde{v}}{\partial\overline{y}}\Big)+\frac{\partial}{\partial\eta}\Big(\frac{1}{\overline{h}_1\overline{h}_2}\frac{\partial(\overline{h}_1\overline{h}_2)}{\partial\eta}\Big)\tilde{w}\Big\}\Bigg]
\end{aligned}
\tag{9}
$$

BIBLIOGRAPHY

[1] ABRAMOWITZ, M. & STEGUN, I. A. (1964) 'A Handbook of Mathematical Functions.' Frankfurt: National Bureau of Standards.

[2] BASSOM, A. P. & HALL, P. (1991) 'Vortex instabilities in three-dimensional boundary layers: the relationship between Görtler and crossflow vortices.' *J. Fluid Mech.* **232**, 647-80.

[3] DENIER, J. P., HALL, P. & SEDDOUGUI, S. O. (1991) 'On the receptivity problem for Görtler vortices: vortex motions induced by wall roughness.' *Phil. Trans. R Soc. Lond.* A **335**, 51-85.

[4] EVANS. (1968) 'Laminar Boundary Layer Theory.' Addison-Wesley.

[5] GAJJAR, J. S. B. (1996) 'Nonlinear stability of crossflow vortices in compressible boundary layers.' *Stud. Appl. Math.* **96**, 53-84.

[6] GAJJAR, J. S. B. (2007) 'Nonlinear critical layers in the boundary layer on a rotating disk.' *J. Eng. Math.* **57**, 205-217.

[7] GARRETT, S. J. (2002) 'The stability and transition of the boundary layer on rotating bodies.' PhD Thesis, Cambridge University.

[8] GARRETT, S. J., HUSSAIN, Z. & STEPHEN, S. O. (2009) 'The crossflow instability of the boundary layer on a rotating cone.' *J. Fluid Mech.* **622**, 209-32.

[9] Garrett, S. J., Hussain, Z. & Stephen, S. O. (2009) 'Boundary-layer transition on broad cones rotating in an imposed axial flow.' *AIAA Conf.*, Texas, USA.

[10] Garrett, S. J. & Peake, N. (2005) 'The absolute instability of the boundary layer on a rotating cone.' *European. J. Mech. B.* **26**, 344-353.

[11] Görtler, H. (1940) 'Uber eine dreidimensionale instabilität laminare Grenzschubten an Konkaven Wänden.' *NACA TM* 1357.

[12] Gray, W. E. (1952) 'The effect of wing sweep on laminar flow.' *RAE TM Aero* **255**.

[13] Gregory, N., Stuart, J. T. & Walker, W. S. (1955) 'On the stability of three-dimensional boundary layers with application to the flow due to a rotating disk.' *Phil. Trans. R. Soc. Lond.* A **248**, 155-99.

[14] Hall, P. (1982) 'Taylor-Görtler vortices in fully developed or boundary-layer flows: linear theory.' *J. Fluid Mech.* **124**, 475-94.

[15] Hall, P. (1985) 'The Görtler vortex instability mechanism in three-dimensional boundary layers.' *Proc. R. Soc. Lond.* A **299**, 135-52.

[16] Hall, P. (1986) 'An asymptotic investigation of the stationary modes of instability of the boundary layer on a rotating disk.' *Proc. R. Soc. Lond.* A **406**, 93-106.

[17] Hall, P. (1988) 'The nonlinear development of Görtler vortices in growing boundary layers.' *J. Fluid Mech.* **193**, 247-66.

[18] Hall, P. (1990) 'Görtler vortices in growing boundary layers: the leading edge receptivity problem, linear growth and the nonlinear breakdown stage.' *Mathematika* **37**, 151-89.

[19] Hall, P. & Malik, M. R. (1986) 'On the stability of a three-dimensional attachment-line boundary layer: weakly non-linear theory and a numerical approach.' *J. Fluid Mech.* **163**, 257-82.

[20] Hussain, Z., Garrett, S. J., & Stephen, S. O. (2009) 'The convective instability of the boundary layer on a rotating disk in axial flow.' *Phys. Fluids*, submitted.

[21] Kappesser, R., Greif, R. & Cornet, I. (1973) 'Mass transfer on rotating cones.' *Appl. Sci. Res.* **28**, 442-52.

[22] Kármán, T. von (1921) 'Uber laminare und turbulente Reiburg.' *Z. Agnew. Math. Mech.* **1**, 233-52.

[23] Kobayashi, R. (1981) 'Linear stability theory of boundary layer along a cone rotating in axial flow.' *Bull. JSME* **24**, 934-40.

[24] Kobayashi, R. (1994) 'Review: Laminar-to-Turbulent Transition of Three-Dimensional Boundary Layers on Rotating Bodies.' *J. Fluids Eng.* **116**, 200-11.

[25] Kobayashi, R., Kohama, Y. & Kurosawa, M. (1983) 'Boundary-layer transition on a rotating cone in axial flow.' *J. Fluid Mech.* **127**, 341-52.

[26] Kobayashi, R. & Izumi, H. (1983) 'Boundary-layer transition on a rotating cone in still fluid.' *J. Fluid Mech.* **127**, 353-64.

[27] Koh, J. C. Y. & Price, J. F. (1967) 'Non-similar boundary-layer heat transfer on a rotating cone in forced flow.' *J. Heat Transfer* **89**, 139-45.

[28] Kohama, Y. (1984) 'Behaviour of spiral vortices on a rotating cone in axial flow.' *Acta Mech.* **51**, 105-17.

[29] Kohama, Y. (1985) 'Flow structures formed by axisymmetric spinning bodies.' *AIAA J.* **23**, 1445.

[30] Kohama, Y. (1985) 'Turbulent transition process of the spiral vortices appearing in the laminar boundary layer of a rotating cone.' *Phys.-Chem. Hydrodyn.* **6(5)**, 659.

[31] Kreith, F., Ellis, D. & Giesing, J. (1962) 'An experimental investigation of the flow engendered by a rotating cone.' *Appl. Sci. Res.* **A11**, 430-40.

[32] MacKerrell, S. O. (1987) 'A nonlinear asymptotic investigation of the stationary modes of instability of the 3 dimensional boundary layer on a rotating disk.' *Proc. R. Soc. Lond.* A **413**, 497-513.

[33] Malik, M. R. (1986) 'The neutral curve for stationary disturbances in rotating-disk flow.' *J. Fluid Mech.* **164**, 275-87.

[34] Meksyn, D. (1946) 'Stability of viscous flow between rotating cylinders. I' *Proc. R. Soc. Lond.* A **187**, 115-28.

[35] Mueller, T. J., Nelson, R. C., Kegelman, J. T. & Morkovin, M. V. (1981) 'Smoke visualisation of boundary-layer transition on a spinning axisymmetric body.' *AIAA J.* **19**, 1607.

[36] Reed, H. L. & Saric, W. S. (1989) 'Stability of three-dimensional boundary layers.' *Ann. Rev. Fluid Mech.* **21**, 235-84.

[37] Reshotko, E. (1994) 'Boundary-layer instability, transition and control.' *AIAA J.* **94**, 0001.

[38] Rosenhead, L. (1963) 'Laminar boundary layers.' Oxford.

[39] Salzberg, F. & Kezios, S. P. (1965) 'Mass transfer from a rotating cone in axisymmetric flow.' *J. Heat Transfer* **87**, 469-76.

[40] Saric, W. S., Reed, H. L. & White, E. B. (2003) 'Stability and transition of three-dimensional boundary layers.' *Ann. Rev. Fluid Mech.* **35**, 413-40.

[41] Smith, A. M. O. (1955) ‘On the growth of Taylor–Görtler vortices along highly concave walls.’ *Q. Appl. Maths* **13**, 233-62.

[42] Smith, F. T. (1979) ‘On the Non-Parallel Flow Stability of the Blasius Boundary Layer.’ *Proc. R. Soc. Lond.* A **366**, 91-109.

[43] Tein, C. L., & Campbell, D. T. (1963) ‘Heat and mass transfer from rotating cones.’ *J. Fluid Mech.* **17**, 105-12.